

5

Information from Paleoclimate Archives

Coordinating Lead Authors:

Valérie Masson-Delmotte (France), Michael Schulz (Germany)

Lead Authors:

Ayako Abe-Ouchi (Japan), Jürg Beer (Switzerland), Andrey Ganopolski (Germany), Jesus Fidel González Rouco (Spain), Eystein Jansen (Norway), Kurt Lambeck (Australia), Jürg Luterbacher (Germany), Tim Naish (New Zealand), Timothy Osborn (UK), Bette Otto-Bliesner (USA), Terrence Quinn (USA), Rengaswamy Ramesh (India), Maisa Rojas (Chile), XueMei Shao (China), Axel Timmermann (USA)

Contributing Authors:

Kevin Anchukaitis (USA), Julie Arblaster (Australia), Patrick J. Bartlein (USA), Gerardo Benito (Spain), Peter Clark (USA), Josefino C. Comiso (USA), Thomas Crowley (UK), Patrick De Deckker (Australia), Anne de Vernal (Canada), Barbara Delmonte (Italy), Pedro DiNezio (USA), Trond Dokken (Norway), Harry J. Dowsett (USA), R. Lawrence Edwards (USA), Hubertus Fischer (Switzerland), Dominik Fleitmann (UK), Gavin Foster (UK), Claus Fröhlich (Switzerland), Aline Govin (Germany), Alex Hall (USA), Julia Hargreaves (Japan), Alan Haywood (UK), Chris Hollis (New Zealand), Ben Horton (USA), Masa Kageyama (France), Reto Knutti (Switzerland), Robert Kopp (USA), Gerhard Krinner (France), Amaelle Landais (France), Camille Li (Norway/Canada), Dan Lunt (UK), Natalie Mahowald (USA), Shayne McGregor (Australia), Gerald Meehl (USA), Jerry X. Mitrovica (USA/Canada), Anders Moberg (Sweden), Manfred Mudelsee (Germany), Daniel R. Muhs (USA), Stefan Mulitz (Germany), Stefanie Müller (Germany), James Overland (USA), Frédéric Parrenin (France), Paul Pearson (UK), Alan Robock (USA), Eelco Rohling (Australia), Ulrich Salzmann (UK), Joel Savarino (France), Jan Sedláček (Switzerland), Jeremy Shakun (USA), Drew Shindell (USA), Jason Smerdon (USA), Olga Solomina (Russian Federation), Pavel Tarasov (Germany), Bo Vinther (Denmark), Claire Waelbroeck (France), Dieter Wolf-Gladrow (Germany), Yusuke Yokoyama (Japan), Masakazu Yoshimori (Japan), James Zachos (USA), Dan Zwart (New Zealand)

Review Editors:

Anil K. Gupta (India), Fatemeh Rahimzadeh (Iran), Dominique Raynaud (France), Heinz Wanner (Switzerland)

This chapter should be cited as:

Masson-Delmotte, V., M. Schulz, A. Abe-Ouchi, J. Beer, A. Ganopolski, J.F. González Rouco, E. Jansen, K. Lambeck, J. Luterbacher, T. Naish, T. Osborn, B. Otto-Bliesner, T. Quinn, R. Ramesh, M. Rojas, X. Shao and A. Timmermann, 2013: Information from Paleoclimate Archives. In: *Climate Change 2013: The Physical Science Basis. Contribution of Working Group I to the Fifth Assessment Report of the Intergovernmental Panel on Climate Change* [Stocker, T.F., D. Qin, G.-K. Plattner, M. Tignor, S.K. Allen, J. Boschung, A. Nauels, Y. Xia, V. Bex and P.M. Midgley (eds.)]. Cambridge University Press, Cambridge, United Kingdom and New York, NY, USA.

Table of Contents

Executive Summary	385
5.1 Introduction	388
5.2 Pre-Industrial Perspective on Radiative Forcing Factors	388
5.2.1 External Forcings.....	388
5.2.2 Radiative Perturbations from Greenhouse Gases and Dust	391
Box 5.1: Polar Amplification	396
5.3 Earth System Responses and Feedbacks at Global and Hemispheric Scales	398
5.3.1 High-Carbon Dioxide Worlds and Temperature.....	398
5.3.2 Glacial–Interglacial Dynamics.....	399
Box 5.2: Climate-Ice Sheet Interactions	402
5.3.3 Last Glacial Maximum and Equilibrium Climate Sensitivity	403
5.3.4 Past Interglacials.....	407
5.3.5 Temperature Variations During the Last 2000 Years	409
5.4 Modes of Climate Variability	415
5.4.1 Tropical Modes.....	415
5.4.2 Extratropical Modes.....	415
5.5 Regional Changes During the Holocene	417
5.5.1 Temperature.....	417
5.5.2 Sea Ice	420
5.5.3 Glaciers.....	421
5.5.4 Monsoon Systems and Convergence Zones	421
5.5.5 Megadroughts and Floods	422
5.6 Past Changes in Sea Level	425
5.6.1 Mid-Pliocene Warm Period	425
5.6.2 The Last Interglacial	425
5.6.3 Last Glacial Termination and Holocene	428
5.7 Evidence and Processes of Abrupt Climate Change	432
5.8 Paleoclimate Perspective on Irreversibility in the Climate System	433
5.8.1 Ice Sheets.....	433
5.8.2 Ocean Circulation.....	433
5.8.3 Next Glacial Inception.....	435
5.9 Concluding Remarks	435
References	436
Appendix 5.A: Additional Information on Paleoclimate Archives and Models	456
Frequently Asked Questions	
FAQ 5.1 Is the Sun a Major Driver of Recent Changes in Climate?	392
FAQ 5.2 How Unusual is the Current Sea Level Rate of Change?	430

Executive Summary

Greenhouse-Gas Variations and Past Climate Responses

It is a fact that present-day (2011) concentrations of the atmospheric greenhouse gases (GHGs) carbon dioxide (CO_2), methane (CH_4) and nitrous oxide (N_2O) exceed the range of concentrations recorded in ice cores during the past 800,000 years. Past changes in atmospheric GHG concentrations can be determined with *very high confidence*¹ from polar ice cores. Since AR4 these records have been extended from 650,000 years to 800,000 years ago. {5.2.2}

With very high confidence, the current rates of CO_2 , CH_4 and N_2O rise in atmospheric concentrations and the associated radiative forcing are unprecedented with respect to the highest resolution ice core records of the last 22,000 years. There is *medium confidence* that the rate of change of the observed GHG rise is also unprecedented compared with the lower resolution records of the past 800,000 years. {5.2.2}

There is high confidence that changes in atmospheric CO_2 concentration play an important role in glacial–interglacial cycles. Although the primary driver of glacial–interglacial cycles lies in the seasonal and latitudinal distribution of incoming solar energy driven by changes in the geometry of the Earth’s orbit around the Sun (“orbital forcing”), reconstructions and simulations together show that the full magnitude of glacial–interglacial temperature and ice volume changes cannot be explained without accounting for changes in atmospheric CO_2 content and the associated climate feedbacks. During the last deglaciation, it is *very likely*² that global mean temperature increased by 3°C to 8°C . While the mean rate of global warming was *very likely* 0.3°C to 0.8°C per thousand years, two periods were marked by faster warming rates, *likely* between 1°C and 1.5°C per thousand years, although regionally and on shorter time scales higher rates may have occurred. {5.3.2}

New estimates of the equilibrium climate sensitivity based on reconstructions and simulations of the Last Glacial Maximum (21,000 years to 19,000 years ago) show that values below 1°C as well as above 6°C for a doubling of atmospheric CO_2 concentration are very unlikely. In some models climate sensitivity differs between warm and cold climates because of differences in the representation of cloud feedbacks. {5.3.3}

With medium confidence, global mean surface temperature was significantly above pre-industrial levels during several past periods characterised by high atmospheric CO_2 concentrations. During the mid-Pliocene (3.3 to 3.0 million years ago), atmospheric

CO_2 concentrations between 350 ppm and 450 ppm (*medium confidence*) occurred when global mean surface temperatures were 1.9°C to 3.6°C (*medium confidence*) higher than for pre-industrial climate {5.3.1}. During the Early Eocene (52 to 48 million years ago), atmospheric CO_2 concentrations exceeded ~ 1000 ppm (*medium confidence*) when global mean surface temperatures were 9°C to 14°C (*medium confidence*) higher than for pre-industrial conditions. {5.3.1}

New temperature reconstructions and simulations of past climates show with high confidence polar amplification in response to changes in atmospheric CO_2 concentration. For high CO_2 climates such as the Early Eocene (52 to 48 million years ago) or mid-Pliocene (3.3 to 3.0 million years ago), and low CO_2 climates such as the Last Glacial Maximum (21,000 to 19,000 years ago), sea surface and land surface air temperature reconstructions and simulations show a stronger response to changes in atmospheric GHG concentrations at high latitudes as compared to the global average. {Box 5.1, 5.3.1, 5.3.3}

Global Sea Level Changes During Past Warm Periods

The current rate of global mean sea level change, starting in the late 19th–early 20th century, is, with medium confidence, unusually high in the context of centennial-scale variations of the last two millennia. The magnitude of centennial-scale global mean sea level variations did not exceed 25 cm over the past few millennia (*medium confidence*). {5.6.3}

There is very high confidence that the maximum global mean sea level during the last interglacial period (129,000 to 116,000 years ago) was, for several thousand years, at least 5 m higher than present and high confidence that it did not exceed 10 m above present. The best estimate is 6 m higher than present. Based on ice sheet model simulations consistent with elevation changes derived from a new Greenland ice core, the Greenland ice sheet *very likely* contributed between 1.4 and 4.3 m sea level equivalent, implying with *medium confidence* a contribution from the Antarctic ice sheet to the global mean sea level during the last interglacial period. {5.6.2}

There is high confidence that global mean sea level was above present during some warm intervals of the mid-Pliocene (3.3 to 3.0 million years ago), implying reduced volume of polar ice sheets. The best estimates from various methods imply with *high confidence* that sea level has not exceeded +20 m during the warmest periods of the Pliocene, due to deglaciation of the Greenland and West Antarctic ice sheets and areas of the East Antarctic ice sheet. {5.6.1}

¹ In this Report, the following summary terms are used to describe the available evidence: limited, medium, or robust; and for the degree of agreement: low, medium, or high. A level of confidence is expressed using five qualifiers: very low, low, medium, high, and very high, and typeset in italics, e.g., *medium confidence*. For a given evidence and agreement statement, different confidence levels can be assigned, but increasing levels of evidence and degrees of agreement are correlated with increasing confidence (see Section 1.4 and Box TS.1 for more details).

² In this Report, the following terms have been used to indicate the assessed likelihood of an outcome or a result: Virtually certain 99–100% probability, Very likely 90–100%, Likely 66–100%, About as likely as not 33–66%, Unlikely 0–33%, Very unlikely 0–10%, Exceptionally unlikely 0–1%. Additional terms (Extremely likely: 95–100%, More likely than not >50–100%, and Extremely unlikely 0–5%) may also be used when appropriate. Assessed likelihood is typeset in italics, e.g., *very likely* (see Section 1.4 and Box TS.1 for more details).

Observed Recent Climate Change in the Context of Interglacial Climate Variability

New temperature reconstructions and simulations of the warmest millennia of the last interglacial period (129,000 to 116,000 years ago) show with *medium confidence* that global mean annual surface temperatures were never more than 2°C higher than pre-industrial. High latitude surface temperature, averaged over several thousand years, was at least 2°C warmer than present (*high confidence*). Greater warming at high latitudes, seasonally and annually, confirm the importance of cryosphere feedbacks to the seasonal orbital forcing. During these periods, atmospheric GHG concentrations were close to the pre-industrial level. {5.3.4, Box 5.1}

There is *high confidence* that annual mean surface warming since the 20th century has reversed long-term cooling trends of the past 5000 years in mid-to-high latitudes of the Northern Hemisphere (NH). New continental- and hemispheric-scale annual surface temperature reconstructions reveal multi-millennial cooling trends throughout the past 5000 years. The last mid-to-high latitude cooling trend persisted until the 19th century, and can be attributed with *high confidence* to orbital forcing, according to climate model simulations. {5.5.1}

There is *medium confidence* from reconstructions that the current (1980–2012) summer sea ice retreat was unprecedented and sea surface temperatures in the Arctic were anomalously high in the perspective of at least the last 1450 years. Lower than late 20th century summer Arctic sea ice cover is reconstructed and simulated for the period between 8000 and 6500 years ago in response to orbital forcing. {5.5.2}

There is *high confidence* that minima in NH extratropical glacier extent between 8000 and 6000 years ago were primarily due to high summer insolation (orbital forcing). The current glacier retreat occurs within a context of orbital forcing that would be favourable for NH glacier growth. If glaciers continue to reduce at current rates, most extratropical NH glaciers will shrink to their minimum extent, which existed between 8000 and 6000 years ago, within this century (*medium confidence*). {5.5.3}

For average annual NH temperatures, the period 1983–2012 was very likely the warmest 30-year period of the last 800 years (*high confidence*) and likely the warmest 30-year period of the last 1400 years (*medium confidence*). This is supported by comparison of instrumental temperatures with multiple reconstructions from a variety of proxy data and statistical methods, and is consistent with AR4. In response to solar, volcanic and anthropogenic radiative changes, climate models simulate multi-decadal temperature changes over the last 1200 years in the NH, that are generally consistent in magnitude and timing with reconstructions, within their uncertainty ranges. {5.3.5}

Continental-scale surface temperature reconstructions show, with *high confidence*, multi-decadal periods during the Medieval Climate Anomaly (950 to 1250) that were in some regions as warm as in the mid-20th century and in others as warm as in the

late 20th century. With *high confidence*, these regional warm periods were not as synchronous across regions as the warming since the mid-20th century. Based on the comparison between reconstructions and simulations, there is *high confidence* that not only external orbital, solar and volcanic forcing, but also internal variability, contributed substantially to the spatial pattern and timing of surface temperature changes between the Medieval Climate Anomaly and the Little Ice Age (1450 to 1850). {5.3.5.3, 5.5.1}

There is *high confidence* for droughts during the last millennium of greater magnitude and longer duration than those observed since the beginning of the 20th century in many regions. There is *medium confidence* that more megadroughts occurred in monsoon Asia and wetter conditions prevailed in arid Central Asia and the South American monsoon region during the Little Ice Age (1450 to 1850) compared to the Medieval Climate Anomaly (950 to 1250). {5.5.4 and 5.5.5}

With *high confidence*, floods larger than those recorded since 1900 occurred during the past five centuries in northern and central Europe, western Mediterranean region and eastern Asia. There is *medium confidence* that modern large floods are comparable to or surpass historical floods in magnitude and/or frequency in the Near East, India and central North America. {5.5.5}

Past Changes in Climate Modes

New results from high-resolution coral records document with *high confidence* that the El Niño-Southern Oscillation (ENSO) system has remained highly variable throughout the past 7000 years, showing no discernible evidence for an orbital modulation of ENSO. This is consistent with the weak reduction in mid-Holocene ENSO amplitude of only 10% simulated by the majority of climate models, but contrasts with reconstructions reported in AR4 that showed a reduction in ENSO variance during the first half of the Holocene. {5.4.1}

With *high confidence*, decadal and multi-decadal changes in the winter North Atlantic Oscillation index (NAO) observed since the 20th century are not unprecedented in the context of the past 500 years. Periods of persistent negative or positive winter NAO phases, similar to those observed in the 1960s and 1990 to 2000s, respectively, are not unusual in the context of NAO reconstructions during at least the past 500 years. {5.4.2}

The increase in the strength of the observed summer Southern Annular Mode since 1950 has been anomalous, with *medium confidence*, in the context of the past 400 years. No similar spatially coherent multi-decadal trend can be detected in tree-ring indices from New Zealand, Tasmania and South America. {5.4.2}

Abrupt Climate Change and Irreversibility

With *high confidence*, the interglacial mode of the Atlantic Ocean meridional overturning circulation (AMOC) can recover from a short-term freshwater input into the subpolar North Atlantic. Approximately 8200 years ago, a sudden freshwater release

occurred during the final stages of North America ice sheet melting. Paleoclimate observations and model results indicate, with *high confidence*, a marked reduction in the strength of the AMOC followed by a rapid recovery, within approximately 200 years after the perturbation. {5.8.2}

Confidence in the link between changes in North Atlantic climate and low-latitude precipitation patterns has increased since AR4. From new paleoclimate reconstructions and modelling studies, there is *very high confidence* that reduced AMOC and the associated surface cooling in the North Atlantic region caused southward shifts of the Atlantic Intertropical Convergence Zone, and also affected the American (North and South), African and Asian monsoon systems. {5.7}

It is *virtually certain* that orbital forcing will be unable to trigger widespread glaciation during the next 1000 years. Paleoclimate records indicate that, for orbital configurations close to the present one, glacial inception only occurred for atmospheric CO₂ concentrations significantly lower than pre-industrial levels. Climate models simulate no glacial inception during the next 50,000 years if CO₂ concentrations remain above 300 ppm. {5.8.3, Box 6.2}

There is *high confidence* that the volumes of the Greenland and West Antarctic ice sheets were reduced during periods of the past few million years that were globally warmer than present. Ice sheet model simulations and geological data suggest that the West Antarctic ice sheet is very sensitive to subsurface Southern Ocean warming and imply with *medium confidence* a West Antarctic ice sheet retreat if atmospheric CO₂ concentration stays within or above the range of 350 ppm to 450 ppm for several millennia. {5.3.1, 5.6.1, 5.8.1}

5.1 Introduction

This chapter assesses the information on past climate obtained prior to the instrumental period. The information is based on data from various paleoclimatic archives and on modelling of past climate, and updates Chapter 6 of AR4 of IPCC Working Group I (Jansen et al., 2007).

The Earth system has responded and will continue to respond to various external forcings (solar, volcanic and orbital) and to changes in atmospheric composition. Paleoclimate data and modelling provide quantitative information on the Earth system response to these forcings. Paleoclimate information facilitates understanding of Earth system feedbacks on time scales longer than a few centuries, which cannot be evaluated from short instrumental records. Past climate changes also document transitions between different climate states, including abrupt events, which occurred on time scales of decades to a few centuries. They inform about multi-centennial to millennial baseline variability, against which the recent changes can be compared to assess whether or not they are unusual.

Major progress since AR4 includes the acquisition of new and more precise information from paleoclimate archives, the synthesis of regional information, and Paleoclimate Modelling Intercomparison Project Phase III (PMIP3) and Coupled Model Intercomparison Project Phase 5 (CMIP5) simulations using the same models as for projections (see Chapter 1). This chapter assesses the understanding of past climate variations, using paleoclimate reconstructions as well as climate models of varying complexity, while the model evaluation based on paleoclimate information is covered in Chapter 9. Additional paleoclimate perspectives are included in Chapters 6, 10 and 13 (see Table 5.1).

The content of this chapter is largely restricted to topics for which substantial new information has emerged since AR4. Examples include proxy-based estimates of the atmospheric carbon dioxide (CO_2) content during the past ~65 million years (Section 5.2.2) and magnitude of sea level variations during interglacial periods (Section 5.6.2). Information from glacial climates has been included only if the underlying processes are of direct relevance for an assessment of projected climate change. The impacts of past climate changes on biological systems and past civilizations are not covered, as these topics are beyond the scope of Working Group I.

The chapter proceeds from evidence for pre-industrial changes in atmospheric composition and external solar and volcanic forcings (Section 5.2, FAQ 5.1), to global and hemispheric responses (Section 5.3). After evaluating the evidence for past changes in climate modes of variability (Section 5.4), a specific focus is given to regional changes in temperature, cryosphere and hydroclimate during the current interglacial period (Section 5.5). Sections on sea level change (Section 5.6, FAQ 5.2), abrupt climate changes (Section 5.7) and illustrations of irreversibility and recovery time scales (Section 5.8) conclude the chapter. While polar amplification of temperature changes is addressed in Box 5.1, the relationships between ice sheets, sea level, atmospheric CO_2 concentration and climate are addressed in several sections (Box 5.2, Sections 5.3.1, 5.5, and 5.8.1).

Additional information to this chapter is available in the Appendix. Processed data underlying the figures are stored in the PANGAEA database (www.pangaea.de), while model output from PMIP3 is available from pmip3.lsce.ipsl.fr. In all sections, information is structured by time, going from past to present. Table 5.1 summarizes the past periods assessed in the subsections.

5.2 Pre-Industrial Perspective on Radiative Forcing Factors

5.2.1 External Forcings

5.2.1.1 Orbital Forcing

The term ‘orbital forcing’ is used to denote the incoming solar radiation changes originating from variations in the Earth’s orbital parameters as well as changes in its axial tilt. Orbital forcing is well known from precise astronomical calculations for the past and future (Laskar et al., 2004). Changes in eccentricity, longitude of perihelion (related to precession) and axial tilt (obliquity) (Berger and Loutre, 1991) predominantly affect the seasonal and latitudinal distribution and magnitude of solar energy received at the top of the atmosphere (AR4, Box 6.1; Jansen et al., 2007), and the durations and intensities of local seasons. Obliquity also modulates the annual mean insolation at any given latitude, with opposite effects at high and low latitudes. Orbital forcing is considered the pacemaker of transitions between glacials and interglacials (*high confidence*), although there is still no consensus on exactly how the different physical processes influenced by insolation changes interact to influence ice sheet volume (Box 5.2; Section 5.3.2). The different orbital configurations make each glacial and interglacial period unique (Yin and Berger, 2010; Tzedakis et al., 2012a). Multi-millennial trends of temperature, Arctic sea ice and glaciers during the current interglacial period, and specifically the last 2000 years, have been related to orbital forcing (Section 5.5).

5.2.1.2 Solar Forcing

Solar irradiance models (e.g., Wenzler et al., 2005) have been improved to explain better the instrumental measurements of total solar irradiance (TSI) and spectral (wavelength dependent) solar irradiance (SSI). Typical changes measured over an 11-year solar cycle are 0.1% for TSI and up to several percent for the ultraviolet (UV) part of SSI (see Section 8.4). Changes in TSI directly impact the Earth’s surface (see solar Box 10.2), whereas changes in UV primarily affect the stratosphere, but can influence the tropospheric circulation through dynamical coupling (Haigh, 1996). Most models attribute all TSI and SSI changes exclusively to magnetic phenomena at the solar surface (sunspots, faculae, magnetic network), neglecting any potential internal phenomena such as changes in energy transport (see also Section 8.4). The basic concept in solar models is to divide the solar surface into different magnetic features each with a specific radiative flux. The balance of contrasting dark sunspots and bright faculae and magnetic network leads to a higher TSI value during solar cycle maxima and at most wavelengths, but some wavelengths may be out of phase with the solar cycle (Harder et al., 2009; Cahalan et al., 2010; Haigh et al., 2010). TSI and SSI are calculated by adding the radiative fluxes of all features plus the contribution from

Table 5.1 | Summary of past periods for which climate information is assessed in the various sections of this chapter and other chapters of AR5. Calendar ages are expressed in Common Era (CE), geological ages are expressed in thousand years (ka) or million years (Ma) before present (BP), with present defined as 1950. Radiocarbon-based ages are quoted as the published calibrated ages.

Time Period	Age	Chapter 5 Sections							Other Chapters
		5.2	5.3	5.4	5.5	5.6	5.7	5.8	
Holocene ^a	11.65 ka ^g to present	✓	✓	✓	✓	✓			6, 9, 10
Pre-industrial period	refers to times before 1850 or 1850 values ^h								
Little Ice Age (LIA)	1450–1850 ⁱ	✓	✓	✓	✓	✓			10
Medieval Climate Anomaly (MCA) ^b	950–1250 ^j	✓	✓	✓	✓	✓			10
Last Millennium	1000–1999 ⁱ	✓	✓	✓	✓	✓			9, 10
Mid-Holocene (MH)	~6 ka				✓				9, 13
8.2-ka event	~8.2 ka ^g							✓	
Last Glacial Termination ^c			✓			✓			6
Younger Dryas ^d	12.85–11.65 ka ^g							✓	6
Bølling-Allerød ^e	14.64–12.85 ka ^g							✓	6
Meltwater Pulse 1A (MWP-1A)	14.65–14.31 ka ^k					✓			
Heinrich stadial 1 (HS1)	~19–14.64 ka ^l						✓		
Last Glacial Maximum (LGM)	~21–19 ka ^m	✓	✓	✓					6, 9
Last Interglacial (LIG) ⁱ	~129–116 ka ⁿ	✓	✓			✓		✓	13
Mid-Pliocene Warm Period (MPWP)	~3.3–3.0 Ma ^o	✓	✓			✓		✓	13
Early Eocene Climatic Optimum (EECO)	~52–50 Ma ^p	✓	✓						
Paleocene-Eocene Thermal Maximum (PETM)	~55.5–55.3 Ma ^q	✓	✓					✓	

Notes:

- ^a Also known as Marine Isotopic Stage (MIS) 1 or current interglacial.
- ^b Also known as Medieval Climate Optimum or the Medieval Warm Period.
- ^c Also known as Termination I or the Last Deglaciation. Based on sea level, Last Glacial Termination occurred between ~19 and ~6 ka.
- ^d Also known as Greenland Stadial GS-1.
- ^e Also known as Greenland Interstadial GI-a-c-e.
- ^f Also known as MIS5e, which overlaps with the Eemian (Shackleton et al., 2003).
- ^g As estimated from the Greenland ice core GICC05 chronology (Rasmussen et al., 2006; Thomas et al., 2007).
- ^h In this chapter, when referring to comparison of radiative forcing or climate variables, pre-industrial refers to 1850 values in accordance with Taylor et al. (2012). Otherwise it refers to an extended period of time before 1850 as stated in the text. Note that Chapter 7 uses 1750 as the reference pre-industrial period.
- ⁱ Different durations are reported in the literature. In Section 5.3.5, time intervals 950–1250 and 1450–1850 are used to calculate Northern Hemisphere temperature anomalies representative of the MCA and LIA, respectively.
- ^j Note that CMIP5 “Last Millennium simulations” have been performed for the period 850–1850 (Taylor et al., 2012).
- ^k As dated on Tahiti corals (Deschamps et al., 2012).
- ^l The duration of Heinrich stadial 1 (e.g., Stanford et al., 2011) is longer than the associated Heinrich event, which is indicated by ice-raftered debris in deep sea sediment cores from the North Atlantic Ocean (Hemming, 2004).
- ^m Period based on MARGO Project Members (2009). LGM simulations are performed for 21 ka. Note that maximum continental ice extent had already occurred at 26.5 ka (Clark et al., 2009).
- ⁿ Ages are maximum date for the onset and minimum age for the end from tectonically stable sites (cf. Section 5.6.2).
- ^o Dowsett et al. (2012).
- ^p Zachos et al. (2008).
- ^q Westerhold et al. (2007).

the magnetically inactive surface. These models can successfully reproduce the measured TSI changes between 1978 and 2003 (Balmaceda et al., 2007; Crouch et al., 2008), but not necessarily the last minimum of 2008 (Krivova et al., 2011). This approach requires detailed information of all the magnetic features and their temporal changes (Wenzler et al., 2006; Krivova and Solanki, 2008) (see Section 8.4).

The extension of TSI and SSI into the pre-satellite period poses two main challenges. First, the satellite period (since 1978) used to calibrate the solar irradiance models does not show any significant long-term trend. Second, information about the various magnetic features at the solar surface decreases back in time and must be deduced from proxies such as sunspot counts for the last 400 years and cosmogenic

radionuclides (^{10}Be and ^{14}C) for the past millennium (Muscheler et al., 2007; Delaygue and Bard, 2011) and the Holocene (Table 5.1) (Steinhilber et al., 2009; Vieira et al., 2011). ^{10}Be and ^{14}C records reflect not only solar activity, but also the geomagnetic field intensity and effects of their respective geochemical cycles and transport pathways (Pedro et al., 2011; Steinhilber et al., 2012). The corrections for these non-solar components, which are difficult to quantify, contribute to the overall error of the reconstructions (grey band in Figure 5.1c).

TSI reconstructions are characterized by distinct grand solar minima lasting 50 to 100 years (e.g., the Maunder Minimum, 1645–1715) that are superimposed upon long-term changes. Spectral analysis of TSI records reveals periodicities of 87, 104, 150, 208, 350, 510, ~980

and ~2200 years (Figure 5.1d) (Stuiver and Braziunas, 1993), but with time-varying amplitudes (Steinhilber et al., 2009; Vieira et al., 2011). All reconstructions rely ultimately on the same data (sunspots and cosmogenic radionuclides), but differ in the details of the methodologies. As a result the reconstructions agree rather well in their shape, but differ in their amplitude (Figure 5.1b) (Wang et al., 2005; Krivova et al., 2011; Lean et al., 2011; Schrijver et al., 2011) (see Section 8.4.1).

Since AR4, most recent reconstructions show a considerably smaller difference (<0.1%) in TSI between the late 20th century and the Late Maunder Minimum (1675–1715) when the sun was very quiet, compared to the often used reconstruction of Lean et al. (1995b) (0.24%) and Shapiro et al. (2011) (~0.4%). The Lean et al. (1995a) reconstruction has been used to scale solar forcing in simulations of the last millennium prior to PMIP3/CMIP5 (Table 5.A.1). PMIP3/CMIP5 last

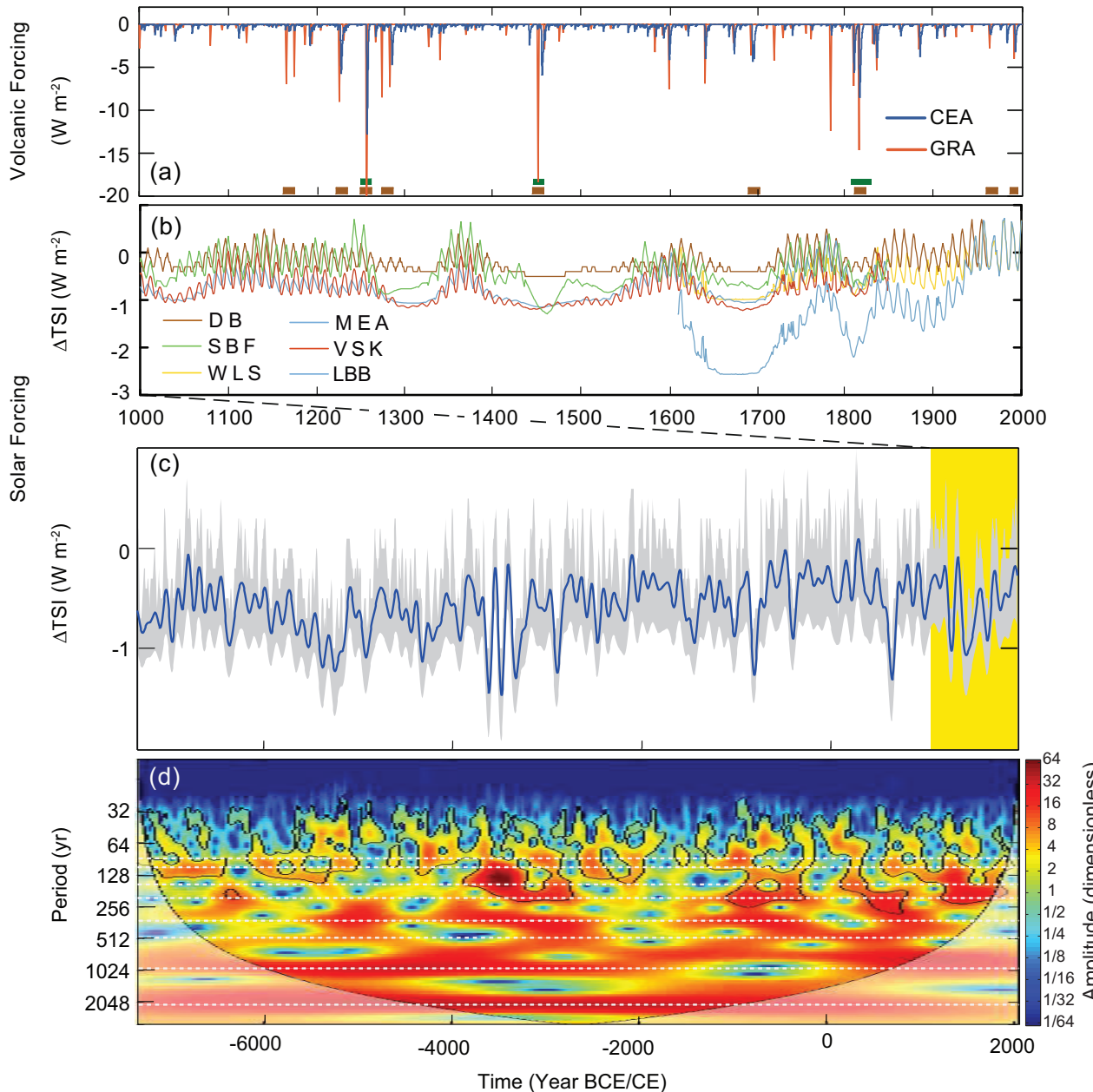


Figure 5.1 | (a) Two reconstructions of volcanic forcing for the past 1000 years derived from ice core sulphate and used for Paleoclimate Modelling Intercomparison Project Phase III (PMIP3) and Coupled Model Intercomparison Project Phase 5 (CMIP5) simulations (Schmidt et al., 2011). GRA: Gao et al. (2012); CEA: Crowley and Unterman (2013). Volcanic sulphate peaks identified from their isotopic composition as originating from the stratosphere are indicated by squares (green: Greenland; brown: Antarctica) (Baroni et al., 2008; Cole-Dai et al., 2009). (b) Reconstructed total solar irradiance (TSI) anomalies back to the year 1000. Proxies of solar activity (e.g., sunspots, ^{10}Be) are used to estimate the parameters of the models or directly TSI. All records except LBB (Lean et al., 1995b) have been used for PMIP3/CMIP5 simulations (Schmidt et al., 2011). DB: Delaygue and Bard (2011); MEA: Muscheler et al. (2007); SBF: Steinhilber et al. (2009); WLS: Wang et al. (2005); VSK: Vieira et al. (2011). For the years prior to 1600, the 11-year cycle has been added artificially to the original data with an amplitude proportional to the mean level of TSI. (c) Reconstructed TSI anomalies (100-year low-pass filtered; grey shading: 1 standard deviation uncertainty range) for the past 9300 years (Steinhilber et al., 2009). The reconstruction is based on ^{10}Be and calibrated using the relationship between instrumental data of the open magnetic field, which modulates the production of ^{10}Be , and TSI for the past four solar minima. The yellow band indicates the past 1000 years shown in more details in (a) and (b). Anomalies are relative to the 1976–2006 mean value (1366.14 W m^{-2}) of Wang et al. (2005). (d) Wavelet analysis (Torrence and Compo, 1998) of TSI anomalies from (c) with dashed white lines highlighting significant periodicities (Stuiver and Braziunas, 1993).

millennium simulations have used the weak solar forcing of recent reconstructions of TSI (Schmidt et al., 2011, 2012b) calibrated (Muscheler et al., 2007; Delaygue and Bard, 2011) or spliced (Steinhilber et al., 2009; Vieira and Solanki, 2010) to Wang et al. (2005). The larger range of past TSI variability in Shapiro et al. (2011) is not supported by studies of magnetic field indicators that suggest smaller changes over the 19th and 20th centuries (Svalgaard and Cliver, 2010; Lockwood and Owens, 2011).

Note that: (1) the recent new measurement of the absolute value of TSI and TSI changes during the past decades are assessed in Section 8.4.1.1; (2) the current state of understanding the effects of galactic cosmic rays on clouds is assessed in Sections 7.4.6 and 8.4.1.5 and (3) the use of solar forcing in simulations of the last millennium is discussed in Section 5.3.5.

5.2.1.3 Volcanic Forcing

Volcanic activity affects global climate through the radiative impacts of atmospheric sulphate aerosols injected by volcanic eruptions (see Sections 8.4.2 and 10.3.1). Quantifying volcanic forcing in the pre-satellite period is important for historical and last millennium climate simulations, climate sensitivity estimates and detection and attribution studies. Reconstructions of past volcanic forcing are based on sulphate deposition from multiple ice cores from Greenland and Antarctica, combined with atmospheric modelling of aerosol distribution and optical depth.

Since AR4, two new reconstructions of the spatial distribution of volcanic aerosol optical depth have been generated using polar ice cores, spanning the last 1500 years (Gao et al., 2008, 2012) and 1200 years (Crowley and Unterman, 2013) (Figure 5.1a). Although the relative size of eruptions for the past 700 years is generally consistent among these and earlier studies (Jansen et al., 2007), they differ in the absolute amplitude of peaks. There are also differences in the reconstructions of Icelandic eruptions, with an ongoing debate on the magnitude of stratospheric inputs for the 1783 Laki eruption (Thordarson and Self, 2003; Wei et al., 2008; Lanciki et al., 2012; Schmidt et al., 2012a). The recurrence time of past large volcanic aerosol injections (eruptions changing the radiative forcing (RF) by more than 1 W m^{-2}) varies from 3 to 121 years, with long-term mean value of 35 years (Gao et al., 2012) and 39 years (Crowley and Unterman, 2013), and only two or three periods of 100 years without such eruptions since 850.

Hegerl et al. (2006) estimated the uncertainty of the RF for a given volcanic event to be approximately 50%. Differences between reconstructions (Figure 5.1a) arise from different proxy data, identification of the type of injection, methodologies to estimate particle distribution and optical depth (Kravitz and Robock, 2011), and parameterization of scavenging for large events (Timmreck et al., 2009). Key limitations are associated with ice core chronologies (Plummer et al., 2012; Sigl et al., 2013), and deposition patterns (Moore et al., 2012).

A new independent methodology has recently been developed to distinguish between tropospheric and stratospheric volcanic aerosol deposits (Baroni et al., 2007). The stratospheric character of several large eruptions has started to be assessed from Greenland and/or

Antarctic ice core sulphur isotope data (Baroni et al., 2008; Cole-Dai et al., 2009; Schmidt et al., 2012b).

The use of different volcanic forcing reconstructions in pre-PMIP3/CMIP5 (see AR4 Chapter 6) and PMIP3/CMIP5 last millennium simulations (Schmidt et al., 2011) (Table 5.A.1), together with the methods used to implement these volcanic indices with different representations of aerosols in climate models, is a source of uncertainty in model intercomparisons. The impact of volcanic forcing on climate variations of the last millennium climate is assessed in Sections 5.3.5, 5.4, 5.5.1 and 10.7.1.

5.2.2 Radiative Perturbations from Greenhouse Gases and Dust

5.2.2.1 Atmospheric Concentrations of Carbon Dioxide, Methane and Nitrous Oxide from Ice Cores

Complementing instrumental data, air enclosed in polar ice provides a direct record of past atmospheric well-mixed greenhouse gas (WMGHG) concentrations albeit smoothed by firn diffusion (Joos and Spahni, 2008; Köhler et al., 2011). Since AR4, the temporal resolution of ice core records has been enhanced (MacFarling Meure et al., 2006; Ahn and Brook, 2008; Loulergue et al., 2008; Lüthi et al., 2008; Mischler et al., 2009; Schilt et al., 2010; Ahn et al., 2012; Bereiter et al., 2012). During the pre-industrial part of the last 7000 years, millennial (20 ppm CO_2 , 125 ppb CH_4) and centennial variations (up to 10 ppm CO_2 , 40 ppb CH_4 and 10 ppb N_2O) are recorded (see Section 6.2.2 and Figure 6.6). Significant centennial variations in CH_4 during the last glacial occur in phase with Northern Hemisphere (NH) rapid climate changes, while millennial CO_2 changes coincide with their Southern Hemisphere (SH) bipolar seesaw counterpart (Ahn and Brook, 2008; Loulergue et al., 2008; Lüthi et al., 2008; Grachev et al., 2009; Capron et al., 2010b; Schilt et al., 2010; Bereiter et al., 2012).

Long-term records have been extended from 650 ka in AR4 to 800 ka (Figures 5.2 and 5.3) (Loulergue et al., 2008; Lüthi et al., 2008; Schilt et al., 2010). During the last 800 ka, the pre-industrial ice core WMGHG concentrations stay within well-defined natural limits with maximum interglacial concentrations of approximately 300 ppm, 800 ppb and 300 ppb for CO_2 , CH_4 and N_2O , respectively, and minimum glacial concentrations of approximately 180 ppm, 350 ppb, and 200 ppb. The new data show lower than pre-industrial (280 ppm) CO_2 concentrations during interglacial periods from 800 to 430 ka (MIS19 to MIS13) (Figure 5.3). It is a fact that present-day (2011) concentrations of CO_2 (390.5 ppm), CH_4 (1803 ppb) and N_2O (324 ppm) (Annex II) exceed the range of concentrations recorded in the ice core records during the past 800 ka. With *very high confidence*, the rate of change of the observed anthropogenic WMGHG rise and its RF is unprecedented with respect to the highest resolution ice core record back to 22 ka for CO_2 , CH_4 and N_2O , accounting for the smoothing due to ice core enclosure processes (Joos and Spahni, 2008; Schilt et al., 2010). There is *medium confidence* that the rate of change of the observed anthropogenic WMGHG rise is also unprecedented with respect to the lower resolution records of the past 800 ka.

Progress in understanding the causes of past WMGHG variations is reported in Section 6.2.

Frequently Asked Questions

FAQ 5.1 | Is the Sun a Major Driver of Recent Changes in Climate?

Total solar irradiance (TSI, Chapter 8) is a measure of the total energy received from the sun at the top of the atmosphere. It varies over a wide range of time scales, from billions of years to just a few days, though variations have been relatively small over the past 140 years. Changes in solar irradiance are an important driver of climate variability (Chapter 1; Figure 1.1) along with volcanic emissions and anthropogenic factors. As such, they help explain the observed change in global surface temperatures during the instrumental period (FAQ 5.1, Figure 1; Chapter 10) and over the last millennium. While solar variability may have had a discernible contribution to changes in global surface temperature in the early 20th century, it cannot explain the observed increase since TSI started to be measured directly by satellites in the late 1970s (Chapters 8, 10).

The Sun's core is a massive nuclear fusion reactor that converts hydrogen into helium. This process produces energy that radiates throughout the solar system as electromagnetic radiation. The amount of energy striking the top of Earth's atmosphere varies depending on the generation and emission of electromagnetic energy by the Sun and on the Earth's orbital path around the Sun.

Satellite-based instruments have directly measured TSI since 1978, and indicate that on average, $\sim 1361 \text{ W m}^{-2}$ reaches the top of the Earth's atmosphere. Parts of the Earth's surface and air pollution and clouds in the atmosphere act as a mirror and reflect about 30% of this power back into space. Higher levels of TSI are recorded when the Sun is more active. Irradiance variations follow the roughly 11-year sunspot cycle: during the last cycles, TSI values fluctuated by an average of around 0.1%.

For pre-satellite times, TSI variations have to be estimated from sunspot numbers (back to 1610), or from radioisotopes that are formed in the atmosphere, and archived in polar ice and tree rings. Distinct 50- to 100-year periods of very low solar activity—such as the Maunder Minimum between 1645 and 1715—are commonly referred to as grand solar minima. Most estimates of TSI changes between the Maunder Minimum and the present day are in the order of 0.1%, similar to the amplitude of the 11-year variability.

How can solar variability help explain the observed global surface temperature record back to 1870? To answer this question, it is important to understand that other climate drivers are involved, each producing characteristic patterns of regional climate responses. However, it is the combination of them all that causes the observed climate change. Solar variability and volcanic eruptions are natural factors. Anthropogenic (human-produced) factors, on the other hand, include changes in the concentrations of greenhouse gases, and emissions of visible air pollution (aerosols) and other substances from human activities. 'Internal variability' refers to fluctuations within the climate system, for example, due to weather variability or phenomena like the El Niño-Southern Oscillation.

The relative contributions of these natural and anthropogenic factors change with time. FAQ 5.1, Figure 1 illustrates those contributions based on a very simple calculation, in which the mean global surface temperature variation represents the sum of four components linearly related to solar, volcanic, and anthropogenic forcing, and to internal variability. Global surface temperature has increased by approximately 0.8°C from 1870 to 2010 (FAQ 5.1, Figure 1a). However, this increase has not been uniform: at times, factors that cool the Earth's surface—volcanic eruptions, reduced solar activity, most anthropogenic aerosol emissions—have outweighed those factors that warm it, such as greenhouse gases, and the variability generated within the climate system has caused further fluctuations unrelated to external influences.

The solar contribution to the record of global surface temperature change is dominated by the 11-year solar cycle, which can explain global temperature fluctuations up to approximately 0.1°C between minima and maxima (FAQ 5.1, Figure 1b). A long-term increasing trend in solar activity in the early 20th century may have augmented the warming recorded during this interval, together with internal variability, greenhouse gas increases and a hiatus in volcanism. However, it cannot explain the observed increase since the late 1970s, and there was even a slight decreasing trend of TSI from 1986 to 2008 (Chapters 8 and 10).

Volcanic eruptions contribute to global surface temperature change by episodically injecting aerosols into the atmosphere, which cool the Earth's surface (FAQ 5.1, Figure 1c). Large volcanic eruptions, such as the eruption of Mt. Pinatubo in 1991, can cool the surface by around 0.1°C to 0.3°C for up to three years. (continued on next page)

FAQ 5.1 (continued)

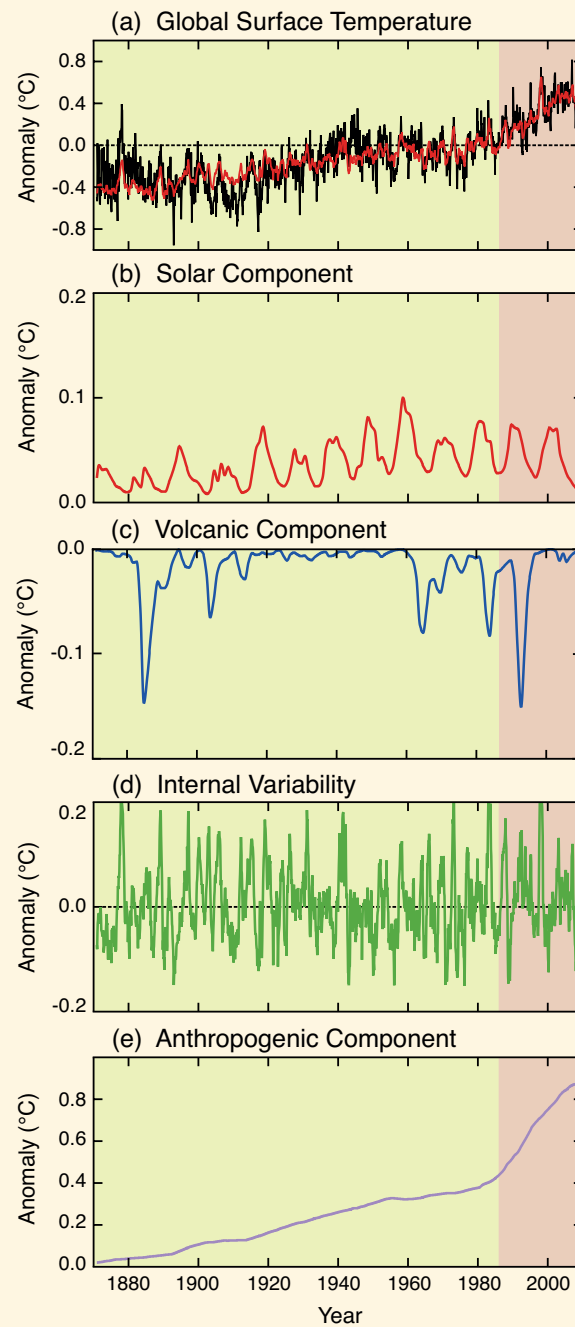
The most important component of internal climate variability is the El Niño Southern Oscillation, which has a major effect on year-to-year variations of tropical and global mean temperature (FAQ 5.1, Figure 1d). Relatively high annual temperatures have been encountered during El Niño events, such as in 1997–1998.

The variability of observed global surface temperatures from 1870 to 2010 (Figure 1a) reflects the combined influences of natural (solar, volcanic, internal; FAQ 5.1, Figure 1b–d) factors, superimposed on the multi-decadal warming trend from anthropogenic factors (FAQ 5.1, Figure 1e).

Prior to 1870, when anthropogenic emissions of greenhouse gases and aerosols were smaller, changes in solar and volcanic activity and internal variability played a more important role, although the specific contributions of these individual factors to global surface temperatures are less certain. Solar minima lasting several decades have often been associated with cold conditions. However, these periods are often also affected by volcanic eruptions, making it difficult to quantify the solar contribution.

At the regional scale, changes in solar activity have been related to changes in surface climate and atmospheric circulation in the Indo-Pacific, Northern Asia and North Atlantic areas. The mechanisms that amplify the regional effects of the relatively small fluctuations of TSI in the roughly 11-year solar cycle involve dynamical interactions between the upper and the lower atmosphere, or between the ocean sea surface temperature and atmosphere, and have little effect on global mean temperatures (see Box 10.2).

Finally, a decrease in solar activity during the past solar minimum a few years ago (FAQ 5.1, Figure 1b) raises the question of its future influence on climate. Despite uncertainties in future solar activity, there is *high confidence* that the effects of solar activity within the range of grand solar maxima and minima will be much smaller than the changes due to anthropogenic effects.



FAQ 5.1, Figure 1 | Global surface temperature anomalies from 1870 to 2010, and the natural (solar, volcanic, and internal) and anthropogenic factors that influence them. (a) Global surface temperature record (1870–2010) relative to the average global surface temperature for 1961–1990 (black line). A model of global surface temperature change (a: red line) produced using the sum of the impacts on temperature of natural (b, c, d) and anthropogenic factors (e). (b) Estimated temperature response to solar forcing. (c) Estimated temperature response to volcanic eruptions. (d) Estimated temperature variability due to internal variability, here related to the El Niño-Southern Oscillation. (e) Estimated temperature response to anthropogenic forcing, consisting of a warming component from greenhouse gases, and a cooling component from most aerosols.

5.2.2.2 Atmospheric Carbon Dioxide Concentrations from Geological Proxy Data

Geological proxies provide indirect information on atmospheric CO₂ concentrations for time intervals older than those covered by ice core records (see Section 5.2.2.1). Since AR4, the four primary proxy CO₂ methods have undergone further development (Table 5.A.2). A reassessment of biological respiration and carbonate formation has reduced CO₂ reconstructions based on fossil soils by approximately 50% (Breecker et al., 2010). Bayesian statistical techniques for calibrating leaf stomatal density reconstructions produce consistently higher CO₂ estimates than previously assessed (Beerling et al., 2009), resulting in more convergence between estimates from these two terrestrial proxies. Recent CO₂ reconstructions using the boron isotope proxy provide an improved understanding of foraminifer species effects and evolution of seawater alkalinity (Hönisch and Hemming, 2005) and seawater boron isotopic composition (Foster et al., 2012). Quantification of the phytoplankton cell-size effects on carbon isotope fractionation has also improved the consistency of the alkenone method (Henderiks and Pagani, 2007). These proxies have also been applied more widely and at higher temporal resolution to a range of geological archives, resulting in an increased number of atmospheric CO₂ estimates since 65 Ma (Beerling and Royer, 2011). Although there is improved consensus between the proxy CO₂ estimates, especially the marine proxy estimates, a significant degree of variation among the different techniques remains. All four techniques have been included in the assessment, as there is insufficient knowledge to discriminate between different proxy estimates on the basis of confidence (assessed in Table 5.A.2).

In the time interval between 65 and 23 Ma, all proxy estimates of CO₂ concentration span a range of 300 ppm to 1500 ppm (Figure 5.2). An independent constraint on Early Eocene atmospheric CO₂ concentration is provided by the occurrence of the sodium carbonate mineral nahcolite, in about 50 Ma lake sediments, which precipitates in association with halite at the sediment–water interface only at CO₂ levels >1125 ppm (Lowenstein and Demicco, 2006), and thus provides a potential lower bound for atmospheric concentration (*medium confidence*) during the warmest period of the last 65 Ma, the Early Eocene Climatic Optimum (EECO; 52 to 50 Ma; Table 5.1), which is inconsistent with lower estimates from stomata and paleosoils. Although the reconstructions indicate a general decrease in CO₂ concentrations since about 50 Ma (Figure 5.2), the large scatter of proxy data precludes a robust assessment of the second-order variation around this overall trend.

Since 23 Ma, CO₂ proxy estimates are at pre-industrial levels with exception of the Middle Miocene climatic optimum (17 to 15 Ma) and the Pliocene (5.3 to 2.6 Ma), which have higher concentrations. Although new CO₂ reconstructions for the Pliocene based on marine proxies have produced consistent estimates mostly in the range 350 ppm to 450 ppm (Pagani et al., 2010; Seki et al., 2010; Bartoli et al., 2011), the uncertainties associated with these marine estimates remain difficult to quantify. Several boron-derived data sets agree within error (± 25 ppm) with the ice core records (Foster, 2008; Hönisch et al., 2009), but alkenone data for the ice core period are outside the error limits (Figure 5.2). We conclude that there is *medium confidence* that CO₂ levels were above pre-industrial interglacial concentration (~280 ppm)

and did not exceed ~450 ppm during the Pliocene, with interglacial values in the upper part of that range between 350 and 450 ppm.

5.2.2.3 Past Changes in Mineral Dust Aerosol Concentrations

Past changes in mineral dust aerosol (MDA) are important for estimates of climate sensitivity (see Section 5.3.3) and for its supply of nutrients, especially iron to the Southern Ocean (see Section 6.2). MDA concentration is controlled by variations in dust sources, and by changes in atmospheric circulation patterns acting on its transport and lifetime.

Since AR4, new records of past MDA flux have been obtained from deep-sea sediment and ice cores. A 4 million-year MDA-flux reconstruction from the Southern Ocean (Figure 5.2) implies reduced dust generation and transport during the Pliocene compared to Holocene levels, followed by a significant rise around 2.7 Ma when NH ice volume increased (Martinez-Garcia et al., 2011). Central Antarctic ice core records show that local MDA deposition fluxes are ~20 times higher during glacial compared to interglacial periods (Fischer et al., 2007; Lambert et al., 2008; Petit and Delmonte, 2009). This is due to enhanced dust production in southern South America and perhaps Australia (Gaiero, 2007; De Deckker et al., 2010; Gabrielli et al., 2010; Martinez-Garcia et al., 2011; Wegner et al., 2012). The impact of changes in MDA lifetime (Petit and Delmonte, 2009) on dust fluxes in Antarctica remains uncertain (Fischer et al., 2007; Wolff et al., 2010). Equatorial Pacific glacial–interglacial MDA fluxes co-vary with Antarctic records, but with a glacial–interglacial ratio in the range of approximately three to four (Winckler et al., 2008), attributed to enhanced dust production from Asian and northern South American sources in glacial times (Maher et al., 2010). The dominant dust source regions (e.g., North Africa, Arabia and Central Asia) show complex patterns of variability (Roberts et al., 2011). A glacial increase of MDA source strength by a factor of 3 to 4 requires low vegetation cover, seasonal aridity, and high wind speeds (Fischer et al., 2007; McGee et al., 2010). In Greenland ice cores, MDA ice concentrations are higher by a factor of 100 and deposition fluxes by a factor 20 during glacial periods (Ruth et al., 2007). This is due mainly to changes in the dust sources for Greenland (Asian desert areas), increased gustiness (McGee et al., 2010) and atmospheric lifetime and transport of MDA (Fischer et al., 2007). A strong coherence is observed between dust in Greenland ice cores and aeolian deposition in European loess formations (Antoine et al., 2009).

Global data synthesis shows two to four times more dust deposition at the Last Glacial Maximum (LGM; Table 5.1) than today (Derbyshire, 2003; Maher et al., 2010). Based on data–model comparisons, estimates of global mean LGM dust RF vary from -3 W m^{-2} to $+0.1\text{ W m}^{-2}$, due to uncertainties in radiative properties. The best estimate value remains at -1 W m^{-2} as in AR4 (Claquin et al., 2003; Mahowald et al., 2006, 2011; Patadia et al., 2009; Takemura et al., 2009; Yue et al., 2010). Models may underestimate the MDA RF at high latitudes (Lambert et al., 2013).

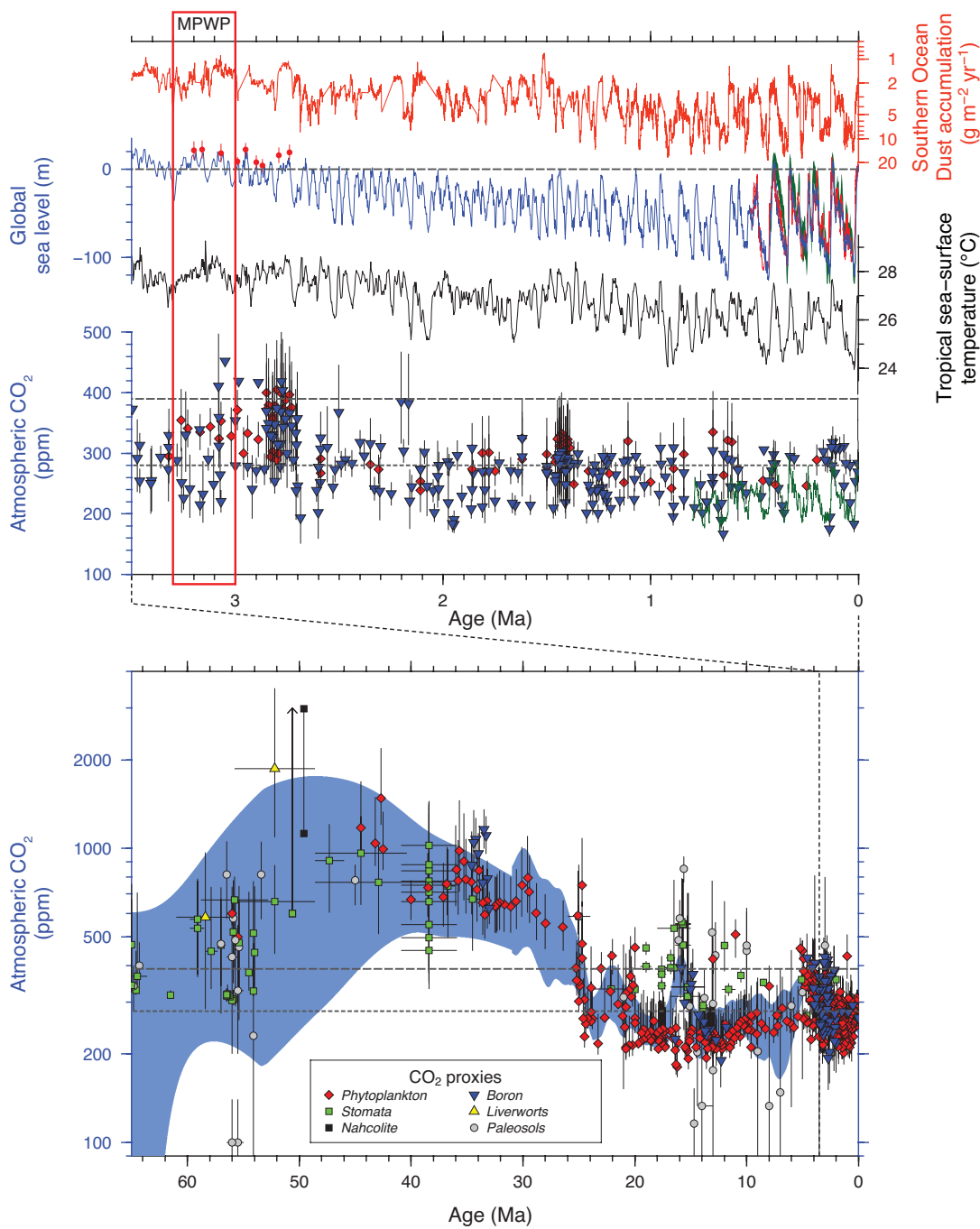


Figure 5.2 | (Top) Orbital-scale Earth system responses to radiative forcings and perturbations from 3.5 Ma to present. Reconstructed dust mass accumulation rate is from the Atlantic sector of the Southern Ocean (red) (Martinez-Garcia et al., 2011). Sea level curve (blue) is the stacked $\delta^{18}\text{O}$ proxy for ice volume and ocean temperature (Lisiecki and Raymo, 2005) calibrated to global average eustatic sea level (Naish and Wilson, 2009; Miller et al., 2012a). Also shown are global eustatic sea level reconstructions for the last 500 kyr based on sea level calibration of the $\delta^{18}\text{O}$ curve using dated coral shorelines (green line; Waelbroeck et al., 2002) and the Red Sea isotopic reconstruction (red line; Rohling et al., 2009). Weighted mean estimates (2 standard deviation uncertainty) for far-field reconstructions of eustatic peaks are shown for mid-Pliocene interglacials (red dots; Miller et al., 2012a). The dashed horizontal line represents present-day sea level. Tropical sea surface temperature (black line) based on a stack of four alkenone-based sea surface temperature reconstructions (Herbert et al., 2010). Atmospheric carbon dioxide (CO_2) measured from Antarctic ice cores (green line, Petit et al., 1999; Siegenthaler et al., 2005; Lüthi et al., 2008), and estimates of CO_2 from boron isotopes ($\delta^{11}\text{B}$) in foraminifera in marine sediments (blue triangles; Hönisch et al., 2009; Seki et al., 2010; Bartoli et al., 2011), and phytoplankton alkenone-derived carbon isotope proxies (red diamonds; Pagani et al., 2010; Seki et al., 2010), plotted with 2 standard deviation uncertainty. Present (2012) and pre-industrial CO_2 concentrations are indicated with long-dashed and short-dashed grey lines, respectively. (Bottom) Concentration of atmospheric CO_2 for the last 65 Ma is reconstructed from marine and terrestrial proxies (Cerling, 1992; Freeman and Hayes, 1992; Koch et al., 1992; Stott, 1992; van der Burgh et al., 1993; Sinha and Stott, 1994; Kürschner, 1996; McElwain, 1998; Ekart et al., 1999; Pagani et al., 1999a, 1999b, 2005a, 2005b, 2010, 2011; Kürschner et al., 2001, 2008; Royer et al., 2001a, 2001b; Beerling et al., 2002, 2009; Beerling and Royer, 2002; Nordt et al., 2002; Greenwood et al., 2003; Royer, 2003; Lowenstein and Demicco, 2006; Fletcher et al., 2008; Pearson et al., 2009; Retallack, 2009b, 2009a; Tripathi et al., 2009; Seki et al., 2010; Smith et al., 2010; Bartoli et al., 2011; Doria et al., 2011; Foster et al., 2012). Individual proxy methods are colour-coded (see also Table A5.1). The light blue shading is a 1-standard deviation uncertainty band constructed using block bootstrap resampling (Mudelsee et al., 2012) for a kernel regression through all the data points with a bandwidth of 8 Myr prior to 30 Ma, and 1 Myr from 30 Ma to present. Most of the data points for CO_2 proxies are based on duplicate and multiple analyses. The red box labelled MPWP represents the mid-Pliocene Warm Period (3.3 to 3.0 Ma; Table 5.1).

Box 5.1 | Polar Amplification

Polar amplification occurs if the magnitude of zonally averaged surface temperature change at high latitudes exceeds the globally averaged temperature change, in response to climate forcings and on time scales greater than the annual cycle. Polar amplification is of global concern due to the potential effects of future warming on ice sheet stability and, therefore, global sea level (see Sections 5.6.1, 5.8.1 and Chapter 13) and carbon cycle feedbacks such as those linked with permafrost melting (see Chapter 6).

Some external climate forcings have an enhanced radiative impact at high latitudes, such as orbital forcing (Section 5.2.1.1), or black carbon (Section 8.3.4). Here, we focus on the latitudinal response of surface temperature to CO₂ perturbations. The magnitude of polar amplification depends on the relative strength and duration of different climate feedbacks, which determine the transient and equilibrium response to external forcings. This box first describes the different feedbacks operating in both polar regions, and then contrasts polar amplification depicted for past high CO₂ and low CO₂ climates with projected temperature patterns for the RCP8.5 future greenhouse gas (WMGHG) emission scenario.

In the Arctic, the sea ice/ocean surface albedo feedback plays an important role (Curry et al., 1995; Serreze and Barry, 2011). With retreating sea ice, surface albedo decreases, air temperatures increase and the ocean can absorb more heat. The resulting ocean warming contributes to further sea ice melting. The sea ice/ocean surface albedo feedback can exhibit threshold behaviour when temperatures exceed the freezing point of sea ice. This may also translate into a strong seasonality of the response characteristics. Other feedbacks, including water vapour and cloud feedbacks have been suggested as important amplifiers of Arctic climate change (Vavrus, 2004; Abbot and Tziperman, 2008, 2009; Graversen and Wang, 2009; Lu and Cai, 2009; Screen and Simmonds, 2010; Bintanja et al., 2011). In continental Arctic regions with seasonal snow cover, changes in radiative forcing (RF) can heavily influence snow cover (Ghatak et al., 2010), and thus surface albedo. Other positive feedbacks operating on time scales of decades-to-centuries in continental high-latitude regions are associated with surface vegetation changes (Bhatt et al., 2010) and thawing permafrost (e.g., Walter et al., 2006). On glacial-to-interglacial time scales, the very slow ice sheet–albedo response to external forcings (see Box 5.2) is a major contributor to polar amplification in the Northern Hemisphere.

An amplified response of Southern Ocean sea surface temperature (SST) to radiative perturbations also emerges from the sea ice–albedo feedback. However, in contrast to the Arctic Ocean, which in parts is highly stratified, mixed-layer depths in the Southern Ocean typically exceed several hundreds of meters, which allows the ocean to take up vast amounts of heat (Böning et al., 2008; Gille, 2008; Sokolov and Rintoul, 2009) and damp the SST response to external forcing. This process, and the presence of the ozone hole over the Antarctic ice sheet (Thompson and Solomon, 2002, 2009), can affect the transient response of surface warming of the Southern Ocean and Antarctica, and lead to different patterns of future polar amplification on multi-decadal to multi-centennial time scales. In response to rapid atmospheric CO₂ changes, climate models indeed project an asymmetric warming between the Arctic and Southern Oceans, with an earlier response in the Arctic and a delayed response in the Southern Ocean (Section 12.4.3). Above the Antarctic ice sheet, however, surface air temperature can respond quickly to radiative perturbations owing to the limited role of latent heat flux in the surface energy budget of Antarctica.

These differences in transient and equilibrium responses of surface temperatures on Antarctica, the Southern Ocean and over continents and oceans in the Arctic domain can explain differences in the latitudinal temperature patterns depicted in Box 5.1, Figure 1 for past periods (equilibrium response) and future projections (transient response).

Box 5.1, Figure 1 illustrates the polar amplification phenomenon for three different periods of the Earth's climate history using temperature reconstructions from natural archives and climate model simulations for: (i) the Early Eocene Climatic Optimum (EECO, 54 to 48 Ma) characterised by CO₂ concentrations of 1000 to 2000 ppm (Section 5.2.2.2) and the absence of continental ice sheets; (ii) the mid-Pliocene Warm Period (MPWP, 3.3 to 3.0 Ma), characterized by CO₂ concentrations in the range of 350 to 450 ppm (Section 5.2.2.2) and reduced Greenland and Antarctic ice sheets compared to today (see Section 5.6.1), (iii) the Last Glacial Maximum (LGM, 21 to 19 ka), characterized by CO₂ concentrations around 200 ppm and large continental ice sheets covering northern Europe and North America.

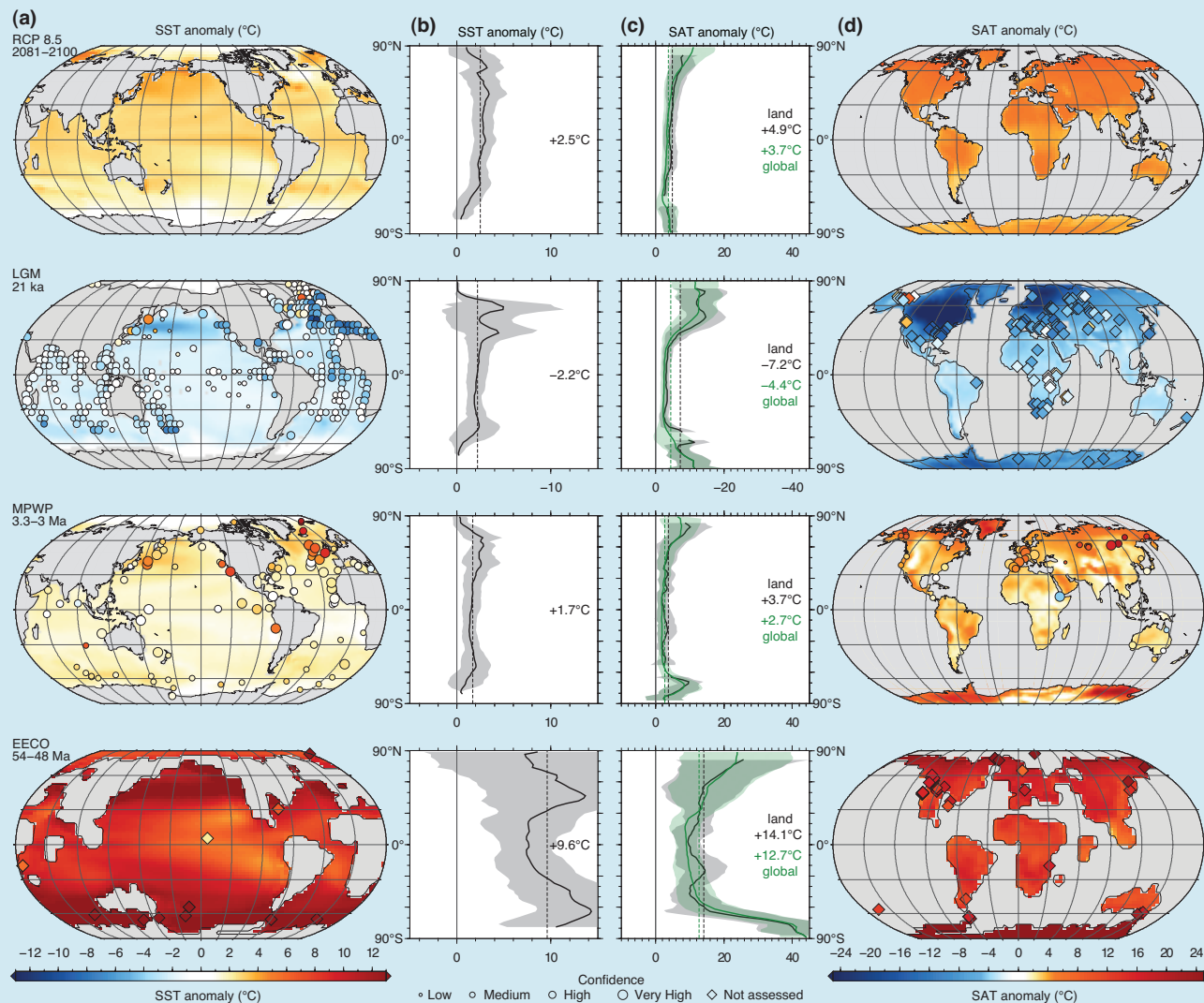
Throughout all three time periods, reconstructions and simulations reveal Arctic and Antarctic surface air temperature amplification of up to two times the global mean (Box 5.1, Figure 1c, d), and this bipolar amplification appears to be a robust feature of the equilibrium Earth system response to changes of CO₂ concentration, irrespective of climate state. The absence (EECO), or expansion (LGM) of continental ice sheets has the potential to affect the zonally averaged surface temperatures due to the lapse-rate effect (see Box 5.2), hence contributing to polar amplification. However, polar amplification is also suppressed in zonally averaged gradients of SST compared with terrestrial surface air temperature (Box 5.1, Figure 1), owing to the presence of high-latitude sea ice in the pre-industrial control,

(continued on next page)

Box 5.1 (continued)

which places a lower limit on SST. Global mean temperature estimates for these three past climates also imply an Earth system climate sensitivity to radiative perturbations up to two times higher than the equilibrium climate sensitivity (Lunt et al., 2010; Haywood et al., 2013) (see Section 5.3.1 and Box 12.2).

Polar amplification explains in part why Greenland Ice Sheet (GIS) and the West Antarctic Ice Sheet (WAIS) appear to be highly sensitive to relatively small increases in CO₂ concentration and global mean temperature. For example, global sea level during MPWP may have been up to +20m higher than present day when atmospheric CO₂ concentrations were ~350 to 450 ppm and global mean surface temperature was 2°C to 3°C above pre-industrial levels (see Sections 5.6.1 and 5.8.1). (continued on next page)



Box 5.1, Figure 1 | Comparison of data and multi-model mean (MMM) simulations, for four periods of time, showing (a) sea surface temperature (SST) anomalies, (b) zonally averaged SST anomalies, (c) zonally averaged global (green) and land (grey) surface air temperature (SAT) anomalies and (d) land SAT anomalies. The time periods are 2081–2100 for the Representative Concentration Pathway (RCP) 8.5 (top row), Last Glacial Maximum (LGM, second row), mid-Pliocene Warm Period (MPWP, third row) and Early Eocene Climatic Optimum (EECO, bottom row). Model temperature anomalies are calculated relative to the pre-industrial value of each model in the ensemble prior to calculating the MMM anomaly (a, d; colour shading). Zonal MMM gradients (b, c) are plotted with a shaded band indicating 2 standard deviations. Site specific temperature anomalies estimated from proxy data are calculated relative to present site temperatures and are plotted (a, d) using the same colour scale as the model data, and a circle-size scaled to estimates of confidence. Proxy data compilations for the LGM are from Multiproxy Approach for the Reconstruction of the Glacial Ocean surface (MARGO) Project Members (2009) and Bartlein et al. (2011), for the MPWP are from Dowsett et al. (2012), Salzmann et al. (2008) and Haywood et al. (2013) and for the EECO are from Hollis et al. (2012) and Lunt et al. (2012). Model ensemble simulations for 2081–2100 are from the CMIP5 ensemble using RCP 8.5, for the LGM are seven Paleoclimate Modelling Intercomparison Project Phase III (PMIP3) and Coupled Model Intercomparison Project Phase 5 (CMIP5) models, for the Pliocene are from Haywood et al. (2013), and for the EECO are after Lunt et al. (2012).

Box 5.1 (continued)

Based on earlier climate data–model comparisons, it has been claimed (summarised in Huber and Caballero, 2011), that models underestimated the strength of polar amplification for high CO₂ climates by 30 to 50%. While recent simulations of the EECO and the MPWP exhibit a wide inter-model variability, there is generally good agreement between new simulations and data, particularly if seasonal biases in some of the marine SST proxies from high-latitude sites are considered (Hollis et al., 2012; Lunt et al., 2012; Haywood et al., 2013).

Transient polar amplification as recorded in historical instrumental data and as projected by coupled climate models for the 21st century involves a different balance of feedbacks than for the “equilibrium” past states featured in Box 5.1, Figure 1. Since 1875, the Arctic north of 60°N latitude has warmed at a rate of 1.36°C per century, approximately twice as fast as the global average (Bekryaev et al., 2010), and since 1979, Arctic land surface has warmed at an even higher rate of 0.5°C per decade (e.g., Climatic Research Unit (CRU) Gridded Dataset of Global Historical Near-Surface Air TEMperature Anomalies Over Land version 4 (CRUTEM4), Jones et al., 2012; Hadley Centre/CRU gridded surface temperature data set version 4 (HadCRUT4), Morice et al., 2012) (see Section 2.4). This recent warming appears unusual in the context of reconstructions spanning the past 2000 years (Section 5.5) and has been attributed primarily to anthropogenic factors (Gillett et al., 2008) (see Section 10.3.1.1.4). The fact that the strongest warming occurs in autumn and early winter (Chylek et al., 2009; Serreze et al., 2009; Polyakov et al., 2010; Screen and Simmonds, 2010; Semenov et al., 2010; Spielhagen et al., 2011) strongly links Arctic amplification to feedbacks associated with the seasonal reduction in sea ice extent and duration, as well as the insulating effect of sea ice in winter (e.g., Soden et al., 2008; Serreze et al., 2009; Serreze and Barry, 2011). For future model projections (Box 5.1, Figure 1), following the RCP8.5 scenarios, annual mean Arctic (68°N to 90°N) warming is expected to exceed the global average by 2.2 to 2.4 times for the period 2081–2100 compared to 1986–2005 (see Section 12.4.3.1), which corresponds to the higher end of polar amplification implied by paleo-reconstructions.

The transient response of Antarctic and Southern Ocean temperatures to the anthropogenic perturbation appears more complex, than for the Arctic region. Zonal mean Antarctic surface warming has been modest at 0.1°C per decade over the past 50 years (Steig et al., 2009; O’Donnell et al., 2010). The Antarctic Peninsula is experiencing one of the strongest regional warming trends (0.5°C per decade over the past 50 years), more than twice that of the global mean temperature. Central West Antarctica may have also experienced a similar strong warming trend, as depicted by the only continuous meteorological station during the last 50 years (Bromwich et al., 2013), and borehole measurements spanning the same period (Orsi et al., 2012). Ice core records show enhanced summer melting in the Antarctic Peninsula since the 1950, which is unprecedented over the past 1000 years (Abram et al., 2013), and warming in West Antarctica that cannot be distinguished from natural variability over the last 2000 years (Steig et al., 2013) (see also Section 10.3.1.1.4, and Section 5.5). Polar amplification in the Southern Ocean and Antarctica is virtually absent in the transient CMIP5 RCP4.5 future simulations (2081–2100 versus 1986–2005) (see Section 12.4.3.1), although CMIP5 RCP8.5 exhibits an amplified warming in the Southern Ocean (Box 5.1, Figure 1), much smaller in magnitude than the equilibrium response implied from paleo-reconstructions for a high-CO₂ world.

In summary, *high confidence* exists for polar amplification in either one or both hemispheres, based on robust and consistent evidence from temperature reconstructions of past climates, recent instrumental temperature records and climate model simulations of past, present and future climate changes.

5

5.3 Earth System Responses and Feedbacks at Global and Hemispheric Scales

This section updates the information available since AR4 on changes in surface temperature on million-year to orbital time scales and for the last 2000 years. New information on changes of the monsoon systems on glacial–interglacial time scales is also assessed.

5.3.1 High-Carbon Dioxide Worlds and Temperature

Cenozoic (last 65 Ma) geological archives provide examples of natural climate states globally warmer than the present, which are associated with atmospheric CO₂ concentrations above pre-industrial levels. This relationship between global warmth and high CO₂ is complicated by

factors such as tectonics and the evolution of biological systems, which play an important role in the carbon cycle (e.g., Zachos et al., 2008). Although new reconstructions of deep-ocean temperatures have been compiled since AR4 (e.g., Cramer et al., 2011), *low confidence* remains in the precise relationship between CO₂ and deep-ocean temperature (Beerling and Royer, 2011).

Since AR4 new proxy and model data have become available from three Cenozoic warm periods to enable an assessment of forcing, feedbacks and the surface temperature response (e.g., Dowsett et al., 2012; Lunt et al., 2012; Haywood et al., 2013). These are the Paleocene–Eocene Thermal Maximum (PETM; Table 5.1), the Early Eocene Climatic Optimum (EECO; Table 5.1) and the mid-Pliocene Warm Period (MPWP; Table 5.1). Reconstructions of surface temperatures based on proxy data remain

challenged by (i) the limited number and uneven geographical distribution of sites, (ii) seasonal biases and (iii) the validity of assumptions required by each proxy method (assessed in Table 5.A.3). There is also a lack of consistency in the way uncertainties are reported for proxy climate estimates. In most cases error bars represent the analytical and calibration error. In some compilations qualitative confidence assessments are reported to account for the quality of the age control, number of samples, fossil preservation and abundance, performance of the proxy method utilized and agreement of multiple proxy estimates (e.g., Multiproxy Approach for the Reconstruction of the Glacial Ocean surface (MARGO) Project Members, 2009; Dowsett et al., 2012).

The PETM was marked by a massive carbon release and corresponding global ocean acidification (Zachos et al., 2005; Ridgwell and Schmidt, 2010) and, with *low confidence*, global warming of 4°C to 7°C relative to pre-PETM mean climate (Sluijs et al., 2007; McInerney and Wing, 2011). The carbon release of 4500 to 6800 PgC over 5 to 20 kyr translates into a rate of emissions of ~0.5 to 1.0 PgC yr⁻¹ (Panchuk et al., 2008; Zeebe et al., 2009). GHG emissions from marine methane hydrate and terrestrial permafrost may have acted as positive feedbacks (DeConto et al., 2012).

The EECO represents the last time atmospheric CO₂ concentrations may have reached a level of ~1000 ppm (Section 5.2.2.2). There were no substantial polar ice sheets, and oceanic and continental configurations, vegetation type and distribution were significantly different from today. Whereas simulated SAT are in reasonable agreement with reconstructions (Huber and Caballero, 2011; Lunt et al., 2012) (Box 5.1, Figure 1d), there are still significant discrepancies between simulated and reconstructed mean annual SST, which are reduced if seasonal biases in some of the marine proxies are considered for the high-latitude sites (Hollis et al., 2012; Lunt et al., 2012). *Medium confidence* is placed on the reconstructed global mean surface temperature anomaly estimate of 9°C to 14°C.

The Pliocene is characterized by a long-term increase in global ice volume and decrease in temperature from ~3.3–2.6 Ma (Lisiecki and Raymo, 2005; Mudelsee and Raymo, 2005; Fedorov et al., 2013), which marks the onset of continental-scale glaciations in the NH. Superimposed on this trend, benthic δ¹⁸O (Lisiecki and Raymo, 2005) and an ice proximal geological archive (Lisiecki and Raymo, 2005; Naish et al., 2009a) imply moderate fluctuations in global ice volume paced by the 41 kyr obliquity cycle. This orbital variability is also evident in far-field sea level reconstructions (Miller et al., 2012a), tropical Pacific SST (Herbert et al., 2010) and Southern Ocean MDA records (Martinez-Garcia et al., 2011), and indicate a close coupling between temperature, atmospheric circulation and ice volume/sea level (Figure 5.2). The MPWP and the following 300 kyr represent the last time atmospheric CO₂ concentrations were in the range 350 to 450 ppm (Section 5.2.2.2, Figure 5.2). Model–data comparisons (Box 5.1, Figure 1) provide *high confidence* that mean surface temperature was warmer than pre-industrial for the average interglacial climate state during the MPWP (Dowsett et al., 2012; Haywood et al., 2013). Global mean SST is estimated at +1.7°C (without uncertainty) above the 1901–1920 mean based on large data syntheses (Lunt et al., 2010; Dowsett et al., 2012). General circulation model (GCM) results agree with this SST anomaly (to within ±0.5°C), and produce a range of global mean SAT of +1.9°C and +3.6°C rela-

tive to the 1901–1920 mean (Haywood et al., 2013). Weakened meridional temperature gradients are shown by all GCM simulations, and have significant implications for the stability of polar ice sheets and sea level (see Box 5.1 and Section 5.6). SST gradients and the Pacific Ocean thermocline gradient along the equator were greatly reduced compared to present (Fedorov et al., 2013) (Section 5.4). Vegetation reconstructions (Salzmann et al., 2008) imply that the global extent of arid deserts decreased and boreal forests replaced tundra, and GCMs predict an enhanced hydrological cycle, but with large inter-model spread (Haywood et al., 2013). The East Asian Summer Monsoon, as well as other monsoon systems, may have been enhanced at this time (e.g., Wan et al., 2010).

Climate reconstructions for the warm periods of the Cenozoic also provide an opportunity to assess Earth-system and equilibrium climate sensitivities. Uncertainties on both global temperature and CO₂ reconstructions preclude deriving robust quantitative estimates from the available PETM data. The limited number of models for MPWP, which take into account slow feedbacks such as ice sheets and the carbon cycle, imply with *medium confidence* that Earth-system sensitivity may be up to two times the model equilibrium climate sensitivity (ECS) (Lunt et al., 2010; Pagani et al., 2010; Haywood et al., 2013). However, if the slow amplifying feedbacks associated with ice sheets and CO₂ are considered as forcings rather than feedbacks, climate records of the past 65 Myr yield an estimate of 1.1°C to 7°C (95% confidence interval) for ECS (PALAEOSENS Project Members, 2012) (see also Section 5.3.3.2).

5.3.2 Glacial–Interglacial Dynamics

5.3.2.1 Role of Carbon Dioxide in Glacial Cycles

Recent modelling work provides strong support for the important role of variations in the Earth's orbital parameters in generating long-term climate variability. In particular, new simulations with GCMs (Carlson et al., 2012; Herrington and Poulsen, 2012) support the fundamental premise of the Milankovitch theory that a reduction in NH summer insolation generates sufficient cooling to initiate ice sheet growth. Climate–ice sheet models with varying degrees of complexity and forced by variations in orbital parameters and reconstructed atmospheric CO₂ concentrations simulate ice volume variations and other climate characteristics during the last and several previous glacial cycles consistent with paleoclimate records (Abe-Ouchi et al., 2007; Bonelli et al., 2009; Ganopolski et al., 2010) (see Figure 5.3).

There is *high confidence* that orbital forcing is the primary external driver of glacial cycles (Kawamura et al., 2007; Cheng et al., 2009; Lisiecki, 2010; Huybers, 2011). However, atmospheric CO₂ content plays an important internal feedback role. Orbital-scale variability in CO₂ concentrations over the last several hundred thousand years covaries (Figure 5.3) with variability in proxy records including reconstructions of global ice volume (Lisiecki and Raymo, 2005), climatic conditions in central Asia (Prokopenko et al., 2006), tropical (Herbert et al., 2010) and Southern Ocean SST (Pahnke et al., 2003; Lang and Wolff, 2011), Antarctic temperature (Parrenin et al., 2013), deep-ocean temperature (Elderfield et al., 2010), biogeochemical conditions in the North Pacific (Jaccard et al., 2010) and deep-ocean ventilation (Lisiecki

et al., 2008). Such close linkages between CO₂ concentration and climate variability are consistent with modelling results suggesting with *high confidence* that glacial–interglacial variations of CO₂ and other GHGs explain a considerable fraction of glacial–interglacial climate variability in regions not directly affected by the NH continental ice sheets (Timmermann et al., 2009; Shakun et al., 2012).

5.3.2.2 Last Glacial Termination

It is *very likely* that global mean surface temperature increased by 3° to 8°C over the last deglaciation (see Table 5.2), which gives a *very likely* average rate of change of 0.3 to 0.8°C kyr⁻¹. Deglacial global warming occurred in two main steps from 17.5 to 14.5 ka and 13.0 to 10.0 ka that *likely* reached maximum rates of change between 1°C kyr⁻¹ and 1.5°C kyr⁻¹ at the millennial time scale (cf. Shakun et al., 2012; Figure 5.3i), although regionally and on shorter time scales higher rates may have occurred, in particular during a sequence of abrupt climate change events (see Section 5.7).

For the last glacial termination, a large-scale temperature reconstruction (Shakun et al., 2012) documents that temperature change in the SH lead NH temperature change. This lead can be explained by the bipolar thermal seesaw concept (Stocker and Johnsen, 2003) (see also Section 5.7) and the related changes in the inter-hemispheric ocean heat transport, caused by weakening of the Atlantic Ocean meridional overturning circulation (AMOC) during the last glacial termination (Ganopolski and Roche, 2009). SH warming prior to NH warming can also be explained by the fast sea ice response to changes in austral spring insolation (Stott et al., 2007; Timmermann et al., 2009). According to these mechanisms, SH temperature lead over the NH is fully consistent with the NH orbital forcing of deglacial ice volume changes (*high confidence*) and the importance of the climate–carbon cycle feedbacks in glacial–interglacial transitions. The tight coupling is further highlighted by the near-zero lag between the deglacial rise in CO₂ and averaged deglacial Antarctic temperature recently reported from improved estimates of gas–ice age differences (Pedro et al., 2012; Parrenin et al., 2013). Previous studies (Monnin et al., 2001; Table 5.A.4)

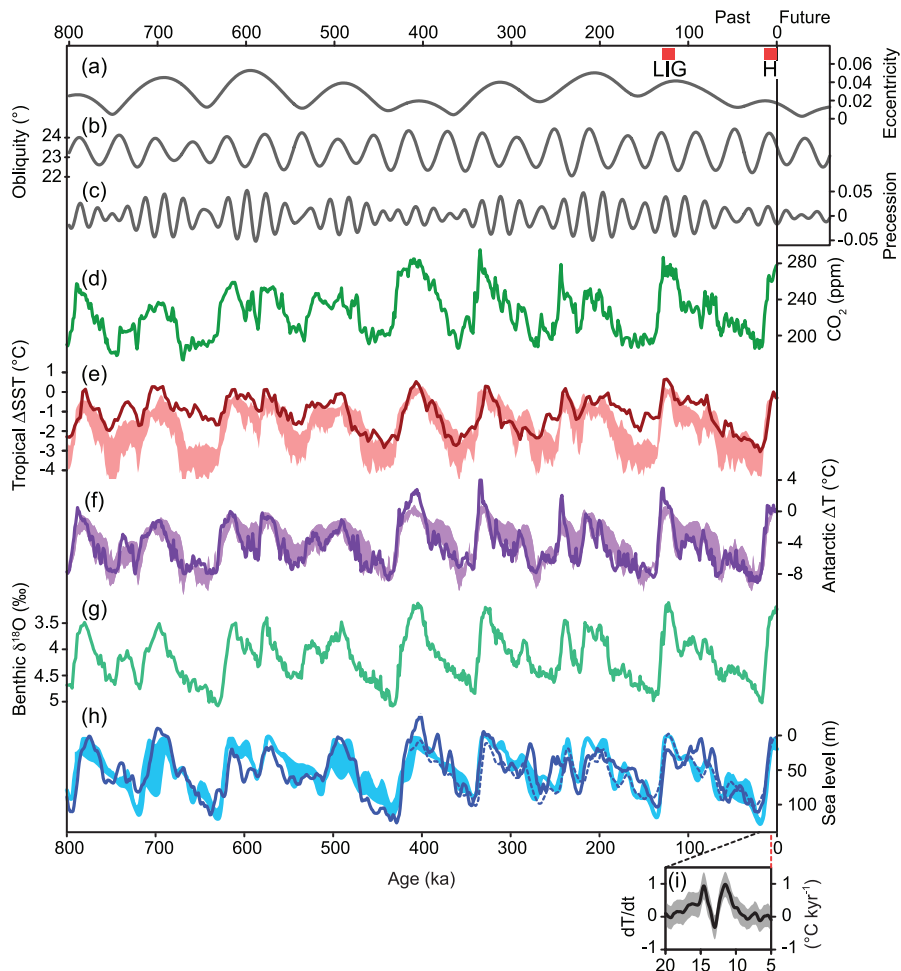


Figure 5.3 | Orbital parameters and proxy records over the past 800 kyr. (a) Eccentricity. (b) Obliquity. (c) Precessional parameter (Berger and Loutre, 1991). (d) Atmospheric concentration of CO₂ from Antarctic ice cores (Petit et al., 1999; Siegenthaler et al., 2005; Ahn and Brook, 2008; Lüthi et al., 2008). (e) Tropical sea surface temperature stack (Herbert et al., 2010). (f) Antarctic temperature stack based on up to seven different ice cores (Petit et al., 1999; Blunier and Brook, 2001; Watanabe et al., 2003; European Project for Ice Coring in Antarctica (EPICA) Community Members, 2006; Jouzel et al., 2007; Stenni et al., 2011). (g) Stack of benthic δ¹⁸O, a proxy for global ice volume and deep-ocean temperature (Lisiecki and Raymo, 2005). (h) Reconstructed sea level (dashed line: Rohling et al., 2010; solid line: Elderfield et al., 2012). Lines represent orbital forcing and proxy records, shaded areas represent the range of simulations with climate models (Grid Enabled Integrated Earth System Model-1, GENIE-1, Holden et al., 2010a; Bern3D, Ritz et al., 2011), climate–ice sheet models of intermediate complexity (CLIMBER and BiosphERe model, CLIMBER-2, Ganopolski and Calov, 2011) and an ice sheet model (Ice sheet model for Integrated Earth system studies, Ices, Abe-Ouchi et al., 2007) forced by variations of the orbital parameters and the atmospheric concentrations of the major greenhouse gases. (i) Rate of changes of global mean temperature during Termination I based on Shakun et al. (2012).

suggesting a temperature lead of 800 ± 600 years over the deglacial CO₂ rise probably overestimated gas-ice age differences.

5.3.2.3 Monsoon Systems

Since AR4, new high-resolution hydroclimate reconstructions using speleothems (Sinha et al., 2007; Hu et al., 2008; Wang et al., 2008; Cruz et al., 2009; Asmerom et al., 2010; Berkelhammer et al., 2010; Stríkis et al., 2011; Kanner et al., 2012), lake sediments (Shanahan et al., 2009; Stager et al., 2009; Wolff et al., 2011), marine sediments (Weldeab et al., 2007b; Mulitza et al., 2008; Tjallingii et al., 2008; Ponton et al., 2012) and tree-ring chronologies (Buckley et al., 2010; Cook et al., 2010a) have provided a more comprehensive view on the dynamics of monsoon systems on a variety of time scales. Water isotope-enabled modelling experiments (LeGrande and Schmidt, 2009; Lewis et al., 2010; Pausata et al., 2011) and evaluation of marine and terrestrial

data (Clemens et al., 2010) document that speleothem δ¹⁸O variations in some monsoon regions can be explained as a combination of changes in local precipitation and large-scale moisture transport.

This subsection focuses on the response of monsoon systems to orbital forcing on glacial–interglacial time scales. Proxy data including speleothem δ¹⁸O from southeastern China (Wang et al., 2008), northern Borneo (Meckler et al., 2013), eastern Brazil (Cruz et al., 2005) and the Arabian Peninsula (Bar-Matthews et al., 2003), along with marine-based records off northwestern Africa (Weldeab et al., 2007a) and from the Arabian Sea (Schulz et al., 1998) document hydrological changes that are dominated by eccentricity-modulated precessional cycles. Increasing boreal summer insolation can generate a strong inter-hemispheric surface temperature gradient that leads to large-scale decreases in precipitation in the SH summer monsoon systems and increased hydrological cycle in the NH tropics (Figure 5.4a, d, g). Qualitatively

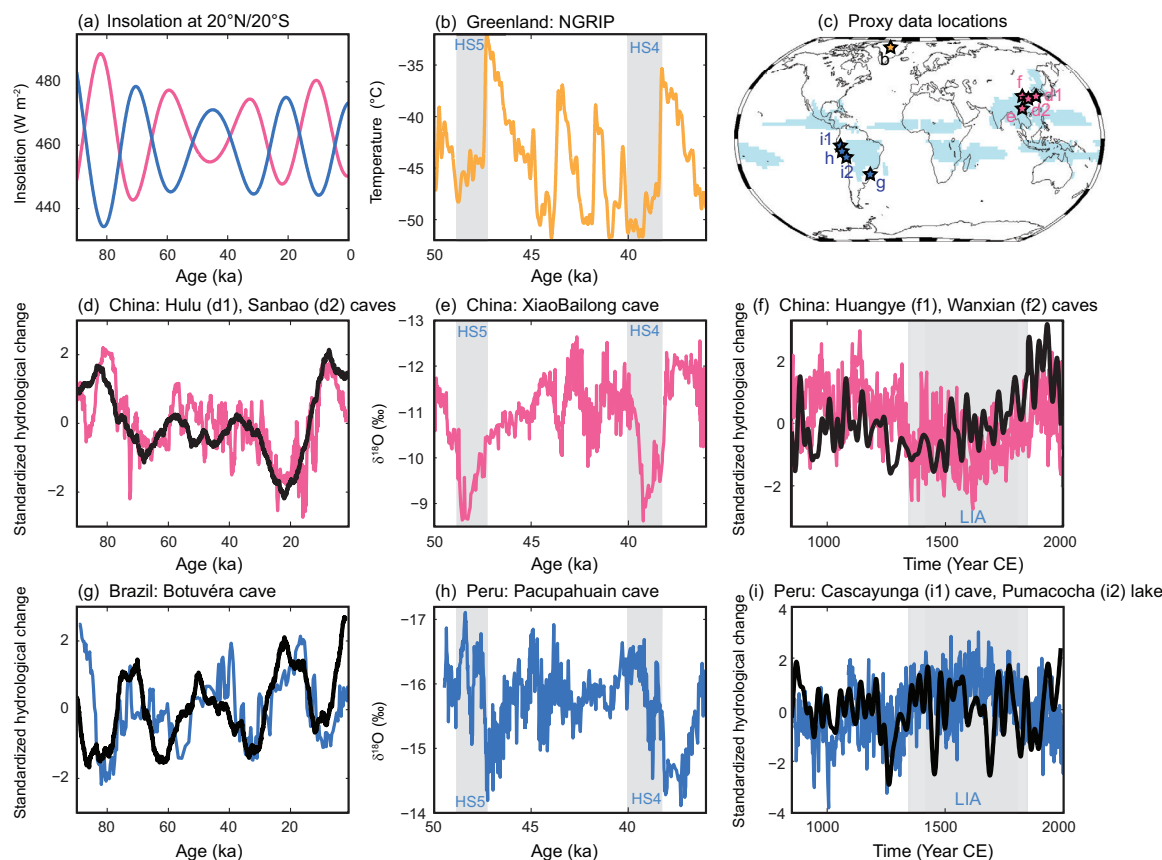


Figure 5.4 | Inter-hemispheric response of monsoon systems at orbital, millennial and centennial scales. (a) Boreal summer insolation changes at 20°N (red) (W m^{-2}) and austral summer insolation changes at 20°S (blue). (b) Temperature changes in Greenland (degrees Celsius) reconstructed from North Greenland Ice Core Project (NGRIP) ice core on SS09 time scale (Huber et al., 2006), location indicated by orange star in c. (c) Location of proxy records displayed in panels a, b, d–i in relation to the global monsoon regions (cyan shading) (Wang and Ding, 2008). (d) Reconstructed (red) standardized negative δ¹⁸O anomaly in East Asian Summer Monsoon region derived from Hulu (Wang et al., 2001) and Sanbao (Wang et al., 2008) cave speleothem records, China and simulated standard multi-model average (black) of annual mean rainfall anomalies averaged over region 108°E to 123°E and 25°N to 40°N using the transient runs conducted with LOCH–Vecode–Ecbilt–Clio–agism Model (LOVECLIM, Timm et al., 2008), FAst Met Office/UK Universities Simulator (FAMOUS, Smith and Gregory, 2012), and the Hadley Centre Coupled Model (HadCM3) snapshot simulations (Singarayer and Valdes, 2010). (e) δ¹⁸O from Xiaobailong cave, China (Cai et al., 2010). (f) Standardized negative δ¹⁸O anomalies (red) in Huangye (Tan et al., 2011) and Wanxian (Zhang et al., 2008) caves, China and simulated standardized annual mean and 30-year low-pass filtered rainfall anomalies (black) in region 100°E to 110°E, 20°N to 35°N, ensemble averaged over externally forced Atmosphere–Ocean General Circulation Model (AOGCM) experiments conducted with Community Climate System Model-4 (CCSM4), ECHAM4+HOPE-G (ECHO-G), Max Planck Institute Earth System Model (MPI-ESM), Commonwealth Scientific and Industrial Research Organisation model (CSIRO-Mk3L-1-2), Model for Interdisciplinary Research on Climate (MIROC), HadCM3 (Table 5.A.1). (g) Standardized negative δ¹⁸O anomaly (blue) from Botuvéra speleothem, Brazil (Cruz et al., 2005) and simulated standard multi-model average (black) of annual mean rainfall anomalies averaged over region 45°W to 60°W and 35°S to 15°S using same experiments as in panel d. (h) Standardized δ¹⁸O anomaly (blue) from Pacupahuain cave, Peru (Kanner et al., 2012). (i) Standardized negative δ¹⁸O anomalies (blue) from Cascayunga Cave, Peru (Reuter et al., 2009) and Pumacocha Lake, Peru (Bird et al., 2011) and simulated standard annual mean and 30-year low-pass filtered rainfall anomalies (black) in region 76°W to 70°W, 16°S to 8°S, ensemble averaged over the same model simulations as in f. HS4/5 denote Heinrich stadials 4 and 5, and LIA denotes Little Ice Age (Table 5.1).

similar, out-of-phase inter-hemispheric responses to insolation forcing have also been documented in coupled time-slice and transient GCM simulations (Braconnot et al., 2008; Kutzbach et al., 2008) (see also Figure 5.4d, g). The similarity in response in both proxy records and models provide *high confidence* that orbital forcing induces inter-hemispheric rainfall variability. Across longitudes, the response of precipitation may, however, be different for the same orbital forcing (Shin et

al., 2006; Marzin and Braconnot, 2009). For example, in the mid-Holocene drier conditions occurred in central North America (Diffenbaugh et al., 2006) and wetter conditions in northern Africa (Liu et al., 2007b; Hély et al., 2009; Tierney et al., 2011). There is further evidence for east–west shifts of precipitation in response to orbital forcing in South America (Cruz et al., 2009).

Box 5.2 | Climate-Ice Sheet Interactions

Ice sheets have played an essential role in the Earth's climate history (see Sections 5.3, 5.6 and 5.7). They interact with the atmosphere, the ocean–sea ice system, the lithosphere and the surrounding vegetation (see Box 5.2, Figure 1). They serve as nonlinear filters and integrators of climate effects caused by orbital and GHG forcings (Ganopolski and Calov, 2011), while at the same time affecting the global climate system on a variety of time scales (see Section 5.7).

Ice sheets form when annual snow accumulation exceeds melting. Growing ice sheets expand on previously vegetated areas, thus leading to an increase of surface albedo, further cooling and an increase in net surface mass balance. As ice sheets grow in height and area, surface temperatures drop further as a result of the lapse-rate effect, but also snow accumulation decreases because colder air holds less moisture (inlay in Box 5.2, Figure 1). This so-called elevation-desert effect (Oerlemans, 1980) is an important negative feedback for ice sheets which limits their growth. Higher elevation ice sheets can be associated with enhanced calving at their margins, because the ice flow will be accelerated directly by increased surface slopes and indirectly by lubrication at the base of the ice sheet. Calving, grounding line processes, basal lubrication and other forms of thermo-mechanical coupling may have played important roles in accelerating glacial terminations following phases of relatively slow ice sheet growth, hence contributing to the temporal saw-tooth structure of the recent glacial–interglacial cycles (Figure 5.3).

Large glacial ice sheets also deflect the path of the extratropical NH westerly winds (Cook and Held, 1988), generating anticyclonic circulation anomalies (Box 5.2, Figure 1), which tend to warm the western side of the ice sheet and cool the remainder (e.g., Roe and Lindzen, 2001). Furthermore, the orographic effects of ice sheets lead to reorganizations of the global atmosphere circulation by changing the major stationary wave patterns (e.g., Abe-Ouchi et al., 2007; Yin et al., 2008) and trade wind systems (Timmermann et al., 2004). This allows for a fast transmission of ice sheet signals to remote regions.

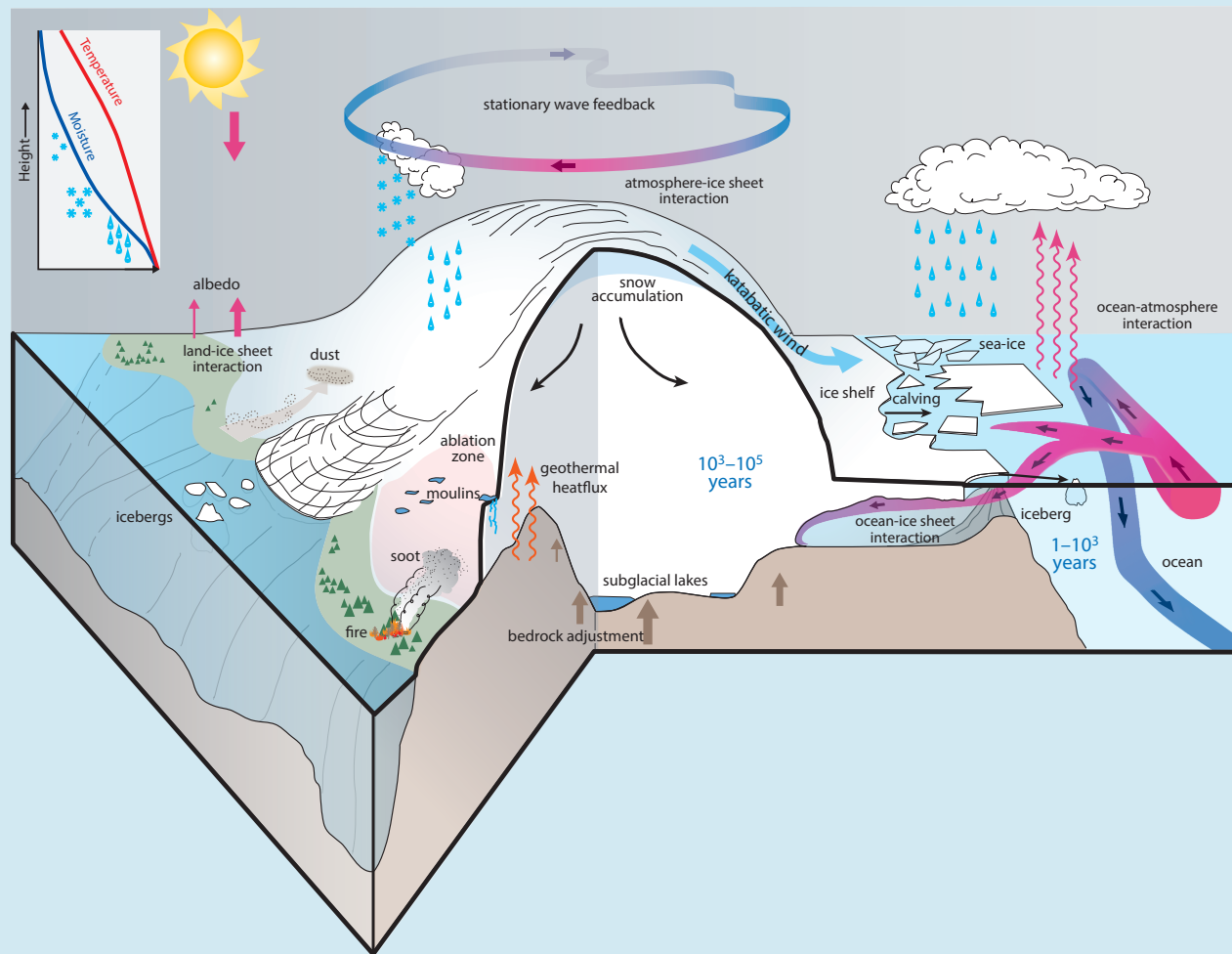
The enormous weight of ice sheets depresses the underlying bedrocks causing a drop in ice sheet height and a surface warming as a result of the lapse-rate effect. The lithospheric adjustment has been shown to play an important role in modulating the ice sheet response to orbital forcing (Birchfield et al., 1981; van den Berg et al., 2008). The presence of terrestrial sedimentary materials (regolith) on top of the unweathered bedrock affects the friction at the base of an ice sheet, and may further alter the response of continental ice sheets to external forcings, with impacts on the dominant periodicities of glacial cycles (Clark and Pollard, 1998).

5

An area of very active research is the interaction between ice sheets, ice shelves and the ocean (see Sections 4.4, 13.4.3 and 13.4.4). The mass balance of marine ice sheets is strongly determined by ocean temperatures (Joughin and Alley, 2011). Advection of warmer waters below ice shelves can cause ice shelf instabilities, reduced buttressing, accelerated ice stream flow (De Angelis and Skvarca, 2003) and grounding line retreat in regions with retrograde bedrock slopes (Schoof, 2012), such as West Antarctica. On orbital and millennial time scales such processes may have played an essential role in driving ice volume changes of the West Antarctic ice sheet (Pollard and DeConto, 2009) and the Laurentide ice sheet (Alvarez-Solas et al., 2010). Massive freshwater release from retreating ice sheets, can feed back to the climate system by altering sea level, oceanic deep convection, ocean circulation, heat transport, sea ice and the global atmospheric circulation (Sections 5.6.3 and 5.7).

Whereas the initial response of ice sheets to external forcings can be quite fast, involving for instance ice shelf processes and outlet glaciers (10 to 10^3 years), their long-term adjustment can take much longer (10^4 to 10^5 years) (see Section 12.5.5.3). As a result, the climate–cryosphere system is not even in full equilibrium with the orbital forcing. This also implies that future anthropogenic radiative perturbations over the next century can determine the evolution of the Greenland (Charbit et al., 2008) and Antarctic ice sheets for centuries and millennia to come with a potential commitment to significant global sea level rise (Section 5.8). (continued on next page)

Box 5.2 (continued)



Box 5.2, Figure 1 | Schematic illustration of multiple interactions between ice sheets, solid earth and the climate system which can drive internal variability and affect the coupled ice sheet-climate response to external forcings on time scales of months to millions of years. The inlay figure represents a typical height profile of atmospheric temperature and moisture in the troposphere.

5.3.3 Last Glacial Maximum and Equilibrium Climate Sensitivity

The LGM is characterized by a large temperature response (Section 5.3.3.1) to relatively well-defined radiative perturbations (Section 5.2), linked to atmospheric CO₂ concentration around 200 ppm (Section 5.2.2) and large ice sheets covering northern Europe and North America. This can be used to evaluate climate models (Braconnot et al. (2012b); see Sections 9.7 and 10.8) and to estimate ECS from the combined use of proxy information and simulations (Section 5.3.3.2).

5.3.3.1 Last Glacial Maximum Climate

Since AR4, synthesis of proxy LGM temperature estimates was completed for SST (MARGO Project Members, 2009), and for land SAT (Bartlein et al., 2011) (Box 5.1, Figure 1). The Multiproxy Approach for the Reconstruction of the Glacial Ocean Surface (MARGO) SST

synthesis expanded earlier work (CLIMAP Project Members, 1976, 1981; Sarnthein et al., 2003a; Sarnthein et al., 2003b) by using multiple proxies (Table 5.2). The land SAT synthesis is based on pollen data, following the Cooperative Holocene Mapping Project (COHMAP Members, 1988).

Climate models and proxy data consistently show that mean annual SST change (relative to pre-industrial) is largest in the mid-latitude North Atlantic (up to –10°C), and the Mediterranean (about –6°C) (MARGO Project Members, 2009, Box 5.1, Table 5.2). Warming and seasonally ice-free conditions are reconstructed, however, in the north-eastern North Atlantic, in the eastern Nordic Seas and north Pacific, albeit with large uncertainty because of the different interpretation of proxy data (de Vernal et al., 2006). SAT reconstructions generally shows year-round cooling, with regional exceptions such as Alaska (Bartlein et al., 2011). Modelling studies show how atmospheric dynamics influenced by ice sheets affect regional temperature patterns in the North

Table 5.2 | Summary of Last Glacial Maximum (LGM) sea surface temperature (SST) and surface air temperature (SAT) reconstructions (anomalies with respect to pre-industrial climate) using proxy data and model ensemble constrained by proxy data. Cooling ranges indicate 90% confidence intervals (C.I., where available).

Region	Cooling (°C) 90% C.I.	Methods	Reference and remarks
Sea Surface Temperature (SST)			
Global	0.7–2.7	Multi-proxy	MARGO Project Members (2009)
Mid-latitude North Atlantic	up to 10	Multi-proxy	MARGO Project Members (2009)
Southern Ocean	2–6	Multi-proxy	MARGO Project Members (2009)
Low-latitude (30°S to 30°N)	0.3–2.7	Multi-proxy	MARGO Project Members (2009) 1.7°C ± 1°C: 15°S to 15°N 2.9°C ± 1.3°C: Atlantic 15°S to 15°N 1.2°C ± 1.1°C : Pacific 15°S to 15°N (1.2°C ± 1°C based on microfossil assemblages; 2.5°C ± 1°C based on Mg/Ca ratios and alkenones)
Low-latitude (30°S to 30°N)	2.2–3.2	Multi-proxy	Ballantyne et al. (2005)
Low-latitude (western and eastern tropical Pacific)	2–3	Multi-proxy	Lea et al. (2000); de Garidel-Thoron et al. (2007); Leduc et al. (2007); Pahnke et al. (2007); Stott et al. (2007); Koutavas and Sachs (2008); Steinke et al. (2008); Linsley et al. (2010)
Surface Air Temperature (SAT)			
Eastern Antarctica	7–10	Water stable isotopes from ice core	Stenni et al. (2010); Uemura et al. (2012)
Central Greenland	21–25	Borehole paleothermometry	Cuffey et al. (1995); Johnsen et al. (1995); Dahl-Jensen et al. (1998)
Global	4.4–7.2	Single-EMIC ensemble with microfossil-assemblage derived tropical Atlantic SST	Schneider von Deimling et al. (2006)
Global	4.6–8.3	Single-EMIC ensemble with multi-proxy derived tropical SST	Holden et al. (2010a)
Global	1.7–3.7	Single-EMIC ensemble with global multi-proxy data	Schmittner et al. (2011)
Global	3.9–4.6	Multi-proxy	Shakun et al. (2012); for the interval 17.5–9.5 ka
Global	3.4–4.6	Multi-AOGCM ensemble with global multi-proxy data	Annan and Hargreaves (2013)
Global	3.1–5.9	Multi-AOGCM ensemble	PMIP2 and PMIP3/CMIP5

Notes:

AOGCM = Atmosphere-Ocean General Circulation Model; CMIP5 = Coupled Model Intercomparison Project Phase 5; EMIC = Earth System Model of Intermediate Complexity; MARGO = Multiproxy Approach for the Reconstruction of the Glacial Ocean surface; PMIP2 and PMIP3 = Paleoclimate Modelling Intercomparison Project Phase II and III, respectively.

Atlantic region (Lainé et al., 2009; Pausata et al., 2011; Unterman et al., 2011; Hofer et al., 2013), and in the north Pacific region (Yanase and Abe-Ouchi, 2010). Larger cooling over land compared to ocean is a robust feature of observations and multiple atmosphere–ocean general circulation models (AOGCM) (Izumi et al., 2013). As in AR4, central Greenland temperature change during the LGM is underestimated by PMIP3/CMIP5 simulations, which show 2°C to 18°C cooling, compared to 21°C to 25°C cooling reconstructed from ice core data (Table 5.2). A mismatch between reconstructions and model results may arise because of missing Earth system feedbacks (dust, vegetation) (see Section 5.2.2.3) or insufficient integration time to reach an equilibrium for LGM boundary conditions.

Uncertainties remain on the magnitude of tropical SST cooling during the LGM. Previous estimates of tropical cooling (2.7°C ± 0.5°C, Ballantyne et al., 2005) are greater than more recent estimates (1.5°C ± 1.2°C, MARGO Project Members, 2009). Such discrepancies may arise from seasonal productivity (Leduc et al., 2010) and habitat depth (Telford et al., 2013) biases. In the western and eastern tropical Pacific, many proxy records show 2°C to 3°C cooling relative to the pre-in-

dustrial period (Lea et al., 2000, 2006; de Garidel-Thoron et al., 2007; Leduc et al., 2007; Pahnke et al., 2007; Stott et al., 2007; Koutavas and Sachs, 2008; Steinke et al., 2008; Linsley et al., 2010). AOGCMs tend to underestimate longitudinal patterns of tropical SST (Otto-Bliesner et al., 2009) and atmospheric circulation (DiNezio et al., 2011).

Larger sea ice seasonality is reconstructed for the LGM compared to the pre-industrial period around Antarctica (Gersonde et al., 2005). Climate models underestimate this feature, as well as the magnitude of Southern Ocean cooling (Roche et al., 2012) (see Box 5.1, Figure 1). In Antarctica 7°C to 10°C cooling relative to the pre-industrial period is reconstructed from ice cores (Stenni et al., 2010; Uemura et al., 2012) and captured in most PMIP3/CMIP5 simulations (Figure 5.5d).

The combined use of proxy reconstructions, with incomplete spatial coverage, and model simulations is used to estimate LGM global mean temperature change (Table 5.2). One recent such study, combining multi-proxy data with multiple AOGCMs, estimates LGM global cooling at 4.0°C ± 0.8°C (95% confidence interval) (Annan and Hargreaves, 2013). This result contrasts with the wider range of global cooling

(1.7°C to 8.3°C) obtained using Earth-system models of intermediate complexity (EMIC) (Schneider von Deimling et al., 2006; Holden et al., 2010b; Schmittner et al., 2011). The source of these differences in the estimate of LGM cooling may be the result of (i) the proxy data used to constrain the simulations, such as data sets associated with mild cooling in the tropics and the North Atlantic; (ii) model resolution and structure, which affects their ability to resolve the land-sea contrast (Annan and Hargreaves, 2013) and polar amplification (Fyke and Eby, 2012); (iii) the experimental design of the simulations, where the lack of dust and vegetation feedbacks (Section 5.2.2.3) and insufficient integration time. Based on the results and the caveats in the studies assessed here (Table 5.2), it is very likely that global mean surface temperature during the LGM was cooler than pre-industrial by 3°C to 8°C.

Some recent AOGCM simulations produce a stronger AMOC under LGM conditions, leading to mild cooling over the North Atlantic and GIS (Otto-Bliesner et al., 2007; Weber et al., 2007). This finding contrasts with proxy-based information (Lynch-Stieglitz et al., 2007; Hesse et al., 2011). Changes in deep-ocean temperature and salinity during the LGM have been constrained by pore-water chemistry in deep-sea sediments. For example, pore-water data indicate that deep water in the Atlantic Ocean cooled by between $-1.7^{\circ}\text{C} \pm 0.9^{\circ}\text{C}$ and $-4.5^{\circ}\text{C} \pm 0.2^{\circ}\text{C}$, and became saltier by up to 2.4 ± 0.2 psu in the South Atlantic and at least 0.95 ± 0.07 psu in the North Atlantic (cf. Adkins et al., 2002). The magnitude of deep-water cooling is supported by other marine proxy data (e.g., Dwyer et al., 2000; Martin et al., 2002; Elderfield et al., 2010), while the increase in salinity is consistent with independent estimates based on $\delta^{18}\text{O}$ (Duplessy et al., 2002; Waelbroeck et al., 2002). Average salinity increased due to storage of freshwater in ice sheets. The much larger than average salinity increase in deep Southern Ocean compared to the North Atlantic is probably due to increased salt rejection through sea ice freezing processes around Antarctica (Miller et al., 2012b) (see also Section 9.4.2.3.2).

As a result of prevailing LGM modelling uncertainties (Chavaillaz et al., 2013; Rojas, 2013) and ambiguities in proxy interpretations (Kohfeld et al., 2013), it cannot be determined robustly whether LGM SH westerlies changed in amplitude and position relative to today.

5.3.3.2 Last Glacial Maximum Constraints on Equilibrium Climate Sensitivity

Temperature change recorded in proxies results from various feedback processes, and external forcings vary before equilibrium of the whole Earth system is reached. Nevertheless, the equilibrium climate sensitivity (ECS) can be estimated from past temperatures by explicitly counting the slow components of the processes (e.g., ice sheets) as forcings, rather than as feedbacks (PALAEOSSENS Project Members, 2012). This is achieved in three fundamentally different ways (Edwards et al., 2007); see also Sections 9.7.3.2 and 10.8.2.4.

In the first approach, ECS is estimated by scaling the reconstructed global mean temperature change in the past with the RF difference of the past and $2 \times \text{CO}_2$ (Hansen et al., 2008; Köhler et al., 2010) (Table 5.3). The results are subject to uncertainties in the estimate of global mean surface temperature based on proxy records of incomplete spatial coverage (see Section 5.3.3.1). Additional uncertainty is introduced when the sensitivity to LGM forcing is scaled to the sensitivity to $2 \times \text{CO}_2$ forcing, as some but not all (Brady et al., 2013) models show that these sensitivities differ due to the difference in cloud feedbacks (Crucifix, 2006; Hargreaves et al., 2007; Yoshimori et al., 2011) (Figure 5.5a, b).

In the second approach, an ensemble of LGM simulations is carried out using a single climate model in which each ensemble member differs in model parameters and the ensemble covers a range of ECS (Annan et al., 2005; Schneider von Deimling et al., 2006; Holden et al., 2010a; Schmittner et al., 2011) (Table 5.3). Model parameters are then constrained by comparison with LGM temperature proxy information, generating a probability distribution of ECS. Although EMICSs are often used in order to attain sufficiently large ensemble size, the uncertainty arising from asymmetric cloud feedbacks cannot be addressed because they are parameterized in the EMICs.

In the third approach, multiple GCM simulations are compared to proxy data, and performance of the models and indirectly their ECSs are assessed (Otto-Bliesner et al., 2009; Braconnot et al., 2012b). Because the cross-model correlation between simulated LGM global cooling

Table 5.3 | Summary of equilibrium climate sensitivity (ECS) estimates based on Last Glacial Maximum (LGM) climate. Uncertainty ranges are 5 to 95% confidence intervals, with the exception of Multiproxy Approach for the Reconstruction of the Glacial Ocean surface (MARGO) Project Members (2009), where the published interval is reported here.

Method (number follows the “approach” in the text)	ECS Estimate (°C)	Reference and Model Name
1. Proxy data	1.0–3.6 1.4–5.2	MARGO Project Members (2009) Köhler et al. (2010)
2. Single-model ensemble constrained by proxy data	<6 1.2–4.3 2.0–5.0 1.4–2.8 ~3.6	Annan et al. (2005), MIROC3.2 AOGCM Schneider von Deimling et al. (2006), CLIMBER-2 Holden et al. (2010a), GENIE-1 Schmittner et al. (2011), UVic Fyke and Eby (2012), UVic
3. Multi-GCM ensemble constrained by proxy data	1.2–4.2 1.6–4.5	Hargreaves et al. (2012), updated with addition of PMIP3/CMIP5 AOGCMs Hargreaves et al. (2012), updated with addition of PMIP3/CMIP5 AOGCMs ^a

Notes:

^a Temperature constraints in the tropics were lowered by 0.4°C according to Annan and Hargreaves (2013).

AOGCM = Atmosphere-Ocean General Circulation Model; CMIP5 = Coupled Model Intercomparison Project Phase 5; CLIMBER-2 = CLIMATE and BiosphERe model-2; GENIE-1 = Grid ENabled Integrated Earth system model, version 1; MIROC3.2 = Model for Interdisciplinary Research on Climate 3.2; UVic = University of Victoria Earth system model; PMIP3 = Paleoclimate Modelling Intercomparison Project Phase III.

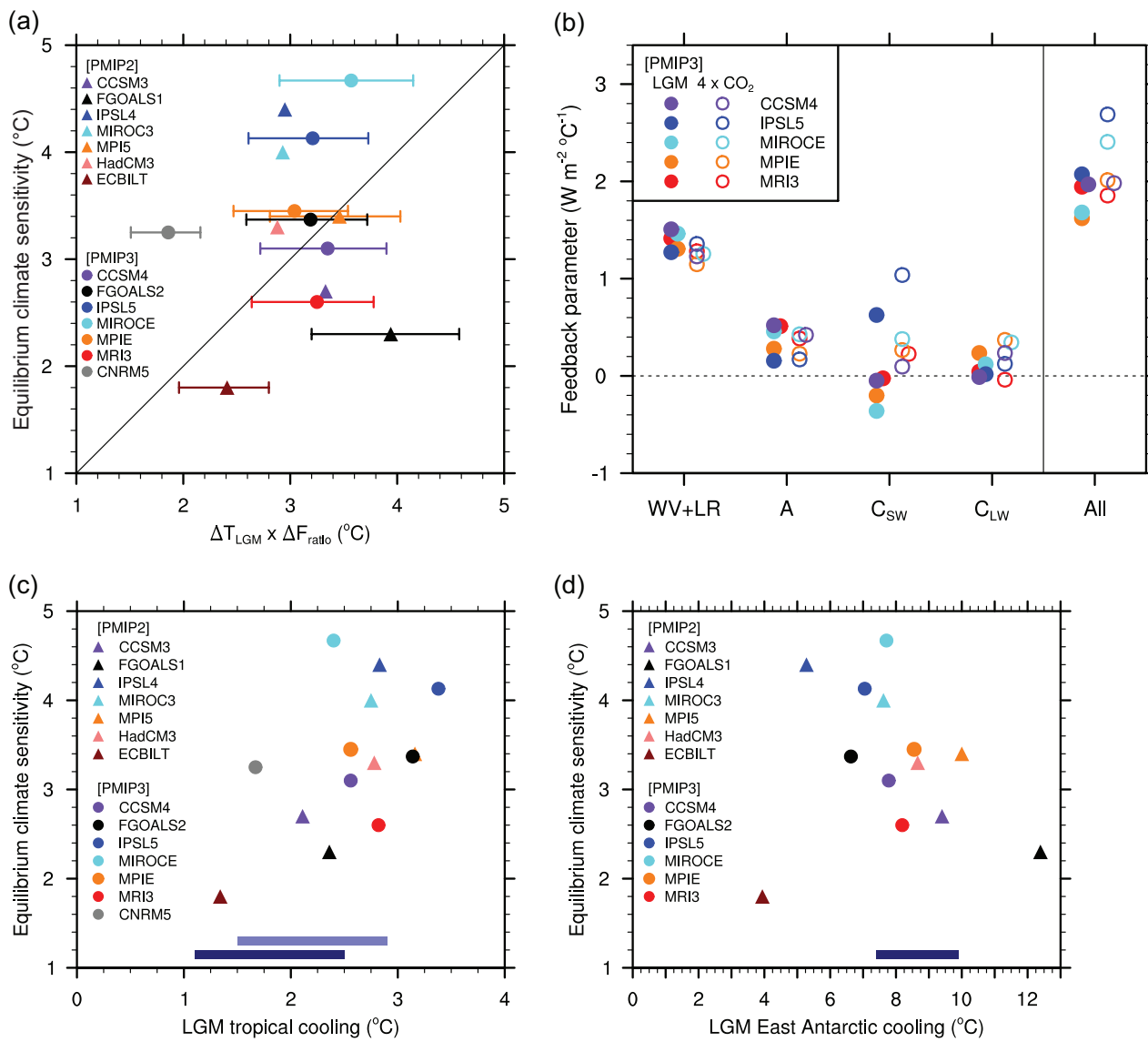


Figure 5.5 | (a) Relation between equilibrium climate sensitivity (ECS) estimated from Last Glacial Maximum (LGM) simulations and that estimated from equilibrium $2 \times \text{CO}_2$ or abrupt $4 \times \text{CO}_2$ experiments. All experiments are referenced to pre-industrial simulations. Flexible Global Ocean Atmosphere Land System model version 1 (FGOALS1), Institut Pierre Simon Laplace version 4 (IPSL4), Max Planck Institute version 5 (MPI5), and ECBILT of Paleoclimate Modelling Intercomparison Project Phase II (PMIP2) models stand for FGOALS-1.0g, IPSL-CM4-V1-MR, European Centre Hamburg Model 5 – and Max Planck Institute Ocean Model – Lund-Potsdam-Jena Dynamic Global Model (LPJ), and Coupled Atmospheric Ocean Model from de Bilt (ECBILT) with Coupled Large-scale Ice-Ocean model (CLIO), respectively. Flexible Global Ocean Atmosphere Land System model-2 (FGOALS2), Institut Pierre Simon Laplace 5 (IPSL5), Model for Interdisciplinary Research on Climate (MIROC3), Max Planck Institute für Meteorologie Earth system model (MPIE), Meteorological Research Institute of Japan Meteorological Agency version 3 (MRI3) and Centre National de Recherches Météorologiques version 5 (CNRM5) of Paleoclimate Modelling Intercomparison Project Phase III (PMIP3) models stand for FGOALS-g2, IPSL-CM5A-LR, MIROC-ESM, MPI-ESM-P, MRI-CGCM3, and CNRM-CM5, respectively. ECS based on LGM simulations (abscissa) was derived by multiplying the LGM global mean temperature anomaly (ΔT_{LGM}) and the ratio of radiative forcing between $2 \times \text{CO}_2$ and LGM (ΔF_{ratio}). ΔF_{ratio} for three PMIP2 models (Community Climate System Model-3 (CCSM3), Met Office Hadley Centre climate prediction models-3 (HadCM3) and IPSL4) were taken from Crucifix (2006), and it was taken from Yoshimori et al. (2009) for MIROC3. Its range, -0.80 to -0.56 , with a mean of -0.69 was used for other PMIP2 and all PMIP3 models. ECS of PMIP2 models (ordinate) was taken from Hargreaves et al. (2012). ECS of PMIP3 models was taken from Andrews et al. (2012) and Brady et al. (2013), or computed using the method of Andrews et al. (2012) for FGOALS2. Also plotted is a one-to-one line. (b) Strength of individual feedbacks for the PMIP3/CMIP5 abrupt $4 \times \text{CO}_2$ (131 to 150 years) and LGM (stable states) experiments following the method in Yoshimori et al. (2011). WV+LR, A, C_{SW} and C_{LW} denote water vapour plus lapse rate, surface albedo, shortwave cloud, and longwave cloud feedbacks, respectively. 'All' denotes the sum of all feedbacks except for the Planck response. Feedback parameter here is defined as the change in net radiation at the top of the atmosphere due to the change in individual fields, such as water vapour, with respect to the pre-industrial simulations. It was normalized by the global mean surface air temperature change. Positive (negative) value indicates that the feedback amplifies (damp) the initial temperature response. Only models with all necessary data available for the analysis are displayed. (c) Relation between LGM tropical (20°S to 30°N) surface air temperature anomaly from pre-industrial simulations and ECS across models. A dark blue bar represents a 90% confidence interval for the estimate of reconstructed temperature anomaly of Annan and Hargreaves (2013). A light blue bar represents the same with additional 0.4°C anomaly increase according to the result of the sensitivity experiment conducted in Annan and Hargreaves (2013), in which additional 1°C lowering of tropical SST proxy data was assumed. (d) Same as in (c) but for the average of East Antarctica ice core sites of Dome F, Vostok, European Project for Ice Coring in Antarctica Dome C and Droning Maud Land ice cores. A dark blue bar represents a range of reconstructed temperature anomaly based on stable isotopes at these core sites (Stenni et al., 2010; Uemura et al., 2012). A value below zero is not displayed (the result of CNRM5). Note that the Antarctic ice sheet used for PMIP3 simulations, based on several different methods (Tarasov and Peltier, 2007; Argus and Peltier, 2010; Lambeck et al., 2010) differs in elevation from that used in PMIP2 (d).

and ECS is poor (Figure 5.5a), ECS cannot be constrained by the LGM global mean cooling. Models that show weaker sensitivity to LGM forcing than $4 \times \text{CO}_2$ forcing in Figure 5.5a tend to show weaker shortwave cloud feedback and hence weaker total feedback under LGM forcing than $4 \times \text{CO}_2$ forcing (Figure 5.5b), consistent with previous studies (Crucifix, 2006). The relation found between simulated LGM tropical cooling and ECS across multi-GCM (Hargreaves et al., 2012; Figure 5.5c) has been used to constrain the ECS with the reconstructed LGM tropical cooling (Table 5.3). Again, the main caveats of this approach are the uncertainties in proxy reconstructions and missing dust and vegetation effects which may lead to underestimated LGM cooling in the simulations.

Based on these different approaches, estimates of ECS yield low probability for values outside the range 1°C to 5°C (Table 5.3). Even though there is some uncertainty in these studies owing to problems in both the paleoclimate data and paleoclimate modelling as discussed in this section, it is *very likely* that ECS is greater than 1°C, and *very unlikely* that ECS exceeds 6°C.

5.3.4 Past Interglacials

Past interglacials are characterized by different combinations of orbital forcing (Section 5.2.1.1), atmospheric composition (Section 5.2.2.1) and climate responses (Tzedakis et al., 2009; Lang and Wolff, 2011). Documenting natural interglacial climate variability in the past provides a deeper understanding of the physical climate responses to orbital forcing. This section reports on interglacials of the past 800 kyr, with emphasis on the Last Interglacial (LIG, Table 5.1) which has more data and modelling studies for assessing regional and global temperature changes than earlier interglacials. The LIG sea level responses are assessed in Section 5.6.2. Section 5.5 is devoted to the current interglacial, the Holocene.

The phasing and strengths of the precessional parameter and obliquity varied over past interglacials (Figure 5.3b, c), influencing their timing, duration, and intensity (Tzedakis et al., 2012b; Yin and Berger, 2012) (Figure 5.3e, f, h). Since 800 ka, atmospheric CO₂ concentrations during interglacials were systematically higher than during glacial periods. Prior to ~430 ka, ice cores from Antarctica record lower interglacial CO₂ concentrations than for the subsequent interglacial periods (Section 5.2.2.1; Figure 5.3d). While LIG WMGHG concentrations were similar to the pre-industrial Holocene values, orbital conditions were very different with larger latitudinal and seasonal insolation variations. Large eccentricity and the phasing of precession and obliquity (Figure 5.3a–c) during the LIG resulted in July 65°N insolation peaking at ~126 ka and staying above the Holocene maximum values from ~129 to 123 ka. The high obliquity (Figure 5.3b) contributed to small, but positive annual insolation anomalies at high latitudes in both hemispheres and negative anomalies at low latitudes.

New data and syntheses from marine and terrestrial archives, with updated age models, have provided an expanded view of temperature patterns during interglacials since 800 ka (Masson-Delmotte et al., 2010a; Lang and Wolff, 2011; Rohling et al., 2012). There is currently no consensus on whether interglacials changed intensity after ~430 ka. EPICA Dome C Antarctic ice cores record warmer temperatures after

this transition (Jouzel et al., 2007) and marine records of deep-water temperatures are characterized by generally higher values during later interglacials than earlier interglacials (Lang and Wolff, 2011). In contrast, similar interglacial magnitudes are observed across the ~430 ka boundary in some terrestrial archives from Eurasia (Prokopenko et al., 2002; Tzedakis et al., 2006; Candy et al., 2010). Simulations with an EMIC relate global and southern high latitude mean annual surface temperature variations to changes in CO₂ variations, while orbital forcing and associated feedbacks of vegetation and sea ice have a major impact on the simulated northern high-latitude mean annual surface temperature (Yin and Berger, 2012). The highest and lowest interglacial temperatures occur in models when WMGHG concentrations and local insolation reinforce each other (Yin and Berger, 2010, 2012; Herold et al., 2012).

At the time of the AR4, a compilation of Arctic records and two AOGCM simulations allowed an assessment of LIG summer temperature changes. New quantitative data syntheses (Figure 5.6a) now allow estimation of maximum annual surface temperatures around the globe for the LIG (Turney and Jones, 2010; McKay et al., 2011). A caveat is that these data syntheses assume that the warmest phases were globally synchronous (see Figure 5.6 legend for details). However, there is *high confidence* that warming in the Southern Ocean (Cortese et al., 2007; Schneider Mor et al., 2012) and over Antarctica (Masson-Delmotte et al., 2010b) occurred prior to peak warmth in the North Atlantic, Nordic Seas, and Greenland (Bauch et al., 2011; Govin et al., 2012; North Greenland Eemian Ice Drilling (NEEM) community members, 2013). Overall, higher annual temperatures than pre-industrial are reconstructed for high latitudes of both hemispheres. At ~128 ka, East Antarctic ice cores record early peak temperatures ~5°C above the present (Jouzel et al., 2007; Sime et al., 2009; Stenni et al., 2010). Higher temperatures are derived for northern Eurasia and Alaska, with sites near the Arctic coast in Northeast Siberia indicating warming of more than 10°C as compared to late Holocene (Velichko et al., 2008). Greenland warming of $8^\circ\text{C} \pm 4^\circ\text{C}$ at 126 ka is estimated from the new Greenland NEEM ice core, after accounting for ice sheet elevation changes (NEEM community members, 2013). Seasonally open waters off northern Greenland and in the central Arctic are recorded during the LIG (Nørsgaard-Pedersen et al., 2007; Adler et al., 2009). Changes in Arctic sea ice cover (Sime et al., 2013) may have affected the Greenland water stable isotope – temperature relationship, adding some uncertainty to LIG Greenland temperature reconstructions. Marine proxies from the Atlantic indicate warmer than late Holocene year-round SSTs north of 30°N, whereas SST changes were more variable south of this latitude (McKay et al., 2011).

Transient LIG simulations with EMICs and low-resolution AOGCMs display peak NH summer warmth between 128 ka and 125 ka in response to orbital and WMGHG forcings. This warming is delayed when NH ice sheets are allowed to evolve (Bakker et al., 2013). Time-slice climate simulations run by 13 modelling groups with a hierarchy of climate models forced with orbital and WMGHG changes for 128 to 125 ka (Figure 5.6b) simulate the reconstructed pattern of NH annual warming (Figure 5.6a). Positive feedbacks with the cryosphere (sea ice and snow cover) provide the memory that allows simulated NH high-latitude warming, annually as well as seasonally, in response to the seasonal orbital forcing (Schurges et al., 2007; Yin and Berger, 2012). The

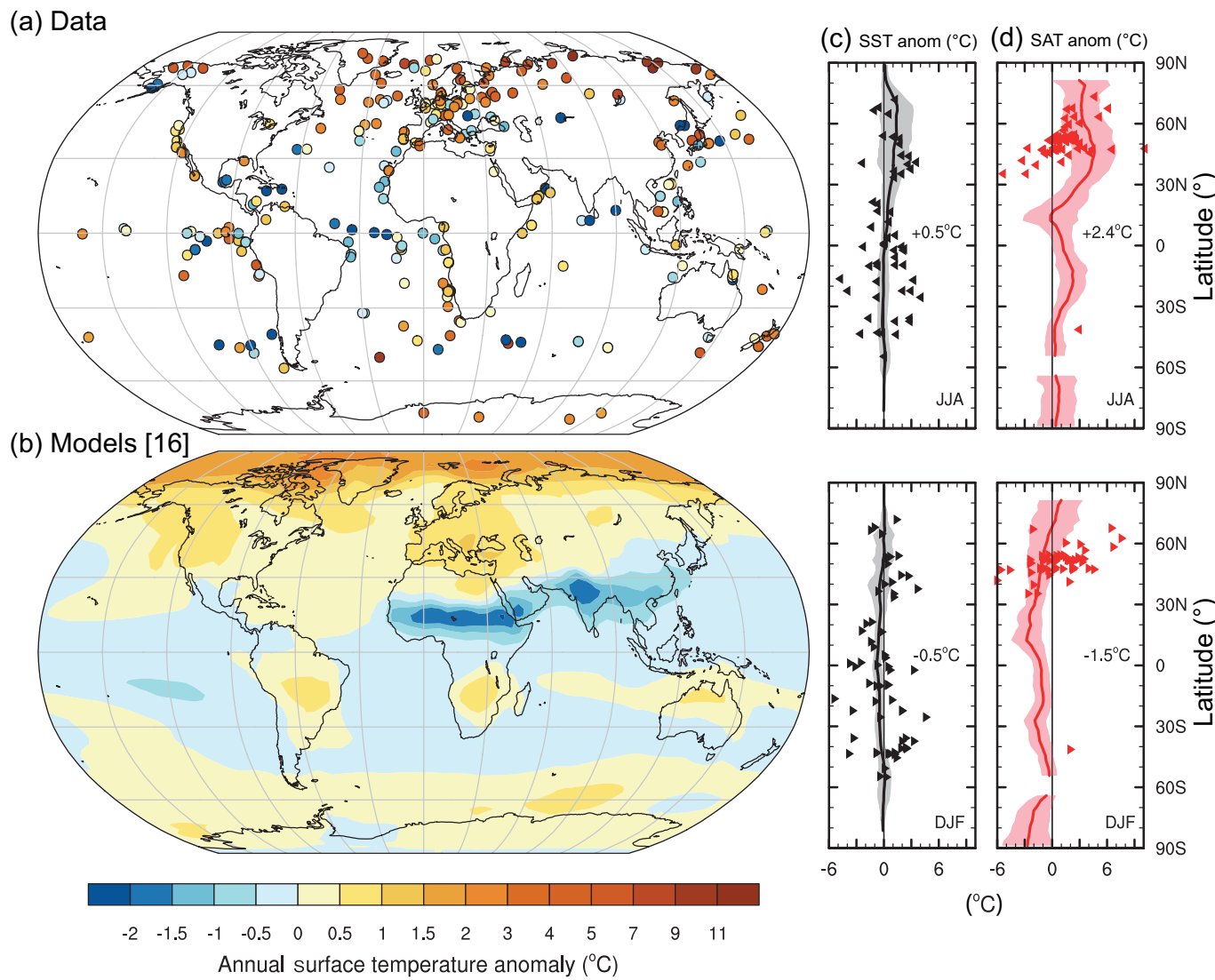


Figure 5.6 | Changes in surface temperature for the Last Interglacial (LIG) as reconstructed from data and simulated by an ensemble of climate model experiments in response to orbital and well-mixed greenhouse gas (WMGHG) forcings. (a) Proxy data syntheses of annual surface temperature anomalies as published by Turney and Jones (2010) and McKay et al. (2011). McKay et al. (2011) calculated an annual anomaly for each record as the average sea surface temperature (SST) of the 5-kyr period centred on the warmest temperature between 135 ka and 118 ka and then subtracting the average SST of the late Holocene (last 5 kyr). Turney and Jones (2010) calculated the annual temperature anomalies relative to 1961–1990 by averaging the LIG temperature estimates across the isotopic plateau in the marine and ice records and the period of maximum warmth in the terrestrial records (assuming globally synchronous terrestrial warmth). (b) Multi-model average of annual surface air temperature anomalies simulated for the LIG computed with respect to pre-industrial. The results for the LIG are obtained from 16 simulations for 128 to 125 ka conducted by 13 modelling groups (Lunt et al., 2013). (c) Seasonal SST anomalies. Multi-model zonal averages are shown as solid line with shaded bands indicating 2 standard deviations. Plotted values are the respective seasonal multi-mean global average. Symbols are individual proxy records of seasonal SST anomalies from McKay et al. (2011). (d) Seasonal terrestrial surface temperature anomalies (SAT). As in (c) but with symbols representing terrestrial proxy records as compiled from published literature (Table 5.A.5). Observed seasonal terrestrial anomalies larger than 10°C or less than -6°C are not shown. In (c) and (d) JJA denotes June – July – August and DJF December – January – February, respectively.

magnitude of observed NH annual warming though is only reached in summer in the simulations (Lunt et al., 2013) (Figure 5.6c, d). The reasons for this discrepancy are not yet fully determined. Error bars on temperature reconstructions vary significantly between methods and regions, due to the effects of seasonality and resolution (Kienast et al., 2011; McKay et al., 2011; Tarasov et al., 2011). Differences may also be related to model representations of cloud and sea ice processes (Born et al., 2010; Fischer and Jungclaus, 2010; Kim et al., 2010; Otto-Bliesner et al., 2013), and that most LIG simulations set the vegetation and ice sheets to their pre-industrial states (Schurgers et al., 2007; Holden et al., 2010b; Bradley et al., 2013). Simulations accounting for the bipolar

5 seesaw response to persistent iceberg melting at high northern latitudes (Govin et al., 2012) and disintegration of the WAIS (Overpeck et al., 2006) (see Section 5.6.2.3) are better able to reproduce the early LIG Antarctic warming (Holden et al., 2010b).

From data synthesis, the LIG global mean annual surface temperature is estimated to be ~1°C to 2°C warmer than pre-industrial (*medium confidence*) (Turney and Jones, 2010; Otto-Bliesner et al., 2013), albeit proxy reconstructions may overestimate the global temperature change. High latitude surface temperature, averaged over several thousand years, was at least 2°C warmer than present (*high confidence*). In

response to orbital forcing and WMGHG concentration changes, time slice simulations for 128 to 125 ka exhibit global mean annual surface temperature changes of $0.0^{\circ}\text{C} \pm 0.5^{\circ}\text{C}$ as compared to pre-industrial. Data and models suggest a land–ocean contrast in the responses to the LIG forcing (Figure 5.6c, d). Peak global annual SST warming is estimated from data to be $0.7^{\circ}\text{C} \pm 0.6^{\circ}\text{C}$ (*medium confidence*) (McKay et al., 2011). Models give more confidence to the lower bound. The ensemble of climate model simulations gives a large range of global annual land temperature change relative to pre-industrial, -0.4°C to 1.7°C , when sampled at the data locations and cooler than when averaged for all model land areas, pointing to difficulties in estimating global mean annual surface temperature with current spatial data coverage (Otto-Btiesner et al., 2013).

5.3.5 Temperature Variations During the Last 2000 Years

The last two millennia allow comparison of instrumental records with multi-decadal-to-centennial variability arising from external forcings and internal climate variability. The assessment benefits from high-resolution proxy records and reconstructions of natural and anthropogenic forcings back to at least 850 (Section 5.2), used as boundary conditions for transient GCM simulations. Since AR4, expanded proxy data networks and better understanding of reconstruction methods have supported new reconstructions of surface temperature changes during

the last 2000 years (Section 5.3.5.1) and their associated uncertainties (Section 5.3.5.2), and supported more extensive comparisons with GCM simulations (Section 5.3.5.3).

5.3.5.1 Recent Warming in the Context of New Reconstructions

New paleoclimate reconstruction efforts since AR4 (Figure 5.7; Table 5.4; Appendix 5.A.1) have provided further insights into the characteristics of the Medieval Climate Anomaly (MCA; Table 5.1) and the Little Ice Age (LIA; Table 5.1). The timing and spatial structure of the MCA and LIA are complex (see Box 6.4 in AR4 and Diaz et al., 2011; and Section 5.5), with different reconstructions exhibiting warm and cold conditions at different times for different regions and seasons. The median of the NH temperature reconstructions (Figure 5.7) indicates mostly warm conditions from about 950 to about 1250 and colder conditions from about 1450 to about 1850; these time intervals are chosen here to represent the MCA and the LIA, respectively.

Based on multiple lines of evidence (using different statistical methods or different compilations of proxy records; see Appendix 5.A.1 for a description of reconstructions and selection criteria), published reconstructions and their uncertainty estimates indicate, with *high confidence*, that the mean NH temperature of the last 30 or 50 years *very likely* exceeded any previous 30- or 50-year mean during the past 800

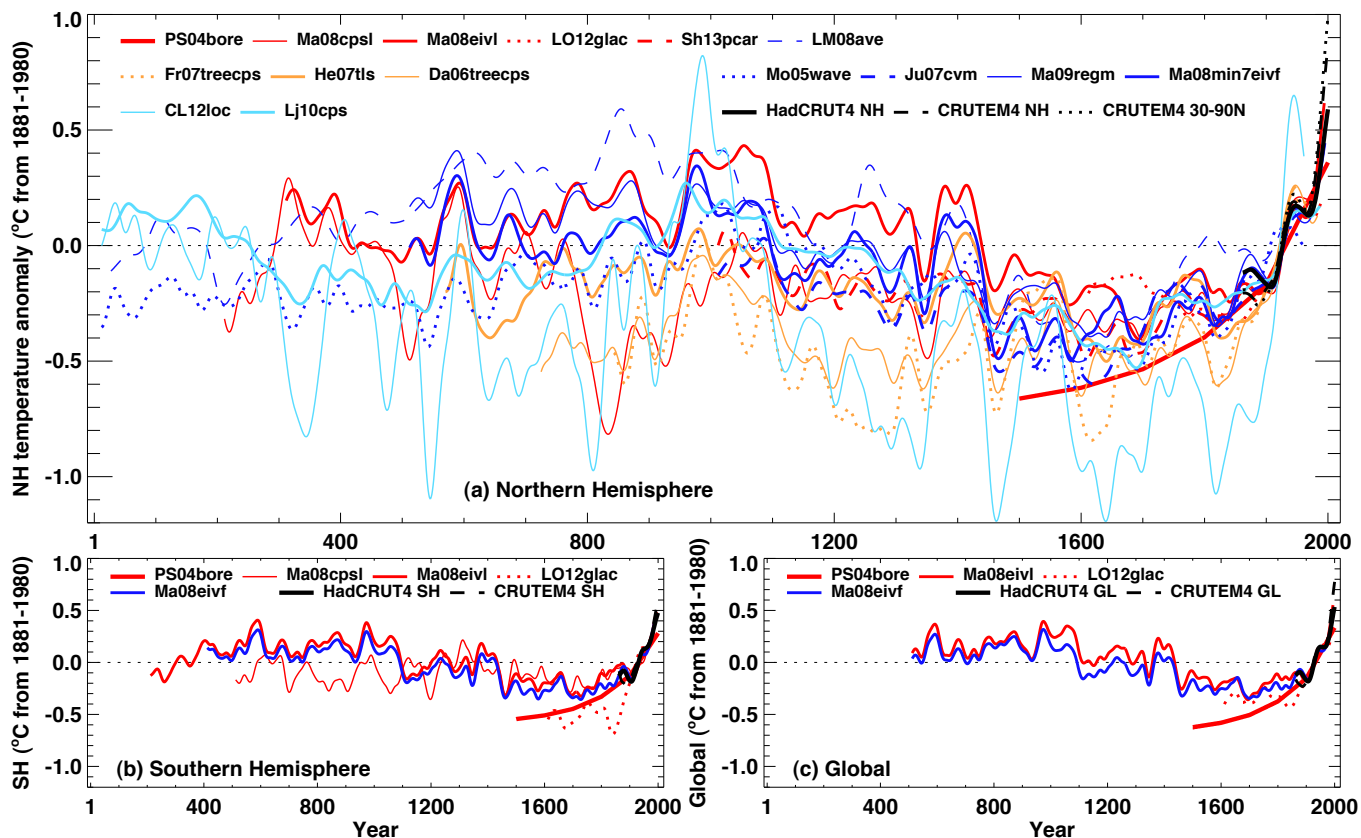


Figure 5.7 | Reconstructed (a) Northern Hemisphere and (b) Southern Hemisphere, and (c) global annual temperatures during the last 2000 years. Individual reconstructions (see Appendix 5.A.1 for further information about each one) are shown as indicated in the legends, grouped by colour according to their spatial representation (red: land-only all latitudes; orange: land-only extratropical latitudes; light blue: land and sea extra-tropical latitudes; dark blue: land and sea all latitudes) and instrumental temperatures shown in black (Hadley Centre/Climatic Research Unit (CRU) gridded surface temperature-4 data set (HadCRUT4) land and sea, and CRU Gridded Dataset of Global Historical Near-Surface Air TEMperature Anomalies Over Land version 4 (CRUTEM4) land-only; Morice et al., 2012). All series represent anomalies ($^{\circ}\text{C}$) from the 1881–1980 mean (horizontal dashed line) and have been smoothed with a filter that reduces variations on time scales less than about 50 years.

years (Table 5.4). The timing of warm and cold periods is mostly consistent across reconstructions (in some cases this is because they use similar proxy compilations) but the magnitude of the changes is clearly sensitive to the statistical method and to the target domain (land or land and sea; the full hemisphere or only the extra-tropics; Figure 5.7a). Even accounting for these uncertainties, almost all reconstructions agree that each 30-year (50-year) period from 1200 to 1899 was *very likely* colder in the NH than the 1983–2012 (1963–2012) instrumental temperature.

NH reconstructions covering part or all of the first millennium suggest that some earlier 50-year periods might have been as warm as the 1963–2012 mean instrumental temperature, but the higher temperature of the last 30 years appear to be at least *likely* the warmest 30-year period in all reconstructions (Table 5.4). However, the confidence in this finding is lower prior to 1200, because the evidence is less reliable and there are fewer independent lines of evidence. There are fewer proxy records, thus yielding less independence among the

Table 5.4 | Comparison of recent hemispheric and global temperature estimates with earlier reconstructed values, using published uncertainty ranges to assess likelihood of unusual warmth. Each reconstructed N -year mean temperature within the indicated period is compared with both the warmest N -year mean reconstructed after 1900 and with the most recent N -year mean instrumental temperature, for $N = 30$ and $N = 50$ years. Blue symbols indicate the periods and reconstructions where the reconstructed temperatures are *very likely* cooler than the post-1900 reconstruction (■), or otherwise *very likely* (*) or *likely* (☒) cooler than the most recent instrumental temperatures; □ indicates that some reconstructed temperatures were as likely warmer or colder than recent temperatures.

Region	NH														SH			Global		
Domain	Land & Sea					Land				Extratropics					Land			Land		
Study	1	2	3	4	5	6	7	8	9	10	11	12	13	14	7	6	9	7	9	15
50-year means																				
1600–1899	■	*	*	*	■	*	■	*	■	■	■	■	■	■	*	■	*	■	*	■
1400–1899	■	*	*	*	■	*	■	*	■	■	■	■	■	■	*	■	*	■	*	
1200–1899	■	*	*	*	■	*	■	*	*	■	■	■	■	■	*	■	*	■	*	
1000–1899	*	*	*	*	☒	■	*	*	■	*	■	■	■	■	*	■	*	■	*	*
800–1899	*	☒	☒	☒		□	■	*		*	□	■	■	■	☒	*	☒	*	☒	*
600–1899	*	☒	☒	☒		□	■	*		*	□	■	■	■	☒	*	☒	*	☒	*
400–1899	*	☒	☒	□		□	*	*		*	□	■	■	■	□		□			
200–1899	*					□	*			*	□	■	■	■	□		□			
1–1899	*									*	□									
30-year means																				
1600–1899	■	*	*	*	■	*	■	*	■	■	■	■	■	■	*	■	■	*	■	*
1400–1899	■	*	*	*	■	*	■	*	■	■	■	■	■	■	*	■	*	■	*	
1200–1899	■	*	*	*	■	*	■	*	■	■	■	■	■	■	*	■	*	■	*	
1000–1899	*	*	*	*	*	■	*	*	■	*	■	■	■	■	*	■	*	■	*	
800–1899	*	*	*		☒	■	*		*	■	■	■	■	■	*	■	*	■	*	
600–1899	*	*	*		☒	■	*		*	■	■	■	■	■	*	■	*	■	*	
400–1899	*	*			☒	*	*		*	■	■	■	■	■	*	■		■		
200–1899	*				☒	*			*	■	■	■	■	■	*	■		■		
1–1899	*									*										

Notes:

Symbols indicate the likelihood (based on the published multi-decadal uncertainty ranges) that each N -year mean of the reconstructed temperature during the indicated period was colder than the warmest N -year mean after 1900. A reconstructed mean temperature X is considered to be *likely* (*very likely*) colder than a modern temperature Y if $X+aE < Y$, where E is the reconstruction standard error and $a = 0.42$ (1.29) corresponding to a 66% (90%) one-tailed confidence interval assuming the reconstruction error is normally distributed. Symbols indicate that the reconstructed temperatures were either:

- ☒ *likely* colder than the 1983–2012 or 1963–2012 mean instrumental temperature;
- *
- *very likely* colder than the 1983–2012 or 1963–2012 mean instrumental temperature;
- *very likely* colder than the 1983–2012 or 1963–2012 mean instrumental temperature and additionally *very likely* colder than the warmest 30- or 50-year mean of the post-1900 reconstruction (which is typically not as warm as the end of the instrumental record);
- indicates that at least one N -year reconstructed mean is about as likely colder or warmer than the 1983–2012 or 1963–2012 mean instrumental temperature.

No symbol is given where the reconstruction does not fully cover the indicated period.

Identification and further information for each study is given in Table 5.A.6 of Appendix 5.A.1:

- 1 = Mo05wave; 2 = Ma08eiv; 3 = Ma09regm; 4 = Ju07cvm; 5 = LM08ave; 6 = Ma08cpsl; 7 = Ma08eivl; 8 = Sh13pcar; 9 = LO12gla; 10 = Lj10cps; 11 = CL12loc; 12 = He07tls; 13 = Da06treecps;
- 14 = Fr07treecps; 15 = PS04bore.

reconstructions while making them more susceptible to errors in individual proxy records. The published uncertainty ranges do not include all sources of error (Section 5.3.5.2), and some proxy records and uncertainty estimates do not fully represent variations on time scales as short as the 30 years considered in Table 5.4. Considering these caveats, there is *medium confidence* that the last 30 years were *likely* the warmest 30-year period of the last 1400 years.

Increasing numbers of proxy records and regional reconstructions are being developed for the SH (see Section 5.5), but few reconstructions of SH or global mean temperatures have been published (Figure 5.7b, c). The SH and global reconstructions with published uncertainty estimates indicate that each 30- or 50-year interval during the last four centuries was *very likely* colder than the warmest 30- or 50-year interval after 1900 (Table 5.4). However, there is only limited proxy evidence and therefore *low confidence* that the recent warming has exceeded the range of reconstructed temperatures for the SH and global scales.

5.3.5.2 Reconstruction Methods, Limitations and Uncertainties

Reconstructing NH, SH or global-mean temperature variations over the last 2000 years remains a challenge due to limitations of spatial sampling, uncertainties in individual proxy records and challenges associated with the statistical methods used to calibrate and integrate multi-proxy information (Hughes and Ammann, 2009; Jones et al., 2009; Frank et al., 2010a). Since AR4, new assessments of the statistical methods used to reconstruct either global/hemispheric temperature averages or spatial fields of past temperature anomalies have been published. The former include approaches for simple compositing and scaling of local or regional proxy records into global and hemispheric averages using uniform or proxy-dependent weighting (Hegerl et al., 2007; Juckes et al., 2007; Mann et al., 2008; Christiansen and Ljungqvist, 2012). The latter correspond to improvements in climate field reconstruction methods (Mann et al., 2009; Smerdon et al., 2011) that apply temporal and spatial relationships between instrumental and proxy records to the pre-instrumental period. New developments for both reconstruction approaches include implementations of Bayesian inference (Li et al., 2010a; Tingley and Huybers, 2010, 2012; McShane and Wyner, 2011; Werner et al., 2013). In particular, Bayesian hierarchical models enable a more explicit representation of the underlying processes that relate proxy (and instrumental) records to climate, allowing a more systematic treatment of the multiple uncertainties that affect the climate reconstruction process. This is done by specifying simple parametric forms for the proxy-temperature relationships that are then used to estimate a probability distribution of the reconstructed temperature evolution that is compatible with the available data (Tingley et al., 2012).

An improved understanding of potential uncertainties and biases associated with reconstruction methods has been achieved, particularly by using millennial GCM simulations as a surrogate reality in which pseudo-proxy records are created and reconstruction methods are replicated and tested (Smerdon, 2012). A key finding is that the methods used for many published reconstructions can underestimate the amplitude of the low-frequency variability (Lee et al., 2008; Christiansen et al., 2009; Smerdon et al., 2010). The magnitude of this amplitude attenuation in real-world reconstructions is uncertain, but for affected methods the

problem will be larger: (i) for cases with weaker correlation between instrumental temperatures and proxies (Lee et al., 2008; Christiansen et al., 2009; Smerdon et al., 2011); (ii) if errors in the proxy data are not incorporated correctly (Hegerl et al., 2007; Ammann et al., 2010); or (iii) if the data are detrended in the calibration phase (Lee et al., 2008; Christiansen et al., 2009). The 20th-century trends in proxies may contain relevant temperature information (Ammann and Wahl, 2007) but calibration with detrended or undetrended data has been an issue of debate (von Storch et al., 2006; Wahl et al., 2006; Mann et al., 2007) because trends in proxy records can be induced by other (non-temperature) climate and non-climatic influences (Jones et al., 2009; Gagen et al., 2011). Recent developments mitigate the loss of low-frequency variance in global and hemispheric reconstructions by increasing the correlation between proxies and temperature through temporal smoothing (Lee et al., 2008) or by correctly attributing part or all of the temperature-proxy differences to imperfect proxy data (Hegerl et al., 2007; Juckes et al., 2007; Mann et al., 2008). Pseudoproxy experiments have shown that the latter approach used with a site-by-site calibration (Christiansen, 2011; Christiansen and Ljungqvist, 2012) can also avoid attenuation of low-frequency variability, though it is debated whether it might instead inflate the variability and thus constitute an upper bound for low-frequency variability (Moberg, 2013). Even those field reconstruction methods that do not attenuate the low-frequency variability of global or hemispheric means may still suffer from attenuation and other errors at regional scales (Smerdon et al., 2011; Annan and Hargreaves, 2012; Smerdon, 2012; Werner et al., 2013).

The fundamental limitations for deriving past temperature variability at global/hemispheric scales are the relatively short instrumental period and the number, temporal and geographical distribution, reliability and climate signal of proxy records (Jones et al., 2009). The database of high-resolution proxies has been expanded since AR4 (Mann et al., 2008; Wahl et al., 2010; Neukom and Gergis, 2011; PAGES 2k Consortium, 2013), but data are still sparse in the tropics, SH and over the oceans (see new developments in Section 5.5). Integration of low-resolution records (e.g., marine or some lake sediment cores and some speleothem records) with high-resolution tree-ring, ice core and coral records in global/hemispheric reconstructions is still challenging. Dating uncertainty, limited replication and the possibility of temporal lags in low-resolution records (Jones et al., 2009) make regression-based calibration particularly difficult (Christiansen et al., 2009) and can be potentially best addressed in the future with Bayesian hierarchical models (Tingley et al., 2012). The short instrumental period and the paucity of proxy data in specific regions may preclude obtaining accurate estimates of the covariance of temperature and proxy records (Juckes et al., 2007), impacting the selection and weighting of proxy records in global/hemispheric reconstructions (Bürger, 2007; Osborn and Briffa, 2007; Emile-Geay et al., 2013b) and resulting in regional errors in climate field reconstructions (Smerdon et al., 2011).

Two further sources of uncertainty have been only partially considered in the published literature. First, some studies have used multiple statistical models (Mann et al., 2008) or generated ensembles of reconstructions by sampling parameter space (Frank et al., 2010b), but this type of structural and parameter uncertainty needs further examination (Christiansen et al., 2009; Smerdon et al., 2011). Second, proxy-temperature relationships may change over time due to the effect of other climate

and non-climate influences on a proxy, a prominent example being the divergence between some tree-ring width and density chronologies and instrumental temperature trends during the last decades of the 20th century (Briffa et al., 1998). In cases that do show divergence, a number of factors may be responsible, such as direct temperature or drought stress on trees, delayed snowmelt, changes in seasonality and reductions in solar radiation (Lloyd and Bunn, 2007; D'Arrigo et al., 2008; Porter and Pisaric, 2011). However, this phenomenon does not affect all tree-ring records (Wilson et al., 2007; Esper and Frank, 2009) and in some cases where divergence is apparent it may arise from the use of inappropriate statistical standardization of the data (Melvin and Briffa, 2008; Briffa and Melvin, 2011) and not from a genuine change in the proxy–temperature relationship. For the European Alps and Siberia, Büntgen et al., (2008) and Esper et al. (2010) demonstrate that divergence can be avoided by careful selection of sites and standardization methods together with large sample replication.

Limitations in proxy data and reconstruction methods suggest that published uncertainties will underestimate the full range of uncertainties of large-scale temperature reconstructions (see Section 5.3.5.1). While this has fostered debate about the extent to which proxy-based reconstructions provide useful climate information (e.g., McShane and Wyner, 2011 and associated comments and rejoinder), it is well established that temperature and external forcing signals are detectable in proxy reconstructions (Sections 5.3.5.3 and 10.7.2). Recently, model experiments assuming a nonlinear sensitivity of tree-rings to climate (Mann et al., 2012) have been used to suggest that the tree-ring response to volcanic cooling may be attenuated and lagged. Tree-ring data and additional tree-growth model assessments (Anchukaitis et al., 2012; Esper et al., 2013) have challenged this interpretation and analyses of instrumental data suggest hemispheric temperature reconstructions agree well with the degree of volcanic cooling during early 19th-century volcanic events (Brohan et al., 2012; see Section 5.3.5.3). These lines of evidence leave the representation of volcanic events in tree-ring records and associated hemispheric scale temperature reconstructions as an emerging area of investigation.

5.3.5.3 Comparing Reconstructions and Simulations

The number of GCM simulations of the last millennium has increased since AR4 (Fernández-Donado et al., 2013). The simulations have used different estimates of natural and anthropogenic forcings (Table 5.A.1). In particular, the PMIP3/CMIP5 simulations are driven by smaller long-term changes in TSI (Section 5.2.1; Figure 5.1b): TSI increases by $\leq 0.10\%$ from the Late Maunder Minimum (LMM; 1675–1715) to the late 20th century (Schmidt et al., 2011), while most previous simulations use increases between 0.23% and 0.29% (Fernández-Donado et al., 2013). Simulated NH temperatures during the last millennium lie mostly within the uncertainties of the available reconstructions (Figure 5.8a). This agreement between GCM simulations and reconstructions provides neither strong constraints on forcings nor on model sensitivities because internal variability and uncertainties in the forcings and reconstructions are considerable factors.

Data have also been assimilated into climate models (see Sections 5.5 and 10.7, Figure 10.19) by either nudging simulations to follow local or regional proxy-based reconstructions (Widmann et al., 2010) or by

selecting simulations from decade-by-decade ensembles to obtain the closest match to reconstructed climate patterns (Annan and Hargreaves, 2012; Goosse et al., 2012a). The resulting simulations provide insight into the relative roles of internal variability and external forcing (Goosse et al., 2012b), and processes that may account for the spatial distribution of past climate anomalies (Crespin et al., 2009; Palastanga et al., 2011).

Figure 5.8b–d provides additional tests of model-data agreement by compositing the temperature response to a number of distinct forcing events. The models simulate a significant NH cooling in response to volcanic events (Figure 5.8b; peaks between 0.1°C and 0.5°C depending on model) that lasts 3 to 5 years, overlapping with the signal inferred from reconstructions with annual resolution (0.05°C to 0.3°C). CMIP5 simulations tend to overestimate cooling following the major 1809 and 1815 eruptions relative to early instrumental data (Brohan et al., 2012). Such differences could arise from uncertainties in volcanic forcing (Section 5.2.1.3) and its implementation in climate models (Joshi and Jones, 2009) or from errors in the reconstructions (Section 5.3.5.2). Since many reconstructions do not have annual resolution, similar composites (Figure 5.8c) are formed to show the response to changes in multi-decadal volcanic forcings (representing clusters of eruptions). Both the simulated and reconstructed responses are significant and comparable in magnitude, although simulations show a faster recovery (<5 years) than reconstructions. Solar forcing estimated over the last millennium shows weaker variations than volcanic forcing (Figure 5.8d), even at multi-decadal time scales. Compositing the response to multi-decadal fluctuations in solar irradiance shows cooling in simulations and reconstructions of NH temperature between 0.0°C and 0.15°C . In both cases, the cooling may be partly a response to concurrent variations in volcanic forcing (green line in Figure 5.8d).

Temperature differences between the warmest and coolest centennial or multi-centennial periods provide an additional comparison of the amplitude of NH temperature variations in the reconstructions and simulations: between 950 and 1250 (nominally the MCA) and 1450–1850 (nominally the LIA; Figures 5.8e; 5.9a–c) and between the LIA and the 20th century (Figures 5.8f; 5.9g–i). Despite similar multi-model and multi-reconstruction means for the warming from the LIA to the present, the range of individual results is very wide (see Sections 9.5.3.1 and 10.7.1 for a comparison of reconstructed and simulated variability across various frequency ranges) and there is no clear difference between runs with weaker or stronger solar forcing (Figure 5.8f; Section 10.7.2). The difference between the MCA and LIA temperatures, however, has a smaller range for the model simulations than the reconstructions, and the simulations (especially those with weaker solar forcing) lie within the lower half of the reconstructed range of temperature changes (Figure 5.8e). Recent studies have assessed the consistency of model simulations and temperature reconstructions at the hemispheric scale. Hind and Moberg (2012) found closer data-model agreement for simulations with 0.1% TSI increase than 0.24% TSI increase, but the result is sensitive to the reconstruction uncertainty and the climate sensitivity of the model. Simulations with an EMIC using a much stronger solar forcing (0.44% TSI increase from LMM to present, Shapiro et al., 2011) appear to be incompatible with most temperature reconstructions (Feulner, 2011).

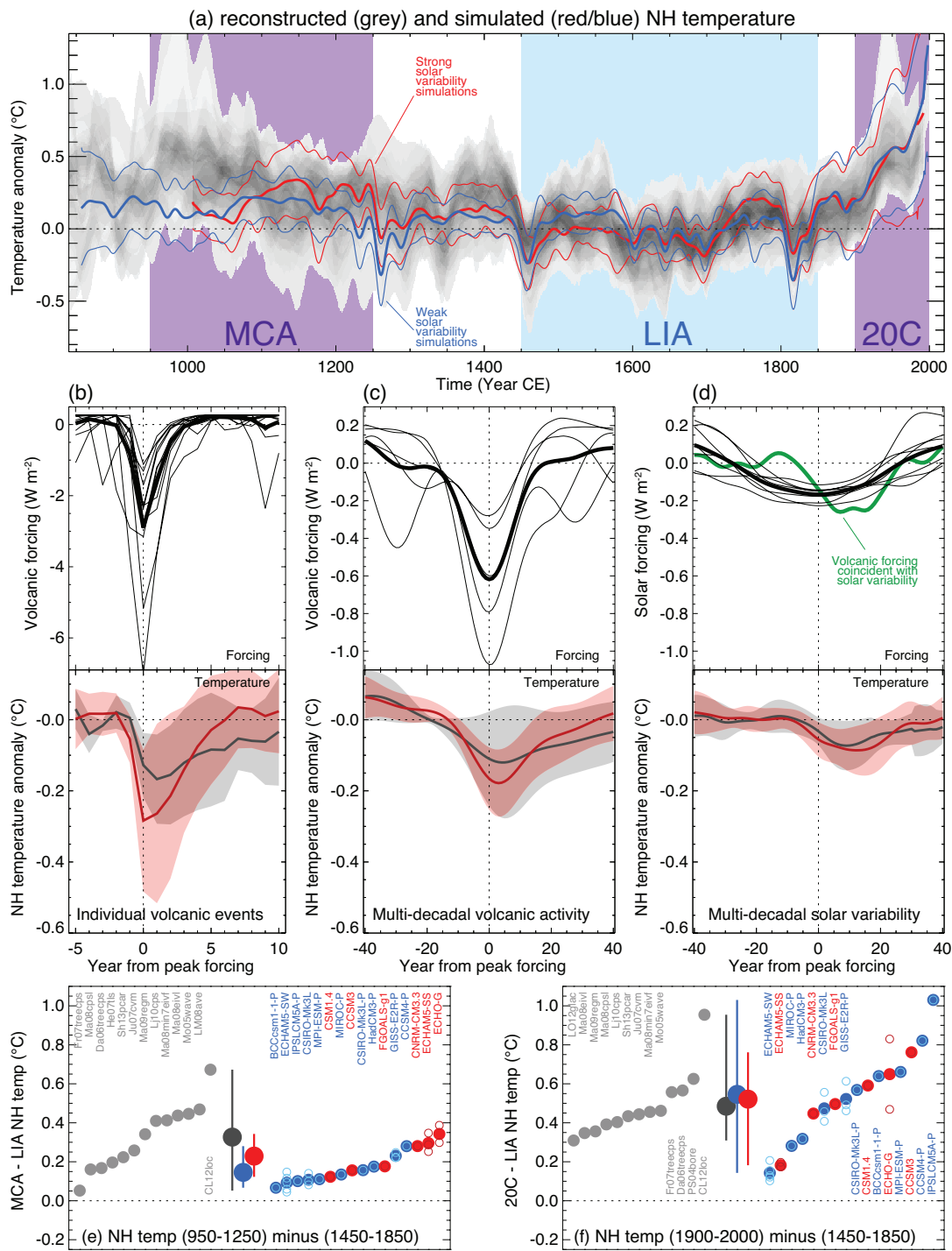
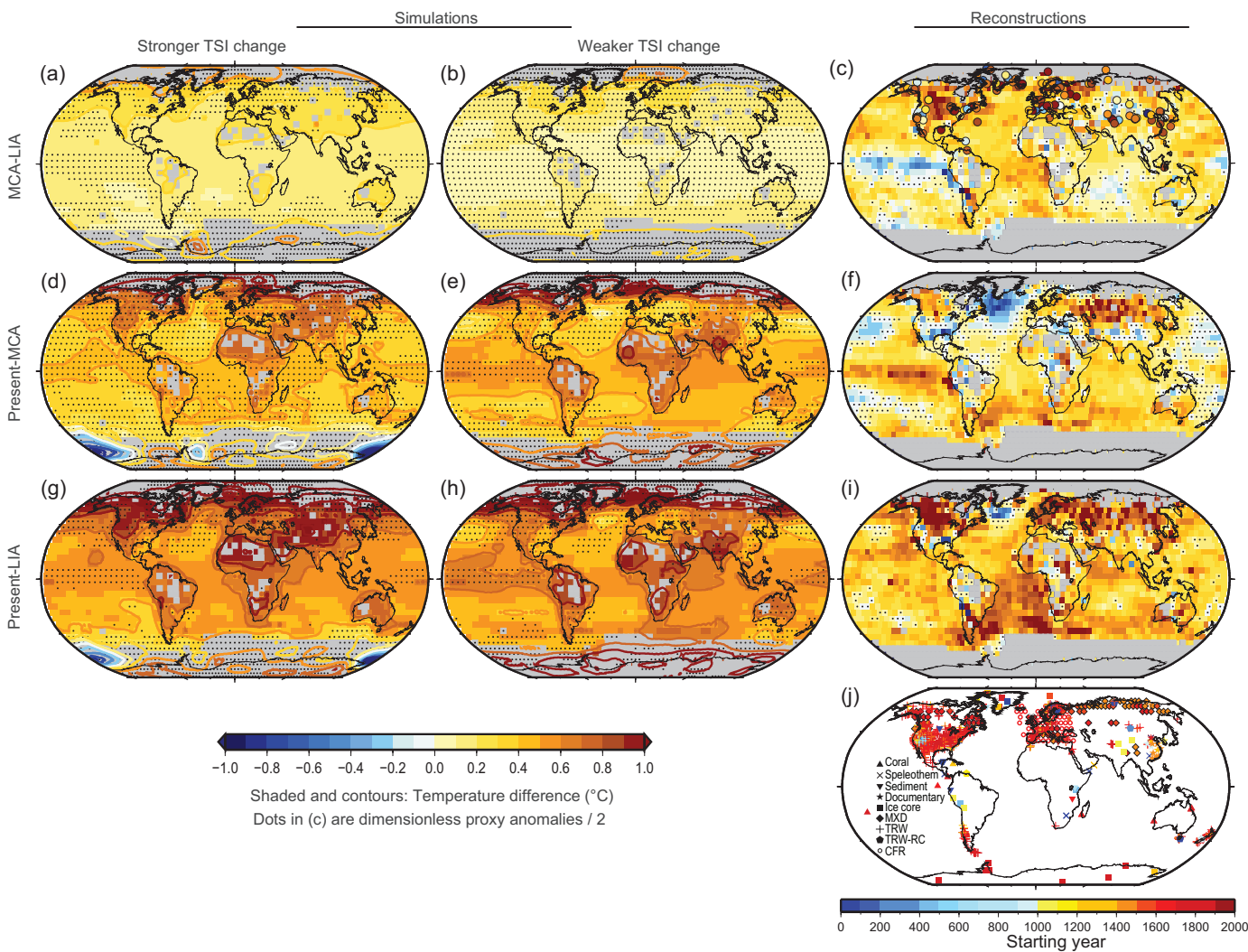


Figure 5.8 | Comparisons of simulated and reconstructed NH temperature changes. (a) Changes over the last millennium (Medieval Climate Anomaly, MCA; Little Ice Age, LIA; 20th century, 20C) (b) Response to individual volcanic events. (c) Response to multi-decadal periods of volcanic activity. (d) Response to multi-decadal variations in solar activity. (e) Mean change from the MCA to the LIA. (f) Mean change from 20th century to LIA. Note that some reconstructions represent a smaller spatial domain than the full Northern Hemisphere (NH) or a specific season, while annual temperatures for the full NH mean are shown for the simulations. (a) Simulations shown by coloured lines (thick lines: multi-model-mean; thin lines: multi-model 90% range; red/blue lines: models forced by stronger/weaker solar variability, though other forcings and model sensitivities also differ between the red and blue groups); overlap of reconstructed temperatures shown by grey shading; all data are expressed as anomalies from their 1500–1850 mean and smoothed with a 30-year filter. Superposed composites (time segments from selected periods positioned so that the years with peak negative forcing are aligned) of the forcing and temperature response to: (b) 12 of the strongest individual volcanic forcing events after 1400 (the data shown are not smoothed); (c) multi-decadal changes in volcanic activity; (d) multi-decadal changes in solar irradiance. Upper panels show volcanic or solar forcing for the individual selected periods together with the composite mean (thick line); in (d), the composite mean of volcanic forcing (green) during the solar composite is also shown. Lower panels show the NH temperature composite means and 90% range of spread between simulations (red line, pink shading) or reconstructions (grey line and shading), with overlap indicated by darker shading. Mean NH temperature difference between (e) MCA (950–1250) and LIA (1450–1850) and (f) 20th century (1900–2000) and LIA, from reconstructions (grey), multi-reconstruction mean and range (dark grey), multi-model mean and range and individual simulations (red/blue for models forced by stronger/weaker solar variability). Where an ensemble of simulations is available from one model, the ensemble mean is shown in solid and the individual ensemble members by open circles. Results are sorted into ascending order and labelled. Reconstructions, models and further details are given in Appendix 5.A.1 and Tables 5.A.1 and 5.A.6.



5 **Figure 5.9 |** Simulated and reconstructed temperature changes for key periods in the last millennium. Annual temperature differences for: (a) to (c) Medieval Climate Anomaly (MCA, 950–1250) minus Little Ice Age (LIA, 1450–1850); (d) to (f) present (1950–2000) minus MCA; (g) to (i) present minus LIA. Model temperature differences (left and middle columns) are average temperature changes in the ensemble of available model simulations of the last millennium, grouped into those using stronger (total solar irradiance (TSI) change from the Late Maunder Minimum (LMM) to present $>0.23\%$; left column; SS in Table 5.A.1) or weaker solar forcing changes (TSI change from the LMM to present $<0.1\%$; middle column; SW in Table 5.A.1). Right column panels (c, f, i) show differences (shading) for the Mann et al. (2009) field reconstruction. In (c), dots represent additionally proxy differences from Ljungqvist et al. (2012), scaled by 0.5 for display purposes. The distribution, type and temporal span of the input data used in the field reconstruction of Mann et al. (2009) are shown in (j); proxy types are included in the legend, acronyms stand for: tree-ring maximum latewood density (MXD); tree-ring width (TRW); regional TRW composite (TRW-RC); and multi-proxy climate field reconstruction (CFR). Dotted grid-cells indicate non-significant differences (<0.05 level) in reconstructed fields (right) or that $<80\%$ of the simulations showed significant changes of the same sign (left and middle). For simulations starting after 950, the period 1000–1250 was used to estimate MCA values. Grid cells outside the domain of the Mann et al. (2009) reconstruction are shaded grey in the model panels to enable easier comparison, though contours (interval 0.2 K) illustrate model output over the complete global domain. Only simulations spanning the whole millennium and including at least solar, volcanic and greenhouse gas forcing have been used (Table 5.A.1): BCC-csm1-1 (1), CCSM3 (1), CCSM4 (1), CNRM-CM3.3, CSIRO-mk3L-1-2 (4), CSM1.4 (1), ECHAM5-MPIOM (8), ECHO-G (1), MPI-ESM-P (1), FGOALS-gl (1), GISS-E2-R (3), HadCM3 (1), IPSL-CM5A-LR (1). Averages for each model are calculated first, to avoid models with multiple simulations having greater influence on the ensemble means shown here.

The spatial distributions of simulated and reconstructed (Mann et al., 2009; Ljungqvist et al., 2012) temperature changes between the MCA, LIA and 20th century are shown in Figure 5.9. Simulated changes tend to be larger, particularly with stronger TSI forcing, over the continents and ice/snow-covered regions, showing polar amplification (see Box 5.1). The largest simulated and reconstructed changes are between the LIA and present, with reconstructions (Figure 5.9i) indicating widespread warming except for the cooling south of Greenland. Models also simulate overall warming between the MCA and present (Figure 5.9d, e), whereas the reconstructions indicate significant regional cooling (in the North Atlantic, southeastern North America, and the mid-latitudes

of the Pacific Ocean). This is not surprising because greater regional variability is expected in the reconstructions compared with the mean of multiple model simulations, though reconstructed changes for such areas with few or no proxy data (Figure 5.9i) should also be interpreted with caution (Smerdon et al., 2011). The reconstructed temperature differences between MCA and LIA (Figure 5.9c) indicate higher medieval temperatures over the NH continents in agreement with simulations (Figure 5.9a, b). The reconstructed MCA warming is higher than in the simulations, even for stronger TSI changes and individual simulations (Fernández-Donado et al., 2013). Simulations with proxy assimilation show that this pattern of change is compatible with a direct response

to a relatively weak solar forcing and internal variability patterns similar to a positive Northern Annular Mode (NAM) phase and northward shifts of the Kuroshio and Gulf Stream currents (Goosse et al., 2012b). For the tropical regions, an enhanced zonal SST gradient produced by either a warmer Indian Ocean (Graham et al., 2011) or a cooler eastern Pacific (La Niña-like state) (Seager et al., 2007; Mann et al., 2009) could explain the reconstructed MCA patterns (Figure 5.9c). However, the enhanced gradients are not reproduced by model simulations (Figure 5.9a, b) and are not robust when considering the reconstruction uncertainties and the limited proxy records in these tropical ocean regions (Emile-Geay et al., 2013b) (Sections 5.4.1 and 5.5.1). This precludes an assessment of the role of external forcing and/or internal variability in these reconstructed patterns.

5.4 Modes of Climate Variability

Since AR4, new proxy reconstructions and model simulations have provided additional insights into the forced and unforced behaviour of modes of climate variability. This section focuses only on the interannual ENSO, the NAM and NAO, the Southern Annular Mode (SAM) and longer term variability associated with the Atlantic Multidecadal Oscillation (AMO) (see Glossary and Chapter 14 for definitions and illustrations and Box 2.5). It is organized from low to high latitudes and from interannual to decadal-scale modes of variability.

5.4.1 Tropical Modes

During the MPWP, climate conditions in the equatorial Pacific were characterized by weaker zonal (Wara et al., 2005) and cross-equatorial (Steph et al., 2010) SST gradients, consistent with the absence of an eastern equatorial cold tongue. This state still supported interannual variability, according to proxy records (Scroxton et al., 2011; Watanabe et al., 2011). These results together with recent GCM experiments (Haywood et al., 2007) indicate (*medium confidence*) that interannual ENSO variability existed, at least sporadically, during the warm background state of the Pliocene (Section 5.3.1).

LGM GCM simulations display wide ranges in the behaviour of ENSO and the eastern equatorial Pacific annual cycle of SST with little consistency (Liu et al., 2007a; Zheng et al., 2008) (Figure 5.10). Currently ENSO variance reconstructions for the LGM are too uncertain to help constrain the simulated responses of the annual cycle and ENSO to LGM boundary conditions. GCMs show that a reduced AMOC *very likely* induces intensification of ENSO amplitude and for the majority of climate models also a reduction of the amplitude of the SST annual cycle in the eastern equatorial Pacific (Timmermann et al., 2007; Merkel et al., 2010; Braconnot et al., 2012a) (Figure 5.10). About 75% of the PMIP2 and PMIP3/CMIP5 mid-Holocene simulations exhibit a weakening of interannual SST amplitude in the eastern equatorial Pacific relative to pre-industrial conditions. More than 87% of these simulations also show a concomitant substantial weakening in the amplitude of the annual cycle of eastern equatorial Pacific SST. Model results are consistent with a reduction of total variance of $\delta^{18}\text{O}$ variations of individual foraminifera in the eastern equatorial Pacific, indicative of an orbital effect on eastern equatorial Pacific SST variance (Koutavas and Joanides, 2012). In contrast to these findings, a recent proxy study

using sub-annually resolved $\delta^{18}\text{O}$ from central equatorial Pacific coral segments (Cobb et al., 2013) reveals no evidence for orbitally-induced changes in interannual ENSO amplitude throughout the last 7 ka (*high confidence*), which is consistent with the weak reduction in mid-Holocene ENSO amplitude of only ~10% simulated by the majority of climate models (Fig. 5.10), but contrasts with reconstructions reported in AR4 that showed a reduction in ENSO variance during the first half of the Holocene. The same study revealed an ENSO system that experienced very large internal variance changes on decadal and centennial time scales. This latter finding is also confirmed by the analysis of about 2000 years of annually varved lake sediments (Wolff et al., 2011) in the ENSO-teleconnected region of equatorial East Africa. Furthermore, Cobb et al. (2013) identify the late 20th century as a period of anomalously high, although not unprecedented, ENSO variability relative to the average reconstructed variance over the last 7000 years.

Reconstructions of ENSO for the last millennium also document multi-decadal-to-centennial variations in the amplitude of reconstructed interannual eastern equatorial Pacific SST anomalies (McGregor et al., 2010; Wilson et al., 2010; Li et al., 2011; Emile-Geay et al., 2013a). Statistical efforts to determine ENSO variance changes in different annually resolved ENSO proxies (D'Arrigo et al., 2005; Braganza et al., 2009; McGregor et al., 2010; Fowler et al., 2012; Hereid et al., 2013) and from documentary sources (Garcia-Herrera et al., 2008; Gergis and Fowler, 2009) reveal (*medium confidence*) extended periods of low ENSO activity during parts of the LIA compared to the 20th century. Direct TSI effects on reconstructed multi-decadal ENSO variance changes cannot be identified (McGregor et al., 2010). According to reconstructions of volcanic events (Section 5.2.1.3) and some ENSO proxies, a slightly increased probability exists (*medium confidence*) for the occurrence of El Niño events 1 to 2 years after major volcanic eruptions (Adams et al., 2003; McGregor et al., 2010; Wilson et al., 2010). This response is not captured robustly by GCMs (McGregor and Timmermann, 2010; Ohba et al., 2013).

5.4.2 Extratropical Modes

Robust evidence from LGM simulations indicates a weakening of the NAM variability, connected with stronger planetary wave activity (Lü et al., 2010). A significant but model-dependent distortion of the simulated LGM NAO pattern may result from the strong topographic ice sheet forcing (Justino and Peltier, 2005; Handorf et al., 2009; Pausata et al., 2009; Riviere et al., 2010). A multimodel analysis of NAO behaviour in mid-Holocene GCM simulations (Gladstone et al., 2005) reveals an NAO structure, similar to its pre-industrial state, but a tendency for more positive NAO values during the early Holocene (Rimbu et al., 2003), with no consistent change in its interannual variability. Robust proxy evidence to test these model-based results has not yet been established. A new 5200-year-long lake sediment record from southwestern Greenland (Olsen et al., 2012) suggests that around 4500 and 650 years ago variability associated with the NAO changed from generally positive to variable, intermittently negative conditions. Since AR4, a few cold-season NAO reconstructions for the last centuries have been published. They are based on long instrumental pressure series (Cornes et al., 2012), a combination of instrumental and ship log-book data (Küttel et al., 2010) and two proxy records (Trouet et al., 2009). Whereas these and earlier NAO reconstructions (Cook et al., 2002;

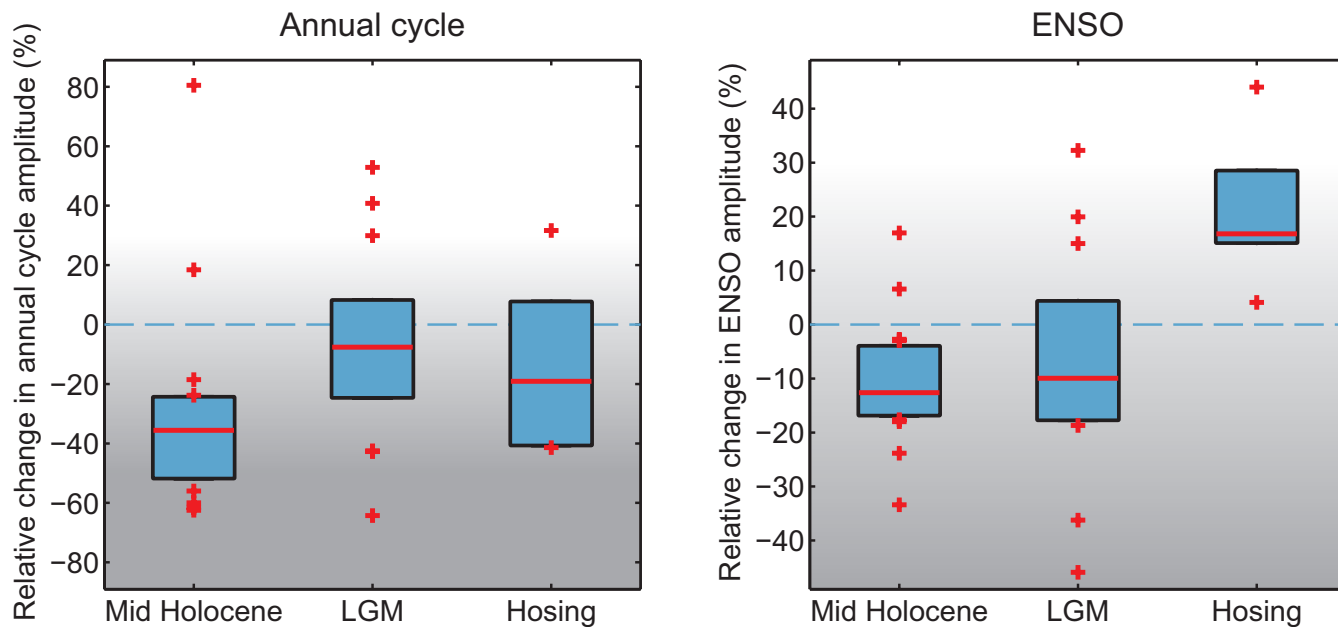


Figure 5.10 | Relative changes in amplitude of the annual cycle of sea surface temperature (SST) in Niño 3 region (average over 5°S to 5°N and 150°W to 90°W) (left) and in amplitude of interannual SST anomalies in the Niño 3.4 region (average over 5°S to 5°N and 170°W to 120°W) (right) simulated by an ensemble of climate model experiments in response to external forcing. Left: Multi-model average of relative changes (%) in amplitude of the mean seasonal cycle of Niño 3 SST for mid Holocene (MH) and Last Glacial Maximum (LGM) time-slice experiments and for freshwater perturbation experiments (Hosing) that lead to a weakening of the Atlantic Ocean meridional overturning circulation (AMOC) by more than 50%. Bars encompass the 25 and 75 percentiles, with the red horizontal lines indicating the median in the respective multi-model ensemble, red crosses are values in the upper and lower quartile of the distribution; Right: same as left, but for the SST anomalies in the Niño 3.4 region, representing El Niño-Southern Oscillation (ENSO) variability. The MH ensemble includes 4 experiments performed by models participating in Paleoclimate Modelling Intercomparison Project Phase II (PMIP2) (FGOALS1.0g, IPSL-CM4, MIROC3.2 medres, CCSM3.0) and 7 experiments (mid-Holocene) performed by models participating in PMIP3/CMIP5 (CCSM4.0, CSIRO-Mk3-6-0, HadGEM2-CC, HadGEM2-ES, MIROC-ESM, MPI-ESM-P, MRI-CGCM3). The LGM ensemble includes 5 experiments performed by models participating in PMIP2 (FGOALS1.0g, IPSL-CM4, MIROC3.2 medres, CCSM3.0, HadCM3) and 5 experiments (LGM) performed by models participating in PMIP3/CMIP5 (CCSM4, GISS-E2-R, IPSL-CM5A-LR, MIROC-ESM, and MPI-ESM-P). The changes in response to MH and LGM forcing are computed with respect to the pre-industrial control simulations coordinated by PMIP2 and PMIP3/CMIP5. The results for Hosing are obtained from freshwater perturbation experiments conducted with CCSM2.0, CCSM3.0, HadCM3, ECHAM5-MPIOM, GFDL-CM2.1 (Timmermann et al., 2007), CSM1.4 (Bozuyik et al., 2011) for pre-industrial or present-day conditions and with CCSM3 for glacial conditions (Merkel et al., 2010). The changes in response to fresh water forcing are computed with respect to the portion of simulations when the AMOC is high.

Luterbacher et al., 2002; Timm et al., 2004; Pinto and Raible, 2012) differ in several aspects, and taking into consideration associated reconstruction uncertainties, they demonstrate with *high confidence* that the strong positive NAO phases of the early 20th century and the mid-1990s are not unusual in the context of the past half millennium. Trouet et al. (2009) presented a winter NAO reconstruction that yielded a persistent positive phase during the MCA in contrast to higher frequency variability during the LIA. This is not consistent with the strong NAO imprint in Greenland ice core data (Vinther et al., 2010) and recent results from transient model simulations that neither support such a persistent positive NAO during the MCA, nor a strong NAO phase shift during the LIA (Lehner et al., 2012; Yiou et al., 2012). A recent pseudo-proxy-based assessment of low-frequency NAO behaviour (Lehner et al., 2012) infers weaknesses in the reconstruction method used by Trouet et al. (2009). Last millennium GCM simulations reveal no significant response of the NAO to solar forcing (Yiou et al., 2012), except for the GISS-ER coupled model which includes ozone photochemistry, extends into the middle atmosphere and exhibits changes in NAO that are weak during the MCA compared to the LIA (Mann et al., 2009).

Changes in the SAM modulate the strength and position of the mean SH westerlies, and leave an important signature on SH present-day surface climate (Gillett et al., 2006) past tree-ring growth (e.g., Urrutia et

al., 2011), wildfires (Holz and Veblen, 2011) as well as on LGM climate (Justino and Peltier, 2008). A first hemispheric-wide, tree-ring-based reconstruction of the austral summer SAM (Villalba et al., 2012) indicates that the late 20th century positive trend may have been anomalous in the context of the last 600 years, thus supporting earlier South American proxy evidence for the last 400 years (e.g., Lara et al., 2008) and GCM (Wilmes et al., 2012). Hence, there is *medium confidence* that the positive trend in SAM since 1950 may be anomalous compared to the last 400 years.

The AMO (Delworth and Mann, 2000; Knight et al., 2005) (see also Sections 9.5.3.3.2 and 14.7.6) has been reconstructed using marine (Black et al., 2007; Kilbourne et al., 2008; Sicre et al., 2008; Chiessi et al., 2009; Saenger et al., 2009) and terrestrial proxy records (Gray et al., 2004; Shanahan et al., 2009) from different locations. Correlations among different AMO reconstructions decrease rapidly prior to 1900 (Winter et al., 2011). An 8000-year long AMO reconstruction (Knudsen et al., 2011) shows no correlation with TSI changes, and is interpreted as internally generated ocean-atmosphere variability. However, GCM experiments (Waple et al., 2002; Ottera et al., 2010) using solar and/or volcanic forcing reconstructions indicate that external forcings may have played a role in driving or at least acting as pacemaker for AMO variations.

5.5 Regional Changes During the Holocene

Reconstructions and simulations of regional changes that have emerged since AR4 are assessed. Most emphasis is on the last 2000 years, which has the best data coverage.

5.5.1 Temperature

5.5.1.1 Northern Hemisphere Mid to High Latitudes

New studies confirm the spatial patterns of SAT and SST distribution as summarised in AR4 (Jansen et al., 2007). According to a recent compilation of proxy data, the global mean annual temperatures around 8 to 6 ka were about 0.7°C higher, and extratropical NH temperatures were about 1°C higher than for pre-industrial conditions (Marcott et al., 2013). Spatial variability in the temperature anomalies and the timing of the thermal maximum implicate atmospheric or oceanic dynamical feedbacks including effects from remaining ice sheets (e.g., Wanner et al., 2008; Leduc et al., 2010; Bartlein et al., 2011; Renssen et al., 2012). The peak early-to-mid-Holocene North Atlantic and sub-Arctic SST anomalies are reconstructed and simulated to primarily occur in summer and in the stratified uppermost surface-ocean layer (Hald et al., 2007; Andersson et al., 2010). Terrestrial MH (~6 ka, Table 5.1) summer-season temperatures were higher than modern in the mid-to-high latitudes of the NH, consistent with minimum glacier extents (Section 5.5.3) and PMIP2 and PMIP3/CMIP5 simulated responses to orbital forcing (Figure 5.11) (Braconnot et al., 2007; Bartlein et al., 2011; Izumi et al., 2013). There is also robust evidence for warmer MH winters compared to the late 20th century (e.g., Wanner et al., 2008; Sundqvist et al., 2010; Bartlein et al., 2011) (Figure 5.11), but the simulated high latitude winter warming is model dependent and is sensitive to ocean and sea-ice changes (Otto et al., 2009; Zhang et al., 2010). Overall, models underestimate the reduction in the latitudinal gradient of European winter temperatures during the MH (Brewer et al., 2007). There is a general, gradual NH cooling after ~5 ka, linked to orbital forcing, and increased amplitude of millennial-scale variability (Wanner et al., 2008; Vinther et al., 2009; Kobashi et al., 2011; Marcott et al., 2013).

Since AR4, regional temperature reconstructions have been produced for the last 2 kyr (Figure 5.12; PAGES 2k Consortium, 2013). A recent multi-proxy 2000-year Arctic temperature reconstruction shows that temperatures during the first centuries were comparable or even higher than during the 20th century (Hanhijärvi et al., 2013; PAGES 2k Consortium, 2013). During the MCA, portions of the Arctic and sub-Arctic experienced periods warmer than any subsequent period, except for the most recent 50 years (Figure 5.12) (Kaufman et al., 2009; Kobashi et al., 2010, 2011; Vinther et al., 2010; Spielhagen et al., 2011). Tingley and Huybers (2013) provided a statistical analysis of northern high-latitude temperature reconstructions back to 1400 and found that recent extreme hot summers are unprecedented over this time span. Marine proxy records indicate anomalously high SSTs north of Iceland and the Norwegian Sea from 900 to 1300, followed by a generally colder period that ended in the early 20th century. Modern SSTs in this region may still be lower than the warmest intervals of the 900–1300 period (Cunningham et al., 2013). Further north, in Fram Strait, modern SSTs from Atlantic Water appear warmer than those reconstructed from foraminifera for any prior period of the last 2000 years

(Spielhagen et al., 2011). However, different results are obtained using dinocysts from the same sediment core (Bonnet et al. (2010) showing a cooling trend over the last 2000 years without a 20th century rise, and warmest intervals centered at years 100 and 600.

Tree-ring data and lake sediment information from the North American treeline (McKay et al., 2008; Bird et al., 2009; D'Arrigo et al., 2009; Anchukaitis et al., 2012) suggest common variability between different records during the last centuries. An annually resolved, tree-ring based 800-year temperature reconstruction over temperate North America (PAGES 2k Consortium, 2013) and a 1500-year long pollen-based temperature estimate (Viau et al., 2012) show cool periods 500–700 and 1200–1900 as well as a warm period between 750 and 1100. The generally colder conditions until 1900 are in broad agreement with other pollen, tree-ring and lake-sediment evidence from northwest Canada, the Canadian Rockies and Colorado (Luckman and Wilson, 2005; Salzer and Kipfmüller, 2005; Loso, 2009; MacDonald et al., 2009; Thomas and Briner, 2009). It is *very likely* that the most recent decades have been, on average, the warmest across mid-latitude western and temperate North America over at least 500 years (Wahl and Smerdon, 2012; PAGES 2k Consortium, 2013; Figure 5.12).

New warm-season temperature reconstructions (PAGES 2k Consortium, 2013; Figure 5.12) covering the past 2 millennia show that warm European summer conditions were prevalent during 1st century, followed by cooler conditions from the 4th to the 7th century. Persistent warm conditions also occurred during the 8th–11th centuries, peaking throughout Europe during the 10th century. Prominent periods with cold summers occurred in the mid-15th and early 19th centuries. There is *high confidence* that northern Fennoscandia from 900 to 1100 was as warm as the mid-to-late 20th century (Helama et al., 2010; Lindholm et al., 2010; Büntgen et al., 2011a; Esper et al., 2012a; 2012b; McCarroll et al., 2013; Melvin et al., 2013). The evidence also suggests warm conditions during the 1st century, but comparison with recent temperatures is restricted because long-term temperature trends from tree-ring data are uncertain (Esper et al., 2012a). In the European Alps region, tree-ring based summer temperature reconstructions (Büntgen et al., 2005; Nicolussi et al., 2009; Corona et al., 2010, 2011; Büntgen et al., 2011b) show higher temperatures in the last decades than during any time in the MCA, while reconstructions based on lake sediments (Larocque-Tobler et al., 2010; Trachsel et al., 2012) show as high, or slightly higher temperatures during parts of the MCA compared to most recent decades. The longest summer temperature reconstructions from parts of the Alps show several intervals during Roman and earlier times as warm (or warmer) than most of the 20th century (Büntgen et al., 2011b; Stewart et al., 2011).

Since AR4, new temperature reconstructions have also been generated for Asia. A tree-ring based summer temperature reconstruction for temperate East Asia back to 800 indicates warm conditions during the period 850–1050, followed by cooler conditions during 1350–1880 and a subsequent 20th century warming (Cook et al., 2012; PAGES 2k Consortium, 2013; Figure 5.12). Tree-ring reconstructions from the western Himalayas, Tibetan Plateau, Tianshan Mountains and western High Asia depict warm conditions from the 10th to the 15th centuries, lower temperature afterwards and a 20th century warming (Esper et al., 2007a; Zhu et al., 2008; Zhang et al., 2009; Yadav et al., 2011).

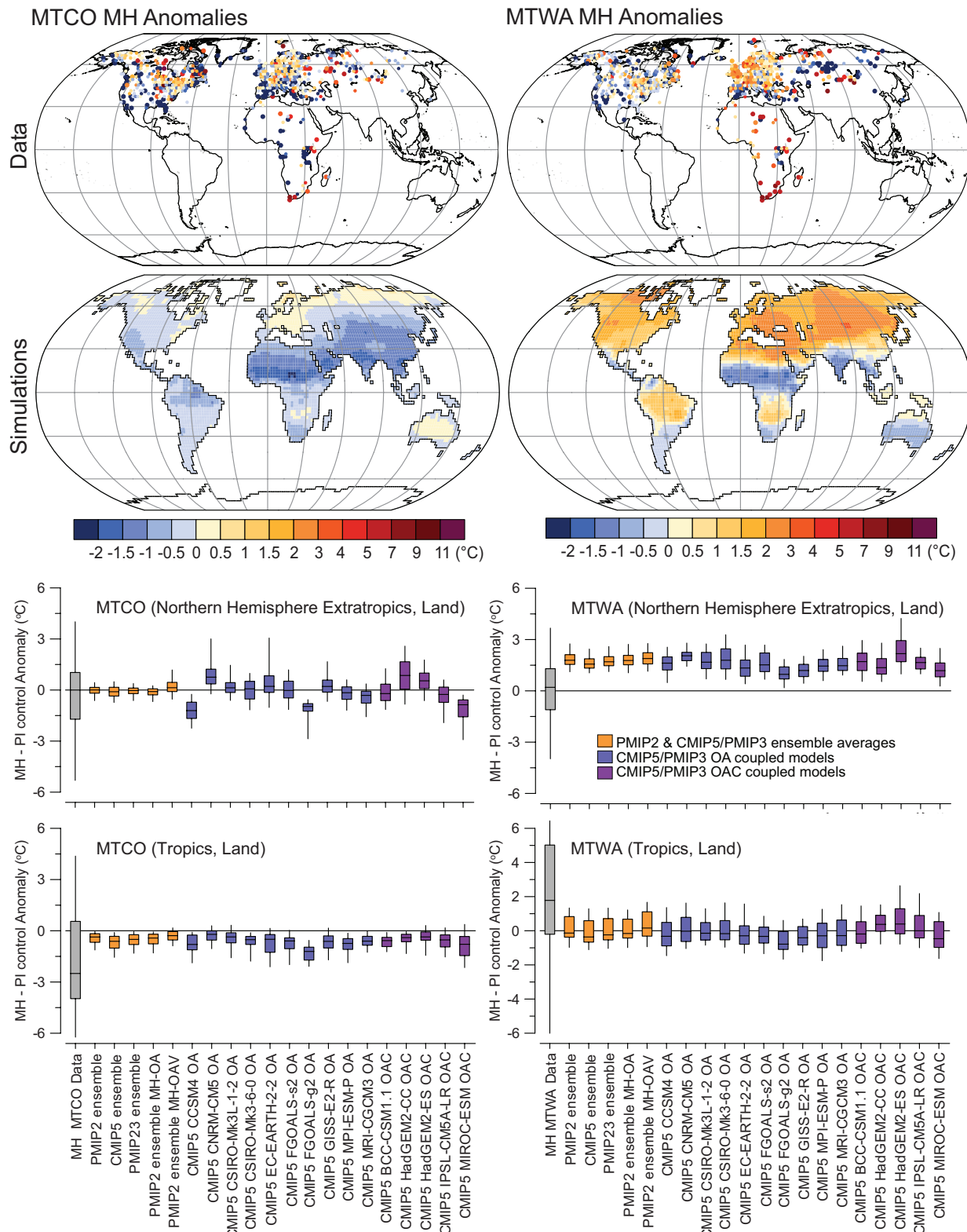


Figure 5.11 | Model-data comparison of surface temperature anomalies for the mid-Holocene (6 ka). MTCO is the mean temperature of the coldest month; MTWA is the mean temperature of the warmest month. Top panels are pollen-based reconstructions of Bartlein et al., (2011) with anomalies defined as compared to modern, which varies among the records. The bulk of the records fall within the range of 5.5 to 6.5 ka, with only 3.5% falling outside this range. Middle panels are corresponding surface temperature anomalies simulated by the Paleoclimate Modelling Intercomparison Project Phase II (PMIP2) and Paleoclimate Modelling Intercomparison Project Phase III (PMIP3)/Coupled Model Intercomparison Project Phase 5 (CMIP5) models for 6 ka as compared to pre-industrial. Bottom panels contain boxplots for reconstructions (grey), for model ensembles and for the individual CMIP5 models interpolated to the locations of the reconstructions. Included are OA (ocean-atmosphere), OAV (ocean-atmosphere-vegetation), and OAC (ocean-atmosphere-carbon cycle) models. The boxes are drawn using the 25th, 50th and 75th percentiles (bottom, middle and top of the box, respectively), and whiskers extend to the 5th and 95th percentiles of data or model results within each area. The northern extratropics are defined as 30°N to 90°N and the tropics as 30°S to 30°N. For additional model-data comparisons for the mid-Holocene, see Section 9.4.1.4 and Figures 9.11 and 9.12.

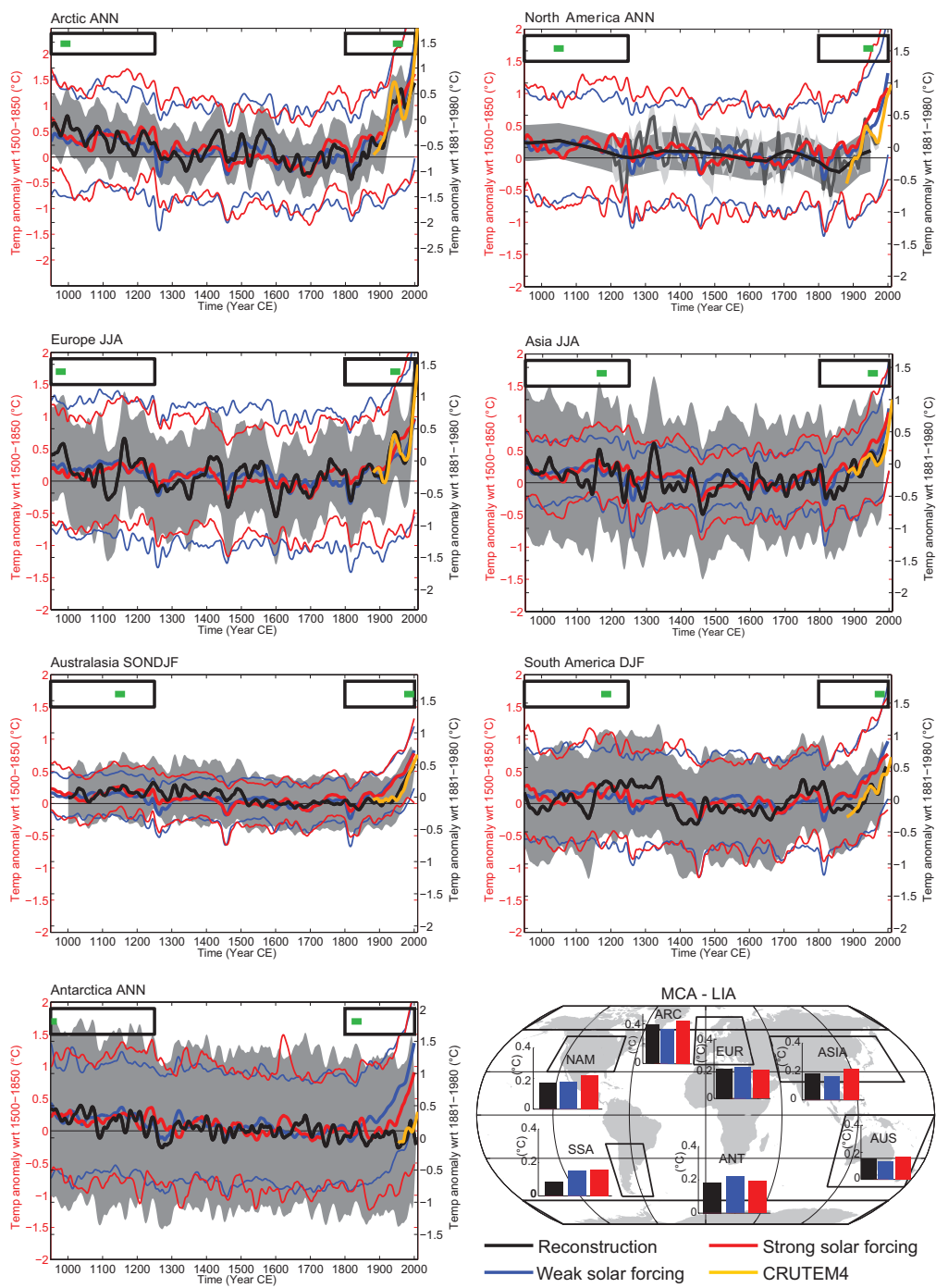


Figure 5.12 | Regional temperature reconstructions, comparison with model simulations over the past millennium (950–2010). Temperature anomalies (thick black line), and uncertainty estimated provided by each individual reconstruction (grey envelope). Uncertainties: Arctic: 90% confidence bands. Antarctica, Australasia, North American pollen and South America: ± 2 standard deviation. Asia: ± 2 root mean square error. Europe: 95% confidence bands. North American trees: upper/lower 5% bootstrap bounds. Simulations are separated into 2 groups: High solar forcing (red thick line), and weak solar forcing (blue thick line). For each model sub-group, uncertainty is shown as 1.645 times sigma level (light red and blue lines). For comparison with instrumental record, the Climatic Research Unit (CRU) Gridded Dataset of Global Historical Near-Surface Air TEMperature Anomalies Over Land version 4 (CRUTEM4) data set is shown (yellow line). These instrumental data are not necessarily those used in calibration of the reconstructions, and thus may show greater or lesser correspondence with the reconstructions than the instrumental data actually used for calibration; cut-off timing may also lead to end effects for the smoothed data shown. Cf. PAGES 2k Consortium (2013, SOM) in this regard for the North America reconstruction. Green bars in rectangles on top of each panel indicate the 30 warmest years in the 950–1250 period (left rectangle) and 1800–2010 period (right rectangle). All lines are smoothed by applying a 30 year moving average. Map at bottom right shows the individual regions for each reconstruction, and in bars the Medieval Climate Anomaly (MCA, 950–1250) – Little Ice Age (LIA, 1450–1850) differences over those regions. Reconstructions: from PAGES 2k Consortium (2013). Models used: simulations with strong solar forcing (mostly pre-Paleoclimate Modelling Intercomparison Project Phase III (pre-PMIP3) simulations): CCSM3 (1), CNRM-CM3.3 (1), CSM1.4 (1), CSIRO-MK3L-1-2 (3), ECHAM5/MPIOM (3), ECHO-G (1) IPSLCM4 (1), FGOALS-gl (1). Simulations with weak solar forcing (mostly PMIP3/CMIP5 simulations): BCC-csm1-1 (1), CCSM4 (1), CSIRO-MK3L-1-2 (1), GISS-E2-R (3, ensemble members 121, 124, 127), HadCM3 (1), MPI-ESM, ECHAM5/MPIOM (5), IPSL-CM5A-LR (1). In parenthesis are the number of simulations used for each model. All simulations are treated individually, in the time series as well as in the MCA–LIA bars. More information about forcings used in simulations and corresponding references are given in Table 5.A.1. Time periods for averaging are JJA for June – July – August, SONDJF for the months from September to February, and DJF for December – January – February, respectively, while ANN denotes annual mean.

Taking associated uncertainties into consideration, 20th century temperatures in those regions were *likely* not higher than during the first part of the last millennium. In different regions of China, temperatures appear higher during recent decades than during earlier centuries, although with large uncertainties (e.g., Ge et al., 2006, 2010; Wang et al., 2007; Holmes et al., 2009; Yang et al., 2009; Zhang et al., 2009; Cook et al., 2012). In northeast China, an alkenone-based reconstruction indicates that the growing season temperature during the periods 480–860, 1260–1300, 1510–1570 and 1800–1900 was about 1°C lower compared with the 20th century (Chu et al., 2011). These reconstructed NH regional temperature evolutions appear consistent with last millennium GCM simulations using a range of solar forcing estimates (Figure 5.12).

There is *high confidence* that in the extratropical NH, both regionally and on a hemispheric basis, the surface warming of the 20th century reversed the long term cooling trend due to orbital forcing.

5.5.1.2 Tropics

Marcott et al. (2013) provide a compilation of tropical SST reconstructions, showing a gradual warming of about 0.5°C until 5 ka and little change thereafter. Holocene tropical SST trends are regionally heterogeneous and variable in magnitude. Alkenone records from the eastern tropical Pacific, western tropical Atlantic, and the Indonesian archipelago document a warming trend of ~0.5°C to 2°C from the early Holocene to present (Leduc et al., 2010), consistent with local insolation. In contrast, regional trends of planktonic foraminiferal Mg/Ca records are heterogeneous, and imply smaller magnitude SST changes (Leduc et al., 2010; Schneider et al., 2010). Foraminiferal Mg/Ca records in the Indo-Pacific warm-pool region show cooling trends with varying magnitudes (Stott et al., 2004; Linsley et al., 2010). When comparing SST records from different paleoclimate proxies it is important to note that they can have different, and also regionally varying, seasonal biases (Schneider et al., 2010).

Terrestrial temperature reconstruction efforts have mostly focussed on Africa and to some extent on southeast Asia (Figure 5.11), with a lack of syntheses from South America and Australia (Bartlein et al., 2011). The PMIP2 and PMIP3/CMIP5 MH simulations show summer cooling compared to pre-industrial conditions and a shorter growing season in the tropical monsoon regions of Africa and southeast Asia (Figure 5.11), attributed to increased cloudiness and local evaporation (Brac-connont et al., 2007). In contrast, MH simulations and reconstructions for the entire tropics (30°S to 30°N) show generally higher mean temperature of the warmest month and lower mean temperature of the coldest month than for the mid-20th century.

5.5.1.3 Southern Hemisphere Mid to High Latitudes

In the high latitude Southern Ocean, Holocene SST trends follow the decrease in austral summer duration, with a cooling trend from the early Holocene into the late Holocene (Kaiser et al., 2008; Shevenell et al., 2011). Similar cooling trends are found in the Australian-New Zealand region (Bostock et al., 2013). Increased amplitude of millennial-to-centennial scale SST variability between 5 ka and 4 ka is recorded in several locations, possibly due to variations in the position and

strength of the westerlies (Moros et al., 2009; Euler and Ninnemann, 2010; Shevenell et al., 2011). The Holocene land-surface temperature history in the SH is difficult to assess. Individual reconstructions generally track the trends registered by Antarctic ice core records with peak values at around 12 to 10 ka (Masson-Delmotte et al., 2011b; Marcott et al., 2013; Mathiot et al., 2013). Pollen-based records indicate positive MH temperature anomalies in southern South Africa that are not reproduced in the PMIP3/CMIP5 simulations (Figure 5.11).

Indices for the position of Southern Ocean fronts and the strength and position of the westerlies diverge (Moros et al., 2009; e.g., Shevenell et al., 2011). For the mid-to-late-Holocene, climate models of different complexity consistently show a poleward shift and intensification of the SH westerlies in response to orbital forcing (Varma et al., 2012). However, the magnitude, spatial pattern and seasonal response vary significantly among the models.

New high-resolution, climate reconstructions for the last millennium are based on tree-ring records from the subtropical and central Andes, northern and southern Patagonia, Tierra del Fuego, New Zealand and Tasmania (Cook et al., 2006; Boninsegna et al., 2009; Villalba et al., 2009), ice cores, lake and marine sediments and documentary evidence from southern South America (Prieto and García Herrera, 2009; Vimeux et al., 2009; von Gunten et al., 2009; Tierney et al., 2010; Neukom et al., 2011), terrestrial and shallow marine geological records from eastern Antarctica (Verleyen et al., 2011), ice cores from Antarctica (Goosse et al., 2012c; Abram et al., 2013; Steig et al., 2013), boreholes from western Antarctica (Orsi et al., 2012) and coral records from the Indian and Pacific Oceans (Linsley et al., 2008; Zinke et al., 2009; Lough, 2011; DeLong et al., 2012). There is *medium confidence* that southern South America (Neukom et al., 2011) austral summer temperatures during 950–1350 were warmer than the 20th century. A 1000-year temperature reconstruction for land and ocean representing Australasia indicates a warm period during 1160–1370 though this reconstruction is based on only three records before 1430 (PAGES 2k Consortium, 2013). In Australasia, 1971–2000 temperatures were *very likely* higher than any other 30-year period over the last 580 years (PAGES 2k Consortium, 2013).

Antarctica was *likely* warmer than 1971–2000 during the late 17th century, and during the period from approximately the mid-2nd century to 1250 (PAGES 2k Consortium, 2013).

In conclusion, continental scale surface temperature reconstructions from 950 to 1250 show multi-decadal periods that were in some regions as warm as in the mid-20th century and in others as warm as in the late 20th century (*high confidence*). These regional warm periods were not as synchronous across regions as the warming since the mid-20th century (*high confidence*).

5.5.2 Sea Ice

Since AR4 several new Holocene sea ice reconstructions for the Arctic and sub-Arctic have been made available that resolve multi-decadal to century-scale variability. Proxies of sea-ice extent have been further developed from biomarkers in deep sea sediments (e.g., IP25, Belt et al., 2007; Müller et al., 2011) and from sea-ice biota preserved

in sediments (e.g., Justwan and Koç, 2008). Indirect information on sea-ice conditions based on drift wood and beach erosion has also been compiled (Funder et al., 2011). In general, these sea-ice reconstructions parallel regional SST, yet they display spatial heterogeneity, and differences between the methods, making it difficult to provide quantitative estimates of past sea-ice extent. Summer sea-ice cover was reduced compared to late 20th century levels both in the Arctic Ocean and along East Greenland between 8 ka and 6.5 ka (e.g., Moros et al., 2006; Polyak et al., 2010; Funder et al., 2011), a feature which is captured by some MH simulations (Berger et al., 2013). The response of this sea ice cover to summer insolation warming was shown to be central for explaining the reconstructed warmer winter temperatures over the adjacent land (Otto et al., 2009; Zhang et al., 2010). During the last 6 kyr available records show a long-term trend of a more extensive Arctic sea ice cover driven by the orbital forcing (e.g., Polyak et al., 2010), but punctuated by strong century-to-millennial scale variability. Consistent with Arctic temperature changes (see Section 5.5.1), sea ice proxies indicate relatively reduced sea-ice cover from 800 to 1200 followed by a subsequent increase during the LIA (Polyak et al., 2010). Proxy reconstructions document the 20th-century ice loss trend, which is also observed in historical sea ice data sets with a decline since the late 19th century (Divine and Dick, 2006). There is *medium confidence* that the current ice loss was unprecedented and that current SSTs in the Arctic were anomalously high at least in the context of the last 1450 years (England et al., 2008; Kinnard et al., 2008; Kaufman et al., 2009; Macias Fauria et al., 2010; Polyakov et al., 2010; Kinnard et al., 2011; Spielhagen et al., 2011). Fewer high-resolution records exist from the Southern Ocean. Data from the Indian Ocean sector document an increasing sea-ice trend during the Holocene, with a rather abrupt increase between 5 ka and 4 ka, consistent with regional temperatures (see Section 5.5.1.3) (Denis et al., 2010).

5.5.3 Glaciers

Due to the response time of glacier fronts, glacier length variations resolve only decadal- to centennial-scale climate variability. Since AR4 new and improved chronologies of glacier size variations were published (Anderson et al., 2008; Joerin et al., 2008; Yang et al., 2008; Jomelli et al., 2009; Licciardi et al., 2009; Menounos et al., 2009; Schaefer et al., 2009; Wiles et al., 2011; Hughes et al., 2012). Studies of sediments from glacier-fed lakes and marine deposits have allowed new continuous reconstructions of glacier fluctuations (Matthews and Dresser, 2008; Russell et al., 2009; Briner et al., 2010; Bowerman and Clark, 2011; Larsen et al., 2011; Bertrand et al., 2012; Vasskog et al., 2012). Reconstructions of the history of ice shelves and ice sheets/caps have also emerged (Antoniades et al., 2011; Hodgson, 2011; Simms et al., 2011; Smith et al., 2011; Krishner et al., 2012). New data confirm a general increase of glacier extent in the NH and decrease in the SH during the Holocene (Davis et al., 2009; Menounos et al., 2009), consistent with the local trends in summer insolation and temperatures. Some exceptions exist (e.g., in the eastern Himalayas), where glaciers were most extensive in the early Holocene (Gayer et al., 2006; Seong et al., 2009), potentially due to monsoon changes (Rupper et al., 2009). Due to dating uncertainties, incompleteness and heterogeneity of most existing glacial chronologies, it is difficult to compare glacier variations between regions at centennial and shorter time scales (Heyman et al., 2011; Kirkbride and Winkler, 2012). There are no definitive conclusions

regarding potential inter-hemispheric synchronicity of sub-millennial scale glacier fluctuations (Wanner et al., 2008; Jomelli et al., 2009; Licciardi et al., 2009; Schaefer et al., 2009; Winkler and Matthews, 2010; Wanner et al., 2011).

Glacial chronologies for the last 2 kyr are better constrained (Yang et al., 2008; Clague et al., 2010; Wiles et al., 2011; Johnson and Smith, 2012). Multi-centennial glacier variability has been linked with variations in solar activity (Holzhauser et al., 2005; Wiles et al., 2008), volcanic forcing (Anderson et al., 2008) and changes in North Atlantic circulation (Linderholm and Jansson, 2007; Nesje, 2009; Marzeion and Nesje, 2012). Glacier response is more heterogeneous and complex during the MCA than the uniform global glacier recession observed at present (see Section 4.3). Glaciers were smaller during the MCA than in the early 21st Century in the western Antarctic Peninsula (Hall et al., 2010) and Southern Greenland (Larsen et al., 2011). However, prominent advances occurred within the MCA in the Alps (Holzhauser et al., 2005), Patagonia (Luckman and Villalba, 2001), New Zealand (Schaefer et al., 2009), East Greenland (Lowell et al., 2013) and SE Tibet (Yang et al., 2008). Glaciers in northwestern North America were similar in size during the MCA compared to the peak during the LIA, probably driven by increased winter precipitation (Koch and Clague, 2011).

There is *high confidence* that glaciers at times have been smaller than at the end of the 20th century in the Alps (Jöerin et al., 2008; Ivy-Ochs et al., 2009; Goehring et al., 2011), Scandinavia (Nesje et al., 2011), Altai in Central Asia (Agatova et al., 2012), Baffin Island (Miller et al., 2005), Greenland (Larsen et al., 2011; Young et al., 2011), Spitsbergen (Humlum et al., 2005), but the precise glacier extent in the previous warm periods of the Holocene is often difficult to assess. While early-to-mid-Holocene glacier minima can be attributed with *high confidence* to high summer insolation (see Section 5.5.1.1), the current glacier retreat, however, occurs within a context of orbital forcing that would be favourable for NH glacier growth. If retreats continue at current rates, most extratropical NH glaciers will shrink to their minimum extent, that existed between 8 ka and 6 ka (*medium confidence*) (e.g., Anderson et al., 2008); and ice shelves on the Antarctic peninsula will retreat to an extent unprecedented through Holocene (Hodgson, 2011; Mulvaney et al., 2012).

5.5.4 Monsoon Systems and Convergence Zones

This subsection focuses on internally and externally driven variability of monsoon systems during the last millennium. Abrupt monsoon changes associated with Dansgaard–Oeschger and Heinrich events (Figure 5.4b, e, h) are further assessed in Section 5.7.1. Orbital-scale monsoon (Figure 5.4a, d, g) changes are evaluated in Section 5.3.2.3.

Hydrological proxy data characterizing the intensity of the East Asian monsoon (South American monsoon) show decreased (increased) hydrological activity during the LIA as compared to the MCA (*medium confidence*) (Figure 5.4f, i) (Zhang et al., 2008; Bird et al., 2011; Vuille et al., 2012). These shifts were accompanied by changes in the occurrence of megadroughts (*high confidence*) in parts of the Asian monsoon region (Buckley et al., 2010; Cook et al., 2010a) (Figure 5.13). Lake sediment data from coastal eastern Africa document dry conditions in the late MCA, a wet LIA, and return toward dry conditions in the 18th or

early 19th century (Verschuren et al., 2000; Stager et al., 2005; Verschuren et al., 2009; Tierney et al., 2011; Wolff et al., 2011), qualitatively similar to the South American monsoon proxies in Figure 5.4i, whereas some inland and southern African lakes suggest dry spells during the LIA (Garcin et al., 2007; Anchukaitis and Tierney, 2013). Rainfall patterns associated with the Pacific ITCZ also shifted southward during the MCA/LIA transition in the central equatorial Pacific (Sachs et al., 2009). Extended intervals of monsoon failures and dry spells have been reconstructed for the last few millennia for west Africa (Shanahan et al., 2009), east Africa (Wolff et al., 2011), northern Africa (Esper et al., 2007b; Touchan et al., 2008; Touchan et al., 2011), India and southeastern Asia (Zhang et al., 2008; Berkelhammer et al., 2010; Buckley et al., 2010; Cook et al., 2010a) and Australia (Mohtadi et al., 2011).

On multi-decadal-to-centennial time scales, influences of North Atlantic SST variations have been demonstrated for the North and South African monsoon, and the Indian and East Asian summer monsoons (see Figure 5.4c for monsoon regions), both using proxy reconstructions (Feng and Hu, 2008; Shanahan et al., 2009) and GCM simulations (Lu et al., 2006; Zhang and Delworth, 2006; Wang et al., 2009; Luo et al., 2011). These simulations suggest that solar and volcanic forcing (Fan et al., 2009; Liu et al., 2009a; Man et al., 2012) may exert only weak regional influences on monsoon systems (Figure 5.4f, i). A five-member multi-model ensemble mean of PMIP3/CMIP5 simulations (Table 5.A.1) exhibits decreased standardized monsoon rainfall accompanying periods of reduced solar forcing during the LIA in the East Asian monsoon regions (Figure 5.4f). There is, however, a considerable inter-model spread in the simulated annual mean precipitation response to solar forcing with the multi-model mean, explaining on average only $\sim 25 \pm 15\%$ (1 standard deviation) of the variance of the individual model simulations. An assessment of the pre-instrumental response of monsoon systems to volcanic forcing using paleo-proxy data has revealed wetter conditions over southeast Asia in the year of a major volcanic eruption and drier conditions in central Asia (Anchukaitis et al., 2010), in contrast to GCM simulations (Oman et al., 2005; Brovkin et al., 2008; Fan et al., 2009; Schneider et al., 2009).

5.5.5 Megadroughts and Floods

Multiple lines of proxy evidence from tree rings, lake sediments, and speleothems indicate with *high confidence* that decadal or multi-decadal episodes of drought have been a prominent feature of North American Holocene hydroclimate (e.g., Axelson et al., 2009; St. George et al., 2009; Cook et al., 2010a, 2010b; Shuman et al., 2010; Woodhouse et al., 2010; Newby et al., 2011; Oswald and Foster, 2011; Routson et al., 2011; Stahle et al., 2011; Stambaugh et al., 2011; Laird et al., 2012; Ault et al., 2013). During the last millennium, western North America drought reconstructions based on tree ring information (Figure 5.13) show longer and more severe droughts than today, particularly during the MCA in the southwestern and central United States (Meko et al., 2007; Cook et al., 2010b). The mid-14th century cooling coincides in southwestern North America with a shift towards overall wetter conditions (Cook et al., 2010a). In the Pacific Northwest, contrasting results emerge from lake sediment records, indicating wetter conditions during the MCA (Steinman et al., 2013), and tree-ring data showing no substantial change (Zhang and Hebda, 2005; Cook et al., 2010a). In Scandinavia, new tree-ring based reconstruc-

tions show a multi-centennial summer drought phase during Medieval times (900–1350) (Helama et al., 2009), while lake sediment proxies from the same region suggest wetter winters (Luoto et al., 2013). New tree-ring reconstructions from the southern-central (Wilson et al., 2013) and southeastern British Isles (Cooper et al., 2013) do not reveal multi-centennial drought during medieval times, but rather alternating multidecades of dry and wet periods. Wilson et al. (2013) reconstructed drier conditions between ~ 1300 and the early 16th century. Büntgen et al. (2011b) identified exceptionally dry conditions in central Europe from 200 to 350 and between 400 and 600. Numerous tree-ring records from the eastern Mediterranean testify to the regular occurrence of droughts in the past few millennia (e.g., Akkemik et al., 2008; Nicault et al., 2008; Luterbacher et al., 2012). In northern Africa, Esper et al. (2007b) and Touchan et al. (2008; 2011) show severe drought events through the last millennium, particularly prior to 1300, in the 1400s, between 1700 and 1900, and in the most recent instrumental data. Using multiple proxies from Chile, Boucher et al. (2011) inferred wetter conditions during 1000–1250, followed by much drier period until 1400 and wetter conditions similar to present afterwards, while Ledru et al. (2013) reconstructed a dry MCA-LIA transition until 1550. For the South American Altiplano Morales et al. (2012) found periods of drier conditions in the 14th, 16th, and 18th centuries, as well as a modern drying trend.

Reconstruction of past flooding from sedimentary, botanical and historical records (Brázdil et al., 2006; Baker, 2008; Brázdil et al., 2012) provides a means to compare recent large, rare floods, and to analyse links between flooding and climate variability. During the last few millennia, flood records reveal strong decadal to secular variability and non-stationarity in flood frequency and clustering of paleofloods, which varied among regions. In Europe, modern flood magnitudes are not unusual within the context of the last 1000 years (e.g., Brázdil et al., 2012). In Central Europe, the Elbe and the Oder/Odra Rivers show a decrease in the frequency of winter floods during the last 80 to 150 years compared to earlier centuries, while summer floods indicate no significant trend (Mudelsee et al., 2003) (Figure 5.14f–i). In the Alps, paleoflood records derived from lake sediments have shown a higher flood frequency during cool and/or wet phases (Stewart et al., 2011; Giguet-Covex et al., 2012; Wilhelm et al., 2012), a feature also found in Central Europe (Starkel et al., 2006) and the British Isles (Macklin et al., 2012). In the western Mediterranean, winter floods were more frequent during relatively cool and wet climate conditions of the LIA (Benito et al., 2003b; Piccarreta et al., 2011; Luterbacher et al., 2012; Figure 5.14a), whereas autumn floods reflect multi-decadal variations (Benito et al., 2010; Machado et al., 2011; Figure 5.14b, c). In China, extraordinary paleoflood events in the Yellow, Weihe and Qishuihe rivers, occurred synchronously with severe droughts and dust accumulations coinciding with a monsoonal shift, the most severe floods dated at 3.1 ka (Zha et al., 2009; Huang et al., 2012). In India, flood frequencies since 1950 are the largest for the last several hundred years for eight rivers, interpreted as a strengthening of the monsoon conditions after the LIA (Kale, 2008). In southwestern United States, increased frequency of high-magnitude paleofloods coincide with periods of cool, wet climate, whereas warm intervals including the MCA, corresponded with significant decreases in the number of large floods (Ely et al., 1993). In the Great Plains of North America, the frequency of large floods increased significantly around 850 with magnitudes

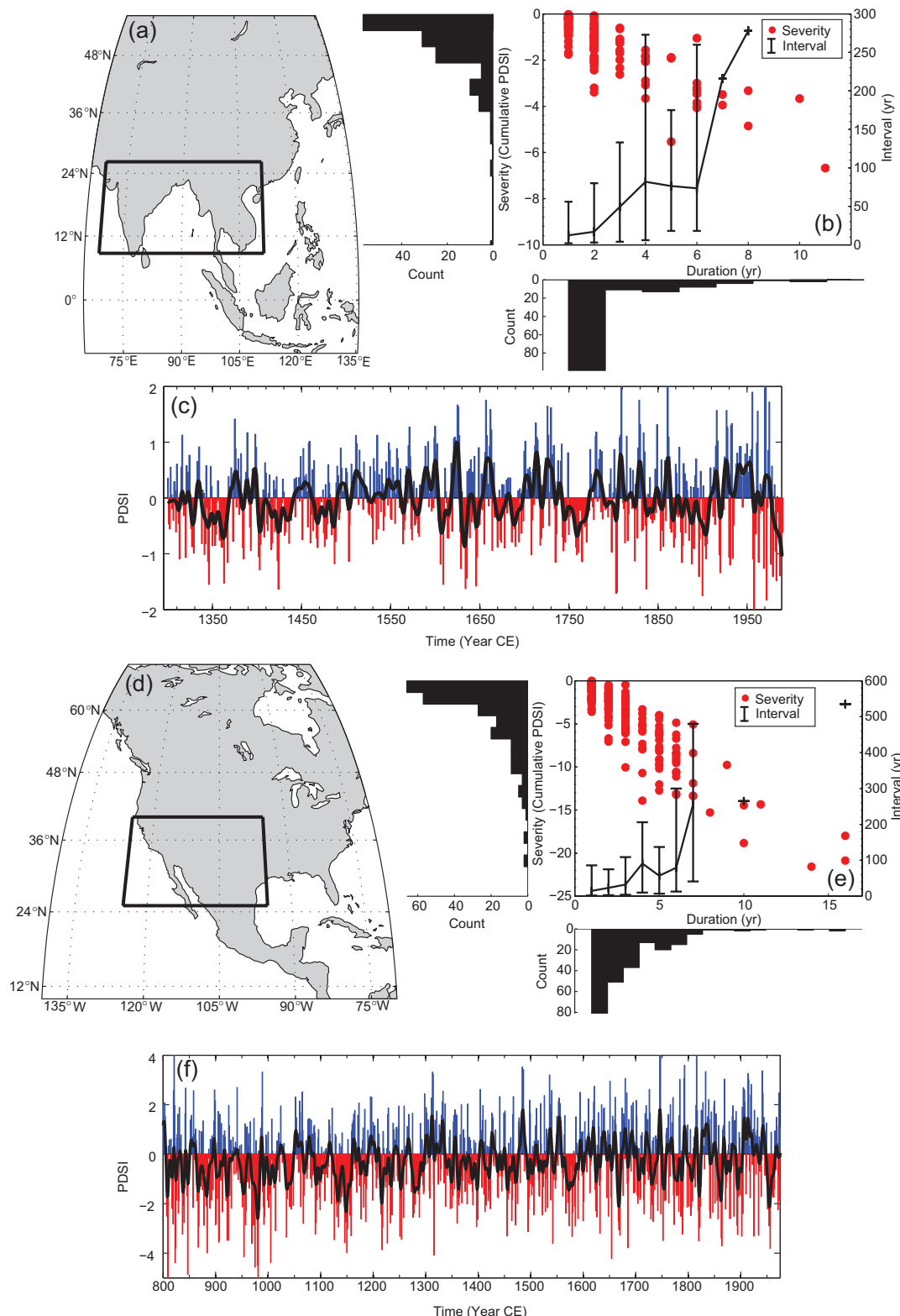


Figure 5.13 | Severity, duration, and frequency of droughts in the Monsoon Asia (Cook et al., 2010b) and North American (Cook et al., 2004) Drought Atlases. The box in (a) and (d) indicates the region over which the tree-ring reconstructed Palmer Drought Severity Index (PDSI) values have been averaged to form the regional mean time series shown in (c) and (f), respectively. Solid black lines in (c) and (f) are a 9-year Gaussian smooth on the annual data shown by the red and blue bars. The covariance of drought ($\text{PDSI} < 0$) duration and cumulative severity for each region is shown in panels (b) and (e) by the red circles (corresponding to the left y-axes), along with the respective marginal frequency histograms for each quantity. Not shown in b) is an outlier with an apparent duration of 24 years, corresponding to the 'Strange Parallels' drought identified in Cook et al. (2010b). Intervals between droughts of given durations are shown in the same panels and are estimated as the mean interval between their occurrence, with the minimum and maximum reconstructed intervals indicated (corresponding to the right y-axes, shown as connected lines and their corresponding range). No error bars are present if there are fewer than three observations of a drought of that duration. The period of analysis is restricted by the availability of tree-ring data to the period 1300–1989 for Monsoon Asia, following Cook et al. (2010a), and from 800 to 1978 for southwestern North America, following Cook et al. (2004).

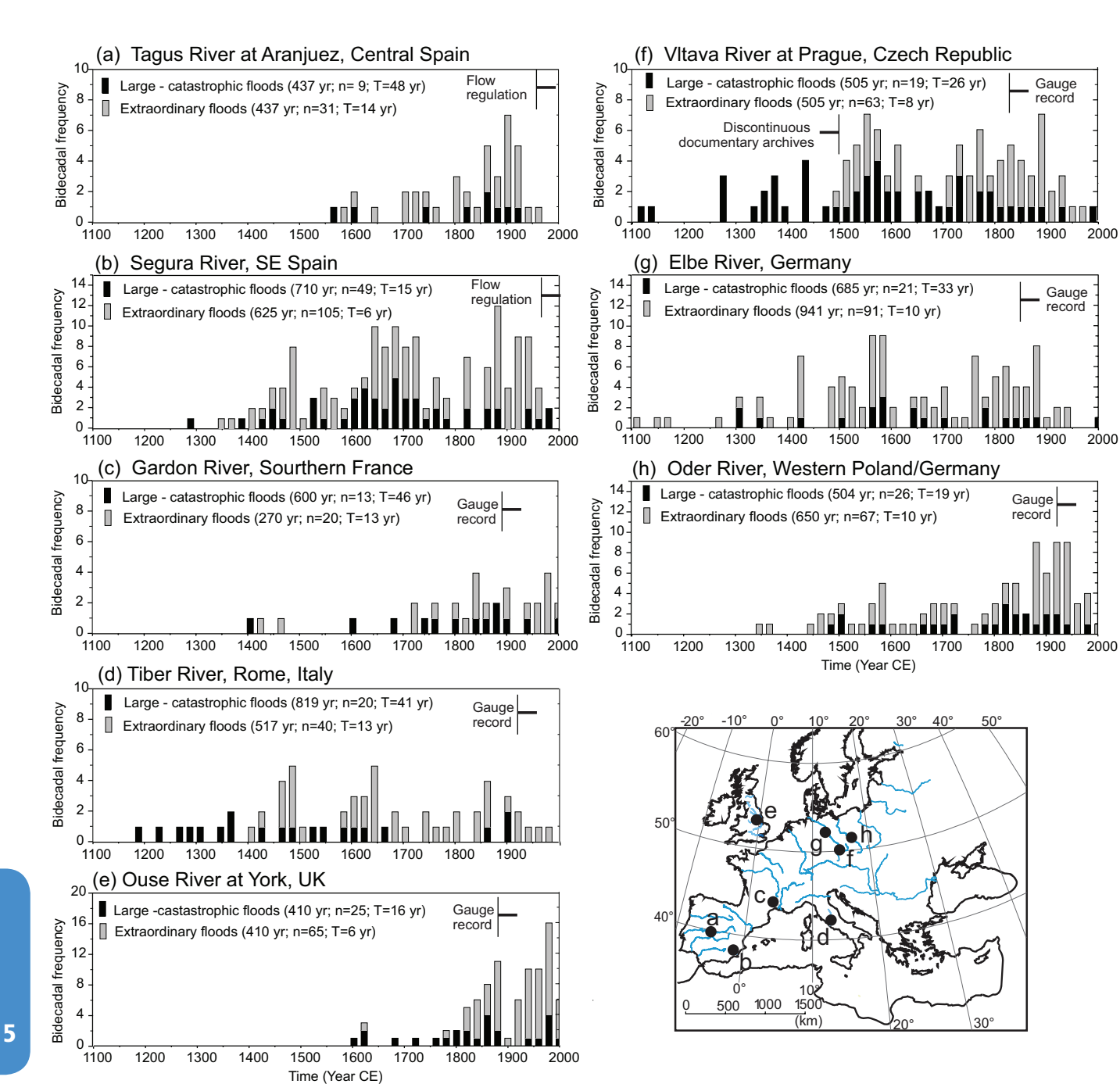


Figure 5.14 | Flood frequency from paleofloods, historical and instrumental records in selected European rivers. Depicted is the number of floods exceeding a particular discharge threshold or flood height over periods of 20 years (bidecadal). Flood categories include rare or catastrophic floods (CAT) associated with high flood discharge or severe damages, and extraordinary floods (EXT) causing inundation of the floodplain with moderate-to-minor damages. Legend at each panel indicates for each category the period of record in years, number of floods (n) over the period, and the average occurrence interval (T in years). (a) Tagus River combined paleoflood, historical and instrumental flood records from Aranjuez and Toledo with thresholds of $100\text{--}400 \text{ m}^3 \text{ s}^{-1}$ (EXT) and $>400 \text{ m}^3 \text{ s}^{-1}$ (CAT) (data from Benito et al., 2003a; 2003b). (b) Segura River Basin (SE Spain) documentary and instrumental records at Murcia (Barriendos and Rodrigo, 2006; Machado et al., 2011). (c) Gardon River combined discharges from paleofloods at La Baume (Sheffer et al., 2008), documented floods (since the 15th century) and historical and daily water stage readings at Anduze (1741–2005; Neppel et al., 2010). Discharge thresholds referred to Anduze are $1000\text{--}3000 \text{ m}^3 \text{ s}^{-1}$ (EXT), $>3000 \text{ m}^3 \text{ s}^{-1}$ (CAT). At least five floods larger than the 2002 flood (the largest in the gauged record) occurred in the period 1400–1800 (Sheffer et al., 2008). (d) Tiber River floods in Rome from observed historical stages (since 1100; Camuffo and Enzi, 1996; Calenda et al., 2005) and continuous stage readings (1870 to present) at the Ripetta landing (Calenda et al., 2005). Discharge thresholds set at $2300\text{--}2900 \text{ m}^3 \text{ s}^{-1}$ (EXT) and $>2900 \text{ m}^3 \text{ s}^{-1}$ (CAT; $>17 \text{ m}$ stage at Ripetta). Recent flooding is difficult to evaluate in context due to river regulation structures. (e) River Ouse at York combined documentary and instrumental flood record (Macdonald and Black, 2010). Discharge thresholds for large floods were set at $500 \text{ m}^3 \text{ s}^{-1}$ (CAT) and $350\text{--}500 \text{ m}^3 \text{ s}^{-1}$ (EXT). (f) Vltava River combined documentary and instrumental flood record at Prague (Brázdil et al., 2005) discharge thresholds: CAT, flood index 2 and 3 or discharge $>2900 \text{ m}^3 \text{ s}^{-1}$; EXT flood index 1 or discharge $2000\text{--}2900 \text{ m}^3 \text{ s}^{-1}$. (g) Elbe River combined documentary and instrumental flood record (Mudelsee et al., 2003). Classes refer to Mudelsee et al. (2003) strong (EXT) and exceptionally strong (CAT) flooding. (h) Oder River combined documentary and instrumental flood record (Mudelsee et al., 2003). The map shows the location of rivers used in the flood frequency plots. Note that flood frequencies obtained from historical sources may be down biased in the early part of the reported periods owing to document loss.

roughly two to three times larger than those of the 1972 flood (Harden et al., 2011). South America large flooding in the Atacama and Peruvian desert streams originated in the highland Altiplano and were particularly intense during El Niño events (Magilligan et al., 2008). In the winter rainfall zone of southern Africa, the frequency of large floods decreased during warmer conditions (e.g., from 1425 to 1600 and after 1925) and increased during wetter, colder conditions (Benito et al., 2011).

In summary, there is *high confidence* that past floods larger than recorded since the 20th century have occurred during the past 500 years in northern and central Europe, western Mediterranean region, and eastern Asia. There is, however, *medium confidence* that in the Near East, India, central North America, modern large floods are comparable to or surpass historical floods in magnitude and/or frequency.

5.6 Past Changes in Sea Level

This section discusses evidence for global mean sea level (GMSL) change from key periods. The MPWP (Table 5.1) has been selected as a period of higher than present sea level (Section 5.6.1), warmer temperature (Section 5.3.1) and 350–450 ppm atmospheric CO₂ concentration (Section 5.2.2.2). Of the recent interglacial periods with evidence for higher than present sea level, the LIG has the best-preserved record (Section 5.6.2). For testing glacio-isostatic adjustment (GIA) models, the principal characteristics of Termination I, including Meltwater Pulse-1A (Section 5.6.3) is assessed. For the Holocene, the emphasis is on the last 6000 years when ice volumes stabilized near present-day values, providing the baseline for discussion of anthropogenic contributions.

5.6.1 Mid-Pliocene Warm Period

Estimates of peak sea levels during the MPWP (Table 5.1, Section 5.3.1) based on a variety of geological records are consistent in suggesting higher-than-present sea levels, but they range widely (10 to 30 m; Miller et al., 2012a), and are each subject to large uncertainties. For example, coastal records (shorelines, continental margin sequences) are influenced by GIA, with magnitudes of the order of 5 m to 30 m for sites in the far and near fields of ice sheets, respectively (Raymo et al., 2011), and global mantle dynamic processes (Mouche et al., 2008; Müller et al., 2008) may contribute up to an additional ±10 m. Consequently, both signals can be as large as the sea level estimate itself and current estimates of their amplitudes are uncertain.

Benthic δ¹⁸O records are better dated than many coastal records and provide a continuous time series, but the δ¹⁸O signal reflects ice volume, temperature and regional hydrographic variability. During the mid-Pliocene warm interval, the 0.1 to 0.25‰ anomalies recorded in the LR04 benthic δ¹⁸O stack (Lisicki and Raymo, 2005) would translate into ~12 to 31 m higher than present GMSL, if they reflected only ice volume. Conversely, these anomalies could be explained entirely by warmer deep-water temperatures (Dowsett et al., 2009). Attempts to constrain the temperature component in benthic δ¹⁸O records conclude higher than present GMSL during the MPWP with large uncertainties (±10 m) (Dwyer and Chandler, 2009; Naish and Wilson, 2009; Sosdian and Rosenthal, 2009; Miller et al., 2012a).

The first appearance of ice-raftered debris across the entire North Atlantic indicates that continental-scale ice sheets in North America and Eurasia did not develop until about 2.7 Ma (Kleiven et al., 2002). This suggests that MPWP high sea levels were due to mass loss from the GIS, the WAIS and possibly the East Antarctic Ice sheet (EAIS). Sedimentary record from the Ross Sea indicates that the WAIS and the marine margin of EAIS retreated periodically during obliquity-paced interglacial periods of MPWP (Naish et al., 2009a). Reconstructed SSTs for the ice free seasons in the Ross Sea range from 2°C to 8°C (McKay et al., 2012b), with mean values >5°C being, according to one ice sheet model, above the stability threshold for ice shelves and marine portions of the WAIS and EAIS (Pollard and DeConto, 2009; see also Section 5.8.1). A synthesis of the geological evidence from the coastal regions of the Transantarctic Mountains (Barrett, 2013) and an iceberg-rafted debris record offshore of Prydz Bay (Passchier, 2011) also supports coastal thinning and retreat of the EAIS between about 5 to 2.7 Ma. In response to Pliocene climate, ice sheet models consistently produce near-complete deglaciation of GIS (+7 m) and WAIS (+4 m) and retreat of the marine margins of EAIS (+3 m) (Lunt et al., 2008; Pollard and DeConto, 2009; Hill et al., 2010), altogether corresponding to a GMSL rise of up to 14 m.

In summary, there is *high confidence* that GMSL was above present, due to deglaciation of GIS, WAIS and areas of EAIS, and that sea level was not higher than 20 m above present during the interglacials of the MPWP.

5.6.2 The Last Interglacial

Proxy indicators of sea level, including emergent shoreline deposits (Blanchon et al., 2009; Thompson et al., 2011; Dutton and Lambeck, 2012) and foraminiferal δ¹⁸O records (Siddall et al., 2003; Rohling et al., 2008a; Grant et al., 2012) are used to reconstruct LIG sea levels. Implicit in these reconstructions is that geophysical processes affecting the elevation of the sea level indicators (uplift, subsidence, GIA) have been properly modelled and/or that the sea level component of the stable isotope signal has been properly isolated. Particularly important issues with regard to the LIG are (1) the ongoing debate on its initiation and duration (cf. 130 to 116 ka, Stirling et al., 1998; 124 to 119 ka, Thompson and Goldstein, 2005), due to coral geochronology issues; (2) the magnitude of its maximum rise; and (3) sea level variability within the interval. Foraminiferal δ¹⁸O records can constrain (2) and possibly (3). Emergent shorelines on tectonically active coasts can constrain (1) and (3) and possibly (2) if vertical tectonic rates are independently known. Shorelines on tectonically stable coasts can constrain all three issues. Here evidence from emergent shorelines that can be dated directly is emphasized.

5.6.2.1 Magnitude of the Last Interglacial Sea Level Rise

AR4 assessed that global sea level was *likely* between 4 and 6 m higher during the LIG than in the 20th century. Since AR4, two studies (Kopp et al., 2009; Dutton and Lambeck, 2012) have addressed GIA effects from observations of coastal sites.

Kopp et al. (2009) obtained a probabilistic estimate of GMSL based on a large and geographically broadly distributed database of LIG sea

level indicators (Figure 5.15a). Their analysis accounted for GIA effects as well as uncertainties in geochronology, the interpretation of sea level indicators, and regional tectonic uplift and subsidence. They concluded that GMSL was *very likely* +6.6 m and *likely* +8.0 m relative to present, and that it is *unlikely* to have exceeded +9.4 m, although some of the most rapid and sustained rates of change occur in the early period when GMSL was still below present (Figure 5.15a).

Dutton and Lambeck (2012) used data from two tectonically stable far-field areas (areas far from the former centres of glaciation), Australia and the Seychelles islands. At these sites, in contrast to sites near the former ice margins, the isostatic signals are less sensitive to the choice of parameters defining the Earth rheology and the glacial ice sheets (Lambeck et al., 2012). On the west coast of Australia, the highest LIG reef elevations are at +3.5 m and the inferred paleo-sea level, allowing for possible reef erosion, is about +5.5 m relative to present. In the Seychelles, LIG coral reefs occur from 0 m to 6 m, but also possibly as high as ~9 m (Israelson and Wohlfarth, 1999, and references therein). Ten of the eleven LIG coral samples from the Seychelles used in Dutton and Lambeck (2012) have reef elevation estimates ranging from +2.1 to +4 m relative to present; whereas a single LIG coral sample has a reef elevation estimate of +6 m. Additional results are needed to support an estimate of a maximum LIG sea level at the Seychelles of + 9 m relative to present.

In conclusion, there is *very high confidence* that the maximum GMSL during the LIG was, for several thousand years, at least 5 m higher than present but that GMSL at this time did not exceed 10 m (*high confidence*). The best estimate from the two available studies is 6 m higher than present.

5.6.2.2 Evidence for Last Interglacial Sea Level Variability

Since AR4, there is evidence for meter-scale variability in local LIG sea level between 126 ka and 120 ka (Thompson and Goldstein, 2005; Hearty et al., 2007; Rohling et al., 2008a; Kopp et al., 2009; Thompson et al., 2011). However, there are considerable differences in the timing and amplitude of the reported fluctuations due to regional sea level variability and uncertainties in sea level proxies and their ages.

5

Two episodes of reef building during the LIG have been reported on the Yucatan coast (Blanchon et al., 2009) and in the Bahamas (Chen et al., 1991; Thompson et al., 2011). Blanchon et al. (2009) provide evidence of Yucatan reef growth early in the LIG at a relative sea level of +3 m, followed by a later episode at +6 m. Thompson et al. (2011) inferred a +4 m relative sea level at ~123 ka, followed by a fall to near present, and finally a rise to +6 m at ~119 ka. This yields a rate of sea level change in the Bahamas of ~2.6 m kyr⁻¹, although the higher estimate at the end of the interval may reflect GIA effects that result in a rise in relative sea level at these locations (Dutton and Lambeck, 2012).

LIG sea level rise rates of between 1.1 and 2.6 m per century have been estimated based on a foraminiferal $\delta^{18}\text{O}$ record from the Red Sea (Rohling et al., 2008a). However, the original Red-Sea chronology was based on a short LIG duration of 124 to 119 ka, after Thompson and Goldstein (2005). The longer LIG duration of 130 to 116 ka indicated by the coral data (Stirling et al., 1998) reduces these rates to 0.4 to

0.9 m per century, and a revised chronology of the Red Sea sea level record adjusted to ages from Soreq Cave yields estimates of sea level rise rates of up to 0.7 m per century when sea level was above present level during the LIG (Grant et al., 2012).

In their probabilistic assessment of LIG sea level, Kopp et al. (2013) concluded that it was *extremely likely* that there were at least two peaks in sea level during the LIG. They further concluded that during the interval following the initial peak at ~126 ka (Figure 5.15a) it is likely that there was a period in which GMSL rose at an average rate exceeding 3 m kyr⁻¹, but unlikely that this rate exceeded 7 m kyr⁻¹.

In summary, there is evidence for two intra-LIG sea level peaks (*high confidence*) during which sea level varied by up to 4 m (*medium confidence*). The millennial-scale rate of sea level rise during these periods exceeded 2 m kyr⁻¹ (*high confidence*).

5.6.2.3 Implications for Ice Sheet Loss During the Last Interglacial

The principal sources for the additional LIG meltwater are the GIS, WAIS and the low elevation, marine-based margins of the EAIS. An upper limit for the contributions from mountain glaciers is ~0.42 ± 0.11 m if all present-day mountain glaciers melted (cf. Section 4.3). The estimated LIG ocean thermal expansion contribution is 0.4 ± 0.3 m (McKay et al., 2011).

Sedimentological evidence indicates that southern Greenland was not ice-free during the LIG (Colville et al., 2011). Since AR4, the evidence for LIG ice layers in Greenland ice cores, which was ambiguous from Dye 3 and unequivocal from Summit and NGRIP ice cores (summarised in Masson-Delmotte et al., 2011a), has been strengthened. Data from the new NEEM ice core (NEEM community members, 2013; see Figure 5.16 for locations) point to an unequivocal existence of ice throughout the LIG with elevations differing a few hundred meter from present, possibly decreasing in elevation by ~ 400 m ± 350 m between 128 and 122 ka BP. GIS simulations give an average contribution of ~2.3 m to LIG GMSL (1.5 m, 1.9 m, 1.4 m and 4.3 m respectively for four models illustrated in Figure 5.16). Each model result has been selected from a series of runs within a range of parameter uncertainties that yield predictions consistent with the occurrence of ice at NEEM and the elevation of that ice reconstructed from the ice core record. In summary, the GIS simulations that are consistent with elevation changes from the ice core analysis show limited ice retreat during this period such that this ice sheet *very likely* contributed between 1.4 and 4.3 m sea level equivalent, implying with *medium confidence* a contribution from the Antarctic ice sheet.

One model of WAIS glacial-interglacial variability shows very little difference in ice volumes between the LIG and present (Pollard and DeConto, 2009) (Figure 5.15g), when the surface climate and ocean melt term were parameterised using the global benthic $\delta^{18}\text{O}$ record for the last 5 Ma. Direct geological evidence of fluctuations in the extent of WAIS margin during the LIG is equivocal due to inadequate age control on two sediment cores which imply that open-water conditions existed in the southeastern sector of the Ross Ice Shelf at some time in the last 1 Ma (Scherer et al., 1998; McKay et al., 2011; Vaughan et al.,

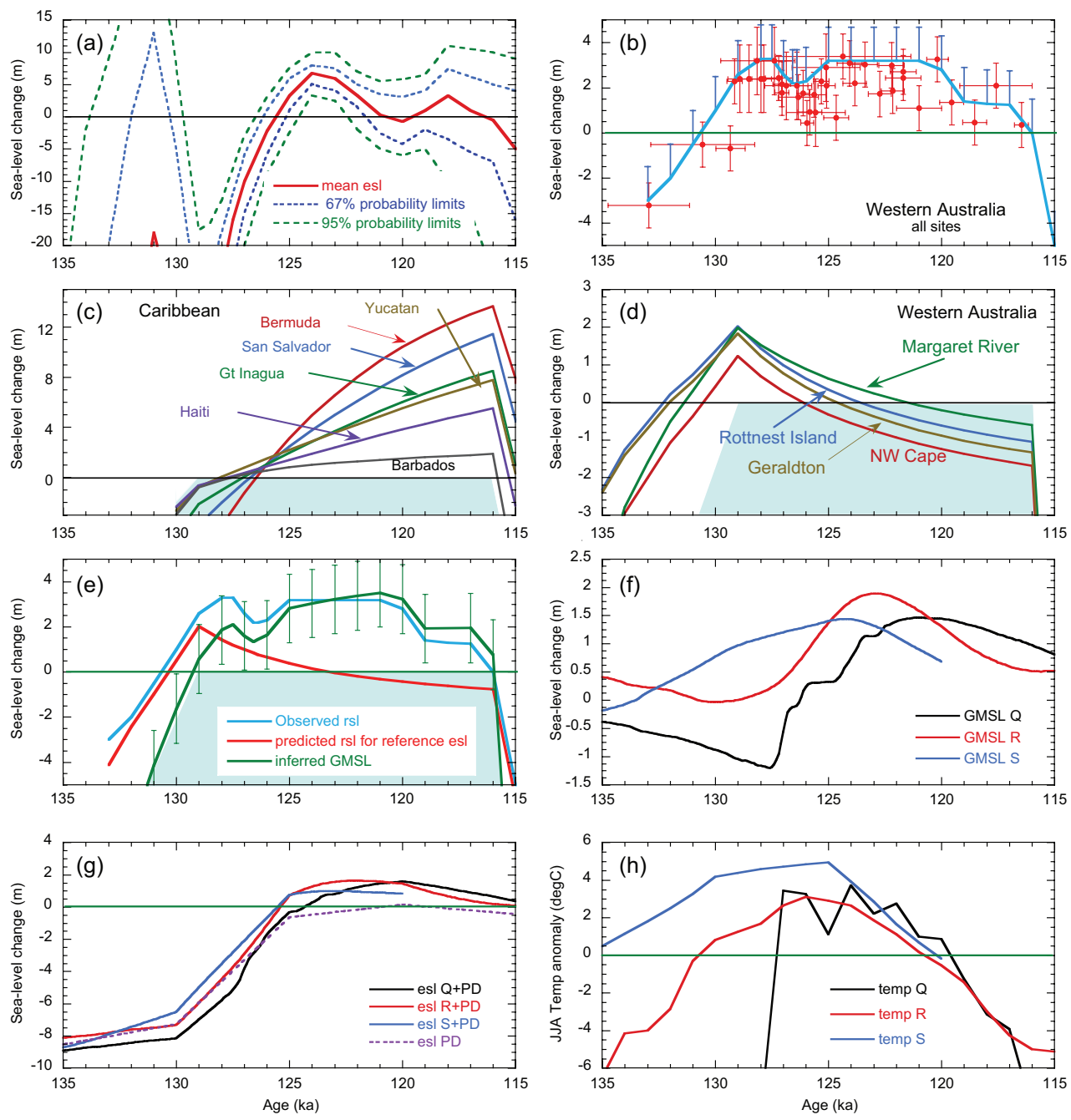


Figure 5.15 | Sea level during the Last Interglacial (LIG) period. (a) Proxy-derived estimate of global mean sea level (GMSL) anomaly from Kopp et al. (2013). Mean GMSL (red line), 67% confidence limits (blue dashed lines) and 95% confidence limits (green dashed lines). The chronology is based on open-system U/Th dates. (b) Local LIG relative sea level reconstructions from Western Australia based on *in situ* coral elevations (red) that pass diagenetic screening (Dutton and Lambeck, 2012). Age error bars correspond to 2 standard deviation uncertainties. All elevations have been normalised to the upper growth limit of corals corresponding to mean low water spring or mean low sea level. The blue line indicates the simplest interpretation of local sea level consistent with reef stratigraphy and should be considered as lower limits by an amount indicated by the blue upper limit error bars. The chronology is based on closed system U/Th dates. (c) Predicted sea levels for selected sites in the Caribbean and North Atlantic in the absence of tectonics with the assumption that ice volumes during the interval from 129 to 116 ka are equal to those of today (Lambeck et al., 2012) illustrating the spatial variability expected across the region due to glacio-isostatic effects of primarily the MIS-6 and MIS-2 deglaciations (see also Raymo and Mitrovica, 2012). The reference ice-volume model for the LIG interval (blue shaded), earth rheology and ice sheet parameters are based on rebound analyses from different regions spanning the interval from Marine Isotope Stage 6 to the present (c.f. Lambeck et al., 2006). LIG sea level observations from these sites contain information on these ice histories and on GMSL. (d) Same as (c) but for different sites along the Western Australia coast contributing to the data set in (b). The dependence on details of the ice sheet and on Earth-model parameters is less important at these sites than for those in (c). Thus data from these locations, assuming tectonic stability, is more appropriate for estimating GMSL. (e) The Western Australian reconstructed evidence (blue) from (b), compared with the model-predicted result (red) for a reference site midway between the northern and southern most localities. The difference between the reconstructed and predicted functions provides an estimate of GMSL (green). Uncertainties in this estimate (67% confidence limits) include the observational uncertainties from (b) and model uncertainties (see e.g., Lambeck et al., 2004a, for a treatment of model errors). (f) Simulated contribution of GIS to GMSL change (black, Q, Quiquet et al. (2013); red, R, Robinson et al. (2011); blue, S, Stone et al. (2013)). The Q, R, S correspond to the labels in Figure 5.16. (g) Simulated total GMSL contribution from the GIS (Q, R, S as in panel (f)) and the Antarctic ice sheet contribution (PD) according to Pollard and DeConto (2009). (h) Central Greenland surface-air temperature anomalies for summer (June–August, JJA) used for ice sheet simulations displayed in panel (f) and in Figure 5.16. Anomalies in all panels are calculated relative to present.

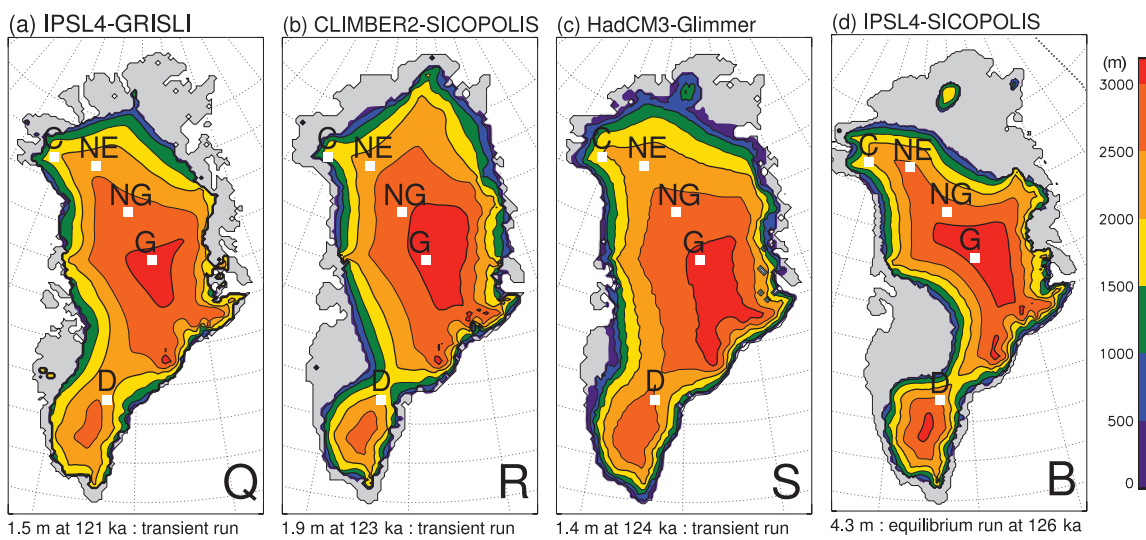


Figure 5.16 | Simulated GIS elevation at the Last Interglacial (LIG) in transient (Q, R, S) and constant-forcing experiments (B). (Q) GRISLI ice sheet model with transient climate forcing derived from IPSL simulations and paleoclimate reconstructions (Quiquet et al., 2013). (R) Simulation, most consistent with independent evidence from ice cores, from ensemble runs SICOPOLIS ice sheet model driven by transient LIG climate simulations downscaled from CLIMBER2 with the regional model REMBO (Robinson et al., 2011). (S) As R but from ensemble simulations with the Glimmer ice sheet model forced with transient climate forcing from 135 to 120 ka with HadCM3 (Stone et al., 2013). (B) SICOPOLIS ice model forced with a constant Eemian climate simulation of IPSL (at 126 ka), running for 6000 years starting from fully glaciated present-day GIS (Born and Nisancioglu, 2012). White squares in each panel show the locations of ice core sites: Greenland Ice Core Project/Greenland Ice Sheet Project (GRIP/GISP) from the summit (G), North Greenland Ice Core Project (NGRIP) (NG), North Greenland Eemian Ice Drilling (NEEM) (NE), Camp Century (C), and Dye3 (D). For ice sheet simulations using transient climate forcing, the minimum in ice volume is illustrated. All panels use original model resolution and grids. Below each panel, maximum contribution to global mean sea level rise and time of minimum ice volume are denoted together with information on experimental design (either “transient” run of the Interglacial period starting from the former glacial or “equilibrium” run of a time slice at the peak interglacial). The differences in model outputs regarding timing and ice elevations result from different methodologies (e.g., transient climate change or equilibrium climate, with the latter assumption leading to the highest estimate of the four models), melt schemes (van de Berg et al., 2011), and the reference climate input (Quiquet et al., 2013).

2011) and in the vicinity of the northwestern Ross Ice Shelf within the last 250,000 years during MIS 7 or LIG (McKay et al., 2012a). Ackert et al. (2011) dated glacial erratics and moraines across the Ohio Mountain Range of the Transantarctic Mountains and concluded that the ice elevations were similar during the LIG and today, but such results cannot be extrapolated beyond this region. East Antarctic ice core LIG data may reflect the impact of a reduced WAIS due to climatic effects (Holden et al., 2010b) but not through isostatic effects (Bradley et al., 2012). Modelling and ice core data suggest EAIS may have retreated in the Wilkes Basin (Bradley et al., 2012).

5 In summary, no reliable quantification of the contribution of the Antarctic ice volume to LIG sea level is currently possible. The only available transient ice sheet model simulation (Pollard and DeConto, 2009) does not have realistic boundary conditions, not enough is known about the subsurface temperatures and there are few direct observational constraints on the location of ice margins during this period. If the above inference of the contribution to GMSL from the GIS (5.6.2.1) is correct, the full GMSL change (section 5.6.2.2) implies significantly less LIG ice in Antarctica than today, but as yet this cannot be supported by the observational and model evidence.

5.6.3 Last Glacial Termination and Holocene

The onset of melting of the LGM ice sheets occurred at approximately 20 ka and was followed by a GMSL rise of ~130 m in ~13 kyr (Lambeck et al., 2002b). Coeval with the onset of the Bølling warming in the NH, a particularly rapid rise of ~ 20 m occurred within ~ 340 years (Meltwater Pulse 1A, MWP-1A), as most recently documented by Deschamps

et al. (2012) from a new Tahiti coral record. At this location sea level rose between 14 and 18 m at a rate approaching 5 m per century. The source of MWP-1A continues to be widely debated with most attention being on scenarios in which the Antarctic ice sheet contributed either significantly (Clark et al., 2002, 2009; Bassett et al., 2005) or very little (Bentley et al., 2010; Mackintosh et al., 2011). Evidence of rapid WAIS retreat at around the time of MWP-1A is also indicated by analysis of marine sediment cores (e.g., Kilfeather et al., 2011; Smith et al., 2011).

If the Antarctic ice sheet was the major contributor to MWP-1A then it must have contained at least $7 \cdot 10^6 \text{ km}^3$ more ice than at present (equivalent to ~17 m GMSL), which is about twice the difference in Antarctic ice volume between the LGM and present found by Whitehouse et al. (2012). Because of the Earth-ocean (including gravitational, deformational and rotational) response to rapid changes in ice volume, the amplitude of the associated sea level change is spatially variable (Clark et al., 2002) and can provide insight into the source region. Based on the comparison of the new Tahiti record with records from Barbados (Fairbanks, 1989) and the Sunda Shelf (Hanebuth et al., 2011), Deschamps et al. (2012) conclude that a significant meltwater contribution to GMSL, of at least 7 m, originated from Antarctica. From ice sheet modelling, Gregoire et al. (2012) argued that the separation of the North American Laurentide and Cordilleran ice sheets may in part be the cause of MWP-1A, contributing ~9 m in 500 years. Another ice sheet modelling study Carlson et al. (2012) suggests a contribution of 6 to 8 m in 500 years from the Laurentide at the onset of the Bølling warming over North America. These studies indicate that there are no glaciological impediments to a major North American contribution to MWP-1A. In contrast, there are as yet no modelling results that show a rapid retreat or partial collapse of the Antarctic ice sheet at that time.

Since AR4, high-resolution sea level records from different localities suggest further periods of rapid ice-mass loss. For example, records from Singapore indicate a rise of ~14 m from ~9.5 to 8.0 ka followed by a short interval of a smaller rise centred on about 7.2 ka (Bird et al., 2010, for Singapore) and records from the US Atlantic (Cronin et al., 2007) and North Sea coasts (Hijma and Cohen, 2010) suggest a rise at around ~9.0–7.5 ka that is possibly punctuated by one or two short intervals of higher rates. These and similar rapid events have to be interpreted against a background of rapid rise that is spatially variable because of the residual isostatic response to the last deglaciation (Milne and Mitrovica, 2008). Different explanations of these short-du-

ration events have been proposed: a multi-stage draining of glacial Lake Agassiz (Hijma and Cohen, 2010), although estimates of the amount of water stored in this lake are less than the required amount; a rapid melting of the Labrador and Baffin ice domes (Carlson et al., 2007; Gregoire et al., 2012); or to Antarctic ice sheet decay (Bird et al., 2007; Cronin et al., 2007).

Ocean volume between about 7 ka and 3 ka is *likely* to have increased by an equivalent sea level rise of 2 to 3 m (Lambeck et al., 2004b, 2010) (Figure 5.17). About 10% of this increase can be attributed to a mid-to-late-Holocene ice reduction over Marie Byrd Land, West Antarctica

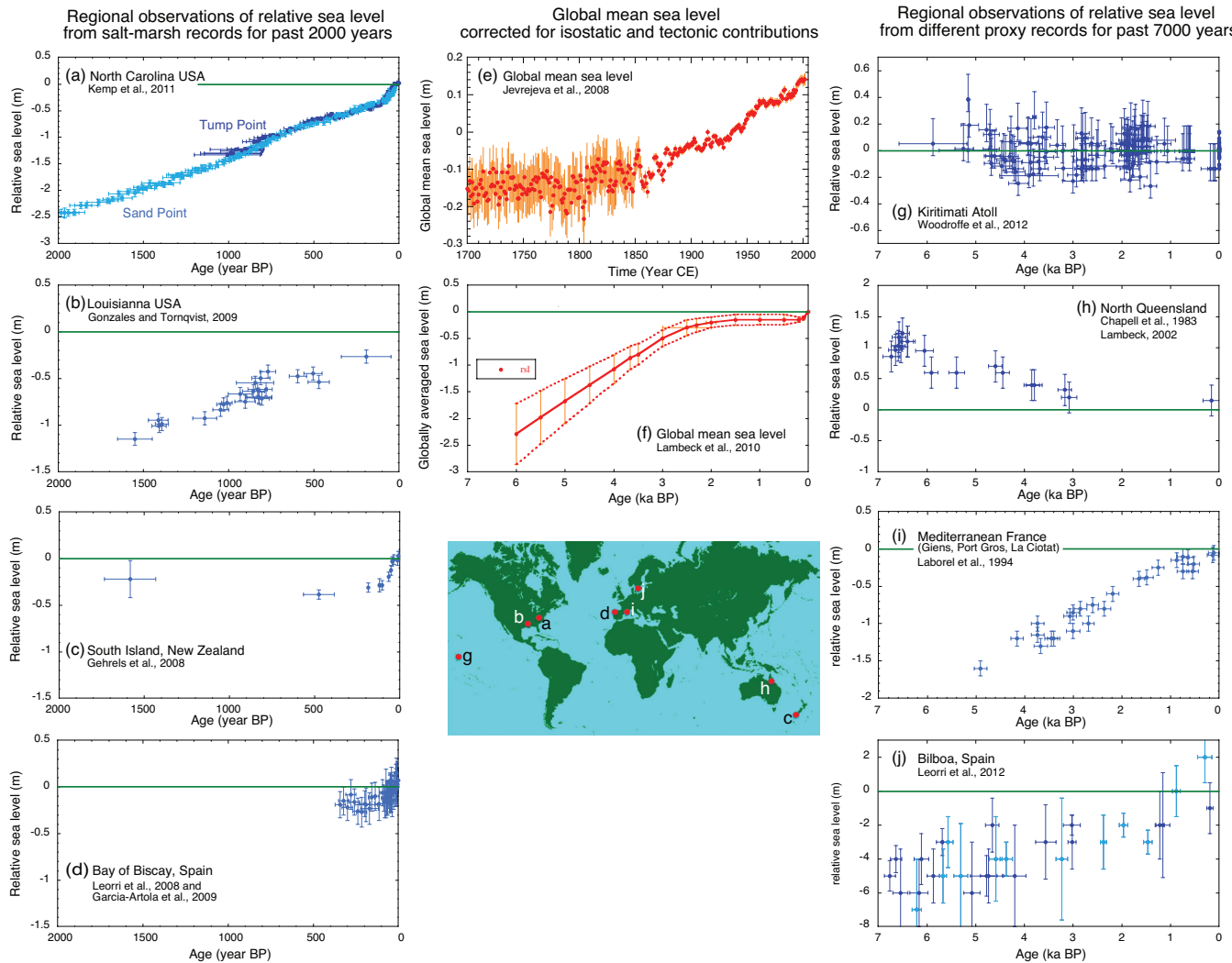


Figure 5.17 | Observational evidence for sea level change in the recent and late Holocene. Left panels (a–d): High-resolution, relative sea level results from salt-marsh data at representative sites, without corrections for glacial isostatic movement of land and sea surfaces. Locations are given on the map. The North Carolina (a) result is based on two nearby locations, Tump Point (dark blue) and Sand Point (light blue). They are representative of other North American Atlantic coast locations (e.g., b; Kemp et al., 2011). The rate of change occurring late in the 19th century are seen in all high resolution salt-marsh records—e.g., in New Zealand (c) (Gehrels et al., 2008; Gehrels and Woodworth, 2013) and in Spain (d) (Leorri et al., 2008; García-Artola et al., 2009)—that extend into modern time and is consistent with Roman archaeological evidence (Lambeck et al., 2004b). The oscillation in sea level seen in the North Carolina record at about 1000 years ago occurs in some (González and Törnqvist, 2009) but not all records (cf. Gehrels et al., 2011; Kemp et al., 2011). Right hand side panels (g–j): Observational evidence for sea level change from lower resolution but longer period records. All records are uncorrected for isostatic effects resulting in spatially variable near-linear trend in sea level over the 7000-year period. The Kiritimati record (Christmas Island) (g) consists of coral microatoll elevations whose fossil elevations are with respect to the growth position of living microatolls (Woodroffe et al., 2012). The North Queensland record (h) is also based on microatoll evidence from several sites on Orpheus Island (Chappell, 1983; Lambeck et al., 2002a). The data from Mediterranean France (i) is based on biological indicators (Laborel et al., 1994) restricted to three nearby locations between which differential isostatic effects are less than the observational errors (Lambeck and Bard, 2000). The Spanish record (j) from estuarine sedimentary deposits is for two nearby localities; Bilbao (dark blue) and Urdaiabai (light blue) (Leorri et al., 2012). The two global records (central panels) are estimates of change in global mean sea level from (i) the instrumental record (Jevrejeva et al., 2008) that overlaps the salt-marsh records, and (j) from a range of geological and archaeological indicators from different localities around the world (Lambeck et al., 2010), with the contributing records corrected individually for the isostatic effects at each location.

Frequently Asked Questions

FAQ 5.2 | How Unusual is the Current Sea Level Rate of Change?

The rate of mean global sea level change—averaging $1.7 \pm 0.2 \text{ mm yr}^{-1}$ for the entire 20th century and between 2.8 and 3.6 mm yr^{-1} since 1993 (Chapter 13)—is unusual in the context of centennial-scale variations of the last two millennia. However, much more rapid rates of sea level change occurred during past periods of rapid ice sheet disintegration, such as transitions between glacial and interglacial periods. Exceptional tectonic effects can also drive very rapid local sea level changes, with local rates exceeding the current global rates of change.

'Sea level' is commonly thought of as the point where the ocean meets the land. Earth scientists define sea level as a measure of the position of the sea surface relative to the land, both of which may be moving relative to the center of the Earth. A measure of sea level therefore reflects a combination of geophysical and climate factors. Geophysical factors affecting sea level include land subsidence or uplift and glacial isostatic adjustments—the earth–ocean system's response to changes in mass distribution on the Earth, specifically ocean water and land ice.

Climate influences include variations in ocean temperatures, which cause sea water to expand or contract, changes in the volume of glaciers and ice sheets, and shifts in ocean currents. Local and regional changes in these climate and geophysical factors produce significant deviations from the global estimate of the mean rate of sea level change. For example, *local* sea level is falling at a rate approaching 10 mm yr^{-1} along the northern Swedish coast (Gulf of Bothnia), due to ongoing uplift caused by continental ice that melted after the last glacial period. In contrast, *local* sea level rose at a rate of $\sim 20 \text{ mm yr}^{-1}$ from 1960 to 2005 south of Bangkok, mainly in response to subsidence due to ground water extraction.

For the past ~ 150 years, sea level change has been recorded at tide gauge stations, and for the past ~ 20 years, with satellite altimeters. Results of these two data sets are consistent for the overlapping period. The globally averaged rate of sea level rise of $\sim 1.7 \pm 0.2 \text{ mm yr}^{-1}$ over the 20th century—and about twice that over the past two decades—may seem small compared with observations of wave and tidal oscillations around the globe that can be orders of magnitude larger. However, if these rates persist over long time intervals, the magnitude carries important consequences for heavily populated, low-lying coastal regions, where even a small increase in sea level can inundate large land areas.

Prior to the instrumental period, local rates of sea level change are estimated from indirect measures recorded in sedimentary, fossil and archaeological archives. These proxy records are spatially limited and reflect both local and global conditions. Reconstruction of a global signal is strengthened, though, when individual proxy records from widely different environmental settings converge on a common signal. It is important to note that geologic archives—particularly those before about 20,000 years ago—most commonly only capture millennial-scale changes in sea level. Estimates of century-scale rates of sea level change are therefore based on millennial-scale information, but it must be recognised that such data do not necessarily preclude more rapid rates of century-scale changes in sea level.

5

Sea level reconstructions for the last two millennia offer an opportunity to use proxy records to overlap with, and extend beyond, the instrumental period. A recent example comes from salt-marsh deposits on the Atlantic Coast of the United States, combined with sea level reconstructions based on tide-gauge data and model predictions, to document an average rate of sea level change since the late 19th century of $2.1 \pm 0.2 \text{ mm yr}^{-1}$. This century-long rise exceeds any other century-scale change rate in the entire 2000-year record for this same section of coast.

On longer time scales, much larger rates and amplitudes of sea level changes have sometimes been encountered. Glacial–interglacial climate cycles over the past 500,000 years resulted in global sea level changes of up to about 120 to 140 m. Much of this sea level change occurred in 10,000 to 15,000 years, during the transition from a full glacial period to an interglacial period, at average rates of 10 to 15 mm yr^{-1} . These high rates are only sustainable when the Earth is emerging from periods of extreme glaciation, when large ice sheets contact the oceans. For example, during the transition from the last glacial maximum (about 21,000 years ago) to the present interglacial (Holocene, last 11,650 years), fossil coral reef deposits indicate that global sea level rose abruptly by 14 to 18 m in less than 500 years. This event is known as Meltwater Pulse 1A, in which the rate of sea level rise reached more than 40 mm yr^{-1} .

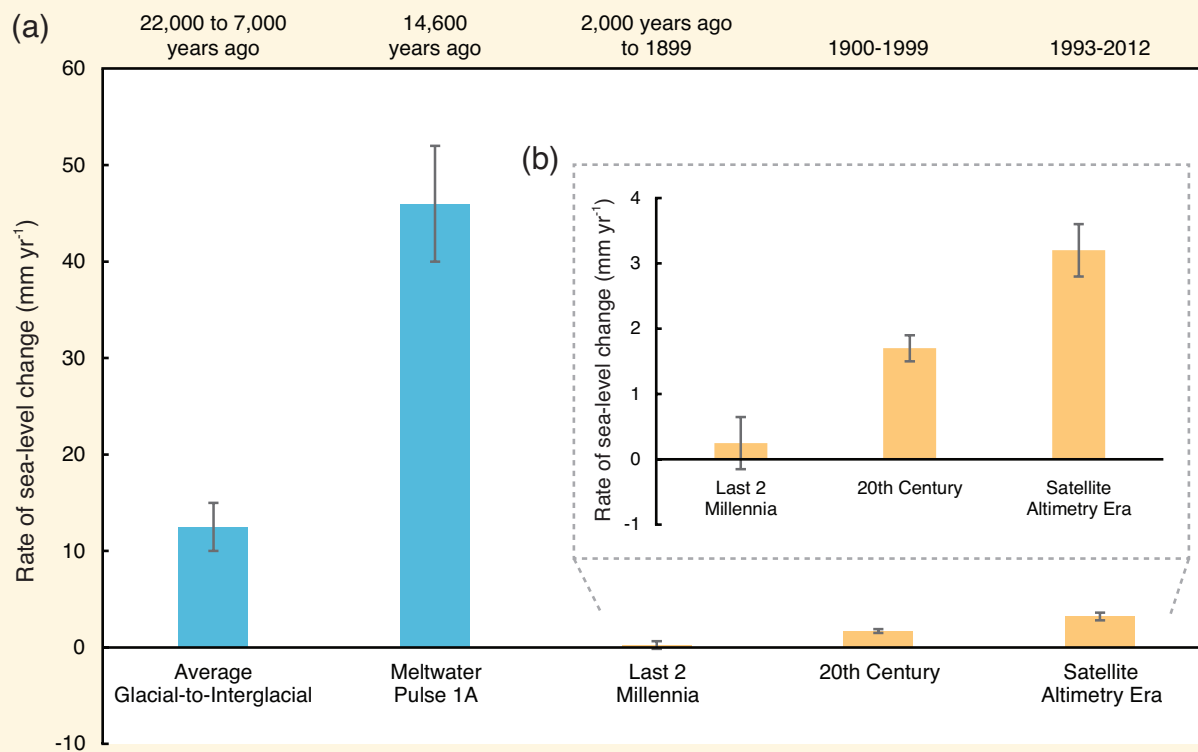
These examples from longer time scales indicate rates of sea level change greater than observed today, but it should be remembered that they all occurred in special circumstances: at times of transition from full glacial to interglacial condition; at locations where the long-term after-effects of these transitions are still occurring; at locations of

(continued on next page)

FAQ 5.2 (continued)

major tectonic upheavals or in major deltas, where subsidence due to sediment compaction—sometimes amplified by ground-fluid extraction—dominates.

The instrumental and geologic record support the conclusion that the current rate of mean global sea level change is unusual relative to that observed and/or estimated over the last two millennia. Higher rates have been observed in the geological record, especially during times of transition between glacial and interglacial periods.



FAQ 5.2, Figure 1 | (a) Estimates of the average rate of global mean sea level change (in mm yr^{-1}) for five selected time intervals: last glacial-to-interglacial transition; Meltwater Pulse 1A; last 2 millennia; 20th century; satellite altimetry era (1993–2012). Blue columns denote time intervals of transition from a glacial to an interglacial period, whereas orange columns denote the current interglacial period. Black bars indicate the range of likely values of the average rate of global mean sea level change. Note the overall higher rates of global mean sea level change characteristic of times of transition between glacial and interglacial periods. (b) Expanded view of the rate of global mean sea level change during three time intervals of the present interglacial.

(Stone et al., 2003). Elevation histories derived from central Greenland ice core data (Vinther et al., 2009; Lecavalier et al., 2013) have presented evidence for thinning from 8 ka to 6 ka but no integrated observation-based estimate for the total ice sheet is available. Contributions from mountain glaciers for this interval are unknown.

Resolving decimeter-scale sea level fluctuations is critical for understanding the causes of sea level change during the last few millennia. Three types of proxies have this capability: salt-marsh plants and microfauna (foraminifera and diatoms) that form distinctive elevation zones reflecting variations in tolerances to the frequency and duration of tidal inundation (Donnelly et al., 2004; Horton and Edwards, 2006; Gehrels et al., 2008; Kemp et al., 2009; Long et al., 2012); coral microatolls found in intertidal environments close to lowest spring tides

(Woodroffe and McLean, 1990; Smithers and Woodroffe, 2001; Goodwin and Harvey, 2008); and coastal archaeological features constructed with direct (e.g., fish ponds and certain harbour structures) or indirect (e.g., changes in water-table level in ancient wells) relationships to sea level (Lambeck et al., 2004b; Sivan et al., 2004; Auriemma and Solinas, 2009; Anzidei et al., 2011). Of these, the salt-marsh records are particularly important because they have been validated against regional tide-gauge records and because they can provide near-continuous records. The most robust signal captured in the salt-marsh proxy sea level records from both the NH and SH is an increase in rate, late in the 19th or in the early 20th century (Figure 5.17), that marks a transition from relatively low rates of change during the late Holocene (order tenths of mm yr^{-1}) to modern rates (order mm yr^{-1}) (see also FAQ 5.2). Variability in both the magnitude and the timing (1840–1920) of

this acceleration has been reported (Gehrels et al., 2006, 2008, 2011; Kemp et al., 2009, 2011), but Gehrels and Woodworth (2013) have concluded that these mismatches can be reconciled within the observational uncertainties. Combined with the instrumental evidence (see Section 3.7) and with inferences drawn from archaeological evidence from 2000 years ago (Lambeck et al., 2004b), rates of sea level rise exceeded the late Holocene background rate after about 1900 (*high confidence*) (Figure 5.17).

Regionally, as along the US Atlantic coast and Gulf of Mexico coast, the salt-marsh records reveal some consistency in multi-decadal and centennial time scales deviations from the linear trends expected from the GIA signal (see e.g., panels (a) and (b) in Figure 5.17) (van de Plassche et al., 1998; González and Törnqvist, 2009; Kemp et al., 2011) but they have not yet been identified as truly global phenomena. For the past 5 millennia the most complete sea level record from a single location consists of microatoll evidence from Kiritimati (Christmas Island; Pacific Ocean) (Woodroffe et al., 2012) that reveals with *medium confidence* that amplitudes of any fluctuations in GMSL during this interval did not exceed approximately ± 25 cm on time scales of a few hundred years. Proxy data from other localities with quasi-continuous records for parts of this pre-industrial period, likewise, do not identify significant global oscillations on centennial time scales (Figure 5.17).

5.7 Evidence and Processes of Abrupt Climate Change

Many paleoclimate archives document climate changes that happened at rates considerably exceeding the average rate of change for longer-term averaging periods prior and after this change (see Glossary for other definition of Abrupt Climate Change). A variety of mechanisms have been suggested to explain the emergence of such abrupt climate changes (see Section 12.5.5). Most of them invoke the existence of nonlinearities or, more specifically, thresholds in the underlying dynamics of one or more Earth-system components. Both internal dynamics and external forcings can generate abrupt changes in the climate state. Documentation of abrupt climate changes in the past using multiple sources of proxy evidence can provide important benchmarks to test instability mechanisms in climate models. This assessment of abrupt climate change on time scales of 10 to 100 years focuses on Dansgaard-Oeschger (DO) events and iceberg/meltwater discharges during Heinrich events, especially the advances since AR4 in reconstructing and understanding their global impacts and in extending the record of millennial-scale variability to about 800 ka.

Twenty-five abrupt DO events (North Greenland Ice Core Project members, 2004) and several centennial-scale events (Capron et al., 2010b) occurred during the last glacial cycle (see Section 5.3.2). DO events in Greenland were marked by an abrupt transition (within a few decades) from a cold phase, referred to as Greenland Stadial (GS) into a warm phase, known as Greenland Interstadial (GI). Subsequently but within a GI, a gradual cooling preceded a rapid jump to GS that lasted for centuries up to millennia. Thermal gas-fractionation methods (Landais et al., 2004; Huber et al., 2006) suggest that for certain DO events Greenland temperatures increased by up to $16^\circ\text{C} \pm 2.5^\circ\text{C}$ (1 standard deviation) within several decades. Such transitions were also

accompanied by abrupt shifts in dust and deuterium excess, indicative of reorganizations in atmospheric circulation (Steffensen et al., 2008; Thomas et al., 2009). Reconstructions from the subtropical Atlantic and Mediterranean reveal concomitant SST changes attaining values up to 5°C (e.g., Martrat et al., 2004; Martrat et al., 2007).

In spite of the visible presence of DO events in many paleoclimate records from both hemispheres, the underlying mechanisms still remain unresolved and range from internally generated atmosphere–ocean–ice sheet events (Timmermann et al., 2003; Ditlevsen and Ditlevsen, 2009), to solar-forced variability (Braun et al., 2008; Braun and Kurths, 2010). However, given the lack of observational evidence for a direct linear modulation of solar irradiance on DO time scales, (Muscheler and Beer, 2006), solar forcing is an improbable candidate to generate DO events. There is robust evidence from multiple lines of paleoceanographic information and modelling that DO variability is often associated with AMOC changes, as suggested by climate models of varying complexity (Ganopolski and Rahmstorf, 2001; Arzel et al., 2009) and marine proxy records (Piotrowski et al., 2005; Kissel et al., 2008; Barker et al., 2010; Roberts et al., 2010); but also potential influences of sea-ice cover (Li et al., 2010b), atmosphere circulation and ice sheet topography (Wunsch, 2006) have been proposed.

The widespread presence of massive layers of ice-raftered detritus in North Atlantic marine sediments provide robust evidence that some DO GS, known as Heinrich stadials, were associated with iceberg discharges originating from the Northern Hemispheric ice sheets. During these periods global sea level rose by up to several tens of meters (Chappell, 2002; Rohling et al., 2008b; Siddall et al., 2008; González and Dupont, 2009; Yokoyama and Esat, 2011), with remaining uncertainties in timing and amplitude of sea level rise, stadial cooling and ocean circulation changes relative to the iceberg discharge (Hall et al., 2006; Arz et al., 2007; Siddall et al., 2008; González and Dupont, 2009; Sierro et al., 2009; Hodell et al., 2010). Internal instabilities of the Laurentide ice sheet can cause massive calving and meltwater events similar to those reconstructed from proxy records (Calov et al., 2002, 2010; Marshall and Koutnik, 2006). Alternatively, an initial weakening of the AMOC can lead to subsurface warming in parts of the North Atlantic (Shaffer et al., 2004) and subsequent basal melting of the Labrador ice shelves, and a resulting acceleration of ice streams and iceberg discharge (Alvarez-Solas et al., 2010; Marcott et al., 2011). At present, unresolved dynamics in ice sheet models and limited proxy information do not allow us to distinguish the two mechanisms with confidence.

Since AR4, climate model simulations (Liu et al., 2009b; Otto-Bliesner and Brady, 2010; Menzel et al., 2011; Kageyama et al., 2013) have further confirmed the finding (*high confidence*) that changes in AMOC strength induce abrupt climate changes with magnitude and patterns resembling reconstructed paleoclimate-proxy data of DO and Heinrich events.

Recent studies have presented a better understanding of the global imprints of DO events and Heinrich events, for various regions. Widespread North Atlantic cooling and sea-ice anomalies during GS induced atmospheric circulation changes (*high confidence*) (Krebs and Timmermann, 2007; Clement and Peterson, 2008; Kageyama et al., 2010; Merkel et al., 2010; Otto-Bliesner and Brady, 2010; Timmermann et

al., 2010) which in turn affected inter-hemispheric tropical rainfall patterns, leading to drying in Northern South America (Peterson and Haug, 2006), the Mediterranean (Fletcher and Sánchez Goñi, 2008; Fleitmann et al., 2009), equatorial western Africa and Arabia (Higginson et al., 2004; Ivanochko et al., 2005; Weldeab et al., 2007a; Mulitz et al., 2008; Tjallingii et al., 2008; Itambi et al., 2009; Weldeab, 2012), wide parts of Asia (Wang et al., 2008; Cai et al., 2010) (see Figure 5.4e) as well as in the Australian-Indonesian monsoon region (Mohtadi et al., 2011). Concomitant wetter conditions have been reconstructed for southwestern North America (Asmerom et al., 2010; Wagner et al., 2010) and southern South America (Kanner et al., 2012) (Figure 5.4h). Moreover, atmospheric circulation changes have been invoked (Zhang and Delworth, 2005; Xie et al., 2008; Okumura et al., 2009) to explain temperature variations in the North Pacific that varied in unison with abrupt climate change in the North Atlantic region (Harada et al., 2008, 2012; Pak et al., 2012). Other factors that may have contributed to North Pacific climate anomalies include large-scale Pacific Ocean circulation changes (Saenko et al., 2004; Schmittner et al., 2007; Harada et al., 2009; Okazaki et al., 2010) during phases of a weak AMOC. Recent high-resolution ice core studies (EPICA Community Members, 2006; Capron et al., 2010a, 2010b, 2012; Stenni et al., 2011) show that Antarctica warmed gradually for most GS, reaching maximum values at the time of GS/GI transitions, which is in agreement with the bipolar seesaw concept (Stock and Johnsen, 2003; Stenni et al., 2011). A recent global temperature compilation (Shakun et al., 2012), Southern Ocean temperature records (Lamy et al., 2007; Barker et al., 2009; De Deckker et al., 2012), evidence from SH terrestrial records (Kaplan et al., 2010; Putnam et al., 2010) and transient climate model experiments (Menkveld et al., 2011) provide multiple lines of evidence for the inter-hemispheric character of millennial-scale variability during the last glacial termination and for DO events (*high confidence*).

Newly available marine records (Martrat et al., 2007; Grützner and Higgins, 2010; Margari et al., 2010; Kleiven et al., 2011), Antarctic WMGHG records (Loulergue et al., 2008; Schilt et al., 2010) and statistical analyses of Antarctic ice core data (Siddall et al., 2010; Lambert et al., 2012) combined with bipolar seesaw modelling (Siddall et al., 2006; Barker et al., 2011) document with *high confidence* that abrupt climate change events, similar to the DO events and Heinrich stadials of the last glacial cycle, occurred during previous glacial periods extending back about 800 ka and, with *medium confidence*, to 1100 ka.

5.8 Paleoclimate Perspective on Irreversibility in the Climate System

For an introduction of the concept of irreversibility see Glossary.

5.8.1 Ice Sheets

Modelling studies suggest the existence of multiple equilibrium states for ice sheets with respect to temperature, CO₂ concentration and orbital forcing phase spaces (DeConto and Pollard, 2003; Calov and Ganopolski, 2005; Ridley et al., 2010). This implies a possibility of irreversible changes in the climate-cryosphere system in the past and future.

The existence of threshold behaviour in the EAIS is consistent with an abrupt increase in Antarctic ice volume at the Eocene/Oligocene boundary, 33 Ma, attributed to gradual atmospheric CO₂ concentration decline on geological time scale (Pagani et al., 2005b; Pearson et al., 2009) (Figure 5.2, Section 5.2.2). Ice sheet models produce a hysteresis behaviour of the EAIS with respect to CO₂ concentrations, leading to EAIS glaciation when CO₂ concentration declined to 600–900 ppm (DeConto and Pollard, 2003; Langebroek et al., 2009) and deglaciation for CO₂ above 1200 ppm (Pollard and DeConto, 2009). Proxy records suggest that the WAIS might have collapsed during last interglacials (Naish et al., 2009b; Vaughan et al., 2011) and was absent during warm periods of the Pliocene when CO₂ concentration was 350 to 450 ppm (see Section 5.2.2.2) and global sea level was higher than present (see Section 5.6.1). These reconstructions and one ice sheet model simulation (Pollard and DeConto, 2009) suggest that WAIS is very sensitive to the subsurface ocean temperature. This implies, with *medium confidence*, that a large part of the WAIS will be eventually lost if the atmospheric CO₂ concentration stays within, or above, the range of 350 to 450 ppm for several millennia.

Observational evidence suggest that the GIS was also much smaller than today during the MPWP (see Sections 5.6.1 and 5.2.2), consistent with the results of simulations with ice sheet models (Dolan et al., 2011; Koenig et al., 2011). Ice sheet model simulations and proxy records show that the volume of the GIS was also reduced during the past interglacial period (Section 5.6.2). This supports modelling results that indicate temperature or CO₂ thresholds for melting and re-growth of the GIS may lie in close proximity to the present and future levels (Gregory and Huybrechts, 2006; Lunt et al., 2008) (Section 5.6.1) and that the GIS may have multiple equilibrium states under present-day climate state (Ridley et al., 2010).

Therefore, proxy records and results of model simulations indicate with *medium confidence* that the GIS and WAIS could be destabilized by projected climate changes, although the time scales of the ice sheets response to climate change are very long (several centuries to millennia).

5.8.2 Ocean Circulation

Numerous modelling studies demonstrate that increased freshwater flux into the North Atlantic leads to weakening of the AMOC. Results of EMICs (Rahmstorf et al., 2005) and coupled GCMs also suggest that AMOC may have multiple equilibrium states under present or glacial climate conditions (Hawkins et al., 2011; Hu et al., 2012). Experiments with climate models provide evidence that the sensitivity of the AMOC to freshwater perturbation is larger for glacial boundary conditions than for interglacial conditions (Swingedouw et al., 2009) and that the recovery time scale of the AMOC is longer for LGM conditions than for the Holocene (Bitz et al., 2007).

The abrupt climate-change event at 8.2 ka permits the study of the recovery time of the AMOC to freshwater perturbation under near-modern boundary conditions (Rohling and Pälike, 2005). Since AR4, new proxy records and simulations confirm that the pattern of surface-ocean and atmospheric climate anomalies is consistent with a reduction in the strength of the AMOC (Figure 5.18a, b, d). Available

proxy records from the North Atlantic support the hypothesis that freshwater input into the North Atlantic reduced the amount of deep and central water-mass formation, Nordic Seas overflows, intermediate water temperatures and the ventilation state of North Atlantic Deep Water (Figure 5.18c, d) (McManus et al., 2004; Ellison et al., 2006; Kleiven et al., 2008; Bamberg et al., 2010). A concomitant decrease of SST

and atmospheric temperatures in the North Atlantic and in Greenland has been observed (Figure 5.18a, b) with the climate anomaly associated with the event lasting 100–160 years (Daley et al., 2011). The additional freshwater that entered the North Atlantic during the 8.2 ka event is estimated between $1.6 \cdot 10^{14} \text{ m}^3$ and $8 \cdot 10^{14} \text{ m}^3$ (von Grafenstein et al., 1998; Barber et al., 1999; Clarke et al., 2004). The duration of the

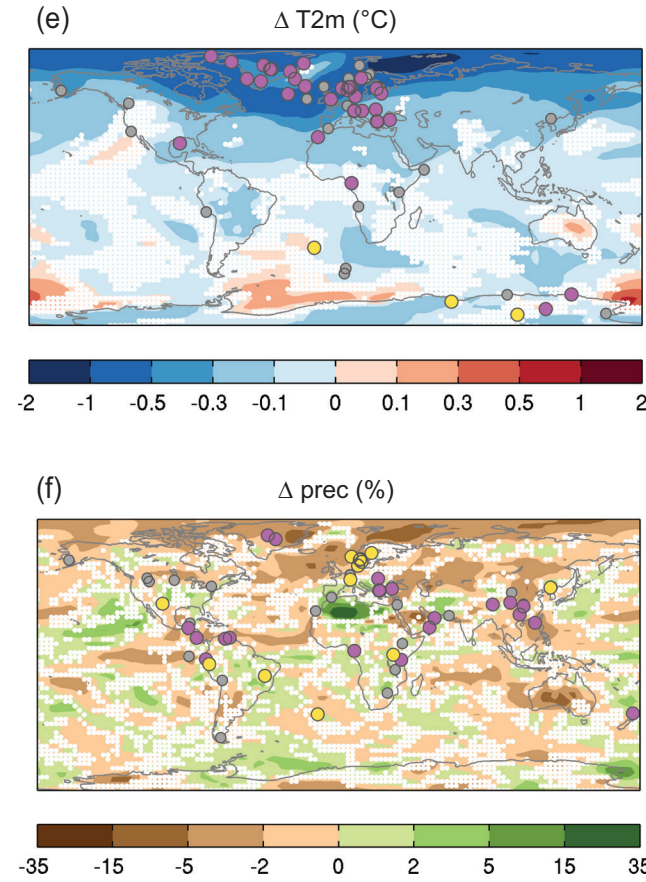
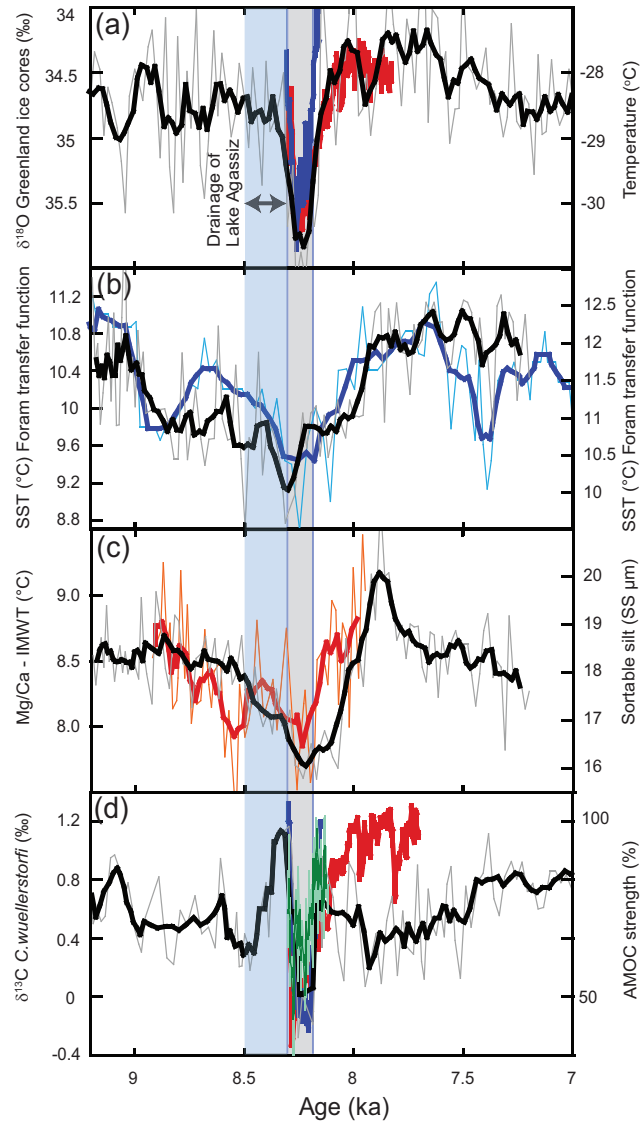


Figure 5.18 | Compilation of selected paleoenvironmental and climate model data for the abrupt Holocene cold event at 8.2 ka, documenting temperature and ocean-circulation changes around the event and the spatial extent of climate anomalies following the event. Published age constraints for the period of release of freshwater from glacier lakes Agassiz and Ojibway are bracketed inside the vertical blue bar. Vertical grey bar denotes the time of the main cold event as found in Greenland ice core records (Thomas et al., 2007). Thick lines in (a–d) denote 5-point running mean of underlying data in thin lines. (a) Black curve: North Greenland Ice Core Project (NGRIP) $\delta^{18}\text{O}$ (temperature proxy) from Greenland Summit (North Greenland Ice Core Project members, 2004). Red curve: Simulated Greenland temperature in an 8.2 ka event simulation with the ECBilt-CLIO-VECODE model (Wiersma et al., 2011). Blue curve: Simulated Greenland temperature in an 8.2 ka event simulation with the CCSM3 model (Morrill et al., 2011). (b) North Atlantic/Nordic Seas sea surface temperature (SST) reconstructions, age models are aligned on the peak of the cold-event (less than 100-year adjustment). Blue curve: Nordic Seas (Risebrobakken et al., 2011). Black curve: Gardar Drift south of Iceland (Ellison et al., 2006). (c) Deep- and intermediate-water records. Black curve: Sortable silt (SS) record (overflow strength proxy) from Gardar Drift south of Iceland (Ellison et al., 2006), Atlantic intermediate water temperature reconstruction (Bamberg et al., 2010). (d) Black curve: $\delta^{13}\text{C}$ (deep water ventilation proxy) at 3.4 km water depth south of Greenland (Kleiven et al., 2008). Age model is aligned on the minimum overflow strength in (c) (less than 100-year adjustment). Modelled change in the strength of the Atlantic Ocean meridional overturning circulation (AMOC)—Green curve: an 8.2 ka event simulation with the GISS model (LeGrande et al., 2006). Red curve: an 8.2 ka event simulation with the ECBilt-CLIO-VECODE (v. 3) model (Wiersma et al., 2011). Blue curve: an 8.2 ka event simulation with the CCSM3 model (Morrill et al., 2011). (e) Spatial distribution of the 4-member ensemble mean annual mean surface temperature anomaly ($^{\circ}\text{C}$) compared with the control experiment from model simulations of the effects of a freshwater release at 8.2 ka (based on Morrill et al., 2013a). White dots indicate regions where less than 3 models agree on the sign of change. Coloured circles show paleoclimate data from records resolving the 8.2 ka event: purple = cold anomaly, yellow = warm anomaly, grey = no significant anomaly. Data source and significance thresholds are as summarized by Morrill et al. (2013b). (f) Same as (e) but for annual mean precipitation anomalies in %. Coloured circles show paleoclimate data from records resolving the 8.2 ka event: purple = dry anomaly, yellow = wet anomaly, grey = no significant anomaly.

meltwater release may have been as short as 0.5 years (Clarke et al., 2004), but new drainage estimates indicate an up to 200 year-duration in two separate stages (Gregoire et al., 2012). A four-model ensemble with a one-year freshwater perturbation of 2.5 Sv only gives temperature anomalies half of what has been reconstructed and with a shorter duration than observed, resulting from unresolved processes in models, imprecise representation of the initial climate state or a too short duration of the freshwater forcing (Morrill et al., 2013a). These marine-based reconstructions consistently show that the recovery time scale of the shallow and deep overturning circulation is on the order of 200 years (Ellison et al., 2006; Bamberg et al., 2010) (Figure 5.18c, d), with one record pointing to a partial recovery on a decadal time scale (Kleiven et al., 2008). Both recovery time scale and sensitivity of the AMOC to the freshwater perturbation are generally consistent with model experiments for the 8.2 ka event using coarse-resolution models, GCMs and eddy permitting models (LeGrande and Schmidt, 2008; Spence et al., 2008; Li et al., 2009). The recovery of temperatures out of the cold anomaly appears overprinted with natural variability in the proxy data, and is more gradual in data than in the AOGCM experiments (Figure 5.18c, d). In summary, multiple lines of evidence indicate, with *high confidence*, that the interglacial mode of the AMOC can recover from a short-term freshwater input into the subpolar North Atlantic.

The characteristic teleconnection patterns associated with a colder North Atlantic Ocean as described in Section 5.7 are evident for the 8.2 ka event in both models and proxy data (Figure 5.18e, f).

5.8.3 Next Glacial Inception

Since orbital forcing can be accurately calculated for the future (see Section 5.2.1), efforts can be made to predict the onset of the next glacial period. However, the glaciation threshold depends not only on insolation but also on the atmospheric CO₂ concentration (Archer and Ganopolski, 2005). Models of different complexity have been used to investigate the response to orbital forcing in the future for a range of atmospheric CO₂ levels. These results consistently show that a glacial inception is not expected to happen within the next approximate 50 kyr if either atmospheric CO₂ concentration remains above 300 ppm or cumulative carbon emissions exceed 1000 PgC (Loutre and Berger, 2000; Archer and Ganopolski, 2005; Cochelin et al., 2006). Only if atmospheric CO₂ content was below the pre-industrial level would a glaciation be possible under present orbital configuration (Loutre and Berger, 2000; Cochelin et al., 2006; Kutzbach et al., 2011; Vettoretti and Peltier, 2011; Tzedakis et al., 2012a). Simulations with climate–carbon cycle models show multi-millennial lifetime of the anthropogenic CO₂ in the atmosphere (see Box 6.1). Even for the lowest RCP 2.6 scenario, atmospheric CO₂ concentrations will exceed 300 ppm until the year 3000. It is therefore *virtually certain* that orbital forcing will not trigger a glacial inception before the end of the next millennium.

5.9 Concluding Remarks

The assessments in this chapter are based on a rapidly growing body of new evidence from the peer-review literature. Since AR4, there exists a wide range of new information on past changes in atmospheric composition, sea level, regional climates including droughts and floods, as well as new results from internationally coordinated model experiments on past climates (PMIP3/CMIP5). At the regional scale proxy-based temperature estimates are still scarce for key regions such as Africa, India and parts of the Americas. Syntheses of past precipitation changes were too limited to support regional assessments.

Precise knowledge of past changes in atmospheric concentrations of well-mixed GHGs prior to the period for which ice core records are available remains a strong limitation on assessing longer-term climate change. Key limitations to our knowledge of past climate continues to be associated with uncertainties of the quantitative information derived from climate proxies, in particular due to seasonality effects, the lack of proxy records sensitive to winter temperature, or the precise water depth at which ocean proxies signals form. Moreover, methodological uncertainties associated with regional, hemispheric or global syntheses need to be further investigated and quantified.

Despite progress on developing proxy records of past changes in sea ice it is not yet possible to provide quantitative and spatially coherent assessments of past sea ice cover in both polar oceans.

While this assessment could build on improved reconstructions of abrupt climate changes during glacial periods, key questions remain open regarding the underlying cause of these changes. Large uncertainties remain on the variations experienced by the West and East Antarctic ice sheets over various time scales of the past. Regarding past sea level change, major difficulties are associated with deconvolving changes in ocean geodynamic effects, as well as for inferring global signals from regional reconstructions.

The PMIP3/CMIP5 model framework offers the opportunity to directly incorporate information from paleoclimate data and simulations into assessments of future projections. This is an emerging field for which only preliminary information was available for AR5.

Acknowledgements

The compilation of this chapter has benefited greatly from the technical support by the chapter's scientific assistants Vera Bender (Germany), Hiroshi Kawamura (Germany/Japan), and Anna Peregon (France/Russian Federation). We are indebted to Hiroshi and Vera for compiling the various drafts, managing the ever-growing reference list and their skilful stylistic overhaul of figures. Anna is thanked for help with output from PMIP3 simulations, for tracking acronyms, and for identifying entries for the glossary.

References

- Abbot, D. S., and E. Tziperman, 2008: A high-latitude convective cloud feedback and equitable climates. *Q. J. R. Meteorol. Soc.*, **134**, 165–185.
- Abbot, D. S., and E. Tziperman, 2009: Controls on the activation and strength of a high-latitude convective cloud feedback. *J. Atmos. Sci.*, **66**, 519–529.
- Abe-Ouchi, A., T. Segawa, and F. Saito, 2007: Climatic Conditions for modelling the Northern Hemisphere ice sheets throughout the ice age cycle. *Clim. Past*, **3**, 423–438.
- Abram, N. J., et al., 2013: Acceleration of snow melt in an Antarctic Peninsula ice core during the twentieth century. *Nature Geosci.*, **6**, 404–411.
- Ackert Jr, R. P., S. Mukhopadhyay, D. Pollard, R. M. DeConto, A. E. Putnam, and H. W. Burns Jr, 2011: West Antarctic Ice Sheet elevations in the Ohio Range: Geologic constraints and ice sheet modeling prior to the last highstand. *Earth Planet. Sci. Lett.*, **307**, 83–93.
- Adams, J. B., M. E. Mann, and C. M. Ammann, 2003: Proxy evidence for an El Niño-like response to volcanic forcing. *Nature*, **426**, 274–278.
- Adkins, J. F., K. McIntyre, and D. P. Schrag, 2002: The salinity, temperature, and $\delta^{18}\text{O}$ of the glacial deep ocean. *Science*, **298**, 1769–1773.
- Adler, R. E., et al., 2009: Sediment record from the western Arctic Ocean with an improved Late Quaternary age resolution: HOTRAX core HLY0503–8JPC, Men-deleev Ridge. *Global Planet. Change*, **68**, 18–29.
- Agatova, A. R., A. N. Nazarov, R. K. Nepop, and H. Rodnight, 2012: Holocene glacier fluctuations and climate changes in the southeastern part of the Russian Altai (South Siberia) based on a radiocarbon chronology. *Quat. Sci. Rev.*, **43**, 74–93.
- Ahn, J., and E. J. Brook, 2008: Atmospheric CO_2 and climate on millennial time scales during the last glacial period. *Science*, **322**, 83–85.
- Ahn, J., E. J. Brook, A. Schmittner, and K. Kreutz, 2012: Abrupt change in atmospheric CO_2 during the last ice age. *Geophys. Res. Lett.*, **39**, L18711.
- Akkemik, Ü., R. D'Arrigo, P. Cherubini, N. Köse, and G. C. Jacoby, 2008: Tree-ring reconstructions of precipitation and streamflow for north-western Turkey. *Int. J. Climatol.*, **28**, 173–183.
- Alvarez-Solas, J., S. Charbit, C. Ritz, D. Paillard, G. Ramstein, and C. Dumas, 2010: Links between ocean temperature and iceberg discharge during Heinrich events. *Nature Geosci.*, **3**, 122–126.
- Ammann, C. M., and E. R. Wahl, 2007: The importance of the geophysical context in statistical evaluations of climate reconstruction procedures. *Clim. Change*, **85**, 71–88.
- Ammann, C. M., M. G. Genton, and B. Li, 2010: Technical Note: Correcting for signal attenuation from noisy proxy data in climate reconstructions. *Clim. Past*, **6**, 273–279.
- Ammann, C. M., G. A. Meehl, W. M. Washington, and C. S. Zender, 2003: A monthly and latitudinally varying volcanic forcing dataset in simulations of 20th century climate. *Geophys. Res. Lett.*, **30**, 1657.
- Ammann, C. M., F. Joos, D. S. Schimel, B. L. Otto-Bliesner, and R. A. Tomas, 2007: Solar influence on climate during the past millennium: Results from transient simulations with the NCAR Climate System Model. *Proc. Natl. Acad. Sci. U.S.A.*, **104**, 3713–3718.
- Anchukaitis, K. J., and J. E. Tierney, 2013: Identifying coherent spatiotemporal modes in time-uncertain proxy paleoclimate records. *Clim. Dyn.*, **41**, 1291–1306.
- Anchukaitis, K. J., B. M. Buckley, E. R. Cook, B. I. Cook, R. D. D'Arrigo, and C. M. Ammann, 2010: Influence of volcanic eruptions on the climate of the Asian monsoon region. *Geophys. Res. Lett.*, **37**, L22703.
- Anchukaitis, K. J., et al., 2012: Tree rings and volcanic cooling. *Nature Geosci.*, **5**, 836–837.
- Anderson, R. K., G. H. Miller, J. P. Briner, N. A. Lifton, and S. B. DeVogel, 2008: A millennial perspective on Arctic warming from ^{14}C in quartz and plants emerging from beneath ice caps. *Geophys. Res. Lett.*, **35**, L01502.
- Andersson, C., F. S. R. Pausata, E. Jansen, B. Risebrobakken, and R. J. Telford, 2010: Holocene trends in the foraminifer record from the Norwegian Sea and the North Atlantic Ocean. *Clim. Past*, **6**, 179–193.
- Andreev, A. A., et al., 2004: Late Saalian and Eemian palaeoenvironmental history of the Bol'shoy Lyakhovsky Island (Laptev Sea region, Arctic Siberia). *Boreas*, **33**, 319–348.
- Andrews, T., J. M. Gregory, M. J. Webb, and K. E. Taylor, 2012: Forcing, feedbacks and climate sensitivity in CMIP5 coupled atmosphere-ocean climate models. *Geophys. Res. Lett.*, **39**, L09712.
- Annan, J. D., and J. C. Hargreaves, 2012: Identification of climatic state with limited proxy data. *Clim. Past*, **8**, 1141–1151.
- , 2013: A new global reconstruction of temperature changes at the Last Glacial Maximum. *Clim. Past*, **9**, 367–376.
- Annan, J. D., J. C. Hargreaves, R. Ohgaito, A. Abe-Ouchi, and S. Emori, 2005: Efficiently constraining climate sensitivity with ensembles of paleoclimate simulations. *Sci. Online Lett. Atmos.*, **1**, 181–184.
- Antoine, P., et al., 2009: Rapid and cyclic aeolian deposition during the Last Glacial in European loess: a high-resolution record from Nussloch, Germany. *Quat. Sci. Rev.*, **28**, 2955–2973.
- Antoniades, D., P. Francus, R. Pienitz, G. St-Onge, and W. F. Vincent, 2011: Holocene dynamics of the Arctic's largest ice shelf. *Proc. Natl. Acad. Sci. U.S.A.*, **108**, 18899–18904.
- Anzidei, M., F. Antonioli, A. Benini, K. Lambeck, D. Sivan, E. Serpelloni, and P. Stocchi, 2011: Sea level change and vertical land movements since the last two millennia along the coasts of southwestern Turkey and Israel. *Quat. Int.*, **232**, 13–20.
- Archer, D., and A. Ganopolski, 2005: A movable trigger: Fossil fuel CO_2 and the onset of the next glaciation. *Geochem. Geophys., Geosyst.*, **6**, Q05003.
- Argus, D. F., and W. R. Peltier, 2010: Constraining models of postglacial rebound using space geodesy: A detailed assessment of model ICE-5G (VM2) and its relatives. *Geophys. J. Int.*, **181**, 697–723.
- Arz, H. W., F. Lamy, A. Ganopolski, N. Nowaczyk, and J. Pätzold, 2007: Dominant Northern Hemisphere climate control over millennial-scale glacial sea level variability. *Quat. Sci. Rev.*, **26**, 312–321.
- Arzel, O., A. Colin de Verdère, and M. H. England, 2009: The role of oceanic heat transport and wind stress forcing in abrupt millennial-scale climate transitions. *J. Clim.*, **23**, 2233–2256.
- Asmerom, Y., V. J. Polyak, and S. J. Burns, 2010: Variable winter moisture in the southwestern United States linked to rapid glacial climate shifts. *Nature Geosci.*, **3**, 114–117.
- Ault, T. R., et al., 2013: The continuum of hydroclimate variability in western North America during the last millennium. *J. Clim.*, **26**, 5863–5878.
- Auriemma, R., and E. Solinas, 2009: Archaeological remains as sea level change markers: A review. *Quat. Int.*, **206**, 134–146.
- Axelson, J. N., D. J. Sauchyn, and J. Barichivich, 2009: New reconstructions of streamflow variability in the South Saskatchewan River Basin from a network of tree ring chronologies, Alberta, Canada. *Water Resour. Res.*, **45**, W09422.
- Baker, V. R., 2008: Paleoflood hydrology: Origin, progress, prospects. *Geomorphology*, **101**, 1–13.
- Bakker, P., et al., 2013: Last interglacial temperature evolution – a model inter-comparison. *Clim. Past*, **9**, 605–619.
- Ballantyne, A. P., M. Lavine, T. J. Crowley, J. Liu, and P. B. Baker, 2005: Meta-analysis of tropical surface temperatures during the Last Glacial Maximum. *Geophys. Res. Lett.*, **32**, L05712.
- Balmaceda, L., N. A. Krivova, and S. K. Solanki, 2007: Reconstruction of solar irradiance using the Group sunspot number. *Adv. Space Res.*, **40**, 986–989.
- Bamberg, A., Y. Rosenthal, A. Paul, D. Heslop, S. Mulitza, C. Rühlemann, and M. Schulz, 2010: Reduced north Atlantic central water formation in response to early Holocene ice-sheet melting. *Geophys. Res. Lett.*, **37**, L17705.
- Bar-Matthews, M., A. Ayalon, M. Gilmour, A. Matthews, and C. J. Hawkesworth, 2003: Sea-land oxygen isotopic relationships from planktonic foraminifera and speleothems in the Eastern Mediterranean region and their implication for paleo-rainfall during interglacial intervals. *Geochim Cosmochim. Acta*, **67**, 3181–3199.
- Barber, D. C., et al., 1999: Forcing of the cold event of 8,200 years ago by catastrophic drainage of Laurentide lakes. *Nature*, **400**, 344–348.
- Bard, E., G. Raisbeck, F. Yiou, and J. Jouzel, 2000: Solar irradiance during the last 1200 years based on cosmogenic nuclides. *Tellus B*, **52**, 985–992.
- Barker, S., G. Knorr, M. J. Vautravers, P. Diz, and L. C. Skinner, 2010: Extreme deepening of the Atlantic overturning circulation during deglaciation. *Nature Geosci.*, **3**, 567–571.
- Barker, S., P. Diz, M. J. Vautravers, J. Pike, G. Knorr, I. R. Hall, and W. S. Broecker, 2009: Interhemispheric Atlantic seesaw response during the last deglaciation. *Nature*, **457**, 1097–1102.
- Barker, S., et al., 2011: 800,000 years of abrupt climate variability. *Science*, **334**, 347–351.

- Baroni, M., M. H. Thiemens, R. J. Delmas, and J. Savarino, 2007: Mass-independent sulfur isotopic compositions in stratospheric volcanic eruptions. *Science*, **315**, 84–87.
- Baroni, M., J. Savarino, J. H. Cole-Dai, V. K. Rai, and M. H. Thiemens, 2008: Anomalous sulfur isotope compositions of volcanic sulfate over the last millennium in Antarctic ice cores. *J. Geophys. Res.*, **113**, D20112.
- Barrett, P. J., 2013: Resolving views on Antarctic Neogene glacial history – the Sirius debate. *Trans. R. Soc. Edinburgh, published online 7 May 2013*, CJ02013, doi:10.1017/S175569101300008X.
- Barriendos, M., and F. S. Rodrigo, 2006: Study of historical flood events on Spanish rivers using documentary data. *Hydrol. Sci. J.*, **51**, 765–783.
- Bartlein, P. J., et al., 2011: Pollen-based continental climate reconstructions at 6 and 21 ka: A global synthesis. *Clim. Dyn.*, **37**, 775–802.
- Bartoli, G., B. Höönsch, and R. E. Zeebe, 2011: Atmospheric CO₂ decline during the Pliocene intensification of Northern Hemisphere glaciations. *Paleoceanography*, **26**, PA4213.
- Bassett, S. E., G. A. Milne, J. X. Mitrovica, and P. U. Clark, 2005: Ice sheet and solid Earth influences on far-field sea level histories. *Science*, **309**, 925–928.
- Battle, M., et al., 1996: Atmospheric gas concentrations over the past century measured in air from firn at the South Pole. *Nature*, **383**, 231–235.
- Bauch, H. A., E. S. Kandiano, J. Helmke, N. Andersen, A. Rosell-Melé, and H. Erlenkeuser, 2011: Climatic bisection of the last interglacial warm period in the Polar North Atlantic. *Quat. Sci. Rev.*, **30**, 1813–1818.
- Berleing, D. J., and D. L. Royer, 2002: Fossil plants as indicator of the Phanerozoic global carbon cycle. *Annu. Rev. Earth Planet. Sci.*, **30**, 527–556.
- Berleing, D. J., and D. L. Royer, 2011: Convergent Cenozoic CO₂ history. *Nature Geosci.*, **4**, 418–420.
- Berleing, D. J., A. Fox, and C. W. Anderson, 2009: Quantitative uncertainty analyses of ancient atmospheric CO₂ estimates from fossil leaves. *Am. J. Sci.*, **309**, 775–787.
- Berleing, D. J., B. H. Lomax, D. L. Royer, G. R. Upchurch, and L. R. Kump, 2002: An atmospheric pCO₂ reconstruction across the Cretaceous-Tertiary boundary from leaf megafossils. *Proc. Natl. Acad. Sci. U.S.A.*, **99**, 7836–7840.
- Beets, D. J., C. J. Beets, and P. Cleveringa, 2006: Age and climate of the late Saalian and early Eemian in the type-area, Amsterdam basin, The Netherlands. *Quat. Sci. Rev.*, **25**, 876–885.
- Bekryaev, R. V., I. V. Polyakov, and V. A. Alexeev, 2010: Role of polar amplification in long-term surface air temperature variations and modern Arctic warming. *J. Clim.*, **23**, 3888–3906.
- Belt, S. T., G. Massé, S. J. Rowland, M. Poulin, C. Michel, and B. LeBlanc, 2007: A novel chemical fossil of palaeo sea ice: IP₂₅. *Org. Geochem.*, **38**, 16–27.
- Benito, G., A. Díez-Herrero, and M. Fernández De Villalba, 2003a: Magnitude and frequency of flooding in the Tagus basin (Central Spain) over the last millennium. *Clim. Change*, **58**, 171–192.
- Benito, G., A. Sopeña, Y. Sánchez-Moya, M. J. Machado, and A. Pérez-González, 2003b: Palaeoflood record of the Tagus River (Central Spain) during the Late Pleistocene and Holocene. *Quat. Sci. Rev.*, **22**, 1737–1756.
- Benito, G., M. Rico, Y. Sánchez-Moya, A. Sopeña, V. R. Thorndycraft, and M. Barriendos, 2010: The impact of late Holocene climatic variability and land use change on the flood hydrology of the Guadalentín River, southeast Spain. *Global Planet. Change*, **70**, 53–63.
- Benito, G., et al., 2011: Hydrological response of a dryland ephemeral river to southern African climatic variability during the last millennium. *Quat. Res.*, **75**, 471–482.
- Bentley, M. J., C. J. Fogwill, A. M. Le Brocq, A. L. Hubbard, D. E. Sugden, T. J. Dunai, and S. P. H. T. Freeman, 2010: Deglacial history of the West Antarctic Ice Sheet in the Weddell Sea embayment: Constraints on past ice volume change. *Geology*, **38**, 411–414.
- Bereiter, B., D. Lüthi, M. Siegrist, S. Schüpbach, T. F. Stocker, and H. Fischer, 2012: Mode change of millennial CO₂ variability during the last glacial cycle associated with a bipolar marine carbon seesaw. *Proc. Natl. Acad. Sci. U.S.A.*, **109**, 9755–9760.
- Berger, A., and M. F. Loutre, 1991: Insolation values for the climate of the last 10 million years. *Quat. Sci. Rev.*, **10**, 297–317.
- Berger, A. L., 1978: Long-term variations of daily insolation and Quaternary climatic changes. *J. Atmos. Sci.*, **35**, 2362–2367.
- Berger, G. W., and P. M. Anderson, 2000: Extending the geochronometry of Arctic lake cores beyond the radiocarbon limit by using thermoluminescence. *J. Geophys. Res.*, **105**, 15439–15455.
- Berger, M., J. Brandefelt, and J. Nilsson, 2013: The sensitivity of the Arctic sea ice to orbitally induced insolation changes: a study of the mid-Holocene Paleoclimate Modelling Intercomparison Project 2 and 3 simulations. *Clim. Past*, **9**, 969–982.
- Berkelhammer, M., A. Sinha, M. Mudelsee, H. Cheng, R. L. Edwards, and K. Cannariato, 2010: Persistent multidecadal power of the Indian Summer Monsoon. *Earth Planet. Sci. Lett.*, **290**, 166–172.
- Bertrand, S., K. A. Hughen, F. Lamy, J.-B. W. Stuut, F. Torrejón, and C. B. Lange, 2012: Precipitation as the main driver of Neoglacial fluctuations of Gualas glacier, Northern Patagonian Icefield. *Clim. Past*, **8**, 519–534.
- Bhatt, U. S., et al., 2010: Circumpolar arctic tundra vegetation change is linked to sea ice decline. *Earth Interact.*, **14**, 1–20.
- Bintanja, R., R. G. Graversen, and W. Hazelgeyer, 2011: Arctic winter warming amplified by the thermal inversion and consequent low infrared cooling to space. *Nature Geosci.*, **4**, 758–761.
- Birchfield, G. E., J. Weertman, and A. T. Lunde, 1981: A paleoclimate model of northern hemisphere ice sheets. *Quat. Res.*, **15**, 126–142.
- Bird, B. W., M. B. Abbott, B. P. Finney, and B. Kutchko, 2009: A 2000 year varve-based climate record from the central Brooks Range, Alaska. *J. Paleolimnol.*, **41**, 25–41.
- Bird, B. W., M. B. Abbott, D. T. Rodbell, and M. Vuille, 2011: Holocene tropical South American hydroclimate revealed from a decadally resolved lake sediment δ¹⁸O record. *Earth Planet. Sci. Lett.*, **310**, 192–202.
- Bird, M. I., L. K. Fifield, T. S. Teh, C. H. Chang, N. Shirlaw, and K. Lambeck, 2007: An inflection in the rate of early mid-Holocene eustatic sea level rise: A new sea level curve from Singapore. *Estuar. Coast. Shelf Sci.*, **71**, 523–536.
- Bird, M. I., W. E. N. Austin, C. M. Wurster, L. K. Fifield, M. Mojtabid, and C. Sargeant, 2010: Punctuated eustatic sea level rise in the early mid-Holocene. *Geology*, **38**, 803–806.
- Bitz, C. M., J. C. H. Chiang, W. Cheng, and J. J. Barsugli, 2007: Rates of thermohaline recovery from freshwater plumes in modern, Last Glacial Maximum, and greenhouse warming climates. *Geophys. Res. Lett.*, **34**, L07708.
- Black, D. E., M. A. Abahazi, R. C. Thunell, A. Kaplan, E. J. Tappa, and L. C. Peterson, 2007: An 8-century tropical Atlantic SST record from the Cariaco Basin: Baseline variability, twentieth-century warming, and Atlantic hurricane frequency. *Paleoceanography*, **22**, PA4204.
- Blanchon, P., A. Eisenhauer, J. Fietzke, and V. Liebetrau, 2009: Rapid sea level rise and reef back-stepping at the close of the last interglacial highstand. *Nature*, **458**, 881–884.
- Blunier, T., and E. Brook, 2001: Timing of millennial-scale climate change in Antarctica and Greenland during the last glacial period. *Science*, **291**, 109–112.
- Blunier, T., J. Chappellaz, J. Schwander, B. Stauffer, and D. Raynaud, 1995: Variations in atmospheric methane concentration during the Holocene epoch. *Nature*, **374**, 46–49.
- Blunier, T., R. Spahni, J. M. Barnola, J. Chappellaz, L. Louergue, and J. Schwander, 2007: Synchronization of ice core records via atmospheric gases. *Clim. Past*, **3**, 325–330.
- Blunier, T., et al., 1997: Timing of the Antarctic cold reversal and the atmospheric CO₂ increase with respect to the Younger Dryas event. *Geophys. Res. Lett.*, **24**, 2683–2686.
- Bonelli, S., S. Charbit, M. Kageyama, M. N. Woillez, G. Ramstein, C. Dumas, and A. Quiquet, 2009: Investigating the evolution of major Northern Hemisphere ice sheets during the last glacial-interglacial cycle. *Clim. Past*, **5**, 329–345.
- Böning, C. W., A. Dispert, M. Visbeck, S. R. Rintoul, and F. U. Schwarzkopf, 2008: The response of the Antarctic Circumpolar Current to recent climate change. *Nature Geosci.*, **1**, 864–869.
- Boninsegna, J. A., et al., 2009: Dendroclimatological reconstructions in South America: A review. *Palaeogeography, Palaeoclimatology, Palaeoecology*, **281**, 210–228.
- Bonnet, S., A. de Vernal, C. Hillaire-Marcel, T. Radi, and K. Husum, 2010: Variability of sea-surface temperature and sea-ice cover in the Fram Strait over the last two millennia. *Mar. Micropaleontol.*, **74**, 59–74.
- Born, A., and K. H. Nisancioglu, 2012: Melting of Northern Greenland during the last interglaciation. *Cryosphere*, **6**, 1239–1250.
- Born, A., K. Nisancioglu, and P. Braconnot, 2010: Sea ice induced changes in ocean circulation during the Eemian. *Clim. Dyn.*, **35**, 1361–1371.
- Bostock, H. C., et al., 2013: A review of the Australian–New Zealand sector of the Southern Ocean over the last 30 ka (Aus-INTIMATE project). *Quat. Sci. Rev.*, **74**, 35–57.
- Boucher, É., J. Guiot, and E. Chapron, 2011: A millennial multi-proxy reconstruction of summer PDSI for Southern South America. *Clim. Past*, **7**, 957–974.

- Boucher, O., and M. Pham, 2002: History of sulfate aerosol radiative forcings. *Geophys. Res. Lett.*, **29**, 22–1–22–4.
- Bowerman, N. D., and D. H. Clark, 2011: Holocene glaciation of the central Sierra Nevada, California. *Quat. Sci. Rev.*, **30**, 1067–1085.
- Bozuyik, A., M. Steinacher, F. Joos, T. F. Stocker, and L. Menviel, 2011: Fingerprints of changes in the terrestrial carbon cycle in response to large reorganizations in ocean circulation. *Clim. Past*, **7**, 319–338.
- Braconnot, P., Y. Luan, S. Brewer, and W. Zheng, 2012a: Impact of Earth's orbit and freshwater fluxes on Holocene climate mean seasonal cycle and ENSO characteristics. *Clim. Dyn.*, **38**, 1081–1092.
- Braconnot, P., C. Marzin, L. Grégoire, E. Mosquet, and O. Martí, 2008: Monsoon response to changes in Earth's orbital parameters: comparisons between simulations of the Eemian and of the Holocene. *Clim. Past*, **4**, 281–294.
- Braconnot, P., et al., 2012b: Evaluation of climate models using palaeoclimatic data. *Nature Clim. Change*, **2**, 417–424.
- Braconnot, P., et al., 2007: Results of PMIP2 coupled simulations of the mid-Holocene and Last Glacial Maximum - Part 1: experiments and large-scale features. *Clim. Past*, **3**, 261–277.
- Bradley, S. L., M. Siddall, G. A. Milne, V. Masson-Delmotte, and E. Wolff, 2012: Where might we find evidence of a Last Interglacial West Antarctic Ice Sheet collapse in Antarctic ice core records? *Global Planet. Change*, **88–89**, 64–75.
- Bradley, S. L., M. Siddall, G. A. Milne, V. Masson-Delmotte, and E. Wolff, 2013: Combining ice core records and ice sheet models to explore the evolution of the East Antarctic Ice sheet during the Last Interglacial period. *Global Planet. Change*, **100**, 278–290.
- Brady, E. C., B. L. Otto-Bliesner, J. E. Kay, and N. Rosenbloom, 2013: Sensitivity to Glacial Forcing in the CCSM4. *J. Clim.*, **26**, 1901–1925.
- Braganza, K., J. L. Gergis, S. B. Power, J. S. Risbey, and A. M. Fowler, 2009: A multi-proxy index of the El Niño–Southern Oscillation, A.D. 1525–1982. *J. Geophys. Res.*, **114**, D05106.
- Braun, H., and J. Kurths, 2010: Were Dansgaard-Oeschger events forced by the Sun? *Eur. Phys. J. Special Top.*, **191**, 117–129.
- Braun, H., P. Ditlevsen, and D. R. Chialvo, 2008: Solar forced Dansgaard-Oeschger events and their phase relation with solar proxies. *Geophys. Res. Lett.*, **35**, L06703.
- Brázdil, R., Z. W. Kundzewicz, and G. Benito, 2006: Historical hydrology for studying flood risk in Europe. *Hydrol. Sci. J.*, **51**, 739–764.
- Brázdil, R., C. Pfister, H. Wanner, H. von Storch, and J. Luterbacher, 2005: Historical climatology in Europe —The state of the art. *Clim. Change*, **70**, 363–430.
- Brázdil, R., Z. W. Kundzewicz, G. Benito, G. Demaree, N. MacDonald, and L. A. Roald, 2012: Historical floods in Europe in the past millennium. In: *Changes of Flood Risk in Europe* [Z. W. Kundzewicz (ed.)]. CRC Press, Boca Raton, FL, USA, pp. 121–166.
- Breecker, D. O., Z. D. Sharp, and L. D. McFadden, 2010: Atmospheric CO₂ concentrations during ancient greenhouse climates were similar to those predicted for A.D. 2100. *Proc. Natl. Acad. Sci. U.S.A.*, **107**, 576–580.
- Bretagnon, P., and G. Francou, 1988: Planetary theories in rectangular and spherical variables - VSOP 87 solutions. *Astronomy & Astrophysics*, **202**, 309–315.
- Brewer, S., J. Guiot, and F. Torre, 2007: Mid-Holocene climate change in Europe: A data-model comparison. *Clim. Past*, **3**, 499–512.
- Briffa, K. R., and T. M. Melvin, 2011: A closer look at Regional Curve Standardization of tree-ring records: Justification of the need, a warning of some pitfalls, and suggested improvements in its application. In: *Dendroclimatology: Progress and Prospects* [M. K. Hughes, H. F. Diaz, and T. W. Swetnam (eds.)]. Springer Science+Business Media, Dordrecht, the Netherlands, pp. 113–145.
- Briffa, K. R., F. H. Schweingruber, P. D. Jones, T. J. Osborn, S. G. Shiyatov, and E. A. Vaganov, 1998: Reduced sensitivity of recent tree-growth to temperature at high northern latitudes. *Nature*, **391**, 678–682.
- Briffa, K. R., T. J. Osborn, F. H. Schweingruber, I. C. Harris, P. D. Jones, S. G. Shiyatov, and E. A. Vaganov, 2001: Low-frequency temperature variations from a northern tree ring density network. *J. Geophys. Res.*, **106**, 2929–2941.
- Briner, J. P., H. A. M. Stewart, N. E. Young, W. Philipps, and S. Losee, 2010: Using proglacial-threshold lakes to constrain fluctuations of the Jakobshavn Isbræ ice margin, western Greenland, during the Holocene. *Quat. Sci. Rev.*, **29**, 3861–3874.
- Brohan, P., R. Allan, E. Freeman, D. Wheeler, C. Wilkinson, and F. Williamson, 2012: Constraining the temperature history of the past millennium using early instrumental observations. *Clim. Past*, **8**, 1551–1563.
- Bromwich, D. H., J. P. Nicolas, A. J. Monaghan, M. A. Lazzara, L. M. Keller, G. A. Weidner, and A. B. Wilson, 2013: Central West Antarctica among the most rapidly warming regions on Earth. *Nature Geosci.*, **6**, 139–145.
- Brovkin, V., J.-H. Kim, M. Hofmann, and R. Schneider, 2008: A lowering effect of reconstructed Holocene changes in sea surface temperatures on the atmospheric CO₂ concentration. *Global Biogeochem. Cycles*, **22**, GB1016.
- Buckley, B. M., et al., 2010: Climate as a contributing factor in the demise of Angkor, Cambodia. *Proc. Natl. Acad. Sci. U.S.A.*, **107**, 6748–6752.
- Büntgen, U., D. C. Frank, D. Nievergelt, and J. Esper, 2006: Summer temperature variations in the European Alps, AD 755–2004. *J. Clim.*, **19**, 5606–5623.
- Büntgen, U., J. Esper, D. Frank, K. Nicolussi, and M. Schmidhalter, 2005: A 1052-year tree-ring proxy for Alpine summer temperatures. *Clim. Dyn.*, **25**, 141–153.
- Büntgen, U., D. Frank, R. Wilson, M. Carrer, C. Urbaniati, and J. Esper, 2008: Testing for tree-ring divergence in the European Alps. *Global Change Biol.*, **14**, 2443–2453.
- Büntgen, U., et al., 2011a: Causes and consequences of past and projected Scandinavian summer temperatures, 500–2100 AD. *PLoS ONE*, **6**, e25133.
- Büntgen, U., et al., 2011b: 2500 years of european climate variability and human susceptibility. *Science*, **331**, 578–582.
- Bürger, G., 2007: Comment on "The spatial extent of 20th-century warmth in the context of the past 1200 years". *Science*, **316**, 1844a.
- Cahalan, R. F., G. Wen, J. W. Harder, and P. Pilewskie, 2010: Temperature responses to spectral solar variability on decadal time scales. *Geophys. Res. Lett.*, **37**, L07705.
- Cai, Y. J., et al., 2010: The variation of summer monsoon precipitation in central China since the last deglaciation. *Earth Planet. Sci. Lett.*, **291**, 21–31.
- Caillan, N., J. P. Severinghaus, J. Jouzel, J.-M. Barnola, J. Kang, and V. Y. Lipenkov, 2003: Timing of atmospheric CO₂ and Antarctic temperature changes across Termination III. *Science*, **299**, 1728–1731.
- Calenda, G., C. P. Mancini, and E. Volpi, 2005: Distribution of the extreme peak floods of the Tiber River from the XV century. *Adv. Water Resour.*, **28**, 615–625.
- Calov, R., and A. Ganopolski, 2005: Multistability and hysteresis in the climate-cryosphere system under orbital forcing. *Geophys. Res. Lett.*, **32**, L21717.
- Calov, R., A. Ganopolski, V. Petoukhov, M. Claussen, and R. Greve, 2002: Large-scale instabilities of the Laurentide ice sheet simulated in a fully coupled climate-system model. *Geophys. Res. Lett.*, **29**, 2216.
- Calov, R., et al., 2010: Results from the Ice-Sheet Model Intercomparison Project—Heinrich Event INtercOmparison (ISMIP HEINO). *J. Glaciol.*, **56**, 371–383.
- Camuffo, D., and S. Enzi, 1996: The analysis of two bi-millenary series: Tiber and Po river floods. In: *Climatic Variations and Forcing Mechanisms of the Last 2000 Years* [P. D. Jones, R. S. Bradley, and J. Jouzel (eds.)]. Springer-Verlag, Heidelberg, Germany, and New York, NY, USA, pp. 433–450.
- Candy, I., G. R. Coope, J. R. Lee, S. A. Parfitt, R. C. Preece, J. Rose, and D. C. Schreve, 2010: Pronounced warmth during early Middle Pleistocene interglacials: Investigating the Mid-Brunhes Event in the British terrestrial sequence. *Earth Sci. Rev.*, **103**, 183–196.
- Capron, E., et al., 2012: A global picture of the first abrupt climatic event occurring during the last glacial inception. *Geophys. Res. Lett.*, **39**, L15703.
- Capron, E., et al., 2010a: Synchronising EDML and NorthGRIP ice cores using δ¹⁸O of atmospheric oxygen (δ¹⁸O_{atm}) and CH₄ measurements over MIS5 (80–123 kyr). *Quat. Sci. Rev.*, **29**, 222–234.
- Capron, E., et al., 2010b: Millennial and sub-millennial scale climatic variations recorded in polar ice cores over the last glacial period. *Clim. Past*, **6**, 345–365.
- Carlson, A. E., P. U. Clark, G. M. Raisbeck, and E. J. Brook, 2007: Rapid Holocene deglaciation of the Labrador sector of the Laurentide Ice Sheet. *J. Clim.*, **20**, 5126–5133.
- Carlson, A. E., D. J. Ullman, F. S. Anslow, F. He, P. U. Clark, Z. Liu, and B. L. Otto-Bliesner, 2012: Modeling the surface mass-balance response of the Laurentide Ice Sheet to Bolling warming and its contribution to Meltwater Pulse 1A. *Earth Planet. Sci. Lett.*, **315–316**, 24–29.
- Cerling, T. E., 1992: Use of carbon isotopes in paleosols as an indicator of the pCO₂ of the paleoatmosphere. *Global Biogeochem. Cycles*, **6**, 307–314.
- Chappell, J., 1983: Evidence for smoothly falling sea level relative to north Queensland, Australia, during the past 6,000 yr. *Nature*, **302**, 406–408.
- Chappell, J., 2002: Sea level changes forced ice breakouts in the Last Glacial cycle: new results from coral terraces. *Quat. Sci. Rev.*, **21**, 1229–1240.
- Charbit, S., D. Paillard, and G. Ramstein, 2008: Amount of CO₂ emissions irreversibly leading to the total melting of Greenland. *Geophys. Res. Lett.*, **35**, L12503.
- Chavaillaz, Y., F. Codron, and M. Kageyama, 2013: Southern Westerlies in LGM and future (RCP4.5) climates. *Clim. Past*, **9**, 517–524.

- Chen, J. H., H. A. Curran, B. White, and G. J. Wasserburg, 1991: Precise chronology of the last interglacial period: ^{234}U - ^{230}Th data from fossil coral reefs in the Bahamas. *Geol. Soc. Am. Bull.*, **103**, 82–97.
- Cheng, H., et al., 2009: Ice Age Terminations. *Science*, **326**, 248–252.
- Chiessi, C. M., S. Mulitza, J. Pätzold, G. Wefer, and J. A. Marengo, 2009: Possible impact of the Atlantic Multidecadal Oscillation on the South American summer monsoon. *Geophys. Res. Lett.*, **36**, L21707.
- Christiansen, B., 2011: Reconstructing the NH mean temperature: Can underestimation of trends and variability be avoided? *J. Clim.*, **24**, 674–692.
- Christiansen, B., and F. C. Ljungqvist, 2012: The extra-tropical Northern Hemisphere temperature in the last two millennia: Reconstructions of low-frequency variability. *Clim. Past*, **8**, 765–786.
- Christiansen, B., T. Schmitt, and P. Thejll, 2009: A surrogate ensemble study of climate reconstruction methods: stochasticity and robustness. *J. Clim.*, **22**, 951–976.
- Chu, G., et al., 2011: Seasonal temperature variability during the past 1600 years recorded in historical documents and varved lake sediment profiles from northeastern China. *Holocene*, **22**, 785–792.
- Chylek, P., C. K. Folland, G. Lesins, M. K. Dubey, and M. Wang, 2009: Arctic air temperature change amplification and the Atlantic Multidecadal Oscillation. *Geophys. Res. Lett.*, **36**, L14801.
- Clague, J. J., J. Koch, and M. Geertsema, 2010: Expansion of outlet glaciers of the Juneau Icefield in northwest British Columbia during the past two millennia. *Holocene*, **20**, 447–461.
- Claquin, T., et al., 2003: Radiative forcing of climate by ice-age atmospheric dust. *Clim. Dyn.*, **20**, 193–202.
- Clark, P. U., and D. Pollard, 1998: Origin of the middle Pleistocene transition by ice sheet erosion of regolith. *Paleoceanography*, **13**, 1–9.
- Clark, P. U., J. X. Mitrovica, G. A. Milne, and M. E. Tamisiea, 2002: Sea level fingerprinting as a direct test for the source of global meltwater pulse IA. *Science*, **295**, 2438–2441.
- Clark, P. U., et al., 2009: The Last Glacial Maximum. *Science*, **325**, 710–714.
- Clarke, G. K. C., D. W. Leverington, J. T. Teller, and A. S. Dyke, 2004: Paleohydraulics of the last outburst flood from glacial Lake Agassiz and the 8200 BP cold event. *Quat. Sci. Rev.*, **23**, 389–407.
- Clemens, S. C., W. L. Prell, and Y. Sun, 2010: Orbital-scale timing and mechanisms driving late Pleistocene Indo-Asian summer monsoons: reinterpreting cave speleothem $\delta^{18}\text{O}$. *Paleoceanography*, **25**, PA4207.
- Clement, A. C., and L. C. Peterson, 2008: Mechanisms of abrupt climate change of the last glacial period. *Rev. Geophys.*, **46**, RG4002.
- CLIMAP Project Members, 1976: The surface of the Ice-Age Earth. *Science*, **191**, 1131–1137.
- CLIMAP Project Members, 1981: Seasonal reconstructions of the earth's surface at the last glacial maximum. *Geol. Soc. Am., MC-36*.
- Cobb, K. M., et al., 2013: Highly variable El Niño-Southern Oscillation throughout the Holocene. *Science*, **339**, 67–70.
- Cochelin, A.-S. B., L. A. Mysak, and Z. Wang, 2006: Simulation of long-term future climate changes with the green McGill paleoclimate model: The next glacial inception. *Clim. Change*, **79**, 381–401.
- COHMAP Members, 1988: Climatic changes of the last 18,000 years: observations and model simulations. *Science*, **241**, 1043–1052.
- Cole-Dai, J., D. Ferris, A. Lanciki, J. Savarino, M. Baroni, and M. Thiemens, 2009: Cold decade (AD 1810–1819) caused by Tambora (1815) and another (1809) stratospheric volcanic eruption. *Geophys. Res. Lett.*, **36**, L22703.
- Colville, E. J., A. E. Carlson, B. L. Beard, R. G. Hatfield, J. S. Stoner, A. V. Reyes, and D. J. Ullman, 2011: Sr-Nd-Pb isotope evidence for ice-sheet presence on southern Greenland during the Last Interglacial. *Science*, **333**, 620–623.
- Cook, E. R., R. D. D'Arrigo, and M. E. Mann, 2002: A well-verified, multiproxy reconstruction of the winter North Atlantic Oscillation index since AD 1400. *J. Clim.*, **15**, 1754–1764.
- Cook, E. R., C. A. Woodhouse, C. M. Eakin, D. M. Meko, and D. W. Stahle, 2004: Long-term aridity changes in the western United States. *Science*, **306**, 1015–1018.
- Cook, E. R., K. J. Anchukaitis, B. M. Buckley, R. D. D'Arrigo, G. C. Jacoby, and W. E. Wright, 2010a: Asian Monsoon Failure and Megadrought During the Last Millennium. *Science*, **328**, 486–489.
- Cook, E. R., R. Seager, R. R. Heim Jr, R. S. Vose, C. Herweijer, and C. Woodhouse, 2010b: Megadroughts in North America: placing IPCC projections of hydroclimatic change in a long-term palaeoclimate context. *J. Quat. Sci.*, **25**, 48–61.
- Cook, E. R., P. J. Krusic, K. J. Anchukaitis, B. M. Buckley, T. Nakatsuka, and M. Sano, 2012: Tree-ring reconstructed summer temperature anomalies for temperate East Asia since 800 C.E. *Clim. Dyn.*, doi:10.1007/s00382-012-1611-x, 1–16, published online 5 December 2012.
- Cook, E. R., B. M. Buckley, J. G. Palmer, P. Fenwick, M. J. Peterson, G. Boswijk, and A. Fowler, 2006: Millennia-long tree-ring records from Tasmania and New Zealand: A basis for modelling climate variability and forcing, past, present and future. *J. Quat. Sci.*, **21**, 689–699.
- Cook, K. H., and I. M. Held, 1988: Stationary Waves of the Ice Age Climate. *J. Clim.*, **1**, 807–819.
- Cooper, R. J., T. M. Melvin, I. Tyers, R. J. S. Wilson, and K. R. Briffa, 2013: A tree-ring reconstruction of East Anglian (UK) hydroclimate variability over the last millennium. *Clim. Dyn.*, **40**, 1019–1039.
- Cornes, R. C., P. D. Jones, K. R. Briffa, and T. J. Osborn, 2012: Estimates of the North Atlantic Oscillation back to 1692 using a Paris-London westerly index. *Int. J. Climatol.*, **32**, 1135–1150.
- Corona, C., J. Guiot, J.-L. Edouard, F. Chalie, U. Büntgen, P. Nola, and C. Urbaniati, 2010: Millennium-long summer temperature variations in the European Alps as reconstructed from tree rings. *Clim. Past*, **6**, 379–400.
- Corona, C., J.-L. Edouard, F. Guibal, J. Guiot, S. Bernard, A. Thomas, and N. Denelle, 2011: Long-term summer (AD 751–2008) temperature fluctuation in the French Alps based on tree-ring data. *Boreas*, **40**, 351–366.
- Cortese, G., A. Abelmann, and R. Gersonde, 2007: The last five glacial-interglacial transitions: A high-resolution 450,000-year record from the subantarctic Atlantic. *Paleoceanography*, **22**, PA4203.
- Cramer, B. S., K. G. Miller, P. J. Barrett, and J. D. Wright, 2011: Late Cretaceous-Neogene trends in deep ocean temperature and continental ice volume: Reconciling records of benthic foraminiferal geochemistry ($\delta^{18}\text{O}$ and Mg/Ca) with sea level history. *J. Geophys. Res.*, **116**, C12023.
- Crespin, E., H. Goosse, T. Fichefet, and M. E. Mann, 2009: The 15th century Arctic warming in coupled model simulations with data assimilation. *Clim. Past*, **5**, 389–401.
- Cronin, T. M., P. R. Vogt, D. A. Willard, R. Thunell, J. Halka, M. Berke, and J. Pohlman, 2007: Rapid sea level rise and ice sheet response to 8,200-year climate event. *Geophys. Res. Lett.*, **34**, L20603.
- Crouch, A. D., P. Charbonneau, G. Beaubien, and D. Paquin-Ricard, 2008: A model for the total solar irradiance based on active region decay. *Astrophys. J.*, **677**, 723–741.
- Crowley, T. J., 2000: Causes of Climate Change Over the Past 1000 Years. *Science*, **289**, 270–277.
- Crowley, T. J., and M. B. Unterman, 2013: Technical details concerning development of a 1200-year proxy index for global volcanism. *Earth Syst. Sci. Data*, **5**, 187–197.
- Crowley, T. J., S. K. Baum, K.-Y. Kim, G. C. Hegerl, and W. T. Hyde, 2003: Modeling ocean heat content changes during the last millennium. *Geophys. Res. Lett.*, **30**, 1932.
- Crucifix, M., 2006: Does the Last Glacial Maximum constrain climate sensitivity? *Geophys. Res. Lett.*, **33**, L18701.
- Cruz, F. W., et al., 2005: Insolation-driven changes in atmospheric circulation over the past 116,000 years in subtropical Brazil. *Nature*, **434**, 63–66.
- Cruz, F. W., et al., 2009: Orbitally driven east-west antiphasing of South American precipitation. *Nature Geosci.*, **2**, 210–214.
- Cuffey, K. M., G. D. Clow, R. B. Alley, M. Stuiver, E. D. Waddington, and R. W. Saltus, 1995: Large Arctic temperature change at the Wisconsin-Holocene glacial transition. *Science*, **270**, 455–458.
- Cunningham, L. K., et al., 2013: Reconstructions of surface ocean conditions from the northeast Atlantic and Nordic seas during the last millennium. *Holocene*, **23**, 921–935.
- Curry, J. A., J. L. Schramm, and E. E. Ebert, 1995: Sea ice-albedo climate feedback mechanism. *J. Clim.*, **8**, 240–247.
- D'Arrigo, R., R. Wilson, and G. Jacoby, 2006: On the long-term context for late twentieth century warming. *J. Geophys. Res.*, **111**, D03103.
- D'Arrigo, R., R. Wilson, B. Liepert, and P. Cherubini, 2008: On the 'Divergence Problem' in Northern Forests: A review of the tree-ring evidence and possible causes. *Global Planet. Change*, **60**, 289–305.
- D'Arrigo, R., E. R. Cook, R. J. Wilson, R. Allan, and M. E. Mann, 2005: On the variability of ENSO over the past six centuries. *Geophys. Res. Lett.*, **32**, L03711.
- D'Arrigo, R., et al., 2009: Tree growth and inferred temperature variability at the North American Arctic treeline. *Global Planet. Change*, **65**, 71–82.

- Dahl-Jensen, D., K. Mosegaard, N. Gundestrup, G. D. Clow, S. J. Johnsen, A. W. Hansen, and N. Balling, 1998: Past temperatures directly from the Greenland Ice Sheet. *Science*, **282**, 268–271.
- Daley, T. J., et al., 2011: The 8200 yr BP cold event in stable isotope records from the North Atlantic region. *Global Planet. Change*, **79**, 288–302.
- Davis, P. T., B. Menounos, and G. Osborn, 2009: Holocene and latest Pleistocene alpine glacier fluctuations: A global perspective. *Quat. Sci. Rev.*, **28**, 2021–2238.
- De Angelis, H., and P. Skvarca, 2003: Glacier surge after ice shelf collapse. *Science*, **299**, 1560–1562.
- De Deckker, P., M. Moros, K. Perner, and E. Jansen, 2012: Influence of the tropics and southern westerlies on glacial interhemispheric asymmetry. *Nature Geosci.*, **5**, 266–269.
- De Deckker, P., M. Norman, I. D. Goodwin, A. Wain, and F. X. Gingele, 2010: Lead isotopic evidence for an Australian source of aeolian dust to Antarctica at times over the last 170,000 years. *Palaeogeogr. Palaeoclimatol. Palaeoecol.*, **285**, 205–223.
- de Garidel-Thoron, T., Y. Rosenthal, L. Beaufort, E. Bard, C. Sonzogni, and A. C. Mix, 2007: A multiproxy assessment of the western equatorial Pacific hydrography during the last 30 kyr. *Paleoceanography*, **22**, PA3204.
- de Vernal, A., et al., 2006: Comparing proxies for the reconstruction of LGM sea-surface conditions in the northern North Atlantic. *Quat. Sci. Rev.*, **25**, 2820–2834.
- DeConto, R. M., and D. Pollard, 2003: Rapid Cenozoic glaciation of Antarctica induced by declining atmospheric CO₂. *Nature*, **421**, 245–249.
- DeConto, R. M., et al., 2012: Past extreme warming events linked to massive carbon release from thawing permafrost. *Nature*, **484**, 87–91.
- Delague, G., and E. Bard, 2011: An Antarctic view of Beryllium-10 and solar activity for the past millennium. *Clim. Dyn.*, **36**, 2201–2218.
- DeLong, K. L., T. M. Quinn, F. W. Taylor, K. Lin, and C.-C. Shen, 2012: Sea surface temperature variability in the southwest tropical Pacific since AD 1649. *Nature Clim. Change*, **2**, 799–804.
- Delworth, T. L., and M. E. Mann, 2000: Observed and simulated multidecadal variability in the Northern Hemisphere. *Clim. Dyn.*, **16**, 661–676.
- Denis, D., X. Crosta, L. Barbara, G. Massé, H. Renssen, O. Ther, and J. Giradeau, 2010: Sea ice and wind variability during the Holocene in East Antarctica: insight on middle–high latitude coupling. *Quat. Sci. Rev.*, **29**, 3709–3719.
- Derbyshire, E., 2003: Loess, and the dust indicators and records of terrestrial and marine palaeoenvironments (DIRTMAP) database. *Quat. Sci. Rev.*, **22**, 1813–1819.
- Deschamps, P., et al., 2012: Ice-sheet collapse and sea level rise at the Bølling warming 14,600 years ago. *Nature*, **483**, 559–564.
- Diaz, H. F., R. M. Trigo, M. K. Hughes, M. E. Mann, E. Xoplaki, and D. Barriopedro, 2011: Spatial and temporal characteristics of Climate in medieval times revisited. *Bull. Am. Meteorol. Soc.*, **92**, 1487–1500.
- Diffenbaugh, N. S., M. Ashfaq, B. Shuman, J. W. Williams, and P. J. Bartlein, 2006: Summer aridity in the United States: Response to mid-Holocene changes in insolation and sea surface temperature. *Geophys. Res. Lett.*, **33**, L22712.
- DiNezio, P. N., A. Clement, G. A. Vecchi, B. Soden, A. J. Broccoli, B. L. Otto-Btiesner, and P. Braconnot, 2011: The response of the Walker circulation to Last Glacial Maximum forcing: Implications for detection in proxies. *Paleoceanography*, **26**, PA3217.
- Ditlevsen, P. D., and O. D. Ditlevsen, 2009: On the stochastic nature of the rapid climate shifts during the Last Ice Age. *J. Clim.*, **22**, 446–457.
- Divine, D. V., and C. Dick, 2006: Historical variability of sea ice edge position in the Nordic Seas. *J. Geophys. Res.*, **111**, C01001.
- Dolan, A. M., A. M. Haywood, D. J. Hill, H. J. Dowsett, S. J. Hunter, D. J. Lunt, and S. J. Pickering, 2011: Sensitivity of Pliocene ice sheets to orbital forcing. *Palaeogeogr. Palaeoclimatol. Palaeoecol.*, **309**, 98–110.
- Donnelly, J. P., P. Cleary, P. Newby, and R. Ettinger, 2004: Coupling instrumental and geological records of sea level change: Evidence from southern New England of an increase in the rate of sea level rise in the late 19th century. *Geophys. Res. Lett.*, **31**, L05203.
- Doria, G., D. L. Royer, A. P. Wolfe, A. Fox, J. A. Westgate, and D. J. Beerling, 2011: Declining atmospheric CO₂ during the late Middle Eocene climate transition. *Am. J. Sci.*, **311**, 63–75.
- Dowsett, H. J., M. M. Robinson, and K. M. Foley, 2009: Pliocene three-dimensional global ocean temperature reconstruction. *Clim. Past*, **5**, 769–783.
- Dowsett, H. J., et al., 2012: Assessing confidence in Pliocene sea surface temperatures to evaluate predictive models. *Nature Clim. Change*, **2**, 365–371.
- Dreimanis, A., 1992: Transition from the Sangamon interglaciation to the Wisconsin glaciation along the southeastern margin of the Laurentide Ice Sheet, North America. In: *Start of a Glacial, NATO ASI Series*, **13** [G. T. Kukla, and E. Went (eds.)]. Springer-Verlag, Heidelberg, Germany, and New York, NY, USA, pp. 225–251.
- Duplessy, J.-C., L. Labeyrie, and C. Waelbroeck, 2002: Constraints on the ocean oxygen isotopic enrichment between the Last Glacial Maximum and the Holocene: Paleoceanographic implications. *Quat. Sci. Rev.*, **21**, 315–330.
- Dutton, A., and K. Lambeck, 2012: Ice volume and sea level during the Last Interglacial. *Science*, **337**, 216–219.
- Dwyer, G. S., and M. A. Chandler, 2009: Mid-Pliocene sea level and continental ice volume based on coupled benthic Mg/Ca palaeotemperatures and oxygen isotopes. *Philos. Trans. R. Soc. London A*, **367**, 157–168.
- Dwyer, G. S., T. M. Cronin, P. A. Baker, and J. Rodriguez-Lazaro, 2000: Changes in North Atlantic deep-sea temperature during climatic fluctuations of the last 25,000 years based on ostracode Mg/Ca ratios. *Geochim. Geophys. Geosyst.*, **1**, 1028.
- Edwards, T. L., M. Crucifix, and S. P. Harrison, 2007: Using the past to constrain the future: How the palaeorecord can improve estimates of global warming. *Prog. Phys. Geogr.*, **31**, 481–500.
- Ekart, D. D., T. E. Cerling, I. P. Montanez, and N. J. Tabor, 1999: A 400 million year carbon isotope record of pedogenic carbonate; implications for paleoatmospheric carbon dioxide. *Am. J. Sci.*, **299**, 805–827.
- Elderfield, H., P. Ferretti, M. Greaves, S. Crowhurst, I. N. McCave, D. Hodell, and A. M. Piotrowski, 2012: Evolution of ocean temperature and ice volume through the mid-Pleistocene climate transition. *Science*, **337**, 704–709.
- Elderfield, H., et al., 2010: A record of bottom water temperature and seawater δ¹⁸O for the Southern Ocean over the past 440 kyr based on Mg/Ca of benthic foraminiferal *Uvigerina* spp. *Quat. Sci. Rev.*, **29**, 160–169.
- Ellison, C. R. W., M. R. Chapman, and I. R. Hall, 2006: Surface and deep ocean interactions during the cold climate event 8200 years ago. *Science*, **312**, 1929–1932.
- Ely, L. L., Y. Enzel, V. R. Baker, and D. R. Cayan, 1993: A 5000-year record of extreme floods and climate change in the southwestern United States. *Science*, **262**, 410–412.
- Emile-Geay, J., K. M. Cobb, M. E. Mann, and A. T. Wittenberg, 2013a: Estimating central equatorial Pacific SST variability over the past millennium. Part I: Methodology and validation. *J. Clim.*, **26**, 2302–2328.
- Emile-Geay, J., K. M. Cobb, M. E. Mann, and A. T. Wittenberg, 2013b: Estimating central equatorial Pacific SST variability over the past millennium. Part II: Reconstructions and implications. *J. Clim.*, **26**, 2329–2352.
- England, J. H., T. R. Lakeman, D. S. Lemmen, J. M. Bednarski, T. G. Stewart, and D. J. A. Evans, 2008: A millennial-scale record of Arctic Ocean sea ice variability and the demise of the Ellesmere Island ice shelves. *Geophys. Res. Lett.*, **35**, L19502.
- EPICA Community Members, 2006: One-to-one coupling of glacial climate variability in Greenland and Antarctica. *Nature*, **444**, 195–198.
- Esper, J., and D. Frank, 2009: Divergence pitfalls in tree-ring research. *Clim. Change*, **94**, 261–266.
- Esper, J., U. Büntgen, M. Timonen, and D. C. Frank, 2012a: Variability and extremes of northern Scandinavian summer temperatures over the past two millennia. *Global Planet. Change*, **88–89**, 1–9.
- Esper, J., U. Büntgen, J. Luterbacher, and P. J. Krusic, 2013: Testing the hypothesis of globally missing rings in temperature sensitive dendrochronological data. *Dendrochronologia*, **31**, 216–222.
- Esper, J., D. Frank, R. Wilson, U. Büntgen, and K. Treydte, 2007a: Uniform growth trends among central Asian low- and high-elevation juniper tree sites. *Trees*, **21**, 141–150.
- Esper, J., D. Frank, U. Büntgen, A. Verstege, J. Luterbacher, and E. Xoplaki, 2007b: Long-term drought severity variations in Morocco. *Geophys. Res. Lett.*, **34**, L17702.
- Esper, J., D. Frank, U. Büntgen, A. Verstege, R. M. Hantemirov, and A. V. Kirdyanov, 2010: Trends and uncertainties in Siberian indicators of 20th century warming. *Global Change Biol.*, **16**, 386–398.
- Esper, J., et al., 2012b: Orbital forcing of tree-ring data. *Nature Clim. Change*, **2**, 862–866.
- Etheridge, D. M., L. P. Steele, R. J. Francey, and R. L. Langenfelds, 1998: Atmospheric methane between 1000 A.D. and present: Evidence of anthropogenic emissions and climatic variability. *J. Geophys. Res.*, **103**, 15979–15993.

- Etheridge, D. M., L. P. Steele, R. L. Langenfelds, R. J. Franney, J. M. Barnola, and V. I. Morgan, 1996: Natural and anthropogenic changes in atmospheric CO₂ over the last 1000 years from air in Antarctic ice and firn. *J. Geophys. Res.*, **101**, 4115–4128.
- Euler, C., and U. S. Ninnemann, 2010: Climate and Antarctic Intermediate Water coupling during the late Holocene. *Geology*, **38**, 647–650.
- Fairbanks, R. G., 1989: A 17,000 year glacio-eustatic sea level record: Influence of glacial melting rates on the Younger Dryas event and deep ocean circulation. *Nature*, **342**, 637–642.
- Fan, F. X., M. E. Mann, and C. M. Ammann, 2009: Understanding changes in the Asian summer monsoon over the past millennium: Insights from a long-term coupled model simulation. *J. Clim.*, **22**, 1736–1748.
- Fedorov, A. V., C. M. Brierley, K. T. Lawrence, Z. Liu, P. S. Dekens, and A. C. Ravelo, 2013: Patterns and mechanisms of early Pliocene warmth. *Nature*, **496**, 43–49.
- Feng, S., and Q. Hu, 2008: How the North Atlantic Multidecadal Oscillation may have influenced the Indian summer monsoon during the past two millennia. *Geophys. Res. Lett.*, **35**, L01707.
- Fernández-Donado, L., et al., 2013: Large-scale temperature response to external forcing in simulations and reconstructions of the last millennium. *Clim. Past*, **9**, 393–421.
- Feulner, G., 2011: Are the most recent estimates for Maunder Minimum solar irradiance in agreement with temperature reconstructions? *Geophys. Res. Lett.*, **38**, L16706.
- Fischer, H., M. Wahlen, J. Smith, D. Mastroiani, and B. Deck, 1999: Ice core records of atmospheric CO₂ around the last three glacial terminations. *Science*, **283**, 1712–1714.
- Fischer, H., M. L. Siggaard-Andersen, U. Ruth, R. Röhlisberger, and E. Wolff, 2007: Glacial/interglacial changes in mineral dust and sea-salt records in polar ice cores: Sources, transport, and deposition. *Rev. Geophys.*, **45**, RG1002.
- Fischer, N., and J. H. Jungclaus, 2010: Effects of orbital forcing on atmosphere and ocean heat transports in Holocene and Eemian climate simulations with a comprehensive Earth system model. *Clim. Past*, **6**, 155–168.
- Fleitmann, D., et al., 2009: Timing and climatic impact of Greenland interstadials recorded in stalagmites from northern Turkey. *Geophys. Res. Lett.*, **36**, L19707.
- Fletcher, B. J., S. J. Brentnall, C. W. Anderson, R. A. Berner, and D. J. Beerling, 2008: Atmospheric carbon dioxide linked with Mesozoic and early Cenozoic climate change. *Nature Geosci.*, **1**, 43–48.
- Fletcher, W. J., and M. F. Sánchez Goñi, 2008: Orbital- and sub-orbital-scale climate impacts on vegetation of the western Mediterranean basin over the last 48,000 yr. *Quat. Res.*, **70**, 451–464.
- Flückiger, J., A. Dällenbach, T. Blunier, B. Stauffer, T. F. Stocker, D. Raynaud, and J.-M. Barnola, 1999: Variations in atmospheric N₂O concentration during abrupt climatic changes. *Science*, **285**, 227–230.
- Flückiger, J., et al., 2002: High-resolution Holocene N₂O ice core record and its relationship with CH₄ and CO₂. *Global Biogeochem. Cycles*, **16**, 1010.
- Foster, G. L., 2008: Seawater pH, pCO₂ and [CO₃²⁻] variations in the Caribbean Sea over the last 130 kyr: a boron isotope and B/Ca study of planktic foraminifera. *Earth Planet. Sci. Lett.*, **271**, 254–266.
- Foster, G. L., C. H. Lear, and J. W. B. Rae, 2012: The evolution of pCO₂, ice volume and climate during the middle Miocene. *Earth Planet. Sci. Lett.*, **341–344**, 243–254.
- Fowler, A. M., et al., 2012: Multi-centennial tree-ring record of ENSO-related activity in New Zealand. *Nature Clim. Change*, **2**, 172–176.
- Frank, D., J. Esper, and E. R. Cook, 2007: Adjustment for proxy number and coherence in a large-scale temperature reconstruction. *Geophys. Res. Lett.*, **34**, L16709.
- Frank, D., J. Esper, E. Zorita, and R. Wilson, 2010a: A noodle, hockey stick, and spaghetti plate: a perspective on high-resolution paleoclimatology. *Clim. Change*, **1**, 507–516.
- Frank, D. C., J. Esper, C. C. Raible, U. Büntgen, V. Trouet, B. Stocker, and F. Joos, 2010b: Ensemble reconstruction constraints on the global carbon cycle sensitivity to climate. *Nature*, **463**, 527–530.
- Fréchette, B., A. P. Wolfe, G. H. Miller, P. J. H. Richard, and A. de Vernal, 2006: Vegetation and climate of the last interglacial on Baffin Island, Arctic Canada. *Palaeogeogr. Palaeoclimatol. Palaeoecol.*, **236**, 91–106.
- Freeman, K. H., and J. M. Hayes, 1992: Fractionation of carbon isotopes by phytoplankton and estimates of ancient CO₂ levels. *Global Biogeochem. Cycles*, **6**, 185–198.
- Funder, S., et al., 2011: A 10,000-year record of Arctic Ocean sea-ice variability—view from the beach. *Science*, **333**, 747–750.
- Fyke, J., and M. Eby, 2012: Comment on “Climate sensitivity estimated from temperature reconstructions of the Last Glacial Maximum”. *Science*, **337**, 1294.
- Gabrielli, P., et al., 2010: A major glacial-interglacial change in aeolian dust composition inferred from Rare Earth Elements in Antarctic ice. *Quat. Sci. Rev.*, **29**, 265–273.
- Gagen, M., et al., 2011: Cloud response to summer temperatures in Fennoscandia over the last thousand years. *Geophys. Res. Lett.*, **38**, L05701.
- Gaiero, D. M., 2007: Dust provenance in Antarctic ice during glacial periods: From where in southern South America? *Geophys. Res. Lett.*, **34**, L17707.
- Ganopolski, A., and S. Rahmstorf, 2001: Rapid changes of glacial climate simulated in a coupled climate model. *Nature*, **409**, 153–158.
- Ganopolski, A., and D. M. Roche, 2009: On the nature of lead-lag relationships during glacial-interglacial climate transitions. *Quat. Sci. Rev.*, **28**, 3361–3378.
- Ganopolski, A., and R. Calov, 2011: The role of orbital forcing, carbon dioxide and regolith in 100 kyr glacial cycles. *Clim. Past*, **7**, 1415–1425.
- Ganopolski, A., R. Calov, and M. Claussen, 2010: Simulation of the last glacial cycle with a coupled climate ice-sheet model of intermediate complexity. *Clim. Past*, **6**, 229–244.
- Gao, C., A. Robock, and C. Ammann, 2008: Volcanic forcing of climate over the past 1500 years: An improved ice core-based index for climate models. *J. Geophys. Res.*, **113**, D23111.
- , 2012: Correction to “Volcanic forcing of climate over the past 1500 years: An improved ice core-based index for climate models”. *J. Geophys. Res.*, **117**, D16112.
- García-Artola, A., A. Cebarreta, E. Leorri, M. Irabien, and W. Blake, 2009: Las marismas costeras como archivos geológicos de las variaciones recientes en el nivel marino/Coastal salt-marshes as geological archives of recent sea level changes. *Geocaceta*, **47**, 109–112.
- García-Herrera, R., D. Barriopedro, E. Hernández, H. F. Diaz, R. R. García, M. R. Prieto, and R. Moyano, 2008: A chronology of El Niño events from primary documentary sources in northern Peru. *J. Clim.*, **21**, 1948–1962.
- Garcin, Y., et al., 2007: Solar and anthropogenic imprints on Lake Masoko (southern Tanzania) during the last 500 years. *J. Paleolimnol.*, **37**, 475–490.
- Gayer, E., J. Lavé, R. Pik, and C. France-Lanord, 2006: Monsoonal forcing of Holocene glacier fluctuations in Ganesh Himal (Central Nepal) constrained by cosmogenic ³⁶He exposure ages of garnets. *Earth Planet. Sci. Lett.*, **252**, 275–288.
- Ge, Q.-S., J.-Y. Zheng, Z.-X. Hao, X.-M. Shao, W.-C. Wang, and J. Luterbacher, 2010: Temperature variation through 2000 years in China: an uncertainty analysis of reconstruction and regional difference. *Geophys. Res. Lett.*, **37**, L03703.
- Ge, Q. S., S. B. Wang, and J. Y. Zheng, 2006: Reconstruction of temperature series in China for the last 5000 years. *Prog. Nat. Sci.*, **16**, 838–845.
- Gehrels, W. R., and P. L. Woodworth, 2013: When did modern rates of sea level rise start? *Global Planet. Change*, **100**, 263–277.
- Gehrels, W. R., B. W. Hayward, R. M. Newnham, and K. E. Southall, 2008: A 20th century acceleration of sea level rise in New Zealand. *Geophys. Res. Lett.*, **35**, L02717.
- Gehrels, W. R., B. P. Horton, A. C. Kemp, and D. Sivan, 2011: Two millennia of sea level data: The key to predicting change. *Eos Trans. AGU*, **92**, 289–290.
- Gehrels, W. R., et al., 2006: Rapid sea level rise in the North Atlantic Ocean since the first half of the nineteenth century. *The Holocene*, **16**, 949–965.
- Gergis, J. L., and A. M. Fowler, 2009: A history of ENSO events since A.D. 1525: Implications for future climate change. *Clim. Change*, **92**, 343–387.
- Gersonde, R., X. Crosta, A. Abelmann, and L. Armand, 2005: Sea-surface temperature and sea ice distribution of the Southern Ocean at the EPICLOG Last Glacial Maximum—a circum-Antarctic view based on siliceous microfossil records. *Quat. Sci. Rev.*, **24**, 869–896.
- Ghatak, D., A. Frei, G. Gong, J. Stroeve, and D. Robinson, 2010: On the emergence of an Arctic amplification signal in terrestrial Arctic snow extent. *J. Geophys. Res.*, **115**, D24105.
- Giguet-Covex, C., et al., 2012: Frequency and intensity of high-altitude floods over the last 3.5 ka in northwestern French Alps (Lake Anterne). *Quat. Res.*, **77**, 12–22.
- Gille, S. T., 2008: Decadal-scale temperature trends in the southern hemisphere ocean. *J. Clim.*, **21**, 4749–4765.
- Gillett, N., T. Kell, and P. Jones, 2006: Regional climate impacts of the Southern Annular Mode. *Geophys. Res. Lett.*, **33**, L23704.
- Gillett, N., et al., 2008: Attribution of polar warming to human influence. *Nature Geosci.*, **1**, 750–754.
- Gladstone, R. M., et al., 2005: Mid-Holocene NAO: A PMIP2 model intercomparison. *Geophys. Res. Lett.*, **32**, L16707.

- Goehring, B. M., et al., 2011: The Rhone Glacier was smaller than today for most of the Holocene. *Geology*, **39**, 679–682.
- Goldewijk, K. K., 2001: Estimating global land use change over the past 300 years: The HYDE Database. *Global Biogeochem. Cycles*, **15**, 417–433.
- González-Rouco, F., H. von Storch, and E. Zorita, 2003: Deep soil temperature as proxy for surface air-temperature in a coupled model simulation of the last thousand years. *Geophys. Res. Lett.*, **30**, 2116.
- González-Rouco, J. F., H. Beltrami, E. Zorita, and H. von Storch, 2006: Simulation and inversion of borehole temperature profiles in surrogate climates: Spatial distribution and surface coupling. *Geophys. Res. Lett.*, **33**, L01703.
- González, C., and L. Dupont, 2009: Tropical salt marsh succession as sea level indicator during Heinrich events. *Quat. Sci. Rev.*, **28**, 939–946.
- González, J. L., and T. E. Törnqvist, 2009: A new Late Holocene sea level record from the Mississippi Delta: evidence for a climate/sea level connection? *Quat. Sci. Rev.*, **28**, 1737–1749.
- Goodwin, I. D., and N. Harvey, 2008: Subtropical sea level history from coral microatolls in the Southern Cook Islands, since 300 AD. *Mar. Geol.*, **253**, 14–25.
- Goosse, H., J. Guiot, M. E. Mann, S. Dubinkina, and Y. Sallaz-Damaz, 2012a: The medieval climate anomaly in Europe: Comparison of the summer and annual mean signals in two reconstructions and in simulations with data assimilation. *Global Planet. Change*, **84–85**, 35–47.
- Goosse, H., et al., 2012b: The role of forcing and internal dynamics in explaining the “Medieval Climate Anomaly”. *Clim. Dyn.*, **39**, 2847–2866.
- Goosse, H., et al., 2012c: Antarctic temperature changes during the last millennium: evaluation of simulations and reconstructions. *Quat. Sci. Rev.*, **55**, 75–90.
- Govin, A., et al., 2012: Persistent influence of ice sheet melting on high northern latitude climate during the early Last Interglacial. *Clim. Past*, **8**, 483–507.
- Grachev, A. M., E. J. Brook, J. P. Severinghaus, and N. G. Pisias, 2009: Relative timing and variability of atmospheric methane and GISP2 oxygen isotopes between 68 and 86 ka. *Global Biogeochem. Cycles*, **23**, GB2009.
- Graham, N., C. Ammann, D. Fleitmann, K. Cobb, and J. Luterbacher, 2011: Support for global climate reorganization during the “Medieval Climate Anomaly”. *Clim. Dyn.*, **37**, 1217–1245.
- Grant, K. M., et al., 2012: Rapid coupling between ice volume and polar temperature over the past 150,000 years. *Nature*, **491**, 744–747.
- Graversen, R. G., and M. H. Wang, 2009: Polar amplification in a coupled climate model with locked albedo. *Clim. Dyn.*, **33**, 629–643.
- Gray, S. T., L. J. Graumlich, J. L. Betancourt, and G. T. Pederson, 2004: A tree-ring based reconstruction of the Atlantic Multidecadal Oscillation since 1567 A.D. *Geophys. Res. Lett.*, **31**, L12205.
- Greenwood, D. R., M. J. Scarr, and D. C. Christophe, 2003: Leaf stomatal frequency in the Australian tropical rainforest tree *Neolitsea dealbata* (Lauraceae) as a proxy measure of atmospheric $p\text{CO}_2$. *Palaeogeogr. Palaeoclimatol. Palaeoecol.*, **196**, 375–393.
- Gregoire, L. J., A. J. Payne, and P. J. Valdes, 2012: Deglacial rapid sea level rises caused by ice-sheet saddle collapses. *Nature*, **487**, 219–222.
- Gregory, J. M., and P. Huybrechts, 2006: Ice-sheet contributions to future sea level change. *Philos. Trans. R. Soc. A*, **364**, 1709–1732.
- Grichuk, V. P., 1985: Reconstructed climatic indexes by means of floristic data and an estimation of their accuracy. In: *Metody rekonstruktii paleoklimatov* [A. A. Velichko and Y. Y. Gurtovaya (eds.)]. Nauka-press, St. Petersburg, Russian Federation, pp. 20–28 (in Russian).
- Grützner, J., and S. M. Higgins, 2010: Threshold behavior of millennial scale variability in deep water hydrography inferred from a 1.1 Ma long record of sediment provenance at the southern Gardar Drift. *Paleoceanography*, **25**, PA4204.
- Haigh, J. D., 1996: The impact of solar variability on climate. *Science*, **272**, 981–984.
- Haigh, J. D., A. R. Winning, R. Toumi, and J. W. Harder, 2010: An influence of solar spectral variations on radiative forcing of climate. *Nature*, **467**, 696–699.
- Hald, M., et al., 2007: Variations in temperature and extent of Atlantic Water in the northern North Atlantic during the Holocene. *Quat. Sci. Rev.*, **26**, 3423–3440.
- Hall, B. L., T. Koffman, and G. H. Denton, 2010: Reduced ice extent on the western Antarctic Peninsula at 700–970 cal. yr B.P. *Geology*, **38**, 635–638.
- Hall, I. R., S. B. Moran, R. Zahn, P. C. Knutz, C. C. Shen, and R. L. Edwards, 2006: Accelerated drawdown of meridional overturning in the late-glacial Atlantic triggered by transient pre-H event freshwater perturbation. *Geophys. Res. Lett.*, **33**, L16616.
- Handorf, D., K. Dethloff, A. G. Marshall, and A. Lynch, 2009: Climate regime variability for past and present time slices simulated by the Fast Ocean Atmosphere Model. *J. Clim.*, **22**, 58–70.
- Hanebuth, T. J. J., H. K. Voris, Y. Yokoyama, Y. Saito, and J. i. Okuno, 2011: Formation and fate of sedimentary depocentres on Southeast Asia’s Sunda Shelf over the past sea level cycle and biogeographic implications. *Earth Sci. Rev.*, **104**, 92–110.
- Hanhijärvi, S., M. P. Tingley, and A. Korhola, 2013: Pairwise comparisons to reconstruct mean temperature in the Arctic Atlantic Region over the last 2,000 years. *Clim. Dyn.*, **41**, 2039–2060.
- Hansen, J., and M. Sato, 2004: Greenhouse gas growth rates. *Proc. Natl. Acad. Sci. U.S.A.*, **101**, 16109–16114.
- Hansen, J., et al., 2008: Target atmospheric CO_2 : Where should humanity aim? *Open Atmos. Sci. J.*, **2**, 217–231.
- Harada, N., M. Sato, and T. Sakamoto, 2008: Freshwater impacts recorded in tetraun-saturated alkenones and alkenone sea surface temperatures from the Okhotsk Sea across millennial-scale cycles. *Paleoceanography*, **23**, PA3201.
- Harada, N., K. Kimoto, Y. Okazaki, K. Nagashima, A. Timmermann, and A. Abe-Ouchi, 2009: Millennial time scale changes in surface to intermediate-deep layer circulation recorded in sediment cores from the northwestern North Pacific. *Quat. Res. (Daiyonki-Kenkyu)*, **48**, 179–194.
- Harada, N., et al., 2012: Sea surface temperature changes in the Okhotsk Sea and adjacent North Pacific during the last glacial maximum and deglaciation. *Deep-Sea Res. Pt. II*, **61–64**, 93–105.
- Harden, T. M., J. E. O’Connor, D. G. Driscoll, and J. F. Stamm, 2011: Flood-frequency analyses from paleoflood investigations for Spring, Rapid, Boxelder, and Elk Creeks, Black Hills, western South Dakota. *U.S. Geological Survey Scientific Investigations Report 2011–5131*, 136 pp.
- Harder, J. W., J. M. Fontenla, P. Pilewskie, E. C. Richard, and T. N. Woods, 2009: Trends in solar spectral irradiance variability in the visible and infrared. *Geophys. Res. Lett.*, **36**, L07801.
- Hargreaves, J., A. Abe-Ouchi, and J. Annan, 2007: Linking glacial and future climates through an ensemble of GCM simulations. *Clim. Past*, **3**, 77–87.
- Hargreaves, J. C., J. D. Annan, M. Yoshimori, and A. Abe-Ouchi, 2012: Can the Last Glacial Maximum constrain climate sensitivity? *Geophys. Res. Lett.*, **39**, L24702.
- Hawkins, E., R. S. Smith, L. C. Allison, J. M. Gregory, T. J. Woollings, H. Pohlmann, and B. de Cuevas, 2011: Bistability of the Atlantic overturning circulation in a global climate model and links to ocean freshwater transport. *Geophys. Res. Lett.*, **38**, L10605.
- Haywood, A. M., P. J. Valdes, and V. L. Peck, 2007: A permanent El Niño-like state during the Pliocene? *Paleoceanography*, **22**, PA1213.
- Haywood, A. M., et al., 2013: Large-scale features of Pliocene climate: results from the Pliocene Model Intercomparison Project. *Clim. Past*, **9**, 191–209.
- Hearty, P. J., J. T. Hollin, A. C. Neumann, M. J. O’Leary, and M. McCulloch, 2007: Global sea level fluctuations during the Last Interglaciation (MIS 5e). *Quat. Sci. Rev.*, **26**, 2090–2112.
- Hegerl, G., T. Crowley, W. Hyde, and D. Frame, 2006: Climate sensitivity constrained by temperature reconstructions over the past seven centuries. *Nature*, **440**, 1029–1032.
- Hegerl, G. C., T. J. Crowley, M. Allen, W. T. Hyde, H. N. Pollack, J. Smerdon, and E. Zorita, 2007: Detection of human influence on a new, validated 1500-year temperature reconstruction. *J. Clim.*, **20**, 650–666.
- Helama, S., J. Meriläinen, and H. Tuomenvirta, 2009: Multicentennial megadrought in northern Europe coincided with a global El Niño–Southern Oscillation drought pattern during the Medieval Climate Anomaly. *Geology*, **37**, 175–178.
- Helama, S., M. M. Fauria, K. Mielikäinen, M. Timonen, and M. Eronen, 2010: Sub-Milankovitch solar forcing of past climates: mid and late Holocene perspectives. *Geol. Soc. Am. Bull.*, **122**, 1981–1988.
- Hély, C., P. Braconnot, J. Watrén, and W. Zheng, 2009: Climate and vegetation: Simulating the African humid period. *C. R. Geosci.*, **341**, 671–688.
- Hemming, S. R., 2004: Heinrich events: Massive late Pleistocene detritus layers of the North Atlantic and their global climate imprint. *Rev. Geophys.*, **42**, RG1005.
- Henderiks, J., and M. Pagani, 2007: Refining ancient carbon dioxide estimates: Significance of coccolithophore cell size for alkenone-based $p\text{CO}_2$ records. *Paleoceanography*, **22**, PA3202.
- Herbert, T. D., L. C. Peterson, K. T. Lawrence, and Z. Liu, 2010: Tropical ocean temperatures over the past 3.5 million years. *Science*, **328**, 1530–1534.
- Hereid, K. A., T. M. Quinn, F. W. Taylor, C.-C. Shen, R. L. Edwards, and H. Cheng, 2013: Coral record of reduced El Niño activity in the early 15th to middle 17th century. *Geology*, **41**, 51–54.
- Herold, N., Q. Z. Yin, M. P. Karami, and A. Berger, 2012: Modeling the diversity of the warm interglacials. *Clim. Dyn.*, **56**, 126–141.

- Herrington, A., and C. Poulsen, 2012: Terminating the Last Interglacial: the role of ice sheet-climate feedbacks in a GCM asynchronously coupled to an Ice Sheet Model. *J. Clim.*, **25**, 1871–1882.
- Hesse, T., M. Butzin, T. Bickert, and G. Lohmann, 2011: A model-data comparison of $\delta^{13}\text{C}$ in the glacial Atlantic Ocean. *Paleoceanography*, **26**, PA3220.
- Heusser, C. J., and L. E. Heusser, 1990: Long continental pollen sequence from Washington State (U.S.A.): Correlation of upper levels with marine pollen-oxygen isotope stratigraphy through substage 5e. *Palaeogeogr. Palaeoclimatol. Palaeoecol.*, **79**, 63–71.
- Heyman, J., A. P. Stroeven, J. M. Harbor, and M. W. Caffee, 2011: Too young or too old: evaluating cosmogenic exposure dating based on an analysis of compiled boulder exposure ages. *Earth Planet. Sci. Lett.*, **302**, 71–80.
- Higginson, M. J., M. A. Altabet, D. W. Murray, R. W. Murray, and T. D. Herbert, 2004: Geochemical evidence for abrupt changes in relative strength of the Arabian monsoons during a stadial/interstadial climate transition. *Geochim Cosmochim. Acta*, **68**, 3807–3826.
- Hijma, M. P., and K. M. Cohen, 2010: Timing and magnitude of the sea level jump preluding the 8200 yr event. *Geology*, **38**, 275–278.
- Hill, D. J., A. M. Dolan, A. M. Haywood, S. J. Hunter, and D. K. Stoll, 2010: Sensitivity of the Greenland Ice Sheet to Pliocene sea surface temperatures. *Stratigraphy*, **7**, 111–122.
- Hind, A., and A. Moberg, 2012: Past millennial solar forcing magnitude: A statistical hemispheric-scale climate model versus proxy data comparison. *Clim. Dyn.*, doi:10.1007/s00382-012-1526-6, published online 22 September 2012.
- Hodell, D. A., H. F. Evans, J. E. T. Channell, and J. H. Curtis, 2010: Phase relationships of North Atlantic ice-raftered debris and surface-deep climate proxies during the last glacial period. *Quat. Sci. Rev.*, **29**, 3875–3886.
- Hodgson, D. A., 2011: First synchronous retreat of ice shelves marks a new phase of polar deglaciation. *Proc. Natl. Acad. Sci. U.S.A.*, **108**, 18859–18860.
- Hofer, D., C. Raible, and T. Stocker, 2011: Variations of the Atlantic Meridional circulation in control and transient simulations of the last millennium. *Clim. Past*, **7**, 133–150.
- Hofer, D., C. C. Raible, N. Merz, A. Dehnert, and J. Kuhleemann, 2013: Simulated winter circulation types in the North Atlantic and European region for preindustrial and glacial conditions. *Geophys. Res. Lett.*, **39**, L15805.
- Holden, P., N. Edwards, K. Oliver, T. Lenton, and R. Wilkinson, 2010a: A probabilistic calibration of climate sensitivity and terrestrial carbon change in GENIE-1. *Clim. Dyn.*, **35**, 785–806.
- Holden, P. B., N. R. Edwards, E. W. Wolff, N. J. Lang, J. S. Singarayer, P. J. Valdes, and T. F. Stocker, 2010b: Interhemispheric coupling, the West Antarctic Ice Sheet and warm Antarctic interglacials. *Clim. Past*, **6**, 431–443.
- Hollis, C. J., et al., 2012: Early Paleogene temperature history of the Southwestern Pacific Ocean: reconciling proxies and models. *Earth Planet. Sci. Lett.*, **349–350**, 53–66.
- Holmes, J. A., E. R. Cook, and B. Yang, 2009: Climate change over the past 2000 years in Western China. *Quaternary International*, **194**, 91–107.
- Holz, A., and T. T. Veblen, 2011: Variability in the Southern Annular Mode determines wildfire activity in Patagonia. *Geophys. Res. Lett.*, **38**, L14710.
- Holzhauser, H., M. Magny, and H. J. Zumbühl, 2005: Glacier and lake-level variations in west-central Europe over the last 3500 years. *Holocene*, **15**, 789–801.
- Hönisch, B., and N. G. Hemming, 2005: Surface ocean pH response to variations in μCO_2 through two full glacial cycles. *Earth Planet. Sci. Lett.*, **236**, 305–314.
- Hönisch, B., N. G. Hemming, D. Archer, M. Siddall, and J. F. McManus, 2009: Atmospheric carbon dioxide concentration across the Mid-Pleistocene transition. *Science*, **324**, 1551–1554.
- Horton, B., and R. Edwards, 2006: Quantifying Holocene Sea Level Change Using Intertidal Foraminifera: Lessons from the British Isles. *Journal of Foraminiferal Research, Special publication* **40**, 1–97.
- Hu, A. X., et al., 2012: Role of the Bering Strait on the hysteresis of the ocean conveyor belt circulation and glacial climate stability. *Proc. Natl. Acad. Sci. U.S.A.*, **109**, 6417–6422.
- Hu, C., G. M. Henderson, J. Huang, S. Xie, Y. Sun, and K. R. Johnson, 2008: Quantification of Holocene Asian monsoon rainfall from spatially separated cave records. *Earth Planet. Sci. Lett.*, **266**, 221–232.
- Huang, C. C., J. Pang, X. Zha, Y. Zhou, H. Su, H. Wan, and B. Ge, 2012: Sedimentary records of extraordinary floods at the ending of the mid-Holocene climatic optimum along the Upper Weihe River, China. *Holocene*, **22**, 675–686.
- Huber, C., et al., 2006: Isotope calibrated Greenland temperature record over Marine Isotope Stage 3 and its relation to CH_4 . *Earth Planet. Sci. Lett.*, **243**, 504–519.
- Huber, M., and R. Caballero, 2011: The early Eocene equitable climate problem revisited. *Clim. Past*, **7**, 603–633.
- Hughes, A. L. C., E. Rainsley, T. Murray, C. J. Fogwill, C. Schnabel, and S. Xu, 2012: Rapid response of Helheim Glacier, southeast Greenland, to early Holocene climate warming. *Geology*, **40**, 427–430.
- Hughes, M. K., and C. M. Ammann, 2009: The future of the past—an Earth system framework for high resolution paleoclimatology: editorial essay. *Clim. Change*, **94**, 247–259.
- Humlum, O., B. Elberling, A. Hormes, K. Fjordheim, O. H. Hansen, and J. Heinemeier, 2005: Late-Holocene glacier growth in Svalbard, documented by subglacial relict vegetation and living soil microbes. *Holocene*, **15**, 396–407.
- Hurt, G. C., et al., 2006: The underpinnings of land-use history: three centuries of global gridded land-use transitions, wood-harvest activity, and resulting secondary lands. *Global Change Biol.*, **12**, 1208–1229.
- Huybers, P., 2011: Combined obliquity and precession pacing of Late Pleistocene deglaciations. *Nature*, **480**, 229–232.
- Israelsen, C., and B. Wohlforth, 1999: Timing of the last-interglacial high sea level on the Seychelles Islands, Indian Ocean. *Quat. Res.*, **51**, 306–316.
- Itambi, A. C., T. von Dobeneck, S. Mulitza, T. Bickert, and D. Heslop, 2009: Millennial-scale northwest African droughts related to Heinrich events and Dansgaard-Oeschger cycles: Evidence in marine sediments from offshore Senegal. *Paleoceanography*, **24**, PA1205.
- Ivanochko, T. S., R. S. Ganeshram, G.-J. A. Brummer, G. Ganssen, S. J. A. Jung, S. G. Moreton, and D. Kroon, 2005: Variations in tropical convection as an amplifier of global climate change at the millennial scale. *Earth Planet. Sci. Lett.*, **235**, 302–314.
- Ivy-Ochs, S., H. Kerschner, M. Maisch, M. Christl, P. W. Kubik, and C. Schlüchter, 2009: Latest Pleistocene and Holocene glacier variations in the European Alps. *Quat. Sci. Rev.*, **28**, 2137–2149.
- Izumi, K., P. J. Bartlein, and S. P. Harrison, 2013: Consistent large-scale temperature responses in warm and cold climates. *Geophys. Res. Lett.*, **40**, 1817–1823.
- Jaccard, S. L., E. D. Galbraith, D. M. Sigman, and G. H. Haug, 2010: A pervasive link between Antarctic ice core and subarctic Pacific sediment records over the past 800 krys. *Quat. Sci. Rev.*, **29**, 206–212.
- Jansen, E., et al., 2007: Palaeoclimate. In: *Climate Change 2007: The Physical Science Basis. Contribution of Working Group I to the Fourth Assessment Report of the Intergovernmental Panel on Climate Change* [Solomon, S., D. Qin, M. Manning, Z. Chen, M. Marquis, K. B. Averyt, M. Tignor and H. L. Miller (eds.)] Cambridge University Press, Cambridge, United Kingdom and New York, NY, USA, pp. 433–497.
- Jevrejeva, S., J. C. Moore, A. Grinsted, and P. L. Woodworth, 2008: Recent global sea level acceleration started over 200 years ago? *Geophys. Res. Lett.*, **35**, L08715.
- Joerin, U. E., K. Nicolussi, A. Fischer, T. F. Stocker, and C. Schlüchter, 2008: Holocene optimum events inferred from subglacial sediments at Tschierva Glacier, Eastern Swiss Alps. *Quat. Sci. Rev.*, **27**, 337–350.
- Johns, T. C., et al., 2003: Anthropogenic climate change for 1860 to 2100 simulated with the HadCM3 model under updated emissions scenarios. *Clim. Dyn.*, **20**, 583–612.
- Johnsen, S. J., D. Dahl-Jensen, W. Dansgaard, and N. Gundestrup, 1995: Greenland palaeotemperatures derived from GRIP bore hole temperature and ice core isotope profiles. *Tellus B*, **47**, 624–629.
- Johnson, K., and D. J. Smith, 2012: Dendroglaciological reconstruction of late-Holocene glacier activity at White and South Flat glaciers, Boundary Range, northern British Columbia Coast Mountains, Canada. *Holocene*, **22**, 987–995.
- Jomelli, V., V. Favier, A. Rabatel, D. Brunstein, G. Hoffmann, and B. Francou, 2009: Fluctuations of glaciers in the tropical Andes over the last millennium and palaeoclimatic implications: A review. *Palaeogeogr. Palaeoclimatol. Palaeoecol.*, **281**, 269–282.
- Jones, P. D., D. H. Lister, T. J. Osborn, C. Harpham, M. Salmon, and C. P. Morice, 2012: Hemispheric and large-scale land-surface air temperature variations: an extensive revision and an update to 2010. *J. Geophys. Res.*, **117**, D05127.
- Jones, P. D., et al., 2009: High-resolution palaeoclimatology of the last millennium: A review of current status and future prospects. *Holocene*, **19**, 3–49.
- Joos, F., and R. Spahni, 2008: Rates of change in natural and anthropogenic radiative forcing over the past 20,000 years. *Proc. Natl. Acad. Sci. U.S.A.*, **105**, 1425–1430.
- Joos, F., et al., 2001: Global warming feedbacks on terrestrial carbon uptake under the Intergovernmental Panel on Climate Change (IPCC) Emission Scenarios. *Global Biogeochem. Cycles*, **15**, 891–907.

- Joshi, M. M., and G. S. Jones, 2009: The climatic effects of the direct injection of water vapour into the stratosphere by large volcanic eruptions. *Atmos. Chem. Phys.*, **9**, 6109–6118.
- Joughin, I., and R. B. Alley, 2011: Stability of the West Antarctic ice sheet in a warming world. *Nature Geosci.*, **4**, 506–513.
- Jouzel, J., et al., 2007: Orbital and millennial Antarctic climate variability over the past 800,000 years. *Science*, **317**, 793–796.
- Juckes, M. N., et al., 2007: Millennial temperature reconstruction intercomparison and evaluation. *Clim. Past*, **3**, 591–609.
- Jungclaus, J. H., et al., 2010: Climate and carbon-cycle variability over the last millennium. *Clim. Past*, **6**, 723–737.
- Justino, F., and W. R. Peltier, 2005: The glacial North Atlantic Oscillation. *Geophys. Res. Lett.*, **32**, L21803.
- Justino, F., and W. R. Peltier, 2008: Climate anomalies induced by the arctic and antarctic oscillations: glacial maximum and present-day perspectives. *J. Clim.*, **21**, 459–475.
- Justwan, A., and N. Koç, 2008: A diatom based transfer function for reconstructing sea ice concentrations in the North Atlantic. *Mar. Micropaleontol.*, **66**, 264–278.
- Kageyama, M., A. Paul, D. M. Roche, and C. J. Van Meerbeek, 2010: Modelling glacial climatic millennial-scale variability related to changes in the Atlantic meridional overturning circulation: a review. *Quat. Sci. Rev.*, **29**, 2931–2956.
- Kageyama, M., et al., 2013: Climatic impacts of fresh water hosing under Last Glacial Maximum conditions: a multi-model study. *Clim. Past*, **9**, 935–953.
- Kaiser, J., E. Schefuß, F. Lamy, M. Mohtadi, and D. Hebbeln, 2008: Glacial to Holocene changes in sea surface temperature and coastal vegetation in north central Chile: high versus low latitude forcing. *Quat. Sci. Rev.*, **27**, 2064–2075.
- Kale, V. S., 2008: Palaeoflood hydrology in the Indian context. *J. Geol. Soc. India*, **71**, 56–66.
- Kanner, L. C., S. J. Burns, H. Cheng, and R. L. Edwards, 2012: High-latitude forcing of the South American Summer Monsoon during the Last Glacial. *Science*, **335**, 570–573.
- Kaplan, J. O., K. M. Krumhardt, E. C. Ellis, W. F. Ruddiman, C. Lemmen, and K. K. Goldewijk, 2011: Holocene carbon emissions as a result of anthropogenic land cover change. *Holocene*, **21**, 775–791.
- Kaplan, M. R., et al., 2010: Glacier retreat in New Zealand during the Younger Dryas stadial. *Nature*, **467**, 194–197.
- Kaufman, D. S., et al., 2009: Recent warming reverses long-term Arctic cooling. *Science*, **325**, 1236–1239.
- Kawamura, K., et al., 2007: Northern Hemisphere forcing of climatic cycles in Antarctica over the past 360,000 years. *Nature*, **448**, 912–916.
- Kemp, A. C., B. P. Horton, J. P. Donnelly, M. E. Mann, M. Vermeer, and S. Rahmstorf, 2011: Climate related sea level variations over the past two millennia. *Proc. Natl. Acad. Sci. U.S.A.*, **108**, 11017–11022.
- Kemp, A. C., et al., 2009: Timing and magnitude of recent accelerated sea level rise (North Carolina, United States). *Geology*, **37**, 1035–1038.
- Kienast, F., et al., 2011: Paleontological records indicate the occurrence of open woodlands in a dry inland climate at the present-day Arctic coast in western Beringia during the Last Interglacial. *Quat. Sci. Rev.*, **30**, 2134–2159.
- Kilbourne, K. H., T. M. Quinn, R. Webb, T. Guilderson, J. Nyberg, and A. Winter, 2008: Paleoclimate proxy perspective on Caribbean climate since the year 1751: Evidence of cooler temperatures and multidecadal variability. *Paleoceanography*, **23**, PA3220.
- Kilfeather, A. A., C. Ó Cofaigh, J. M. Lloyd, J. A. Dowdeswell, S. Xu, and S. G. Moreton, 2011: Ice-stream retreat and ice-shelf history in Marguerite Trough, Antarctic Peninsula: Sedimentological and foraminiferal signatures. *Geol. Soc. Am. Bull.*, **123**, 997–1015.
- Kim, S. J., et al., 2010: Climate response over Asia/Arctic to change in orbital parameters for the last interglacial maximum. *Geosci. J.*, **14**, 173–190.
- Kinnard, C., C. M. Zdanowicz, R. M. Koerner, and D. A. Fisher, 2008: A changing Arctic seasonal ice zone: Observations from 1870–2003 and possible oceanographic consequences. *Geophys. Res. Lett.*, **35**, L02507.
- Kinnard, C., C. M. Zdanowicz, D. A. Fisher, E. Isaksson, A. de Vernal, and L. G. Thompson, 2011: Reconstructed changes in Arctic sea ice over the past 1,450 years. *Nature*, **479**, 509–512.
- Kirkbride, M. P., and S. Winkler, 2012: Correlation of Late Quaternary moraines: Impact of climate variability, glacier response, and chronological resolution. *Quat. Sci. Rev.*, **46**, 1–29.
- Kirshner, A. E., J. B. Anderson, M. Jakobsson, M. O'Regan, W. Majewski, and F. O. Nitsche, 2012: Post-LGM deglaciation in Pine Island Bay, West Antarctica. *Quat. Sci. Rev.*, **38**, 11–26.
- Kissel, C., C. Laj, A. M. Piotrowski, S. L. Goldstein, and S. R. Hemming, 2008: Millennial-scale propagation of Atlantic deep waters to the glacial Southern Ocean. *Paleoceanography*, **23**, PA2102.
- Kleiven, H. F., E. Jansen, T. Fronval, and T. M. Smith, 2002: Intensification of Northern Hemisphere glaciations in the circum Atlantic region (3.5–2.4 Ma)—ice rafted detritus evidence. *Palaeogeogr. Palaeoclimatol. Palaeoecol.*, **184**, 213–223.
- Kleiven, H. F., I. R. Hall, I. N. McCave, G. Knorr, and E. Jansen, 2011: Coupled deep-water flow and climate variability in the middle Pleistocene North Atlantic. *Geology*, **39**, 343–346.
- Kleiven, H. F., C. Kissel, C. Laj, U. S. Ninnemann, T. O. Richter, and E. Cortijo, 2008: Reduced North Atlantic Deep Water coeval with the glacial Lake Agassiz freshwater outburst. *Science*, **319**, 60–64.
- Klotz, S., J. Guiot, and V. Mosbrugger, 2003: Continental European Eemian and early Würmian climate evolution: comparing signals using different quantitative reconstruction approaches based on pollen. *Global Planet. Change*, **36**, 277–294.
- Knight, J. R., R. J. Allan, C. K. Folland, M. Vellinga, and M. E. Mann, 2005: A signature of persistent natural thermohaline circulation cycles in observed climate. *Geophys. Res. Lett.*, **32**, L20708.
- Knudsen, M. F., M.-S. Seidenkrantz, B. H. Jacobsen, and A. Kuijpers, 2011: Tracking the Atlantic Multidecadal Oscillation through the last 8,000 years. *Nature Commun.*, **2**, 178.
- Kobashi, T., J. P. Severinghaus, J. M. Barnola, K. Kawamura, T. Carter, and T. Nakaegawa, 2010: Persistent multi-decadal Greenland temperature fluctuation through the last millennium. *Clim. Change*, **100**, 733–756.
- Kobashi, T., et al., 2011: High variability of Greenland surface temperature over the past 4000 years estimated from trapped air in an ice core. *Geophys. Res. Lett.*, **38**, L21501.
- Koch, J., and J. Clague, 2011: Extensive glaciers in northwest North America during medieval time. *Clim. Change*, **107**, 593–613.
- Koch, P. L., J. C. Zachos, and P. D. Gingerich, 1992: Correlation between isotope records in marine and continental carbon reservoirs near the Palaeocene/Eocene boundary. *Nature*, **358**, 319–322.
- Koenig, S. J., R. M. DeConto, and D. Pollard, 2011: Late Pliocene to Pleistocene sensitivity of the Greenland Ice Sheet in response to external forcing and internal feedbacks. *Clim. Dyn.*, **37**, 1247–1268.
- Kohfeld, K. E., R. M. Graham, A. M. de Boer, L. C. Sime, E. W. Wolff, C. Le Quéré, and L. Bopp, 2013: Southern hemisphere westerly wind changes during the Last Glacial Maximum: paleo-data synthesis. *Quat. Sci. Rev.*, **68**, 76–95.
- Köhler, P., G. Knorr, D. Buiron, A. Lourantou, and J. Chappellaz, 2011: Abrupt rise in atmospheric CO₂ at the onset of the Bølling/Allerød: in-situ ice core data versus true atmospheric signals. *Clim. Past*, **7**, 473–486.
- Köhler, P., R. Bintanja, H. Fischer, F. Joos, R. Knutti, G. Lohmann, and V. Masson-Delmotte, 2010: What caused Earth's temperature variations during the last 800,000 years? Data-based evidence on radiative forcing and constraints on climate sensitivity. *Quat. Sci. Rev.*, **29**, 129–145.
- Kopp, R. E., F. J. Simons, J. X. Mitrovica, A. C. Maloof, and M. Oppenheimer, 2009: Probabilistic assessment of sea level during the last interglacial stage. *Nature*, **462**, 863–867.
- Kopp, R. E., F. J. Simons, J. X. Mitrovica, A. C. Maloof, and M. Oppenheimer, 2013: A probabilistic assessment of sea level variations within the last interglacial stage. *Geophys. J. Int.*, **193**, 711–716.
- Koutavas, A., and J. P. Sachs, 2008: Northern timing of deglaciation in the eastern equatorial Pacific from alkenone paleothermometry. *Paleoceanography*, **23**, PA4205.
- Koutavas, A., and S. Joanides, 2012: El Niño-Southern Oscillation extrema in the Holocene and Last Glacial Maximum. *Paleoceanography*, **27**, PA4208.
- Kravitz, B., and A. Robock, 2011: Climate effects of high-latitude volcanic eruptions: Role of the time of year. *J. Geophys. Res.*, **116**, D01105.
- Krebs, U., and A. Timmermann, 2007: Tropical air-sea interactions accelerate the recovery of the Atlantic Meridional Overturning Circulation after a major shutdown. *J. Clim.*, **20**, 4940–4956.
- Krivova, N., and S. Solanki, 2008: Models of solar irradiance variations: Current status. *J. Astrophys. Astron.*, **29**, 151–158.

- Krivova, N., L. Balmaceda, and S. Solanki, 2007: Reconstruction of solar total irradiance since 1700 from the surface magnetic flux. *Astron. Astrophys.*, **467**, 335–346.
- Krivova, N., S. Solanki, and Y. Unruh, 2011: Towards a long-term record of solar total and spectral irradiance. *J. Atmos. Solar-Terres. Phys.*, **73**, 223–234.
- Kühl, N., 2003: *Die Bestimmung botanisch-klimatologischer Transferfunktionen und die Rekonstruktion des bodennahen Klimazustandes in Europa während der Eem-Warmzeit*. Vol. 375, *Dissertationes Botanicae*, Cramer, Berlin, 149 pp.
- Kürschner, W. M., 1996: Leaf stomata as biosensors of paleoatmospheric CO₂ levels. *LPP Contributions Series*, **5**, 1–153.
- Kürschner, W. M., Z. Kvaček, and D. L. Dilcher, 2008: The impact of Miocene atmospheric carbon dioxide fluctuations on climate and the evolution of terrestrial ecosystems. *Proc. Natl. Acad. Sci. U.S.A.*, **105**, 449–453.
- Kürschner, W. M., F. Wagner, D. L. Dilcher, and H. Visscher, 2001: Using fossil leaves for the reconstruction of Cenozoic paleoatmospheric CO₂ concentrations. In: *Geological Perspectives of Global Climate Change: APPG Studies in Geology* 47, Tulsa, [L. C. Gerhard, W. E. Harrison, and B. M. Hanson (eds.)]. The American Association of Petroleum Geologists, pp. 169–189.
- Küttel, M., et al., 2010: The importance of ship log data: Reconstructing North Atlantic, European and Mediterranean sea level pressure fields back to 1750. *Clim. Dyn.*, **34**, 1115–1128.
- Kutzbach, J. E., X. D. Liu, Z. Y. Liu, and G. S. Chen, 2008: Simulation of the evolutionary response of global summer monsoons to orbital forcing over the past 280,000 years. *Clim. Dyn.*, **30**, 567–579.
- Kutzbach, J. E., S. J. Vavrus, W. F. Ruddiman, and G. Philippon-Berthier, 2011: Comparisons of atmosphere–ocean simulations of greenhouse gas-induced climate change for pre-industrial and hypothetical ‘no-anthropogenic’ radiative forcing, relative to present day. *Holocene*, **21**, 793–801.
- Laborel, J., C. Morhange, R. Lafont, J. Le Campion, F. Laborel-Deguen, and S. Sartoretto, 1994: Biological evidence of sea level rise during the last 4500 years on the rocky coasts of continental southwestern France and Corsica. *Mar. Geol.*, **120**, 203–223.
- Lainé, A., et al., 2009: Northern hemisphere storm tracks during the last glacial maximum in the PMIP2 ocean-atmosphere coupled models: Energetic study, seasonal cycle, precipitation. *Clim. Dyn.*, **32**, 593–614.
- Laird, K. R., et al., 2012: Expanded spatial extent of the Medieval Climate Anomaly revealed in lake-sediment records across the boreal region in northwest Ontario. *Global Change Biol.*, **18**, 2869–2881.
- Lamarque, J. F., et al., 2010: Historical (1850–2000) gridded anthropogenic and biomass burning emissions of reactive gases and aerosols: methodology and application. *Atmos. Chem. Phys.*, **10**, 7017–7039.
- Lambeck, K., and E. Bard, 2000: Sea level change along the French Mediterranean coast for the past 30 000 years. *Earth Planet. Sci. Lett.*, **175**, 203–222.
- Lambeck, K., Y. Yokoyama, and T. Purcell, 2002a: Into and out of the Last Glacial Maximum: sea level change during oxygen isotope stages 3 and 2. *Quat. Sci. Rev.*, **21**, 343–360.
- Lambeck, K., T. Esat, and E. Potter, 2002b: Links between climate and sea levels for the past three million years. *Nature*, **419**, 199–206.
- Lambeck, K., A. Purcell, and A. Dutton, 2012: The anatomy of interglacial sea levels: The relationship between sea levels and ice volumes during the Last Interglacial. *Earth Planet. Sci. Lett.*, **315–316**, 4–11.
- Lambeck, K., F. Antonioli, A. Purcell, and S. Silenzi, 2004a: Sea level change along the Italian coast for the past 10,000 yr. *Quat. Sci. Rev.*, **23**, 1567–1598.
- Lambeck, K., M. Anzidei, F. Antonioli, A. Benini, and A. Esposito, 2004b: Sea level in Roman time in the Central Mediterranean and implications for recent change. *Earth Planet. Sci. Lett.*, **224**, 563–575.
- Lambeck, K., A. Purcell, S. Funder, K. H. Kjær, E. Larsen, and P. E. R. Moller, 2006: Constraints on the late Saalian to early middle Weichselian ice sheet of Eurasia from field data and rebound modelling. *Boreas*, **35**, 539–575.
- Lambeck, K., C. D. Woodroffe, F. Antonioli, M. Anzidei, W. R. Gehrels, J. Laborel, and A. J. Wright, 2010: Paleoenvironmental records, geophysical modelling, and reconstruction of sea level trends and variability on centennial and longer timescales. In: *Understanding Sea Level Rise and Variability* [J. A. Church, P. L. Woodworth, T. Aarup, and W. S. Wilson (eds.)]. Wiley-Blackwell, Hoboken, NJ, USA, pp. 61–121.
- Lambert, F., M. Bigler, J. P. Steffensen, M. A. Hutterli, and H. Fischer, 2012: Centennial mineral dust variability in high-resolution ice core data from Dome C, Antarctica. *Clim. Past*, **8**, 609–623.
- Lambert, F., et al., 2013: The role of mineral dust aerosols in polar amplification. *Nature Clim. Change*, **3**, 487–491.
- Lambert, F., et al., 2008: Dust-climate couplings over the past 800,000 years from the EPICA Dome C ice core. *Nature*, **452**, 616–619.
- Lamy, F., et al., 2007: Modulation of the bipolar seesaw in the southeast Pacific during Termination 1. *Earth Planet. Sci. Lett.*, **259**, 400–413.
- Lanciki, A., J. Cole-Dai, M. H. Thiemens, and J. Savarino, 2012: Sulfur isotope evidence of little or no stratospheric impact by the 1783 Laki volcanic eruption. *Geophys. Res. Lett.*, **39**, L01806.
- Landais, A., et al., 2004: A continuous record of temperature evolution over a sequence of Dansgaard-Oeschger events during marine isotopic stage 4 (76 to 62 kyr BP). *Geophys. Res. Lett.*, **31**, L22211.
- Landrum, L., B. L. Otto-Bliesner, E. R. Wahl, A. Conley, P. J. Lawrence, and H. Teng, 2013: Last millennium climate and its variability in CCSM4. *J. Clim.*, **26**, 1085–1111.
- Lang, N., and E. W. Wolff, 2011: Interglacial and glacial variability from the last 800 ka in marine, ice and terrestrial archives. *Clim. Past*, **7**, 361–380.
- Langebroek, P. M., A. Paul, and M. Schulz, 2009: Antarctic ice-sheet response to atmospheric CO₂ and insolation in the Middle Miocene. *Clim. Past*, **5**, 633–646.
- Lara, A., R. Villalba, and R. Urrutia, 2008: A 400-year tree-ring record of the Puelo river summer–fall streamflow in the valdivian rainforest eco-region, Chile. *Clim. Change*, **86**, 331–356.
- Larocque-Tobler, I., M. Grosjean, O. Heiri, M. Trachsel, and C. Kamenik, 2010: Thousand years of climate change reconstructed from chironomid subfossils preserved in varved lake Silvaplana, Engadine, Switzerland. *Quat. Sci. Rev.*, **29**, 1940–1949.
- Larocque-Tobler, I., M. M. Stewart, R. Quinlan, M. Trachsel, C. Kamenik, and M. Grosjean, 2012: A last millennium temperature reconstruction using chironomids preserved in sediments of anoxic Seebergsee (Switzerland): Consensus at local, regional and central European scales. *Quat. Sci. Rev.*, **41**, 49–56.
- Larsen, N. K., K. H. Kjær, J. Olsen, S. Funder, K. K. Kjeldsen, and N. Nørgaard-Pedersen, 2011: Restricted impact of Holocene climate variations on the southern Greenland Ice Sheet. *Quat. Sci. Rev.*, **30**, 3171–3180.
- Laskar, J., P. Robutel, F. Joutel, M. Gastineau, A. C. M. Correia, and B. Levrard, 2004: A long-term numerical solution for the insolation quantities of the earth. *Astron. Astrophys.*, **428**, 261–285.
- Lea, D. W., D. K. Pak, and H. J. Spero, 2000: Climate impact of late Quaternary equatorial Pacific sea surface temperature variations. *Science*, **289**, 1719–1724.
- Lea, D. W., D. K. Pak, C. L. Belanger, H. J. Spero, M. A. Hall, and N. J. Shackleton, 2006: Paleoclimate history of Galápagos surface waters over the last 135,000 yr. *Quat. Sci. Rev.*, **25**, 1152–1167.
- Lean, J., J. Beer, and R. Bradley, 1995a: Reconstruction of solar irradiance since 1610: implications for climate change. *Geophys. Res. Lett.*, **22**, 3195–3198.
- Lean, J. L., O. R. White, and A. Skumanich, 1995b: On the solar ultraviolet spectral irradiance during the Maunder Minimum. *Global Biogeochem. Cycles*, **9**, 171–182.
- Lean, J. L., T. N. Woods, F. G. Eparvier, R. R. Meier, D. J. Strickland, J. T. Correira, and J. S. Evans, 2011: Solar extreme ultraviolet irradiance: Present, past, and future. *J. Geophys. Res.*, **116**, A01102.
- Lecavalier, B. S., G. A. Milne, B. M. Vinther, D. A. Fisher, A. S. Dyke, and M. J. R. Simpson, 2013: Revised estimates of Greenland ice sheet thinning histories based on ice-core records. *Quat. Sci. Rev.*, **63**, 73–82.
- Leclercq, P. W., and J. Oerlemans, 2012: Global and Hemispheric temperature reconstruction from glacier length fluctuations. *Clim. Dyn.*, **38**, 1065–1079.
- Ledru, M. P., V. Jomelli, P. Samaniego, M. Vuille, S. Hidalgo, M. Herrera, and C. Cerón, 2013: The Medieval Climate Anomaly and the Little Ice Age in the eastern Ecuadorian Andes. *Clim. Past*, **9**, 307–321.
- Leduc, G., R. Schneider, J. H. Kim, and G. Lohmann, 2010: Holocene and Eemian sea surface temperature trends as revealed by alkenone and Mg/Ca paleothermometry. *Quat. Sci. Rev.*, **29**, 989–1004.
- Leduc, G., L. Vidal, K. Tachikawa, F. Rostek, C. Sonzogni, L. Beaufort, and E. Bard, 2007: Moisture transport across Central America as a positive feedback on abrupt climatic changes. *Nature*, **445**, 908–911.
- Lee, T. C. K., F. W. Zwiers, and M. Tsao, 2008: Evaluation of proxy-based millennial reconstruction methods. *Clim. Dyn.*, **31**, 263–281.
- Lefohn, A. S., J. D. Husar, and R. B. Husar, 1999: Estimating historical anthropogenic global sulfur emission patterns for the period 1850–1990. *Atmos. Environ.*, **33**, 3435–3444.
- LeGrande, A. N., and G. A. Schmidt, 2008: Ensemble, water isotope-enabled, coupled general circulation modeling insights into the 8.2 ka event. *Paleoceanography*, **23**, PA3207.

- LeGrande, A. N., and G. A. Schmidt, 2009: Sources of Holocene variability of oxygen isotopes in paleoclimate archives. *Clim. Past*, **5**, 441–455.
- LeGrande, A. N., et al., 2006: Consistent simulation of multiple proxy responses to an abrupt climate change event. *Proc. Natl. Acad. Sci. U.S.A.*, **103**, 10527–10527.
- Lehner, F., C. C. Raible, and T. F. Stocker, 2012: Testing the robustness of a precipitation proxy-based North Atlantic Oscillation reconstruction. *Quat. Sci. Rev.*, **45**, 85–94.
- Lemieux-Dudon, B., et al., 2010: Consistent dating for Antarctic and Greenland ice cores. *Quat. Sci. Rev.*, **29**, 8–20.
- Leorri, E., B. P. Horton, and A. Cearreta, 2008: Development of a foraminifera-based transfer function in the Basque marshes, N. Spain: implications for sea level studies in the Bay of Biscay. *Mar. Geol.*, **251**, 60–74.
- Leorri, E., A. Cearreta, and G. Milne, 2012: Field observations and modelling of Holocene sea level changes in the southern Bay of Biscay: implication for understanding current rates of relative sea level change and vertical land motion along the Atlantic coast of SW Europe. *Quat. Sci. Rev.*, **42**, 59–73.
- Lewis, S. C., A. N. LeGrande, M. Kelley, and G. A. Schmidt, 2010: Water vapour source impacts on oxygen isotope variability in tropical precipitation during Heinrich events. *Clim. Past*, **6**, 325–343.
- Li, B., D. W. Nychka, and C. M. Ammann, 2010a: The value of multiproxy reconstruction of past climate. *J. Am. Stat. Assoc.*, **105**, 883–895.
- Li, C., D. S. Battisti, and C. M. Bitz, 2010b: Can North Atlantic sea ice anomalies account for Dansgaard-Oeschger climate signals? *J. Clim.*, **23**, 5457–5475.
- Li, J., et al., 2011: Interdecadal modulation of El Niño amplitude during the past millennium. *Nature Clim. Change*, **1**, 114–118.
- Li, Y. X., H. Renssen, A. P. Wiersma, and T. E. Törnqvist, 2009: Investigating the impact of Lake Agassiz drainage routes on the 8.2 ka cold event with a climate model. *Clim. Past*, **5**, 471–480.
- Licciardi, J. M., J. M. Schaefer, J. R. Taggart, and D. C. Lund, 2009: Holocene glacier fluctuations in the Peruvian Andes indicate northern climate linkages. *Science*, **325**, 1677–1679.
- Linderholm, H. W., and P. Jansson, 2007: Proxy data reconstructions of the Storgläcären (Sweden) mass-balance record back to AD 1500 on annual to decadal timescales. *Ann. Glaciol.*, **46**, 261–267.
- Linderholm, H. W., et al., 2010: Dendroclimatology in Fennoscandia—from past accomplishments to future potential. *Clim. Past*, **5**, 1415–1462.
- Linsley, B. K., Y. Rosenthal, and D. W. Oppo, 2010: Holocene evolution of the Indonesian throughflow and the western Pacific warm pool. *Nature Geosci.*, **3**, 578–583.
- Linsley, B. K., P. P. Zhang, A. Kaplan, S. S. Howe, and G. M. Wellington, 2008: Interdecadal-decadal climate variability from multicoral oxygen isotope records in the South Pacific convergence zone region since 1650 AD. *Paleoceanography*, **23**, PA2219.
- Lisiecki, L. E., and M. E. Raymo, 2005: A Pliocene-Pleistocene stack of 57 globally distributed benthic $\delta^{18}\text{O}$ records. *Paleoceanography*, **20**, PA1003.
- Lisiecki, L. E., M. E. Raymo, and W. B. Curry, 2008: Atlantic overturning responses to late Pleistocene climate forcings. *Nature*, **456**, 85–88.
- Lisiecki, L. E., 2010: Links between eccentricity forcing and the 100,000-year glacial cycle. *Nature Geoscience*, **3**, 349–352.
- Liu, J., B. Wang, Q. Ding, X. Kuang, W. Soon, and E. Zorita, 2009a: Centennial variations of the global monsoon precipitation in the last millennium: results from ECHO-G model. *J. Clim.*, **22**, 2356–2371.
- Liu, X. D., Z. Y. Liu, S. Clemens, W. Prell, and J. Kutzbach, 2007a: A coupled model study of glacial Asian monsoon variability and Indian ocean dipole. *J. Meteorol. Soc. Jpn.*, **85**, 1–10.
- Liu, Z., et al., 2007b: Simulating the transient evolution and abrupt change of Northern Africa atmosphere-ocean-terrestrial ecosystem in the Holocene. *Quat. Sci. Rev.*, **26**, 1818–1837.
- Liu, Z., et al., 2009b: Transient simulation of last deglaciation with a new mechanism for Bølling-Allerød warming. *Science*, **325**, 310–314.
- Ljungqvist, F. C., 2010: A new reconstruction of temperature variability in the extra-tropical northern hemisphere during the last two millennia. *Geograf. Annal. A*, **92**, 339–351.
- Ljungqvist, F. C., P. J. Krusic, G. Brattström, and H. S. Sundqvist, 2012: Northern hemisphere temperature patterns in the last 12 centuries. *Clim. Past*, **8**, 227–249.
- Lloyd, A. H., and A. G. Bunn, 2007: Responses of the circumpolar boreal forest to 20th century climate variability. *Environ. Res. Lett.*, **2**, 045013.
- Lockwood, M., and M. J. Owens, 2011: Centennial changes in the heliospheric magnetic field and open solar flux: the consensus view from geomagnetic data and cosmogenic isotopes and its implications. *J. Geophys. Res.*, **116**, A04109.
- Loehle, C., and J. H. McCulloch, 2008: Correction to: A 2000-year global temperature reconstruction based on non-tree ring proxies. *Energy Environ.*, **19**, 93–100.
- Long, A. J., S. A. Woodroffe, G. A. Milne, C. L. Bryant, M. J. R. Simpson, and L. M. Wake, 2012: Relative sea level change in Greenland during the last 700–yrs and ice sheet response to the Little Ice Age. *Earth Planet. Sci. Lett.*, **315–316**, 76–85.
- Loso, M. G., 2009: Summer temperatures during the Medieval Warm Period and Little Ice Age inferred from varved proglacial lake sediments in southern Alaska. *J. Paleolimnol.*, **41**, 117–128.
- Lough, J. M., 2011: Great Barrier Reef coral luminescence reveals rainfall variability over northeastern Australia since the 17th century. *Paleoceanography*, **26**, PA2201.
- Louergue, L., et al., 2008: Orbital and millennial-scale features of atmospheric CH_4 over the past 800,000 years. *Nature*, **453**, 383–386.
- Loutre, M. F., and A. Berger, 2000: Future climatic changes: are we entering an exceptionally long interglacial? *Clim. Change*, **46**, 61–90.
- Lowell, T. V., et al., 2013: Late Holocene expansion of Istvortet ice cap, Liverpool Land, east Greenland. *Quat. Sci. Rev.*, **63**, 128–140.
- Lowenstein, T. K., and R. V. Demicco, 2006: Elevated Eocene atmospheric CO_2 and its subsequent decline. *Science*, **313**, 1928–1928.
- Lozhkin, A. V., and P. A. Anderson, 2006: A reconstruction of the climate and vegetation of northeastern Siberia based on lake sediments. *Paleontol. J.*, **40**, 622–628.
- Lu, J., and M. Cai, 2009: Seasonality of polar surface warming amplification in climate simulations. *Geophys. Res. Lett.*, **36**, L16704.
- Lü, J. M., S. J. Kim, A. Abe-Ouchi, Y. Q. Yu, and R. Ohgaito, 2010: Arctic oscillation during the mid-Holocene and Last Glacial Maximum from PMIP2 coupled model simulations. *J. Clim.*, **23**, 3792–3813.
- Lu, R., B. Dong, and H. Ding, 2006: Impact of the Atlantic multidecadal oscillation on the Asian summer monsoon. *Geophys. Res. Lett.*, **33**, L24701.
- Luckman, B. H., and R. Villalba, 2001: Assessing the synchronicity of glacier fluctuations in the western Cordillera of the Americas during the last millennium. In: *Interhemispheric Climate Linkages* [V. Markgraf (ed.)]. Academic Press, San Diego, CA, USA, pp. 119–140.
- Luckman, B. H., and R. J. S. Wilson, 2005: Summer temperatures in the Canadian Rockies during the last millennium: a revised record. *Clim. Dyn.*, **24**, 131–144.
- Lunt, D. J., G. L. Foster, A. M. Haywood, and E. J. Stone, 2008: Late Pliocene Greenland glaciation controlled by a decline in atmospheric CO_2 levels. *Nature*, **454**, 1102–1105.
- Lunt, D. J., A. M. Haywood, G. A. Schmidt, U. Salzmann, P. J. Valdes, and H. J. Dowsett, 2010: Earth system sensitivity inferred from Pliocene modelling and data. *Nature Geosci.*, **3**, 60–64.
- Lunt, D. J., T. Dunkley Jones, M. Heinemann, M. Huber, A. Legrande, A. Winguth, C. Lopston, J. Marotzke, C. D. Roberts, J. Tindall, P. Valdes, C. Winguth, 2012: A model-data comparison for a multi-model ensemble of early Eocene atmosphere-ocean simulations: EoMIP. *Climate of the Past*, **8**, 1717–1736.
- Lunt, D. J., et al., 2013: A multi-model assessment of last interglacial temperatures. *Clim. Past*, **9**, 699–717.
- Luo, F. F., S. L. Li, and T. Furevik, 2011: The connection between the Atlantic multidecadal oscillation and the Indian summer monsoon in Bergen climate model version 2.0. *J. Geophys. Res.*, **116**, D19117.
- Luoto, T. P., S. Helama, and L. Nevalainen, 2013: Stream flow intensity of the Saavojoki River, eastern Finland, during the past 1500 years reflected by mayfly and caddisfly mandibles in adjacent lake sediments. *J. Hydrol.*, **476**, 147–153.
- Luterbacher, J., et al., 2002: Reconstruction of sea level pressure fields over the Eastern North Atlantic and Europe back to 1500. *Clim. Dyn.*, **18**, 545–561.
- Luterbacher, J., et al., 2012: A review of 2000 years of paleoclimatic evidence in the Mediterranean. In: *The Climate of the Mediterranean Region: From the Past to the Future* [P. Lionello (ed.)]. Elsevier, Philadelphia, PA, USA, pp. 87–185.
- Lüthi, D., et al., 2008: High-resolution carbon dioxide concentration record 650,000–800,000 years before present. *Nature*, **453**, 379–382.
- Lynch-Stieglitz, J., et al., 2007: Atlantic meridional overturning circulation during the Last Glacial Maximum. *Science*, **316**, 66–69.
- MacDonald, G. M., D. F. Porinchu, N. Rolland, K. V. Kremenetsky, and D. S. Kaufman, 2009: Paleolimnological evidence of the response of the central Canadian treeline zone to radiative forcing and hemispheric patterns of temperature change over the past 2000 years. *J. Paleolimnol.*, **41**, 129–141.
- Macdonald, N., and A. R. Black, 2010: Reassessment of flood frequency using historical information for the River Ouse at York, UK (1200–2000). *Hydrolog. Sci. J.*, **55**, 1152–1162.

- MacFarling Meure, C. M., et al., 2006: Law Dome CO₂, CH₄ and N₂O ice core records extended to 2000 years BP. *Geophys. Res. Lett.*, **10**, L14810.
- Machado, M. J., G. Benito, M. Barriendos, and F. S. Rodrigo, 2011: 500 years of rainfall variability and extreme hydrological events in southeastern Spain drylands. *J. Arid Environ.*, **75**, 1244–1253.
- Machida, T., T. Nakazawa, Y. Fujii, S. Aoki, and O. Watanabe, 1995: Increase in the atmospheric nitrous oxide concentration during the last 250 years. *Geophys. Res. Lett.*, **22**, 2921–2924.
- Macias Fauria, M., et al., 2010: Unprecedented low twentieth century winter sea ice extent in the western Nordic Seas since AD 1200. *Clim. Dyn.*, **34**, 781–795.
- Mackintosh, A., et al., 2011: Retreat of the East Antarctic ice sheet during the last glacial termination. *Nature Geosci.*, **4**, 195–202.
- Macklin, M. G., J. Lewin, and J. C. Woodward, 2012: The fluvial record of climate change. *Philos. Trans. R. Soc. London A*, **370**, 2143–2172.
- Magilligan, F. J., P. S. Goldstein, G. B. Fisher, B. C. Bostick, and R. B. Manners, 2008: Late Quaternary hydroclimatology of a hyper-arid Andean watershed: climate change, floods, and hydrologic responses to the El Niño-Southern Oscillation in the Atacama Desert. *Geomorphology*, **101**, 14–32.
- Maher, B. A., J. M. Prospero, D. Mackie, D. Gaiero, P. P. Hesse, and Y. Balkanski, 2010: Global connections between aeolian dust, climate and ocean biogeochemistry at the present day and at the last glacial maximum. *Earth Sci. Rev.*, **99**, 61–97.
- Mahowald, N., S. Albani, S. Engelstaedter, G. Winckler, and M. Goman, 2011: Model insight into glacial–interglacial paleodust records. *Quat. Sci. Rev.*, **30**, 832–854.
- Mahowald, N. M., M. Yoshioka, W. D. Collins, A. J. Conley, D. W. Fillmore, and D. B. Coleman, 2006: Climate response and radiative forcing from mineral aerosols during the last glacial maximum, pre-industrial, current and doubled-carbon dioxide climates. *Geophys. Res. Lett.*, **33**, L20705.
- Man, W. M., T. J. Zhou, and J. H. Jungclaus, 2012: Simulation of the East Asian Summer Monsoon during the last millennium with the MPI Earth System Model. *J. Clim.*, **25**, 7852–7866.
- Mann, M. E., J. D. Fuentes, and S. Rutherford, 2012: Underestimation of volcanic cooling in tree-ring-based reconstructions of hemispheric temperatures. *Nature Geosci.*, **5**, 202–205.
- Mann, M. E., S. Rutherford, E. R. Wahl, and C. Ammann, 2007: Robustness of proxy-based climate field reconstruction methods. *J. Geophys. Res.*, **112**, D12109.
- Mann, M. E., Z. H. Zhang, M. K. Hughes, R. S. Bradley, S. K. Miller, S. Rutherford, and F. B. Ni, 2008: Proxy-based reconstructions of hemispheric and global surface temperature variations over the past two millennia. *Proc. Natl. Acad. Sci. U.S.A.*, **105**, 13252–13257.
- Mann, M. E., et al., 2009: Global signatures and dynamical origins of the Little Ice Age and Medieval Climate Anomaly. *Science*, **326**, 1256–1260.
- Marcott, S. A., J. D. Shakun, P. U. Clark, and A. C. Mix, 2013: A reconstruction of regional and global temperature for the past 11,300 years. *Science*, **339**, 1198–1201.
- Marcott, S. A., et al., 2011: Ice-shelf collapse from subsurface warming as a trigger for Heinrich events. *Proc. Natl. Acad. Sci. U.S.A.*, **108**, 13415–13419.
- Margari, V., L. C. Skinner, P. C. Tzedakis, A. Ganopolski, M. Vautravers, and N. J. Shackleton, 2010: The nature of millennial-scale climate variability during the past two glacial periods. *Nature Geosci.*, **3**, 127–131.
- MARGO Project Members, 2009: Constraints on the magnitude and patterns of ocean cooling at the Last Glacial Maximum. *Nature Geosci.*, **2**, 127–132.
- Marra, M. J., 2003: Last interglacial beetle fauna from New Zealand. *Quat. Res.*, **59**, 122–131.
- Marshall, S. J., and M. R. Koutnik, 2006: Ice sheet action versus reaction: distinguishing between Heinrich events and Dansgaard-Oeschger cycles in the North Atlantic. *Paleoceanography*, **21**, PA2021.
- Martin, P. A., D. W. Lea, Y. Rosenthal, N. J. Shackleton, M. Sarnthein, and T. Papenfuss, 2002: Quaternary deep sea temperature histories derived from benthic foraminiferal Mg/Ca. *Earth Planet. Sci. Lett.*, **198**, 193–209.
- Martínez-García, A., A. Rosell-Melé, S. L. Jaccard, W. Geibert, D. M. Sigman, and G. H. Haug, 2011: Southern Ocean dust-climate coupling over the past four million years. *Nature*, **476**, 312–315.
- Martrat, B., J. O. Grimalt, N. J. Shackleton, L. de Abreu, M. A. Hutterli, and T. F. Stocker, 2007: Four climate cycles of recurring deep and surface water destabilizations on the Iberian margin. *Science*, **317**, 502–507.
- Martrat, B., et al., 2004: Abrupt temperature changes in the western Mediterranean over the past 250,000 years. *Science*, **306**, 1762–1765.
- Marzeion, B., and A. Nesje, 2012: Spatial patterns of North Atlantic Oscillation influence on mass balance variability of European glaciers. *Cryosphere*, **6**, 661–673.
- Marzin, C., and P. Braconnot, 2009: Variations of Indian and African monsoons induced by insolation changes at 6 and 9.5 kyr BP. *Clim. Dyn.*, **33**, 215–231.
- Masson-Delmotte, V., et al., 2011a: Sensitivity of interglacial Greenland temperature and δ¹⁸O: ice core data, orbital and increased CO₂ climate simulations. *Clim. Past*, **7**, 1041–1059.
- Masson-Delmotte, V., et al., 2010a: EPICA Dome C record of glacial and interglacial intensities. *Quat. Sci. Rev.*, **29**, 113–128.
- Masson-Delmotte, V., et al., 2011b: A comparison of the present and last interglacial periods in six Antarctic ice cores. *Clim. Past*, **7**, 397–423.
- Masson-Delmotte, V., et al., 2010b: Abrupt change of Antarctic moisture origin at the end of Termination II. *Proc. Natl. Acad. Sci. U.S.A.*, **107**, 12091–12094.
- Mathiot, P., et al., 2013: Using data assimilation to investigate the causes of Southern Hemisphere high latitude cooling from 10 to 8 ka BP. *Clim. Past*, **9**, 887–901.
- Matthews, J. A., and P. Q. Dresser, 2008: Holocene glacier variation chronology of the Smørstabbtindan massif, Jotunheimen, southern Norway, and the recognition of century- to millennial-scale European Neoglacial Events. *Holocene*, **18**, 181–201.
- McCarroll, D., et al., 2013: A 1200-year multiproxy record of tree growth and summer temperature at the northern pine forest limit of Europe. *Holocene*, **23**, 471–484.
- McElwain, J. C., 1998: Do fossil plants signal palaeoatmospheric CO₂ concentration in the geological past? *Philos. Trans. R. Soc. London B*, **353**, 83–96.
- McGee, D., W. S. Broecker, and G. Winckler, 2010: Gustiness: the driver of glacial dustiness? *Quat. Sci. Rev.*, **29**, 2340–2350.
- McGregor, S., and A. Timmermann, 2010: The effect of explosive tropical volcanism on ENSO. *J. Clim.*, **24**, 2178–2191.
- McGregor, S., A. Timmermann, and O. Timm, 2010: A unified proxy for ENSO and PDO variability since 1650. *Clim. Past*, **6**, 1–17.
- McInerney, F. A., and S. L. Wing, 2011: The Paleocene-Eocene Thermal Maximum: A perturbation of carbon cycle, climate, and biosphere with implications for the future. *Annu. Rev. Earth Planet. Sci.*, **39**, 489–516.
- McKay, N. P., D. S. Kaufman, and N. Michelutti, 2008: Biogenic silica concentration as a high-resolution, quantitative temperature proxy at Hallet Lake, south-central Alaska. *Geophys. Res. Lett.*, **35**, L05709.
- McKay, N. P., J. T. Overpeck, and B. L. Otto-Bliesner, 2011: The role of ocean thermal expansion in Last Interglacial sea level rise. *Geophys. Res. Lett.*, **38**, L14605.
- McKay, R., et al., 2012a: Pleistocene variability of Antarctic ice sheet extent in the Ross embayment. *Quat. Sci. Rev.*, **34**, 93–112.
- McKay, R., et al., 2012b: Antarctic and Southern Ocean influences on Late Pliocene global cooling. *Proc. Natl. Acad. Sci. U.S.A.*, **109**, 6423–6428.
- McManus, J., R. Francois, J. Gherardi, L. Keigwin, and S. Brown-Leger, 2004: Collapse and rapid resumption of Atlantic meridional circulation linked to deglacial climate changes. *Nature*, **428**, 834–837.
- McShane, B. B., and A. J. Wyner, 2011: A statistical analysis of multiple temperature proxies: Are reconstructions of surface temperatures over the last 1000 years reliable? *Ann. Appl. Stat.*, **5**, 5–44.
- Meckler, A. N., M. O. Clarkson, K. M. Cobb, H. Sodemann, and J. F. Adkins, 2013: Inter-glacial hydroclimate in the tropical West Pacific through the Late Pleistocene. *Science*, **336**, 1301–1304.
- Meko, D. M., C. A. Woodhouse, C. A. Baisan, T. Knight, J. J. Lukas, M. K. Hughes, and M. W. Salzer, 2007: Medieval drought in the upper Colorado River Basin. *Geophys. Res. Lett.*, **34**, L10705.
- Melvin, T. M., and K. R. Briffa, 2008: A “signal-free” approach to dendroclimatic standardisation. *Dendrochronologia*, **26**, 71–86.
- Melvin, T. M., H. Rudd, and K. R. Briffa, 2013: Potential bias in ‘updating’ tree-ring chronologies using regional curve standardisation: Re-processing 1500 years of Tornetrask density and ring-width data. *Holocene*, **23**, 364–373.
- Menounos, B., G. Osborn, J. Clague, and B. Luckman, 2009: Latest Pleistocene and Holocene glacier fluctuations in western Canada. *Quat. Sci. Rev.*, **28**, 2049–2074.
- Menviel, L., A. Timmermann, O. E. Timm, and A. Mouchet, 2011: Deconstructing the last glacial termination: the role of millennial and orbital-scale forcings. *Quat. Sci. Rev.*, **30**, 1155–1172.
- Merkel, U., M. Prange, and M. Schulz, 2010: ENSO variability and teleconnections during glacial climates. *Quat. Sci. Rev.*, **29**, 86–100.
- Miller, G. H., A. P. Wolfe, J. P. Briner, P. E. Sauer, and A. Nesje, 2005: Holocene glaciation and climate evolution of Baffin Island, Arctic Canada. *Quat. Sci. Rev.*, **24**, 1703–1721.
- Miller, G. H., et al., 1999: Stratified interglacial lacustrine sediments from Baffin Island, Arctic Canada: Chronology and paleoenvironmental implications. *Quat. Sci. Rev.*, **18**, 789–810.

- Miller, K. G., et al., 2012a: High tide of the warm Pliocene: implications of global sea level for Antarctic deglaciation. *Geology*, **40**, 407–410.
- Miller, M. D., J. F. Adkins, D. Menemenlis, and M. P. Schodlok, 2012b: The role of ocean cooling in setting glacial southern source bottom water salinity. *Paleoceanography*, **27**, PA3207.
- Milne, G., and J. Mitrovica, 2008: Searching for eustasy in deglacial sea level histories. *Quat. Sci. Rev.*, **27**, 2292–2302.
- Mischler, J. A., et al., 2009: Carbon and hydrogen isotopic composition of methane over the last 1000 years. *Global Biogeochem. Cycles*, **23**, GB4024.
- Moberg, A., 2013: Comments on "Reconstruction of the extra-tropical NH mean temperature over the last millennium with a method that preserves low-frequency variability". *J. Clim.*, **25**, 7991–7997.
- Moberg, A., D. M. Sonechkin, K. Holmgren, N. M. Datsenko, and W. Karlén, 2005: Highly variable Northern Hemisphere temperatures reconstructed from low- and high-resolution proxy data. *Nature*, **433**, 613–617.
- Mohtadi, M., D. W. Oppo, S. Steinke, J.-B. W. Stuut, R. De Pol-Holz, D. Hebbeln, and A. Lückge, 2011: Glacial to Holocene swings of the Australian-Indonesian monsoon. *Nature Geosci.*, **4**, 540–544.
- Monnin, E., et al., 2001: Atmospheric CO₂ concentrations over the last glacial termination. *Science*, **291**, 112–114.
- Moore, J. C., E. Beaudon, S. Kang, D. Divine, E. Isaksson, V. A. Pohjola, and R. S. W. van de Wal, 2012: Statistical extraction of volcanic sulphate from nonpolar ice cores. *J. Geophys. Res.*, **117**, D03306.
- Morales, M. S., et al., 2012: Precipitation changes in the South American Altiplano since 1300 AD reconstructed by tree-rings. *Clim. Past*, **8**, 653–666.
- Morice, C. P., J. J. Kennedy, N. A. Rayner, and P. D. Jones, 2012: Quantifying uncertainties in global and regional temperature change using an ensemble of observational estimates: The HadCRUT4 data set. *J. Geophys. Res.*, **117**, D08101.
- Moros, M., J. T. Andrews, D. D. Eberl, and E. Jansen, 2006: Holocene history of drift ice in the northern North Atlantic: Evidence for different spatial and temporal modes. *Paleoceanography*, **21**, PA2017.
- Moros, M., P. De Deckker, E. Jansen, K. Perner, and R. J. Telford, 2009: Holocene climate variability in the Southern Ocean recorded in a deep-sea sediment core off South Australia. *Quat. Sci. Rev.*, **28**, 1932–1940.
- Morrill, C., A. J. Wagner, B. L. Otto-Btiesner, and N. Rosenbloom, 2011: Evidence for significant climate impacts in monsoonal Asia at 8.2 ka from multiple proxies and model simulations. *J. Earth Environ.*, **2**, 426–441.
- Morrill, C., A. N. LeGrande, H. Renessen, P. Bakker, and B. L. Otto-Btiesner, 2013a: Model sensitivity to North Atlantic freshwater forcing at 8.2 ka. *Clim. Past*, **9**, 955–968.
- Morrill, C., et al., 2013b: Proxy benchmarks for intercomparison of 8.2 ka simulations. *Clim. Past*, **9**, 423–432.
- Moucha, R., A. M. Forte, J. X. Mitrovica, D. B. Rowley, S. Quéré, N. A. Simmons, and S. P. Grand, 2008: Dynamic topography and long-term sea level variations: There is no such thing as a stable continental platform. *Earth Planet. Sci. Lett.*, **271**, 101–108.
- Mudelsee, M., 2001: The phase relations among atmospheric CO₂ content, temperature and global ice volume over the past 420 ka. *Quat. Sci. Rev.*, **20**, 583–589.
- Mudelsee, M., and M. E. Raymo, 2005: Slow dynamics of the Northern Hemisphere glaciation. *Paleoceanography*, **20**, PA4022.
- Mudelsee, M., J. Fohlmeister, and D. Scholz, 2012: Effects of dating errors on non-parametric trend analyses of speleothem time series. *Clim. Past*, **8**, 1637–1648.
- Mudelsee, M., M. Börngen, G. Tetzlaff, and U. Grunewald, 2003: No upward trends in the occurrence of extreme floods in central Europe. *Nature*, **425**, 166–169.
- Mulitza, S., et al., 2008: Sahel megadroughts triggered by glacial slowdowns of Atlantic meridional overturning. *Paleoceanography*, **23**, PA4206.
- Müller, J., A. Wagner, K. Fahl, R. Stein, M. Prange, and G. Lohmann, 2011: Towards quantitative sea ice reconstructions in the northern North Atlantic: A combined biomarker and numerical modelling approach. *Earth Planet. Sci. Lett.*, **306**, 137–148.
- Müller, R. D., M. Sdrolias, C. Gaina, B. Steinberger, and C. Heine, 2008: Long-term sea level fluctuations driven by ocean basin dynamics. *Science*, **319**, 1357–1362.
- Müller, U., 2001: *Die Vegetations-und Klimaentwicklung im jüngeren Quartär anhand ausgewählter Profile aus dem südwestdeutschen Alpenvorland*. Tübinger Geowissenschaftliche Arbeiten D7, Geographisches Institut der Universität Tübingen, 118 pp.
- Mulvaney, R., et al., 2012: Recent Antarctic Peninsula warming relative to Holocene climate and ice-shelf history. *Nature*, **489**, 141–144.
- Muscheler, R., and J. Beer, 2006: Solar forced Dansgaard/Oeschger events? *Geophys. Res. Lett.*, **33**, L20706.
- Muscheler, R., F. Joos, J. Beer, S. A. Müller, M. Vonmoos, and I. Snowball, 2007: Solar activity during the last 1000 yr inferred from radionuclide records. *Quat. Sci. Rev.*, **26**, 82–97.
- Naish, T., et al., 2009a: Obliquity-paced Pliocene West Antarctic ice sheet oscillations. *Nature*, **458**, 322–328.
- Naish, T. R., and G. S. Wilson, 2009: Constraints on the amplitude of mid-Pliocene (3.6–2.4 Ma) eustatic sea level fluctuations from the New Zealand shallow-marine sediment record. *Philos. Trans. R. Soc. London A*, **367**, 169–187.
- Naish, T. R., L. Carter, E. Wolff, D. Pollard, and R. D. Powell, 2009b: Late Pliocene–Pleistocene Antarctic climate variability at orbital and suborbital scale: Ice sheet, ocean and atmospheric interactions. In: *Developments in Earth & Environmental Sciences* [F. Florindo and S. M. (eds.)]. Elsevier, Philadelphia, PA, USA, pp. 465–529.
- Nakagawa, T., et al., 2008: Regulation of the monsoon climate by two different orbital rhythms and forcing mechanisms. *Geology*, **36**, 491–494.
- NEEM community members, 2013: Eemian interglacial reconstructed from Greenland folded ice core. *Nature*, **493**, 489–494.
- Neppel, L., et al., 2010: Flood frequency analysis using historical data: Accounting for random and systematic errors. *Hydrol. Sci. J. J. Sci. Hydrol.*, **55**, 192–208.
- Nesje, A., 2009: Latest Pleistocene and Holocene alpine glacier fluctuations in Scandinavia. *Quat. Sci. Rev.*, **28**, 2119–2136.
- Nesje, A., et al., 2011: The climatic significance of artefacts related to prehistoric reindeer hunting exposed at melting ice patches in southern Norway. *Holocene*, **22**, 485–496.
- Neukom, R., and J. Gergis, 2011: Southern Hemisphere high-resolution palaeoclimate records of the last 2000 years. *Holocene*, **22**, 501–524.
- Neukom, R., et al., 2011: Multiproxy summer and winter surface air temperature field reconstructions for southern South America covering the past centuries. *Clim. Dyn.*, **37**, 35–51.
- Newby, P. E., B. N. Shuman, J. P. Donnelly, and D. MacDonald, 2011: Repeated century-scale droughts over the past 13,000 yr near the Hudson River watershed, USA. *Quat. Res.*, **75**, 523–530.
- Nicault, A., S. Alleaume, S. Brewer, M. Carrer, P. Nola, and J. Guiot, 2008: Mediterranean drought fluctuation during the last 500 years based on tree-ring data. *Clim. Dyn.*, **31**, 227–245.
- Nicolussi, K., M. Kaufmann, T. M. Melvin, J. van der Plicht, P. Schießling, and A. Thurner, 2009: A 9111 year long conifer tree-ring chronology for the European Alps: a base for environmental and climatic investigations. *Holocene*, **19**, 909–920.
- Nordt, L., S. Atchley, and S. I. Dworkin, 2002: Paleosol barometer indicates extreme fluctuations in atmospheric CO₂ across the Cretaceous-Tertiary boundary. *Geology*, **30**, 703–706.
- Nørgaard-Pedersen, N., N. Mikkelsen, S. J. Lassen, Y. Kristoffersen, and E. Sheldon, 2007: Reduced sea ice concentrations in the Arctic Ocean during the last interglacial period revealed by sediment cores off northern Greenland. *Paleoceanography*, **22**, PA1218.
- North Greenland Ice Core Project members, 2004: High-resolution record of Northern Hemisphere climate extending into the last interglacial period. *Nature*, **431**, 147–151.
- Novenko, E. Y., M. Seifert-Eulen, T. Boettger, and F. W. Junge, 2008: Eemian and early Weichselian vegetation and climate history in Central Europe: a case study from the Klinge section (Lusatia, eastern Germany). *Rev. Palaeobot. Palynol.*, **151**, 72–78.
- O'Donnell, R., N. Lewis, S. McIntyre, and J. Condon, 2010: Improved methods for PCA-based reconstructions: case study using the Steig et al. (2009) Antarctic temperature reconstruction. *J. Clim.*, **24**, 2099–2115.
- Oerlemans, J., 1980: Model experiments on the 100,000-yr glacial cycle. *Nature*, **287**, 430–432.
- Ohba, M., H. Shiogama, T. Yokohata, and M. Watanabe, 2013: Impact of strong tropical volcanic eruptions on ENSO simulated in a coupled GCM. *J. Clim.*, **26**, 5169–5182.
- Okazaki, Y., et al., 2010: Deepwater formation in the north Pacific during the Last Glacial Termination. *Science*, **329**, 200–204.
- Okumura, Y. M., C. Deser, A. Hu, A. Timmermann, and S. P. Xie, 2009: North Pacific climate response to freshwater forcing in the subarctic North Atlantic: Oceanic and atmospheric pathways. *J. Clim.*, **22**, 1424–1445.
- Olsen, J., N. J. Anderson, and M. F. Knudsen, 2012: Variability of the North Atlantic Oscillation over the past 5,200 years. *Nature Geosci.*, **5**, 808–812.

- Oman, L., A. Robock, G. Stenchikov, G. A. Schmidt, and R. Ruedy, 2005: Climatic response to high-latitude volcanic eruptions. *J. Geophys. Res.*, **110**, D13103.
- Orsi, A. J., B. D. Cornuelle, and J. P. Severinghaus, 2012: Little Ice Age cold interval in West Antarctica: Evidence from borehole temperature at the West Antarctic Ice Sheet (WAIS) Divide. *Geophys. Res. Lett.*, **39**, L09710.
- Osborn, T., and K. Briffa, 2007: Response to comment on "The spatial extent of 20th-century warmth in the context of the past 1200 years". *Science*, **316**, 1844.
- Osborn, T., S. Raper, and K. Briffa, 2006: Simulated climate change during the last 1,000 years: Comparing the ECHO-G general circulation model with the MAGICC simple climate model. *Clim. Dyn.*, **27**, 185–197.
- Oswald, W. W., and D. R. Foster, 2011: A record of late-Holocene environmental change from southern New England, USA. *Quat. Res.*, **76**, 314–318.
- Ottera, O. H., M. Bentzen, H. Drange, and L. L. Suo, 2010: External forcing as a metronome for Atlantic multidecadal variability. *Nature Geosci.*, **3**, 688–694.
- Otto-Btiesner, B., et al., 2009: A comparison of PMIP2 model simulations and the MARGO proxy reconstruction for tropical sea surface temperatures at Last Glacial Maximum. *Clim. Dyn.*, **32**, 799–815.
- Otto-Btiesner, B. L., and E. C. Brady, 2010: The sensitivity of the climate response to the magnitude and location of freshwater forcing: Last glacial maximum experiments. *Quat. Sci. Rev.*, **29**, 56–73.
- Otto-Btiesner, B. L., N. Rosenbloom, E. J. Stone, N. McKay, D. Lunt, E. C. Brady, and J. T. Overpeck, 2013: How warm was the last interglacial? New model-data comparisons. *Philos. Trans. R. Soc. London A*, **371**, 20130097, published online 16 September 2013.
- Otto-Btiesner, B. L., et al., 2007: Last Glacial Maximum ocean thermohaline circulation: PMIP2 model intercomparisons and data constraints. *Geophys. Res. Lett.*, **34**, L12706.
- Otto, J., T. Raddatz, M. Claussen, V. Brovkin, and V. Gayler, 2009: Separation of atmosphere-ocean-vegetation feedbacks and synergies for mid-Holocene climate. *Geophys. Res. Lett.*, **36**, L09701.
- Overpeck, J., B. Otto-Btiesner, G. Miller, D. Muhs, R. Alley, and J. Kiehl, 2006: Paleoclimatic evidence for future ice-sheet instability and rapid sea level rise. *Science*, **311**, 1747–1750.
- Pagani, M., K. H. Freeman, and M. A. Arthur, 1999a: Late Miocene Atmospheric CO₂ concentrations and the expansion of C4 grasses. *Science*, **285**, 876–879.
- Pagani, M., M. A. Arthur, and K. H. Freeman, 1999b: Miocene evolution of atmospheric carbon dioxide. *Paleoceanography*, **14**, 273–292.
- Pagani, M., D. Lemarchand, A. Spivack, and J. Gaillardet, 2005a: A critical evaluation of the boron isotope-pH proxy: The accuracy of ancient ocean pH estimates. *Geochim. Cosmochim. Acta*, **69**, 953–961.
- Pagani, M., Z. H. Liu, J. LaRiviere, and A. C. Ravelo, 2010: High Earth-system climate sensitivity determined from Pliocene carbon dioxide concentrations. *Nature Geosci.*, **3**, 27–30.
- Pagani, M., J. C. Zachos, K. H. Freeman, B. Tipple, and S. Bohaty, 2005b: Marked decline in atmospheric carbon dioxide concentrations during the Paleogene. *Science*, **309**, 600–603.
- Pagani, M., et al., 2011: The role of carbon dioxide during the onset of Antarctic glaciation. *Science*, **334**, 1261–1264.
- PAGES 2k Consortium, 2013: Continental-scale temperature variability during the last two millennia. *Nature Geosci.*, **6**, 339–346.
- Pahnke, K., R. Zahn, H. Elderfield, and M. Schulz, 2003: 340,000-year centennial-scale marine record of Southern Hemisphere climatic oscillation. *Science*, **301**, 948–952.
- Pahnke, K., J. P. Sachs, L. Keigwin, A. Timmermann, and S. P. Xie, 2007: Eastern tropical Pacific hydrologic changes during the past 27,000 years from D/H ratios in alkenones. *Paleoceanography*, **22**, PA4214.
- Pak, D. K., D. W. Lea, and J. P. Kennett, 2012: Millennial scale changes in sea surface temperature and ocean circulation in the northeast Pacific, 10–60 kyr BP. *Paleoceanography*, **27**, PA1212.
- PALAEOSENS Project Members, 2012: Making sense of palaeoclimate sensitivity. *Nature*, **491**, 683–691.
- Palastanga, V., G. van der Schrier, S. Weber, T. Kleinen, K. Briffa, and T. Osborn, 2011: Atmosphere and ocean dynamics: contributors to the European Little Ice Age? *Clim. Dyn.*, **36**, 973–987.
- Panchuk, K., A. Ridgwell, and L. R. Kump, 2008: Sedimentary response to Paleocene-Eocene Thermal Maximum carbon release: a model-data comparison. *Geology*, **36**, 315–318.
- Parrenin, F., et al., 2013: Synchronous change of atmospheric CO₂ and Antarctic temperature during the last deglacial warming. *Science*, **339**, 1060–1063.
- Passchier, S., 2011: Linkages between East Antarctic ice sheet extent and Southern Ocean temperatures based on a Pliocene high-resolution record of ice-rafter debris off Prydz Bay, East Antarctica. *Paleoceanography*, **26**, PA4204.
- Patadia, F., E.-S. Yang, and S. A. Christopher, 2009: Does dust change the clear sky top of atmosphere shortwave flux over high surface reflectance regions? *Geophys. Res. Lett.*, **36**, L15825.
- Pausata, F. S. R., C. Li, J. J. Wattstein, K. H. Nisancioğlu, and D. S. Battisti, 2009: Changes in atmospheric variability in a glacial climate and the impacts on proxy data: A model intercomparison. *Clim. Past*, **5**, 489–502.
- Pausata, F. S. R., C. Li, J. J. Wattstein, M. Kageyama, and K. H. Nisancioğlu, 2011: The key role of topography in altering North Atlantic atmospheric circulation during the last glacial period. *Clim. Past*, **7**, 1089–1101.
- Pearson, P. N., G. L. Foster, and B. S. Wade, 2009: Atmospheric carbon dioxide through the Eocene-Oligocene climate transition. *Nature*, **461**, 1110–1113.
- Pedro, J., et al., 2011: The last deglaciation: timing the bipolar seesaw. *Clim. Past*, **7**, 671–683.
- Pedro, J. B., S. O. Rasmussen, and T. D. van Ommen, 2012: Tightened constraints on the time-lag between Antarctic temperature and CO₂ during the last deglaciation. *Clim. Past*, **8**, 1213–1221.
- Pépin, L., D. Raynaud, J.-M. Barnola, and M. F. Loutre, 2001: Hemispheric roles of climate forcings during glacial-interglacial transitions as deduced from the Vostok record and LLN-2D model experiments. *J. Geophys. Res.*, **106**, 31885–31892.
- Peschke, P., C. Hannss, and S. Klotz, 2000: Neuere Ergebnisse aus der Banquette von Barraux (Grésivaudan, französische Nordalpen) zur spätpleistozänen Vegetationsentwicklung mit Beiträgen zur Reliefgenese und Klimarekonstruktion. *Eiszeitalter Gegenwart*, **50**, 1–24.
- Peterson, L. C., and G. H. Haug, 2006: Variability in the mean latitude of the Atlantic Intertropical Convergence Zone as recorded by riverine input of sediments to the Cariaco Basin (Venezuela). *Palaeogeogr. Palaeoclimatol. Palaeoecol.*, **234**, 97–113.
- Petit, J. R., and B. Delmonte, 2009: A model for large glacial-interglacial climate-induced changes in dust and sea salt concentrations in deep ice cores (central Antarctica): palaeoclimatic implications and prospects for refining ice core chronologies. *Tellus B*, **61B**, 768–790.
- Petit, J. R., et al., 1999: Climate and atmospheric history of the past 420,000 years from the Vostok ice core, Antarctica. *Nature*, **399**, 429–436.
- Phipps, S., et al., 2013: Palaeoclimate data-model comparison and the role of climate forcings over the past 1500 years. *J. Clim.*, **26**, 6915–6936.
- Piccarreta, M., M. Caldara, D. Capolongo, and F. Boenzi, 2011: Holocene geomorphic activity related to climatic change and human impact in Basilicata, Southern Italy. *Geomorphology*, **128**, 137–147.
- Pinto, J. G., and C. C. Raible, 2012: Past and recent changes in the North Atlantic Oscillation. *WIREs Clim. Change*, **3**, 79–90.
- Piotrowski, A. M., S. L. Goldstein, S. R. Hemming, and R. G. Fairbanks, 2005: Temporal relationships of carbon cycling and ocean circulation at glacial boundaries. *Science*, **307**, 1933–1938.
- Plummer, C. T., et al., 2012: An independently dated 2000-yr volcanic record from Law Dome, East Antarctica, including a new perspective on the dating of the 1450s CE eruption of Kuwae, Vanuatu. *Clim. Past*, **8**, 1929–1940.
- Pollack, H. N., and J. E. Smerdon, 2004: Borehole climate reconstructions: Spatial structure and hemispheric averages. *J. Geophys. Res.*, **109**, D11106.
- Pollard, D., and R. M. DeConto, 2009: Modelling West Antarctic ice sheet growth and collapse through the past five million years. *Nature*, **458**, 329–332.
- Polyak, L., et al., 2010: History of sea ice in the Arctic. *Quat. Sci. Rev.*, **29**, 1757–1778.
- Polyakov, I. V., et al., 2010: Arctic Ocean warming contributes to reduced polar ice cap. *J. Phys. Oceanogr.*, **40**, 2743–2756.
- Pongratz, J., C. Reick, T. Raddatz, and M. Claussen, 2008: A reconstruction of global agricultural areas and land cover for the last millennium. *Global Biogeochem. Cycles*, **22**, GB3018.
- Pongratz, J., T. Raddatz, C. H. Reick, M. Esch, and M. Claussen, 2009: Radiative forcing from anthropogenic land cover change since A.D. 800. *Geophys. Res. Lett.*, **36**, L02709.
- Ponton, C., L. Giosan, T. I. Eglinton, D. Q. Fuller, J. E. Johnson, P. Kumar, and T. S. Collett, 2012: Holocene aridification of India. *Geophys. Res. Lett.*, **39**, L03704.
- Porter, T. J., and M. F. J. Pisaric, 2011: Temperature-growth divergence in white spruce forests of Old Crow Flats, Yukon Territory, and adjacent regions of northwestern North America. *Global Change Biol.*, **17**, 3418–3430.

- Prieto, M. d. R., and R. García Herrera, 2009: Documentary sources from South America: Potential for climate reconstruction. *Palaeogeogr. Palaeoclimatol. Palaeoecol.*, **281**, 196–209.
- Prokopenko, A., L. Hinnov, D. Williams, and M. Kuzmin, 2006: Orbital forcing of continental climate during the Pleistocene: A complete astronomically tuned climatic record from Lake Baikal, SE Siberia. *Quat. Sci. Rev.*, **25**, 3431–3457.
- Prokopenko, A. A., D. F. Williams, M. I. Kuzmin, E. B. Karabanova, G. K. Khurshovich, and J. A. Peck, 2002: Muted climate variations in continental Siberia during the mid-Pleistocene epoch. *Nature*, **418**, 65–68.
- Putnam, A. E., et al., 2010: Glacier advance in southern middle-latitudes during the Antarctic Cold Reversal. *Nature Geosci.*, **3**, 700–704.
- Quiquet, A., C. Ritz, H. J. Punge, and D. Salas y Melia, 2013: Greenland ice sheet contribution to sea level rise during the last interglacial period: A modelling study driven and constrained by ice core data. *Clim. Past*, **8**, 353–366.
- Rahmstorf, S., et al., 2005: Thermohaline circulation hysteresis: A model intercomparison. *Geophys. Res. Lett.*, **32**, L23605.
- Ramankutty, N., and J. A. Foley, 1999: Estimating historical changes in global land cover: Croplands from 1700 to 1992. *Global Biogeochem. Cycles*, **13**, 997–1027.
- Rasmussen, S. O., et al., 2006: A new Greenland ice core chronology for the last glacial termination. *J. Geophys. Res.*, **111**, D06102.
- Raymo, M. E., and J. X. Mitrovica, 2012: Collapse of polar ice sheets during the stage 11 interglacial. *Nature*, **483**, 453–456.
- Raymo, M. E., J. X. Mitrovica, M. J. O’Leary, R. M. DeConto, and P. J. Hearty, 2011: Departures from eustasy in Pliocene sea level records. *Nature Geosci.*, **4**, 328–332.
- Renssen, H., H. Seppä, X. Crosta, H. Goosse, and D. M. Roche, 2012: Global characterization of the Holocene Thermal Maximum. *Quat. Sci. Rev.*, **48**, 7–19.
- Retallack, G. J., 2009a: Refining a pedogenic-carbonate CO₂ paleobarometer to quantify a middle Miocene greenhouse spike. *Palaeogeogr. Palaeoclimatol. Palaeoecol.*, **281**, 57–65.
- Retallack, G. J., 2009b: Greenhouse crises of the past 300 million years. *Geol. Soc. Am. Bull.*, **121**, 1441–1455.
- Reuter, J., L. Stott, D. Khider, A. Sinha, H. Cheng, and R. L. Edwards, 2009: A new perspective on the hydroclimate variability in northern South America during the Little Ice Age. *Geophys. Res. Lett.*, **36**, L21706.
- Ridgwell, A., and D. N. Schmidt, 2010: Past constraints on the vulnerability of marine calcifiers to massive carbon dioxide release. *Nature Geosci.*, **3**, 196–200.
- Ridley, J., J. Gregory, P. Huybrechts, and J. Lowe, 2010: Thresholds for irreversible decline of the Greenland ice sheet. *Clim. Dyn.*, **35**, 1049–1057.
- Rimbu, N., G. Lohmann, J. H. Kim, H. W. Arz, and R. Schneider, 2003: Arctic/North Atlantic Oscillation signature in Holocene sea surface temperature trends as obtained from alkenone data. *Geophys. Res. Lett.*, **30**, 4.
- Risebrobakken, B., T. Dokken, L. H. Smedsrød, C. Andersson, E. Jansen, M. Moros, and E. V. Ivanova, 2011: Early Holocene temperature variability in the Nordic Seas: The role of oceanic heat advection versus changes in orbital forcing. *Paleoceanography*, **26**, PA4206.
- Ritz, S., T. Stocker, and F. Joos, 2011: A coupled dynamical ocean-energy balance atmosphere model for paleoclimate studies. *J. Clim.*, **24**, 349–375.
- Riviere, G., A. Laîné, G. Lapeyre, D. Salas-Melia, and M. Kageyama, 2010: Links between Rossby wave breaking and the North Atlantic Oscillation-Arctic Oscillation in present-day and Last Glacial Maximum climate simulations. *J. Clim.*, **23**, 2987–3008.
- Roberts, A. P., E. J. Rohling, K. M. Grant, J. C. Larrasoña, and Q. Liu, 2011: Atmospheric dust variability from Arabia and China over the last 500,000 years. *Quat. Sci. Rev.*, **30**, 3537–3541.
- Roberts, N. L., A. M. Piotrowski, J. F. McManus, and L. D. Keigwin, 2010: Synchronous deglacial overturning and water mass source changes. *Science*, **327**, 75–78.
- Robertson, A., et al., 2001: Hypothesized climate forcing time series for the last 500 years. *J. Geophys. Res.*, **106**, 14783–14803.
- Robinson, A., R. Calov, and A. Ganopolski, 2011: Greenland ice sheet model parameters constrained using simulations of the Eemian Interglacial. *Clim. Past*, **7**, 381–396.
- Roche, D. M., X. Crosta, and H. Renssen, 2012: Evaluating Southern Ocean sea-ice for the Last Glacial Maximum and pre-industrial climates: PMIP-2 models and data evidence. *Quat. Sci. Rev.*, **56**, 99–106.
- Roe, G. H., and R. S. Lindzen, 2001: The mutual interaction between continental-scale ice sheets and atmospheric stationary waves. *J. Clim.*, **14**, 1450–1465.
- Roeckner, E., L. Bengtsson, J. Feichter, J. Lelieveld, and H. Rodhe, 1999: Transient climate change simulations with a coupled atmosphere–ocean GCM including the tropospheric sulfur cycle. *J. Clim.*, **12**, 3004–3032.
- Rohling, E. J., and H. Pälike, 2005: Centennial-scale climate cooling with a sudden cold event around 8,200 years ago. *Nature*, **434**, 975–979.
- Rohling, E. J., M. Medina-Elizalde, J. G. Shepherd, M. Siddall, and J. D. Stanford, 2012: Sea surface and high-latitude temperature sensitivity to radiative forcing of climate over several glacial cycles. *J. Clim.*, **25**, 1635–1656.
- Rohling, E. J., K. Grant, C. Hemleben, M. Siddall, B. A. A. Hoogakker, M. Bolshaw, and M. Kucera, 2008a: High rates of sea level rise during the last interglacial period. *Nature Geosci.*, **1**, 38–42.
- Rohling, E. J., K. Grant, M. Bolshaw, A. P. Roberts, M. Siddall, C. Hemleben, and M. Kucera, 2009: Antarctic temperature and global sea level closely coupled over the past five glacial cycles. *Nature Geosci.*, **2**, 500–504.
- Rohling, E. J., K. Braun, K. Grant, M. Kucera, A. P. Roberts, M. Siddall, and G. Trommer, 2010: Comparison between Holocene and Marine Isotope Stage-11 sea level histories. *Earth Planet. Sci. Lett.*, **291**, 97–105.
- Rohling, E. J., et al., 2008b: New constraints on the timing of sea level fluctuations during early to middle marine isotope stage 3. *Paleoceanography*, **23**, PA3219.
- Rojas, M., 2013: Sensitivity of Southern Hemisphere circulation to LGM and 4 × CO₂ climates. *Geophys. Res. Lett.*, **40**, 965–970.
- Rousseau, D.-D., C. Hatté, D. Duzer, P. Schevin, G. Kukla, and J. Guiot, 2007: Estimates of temperature and precipitation variations during the Eemian interglacial: New data from the grande pile record (GP XXI). In: *Developments in Quaternary Sciences* [F. Sirocko, M. Claussen, M. F. Sánchez Goñi, and T. Litt (eds.)]. Elsevier, Philadelphia, PA, USA, pp. 231–238.
- Routson, C. C., C. A. Woodhouse, and J. T. Overpeck, 2011: Second century megadrought in the Rio Grande headwaters, Colorado: How unusual was medieval drought? *Geophys. Res. Lett.*, **38**, L22703.
- Royer, D. L., 2003: Estimating latest Cretaceous and Tertiary atmospheric CO₂ from stomatal indices. In: *Causes and Consequences of Globally Warm Climates in the Early Paleogen* [S. L. Wing, P. D. Gingerich, B. Schmitz and E. Thomas (eds.)]. Geological Society of America Special Paper 369, pp. 79–93.
- Royer, D. L., R. A. Berner, and D. J. Beerling, 2001a: Phanerozoic atmospheric CO₂ change: evaluating geochemical and paleobiological approaches. *Earth Sci. Rev.*, **54**, 349–392.
- Royer, D. L., S. L. Wing, D. J. Beerling, D. W. Jolley, P. L. Koch, L. J. Hickey, and R. A. Berner, 2001b: Paleobotanical evidence for near present-day levels of atmospheric CO₂ during part of the Tertiary. *Science*, **292**, 2310–2313.
- Rupper, S., G. Roe, and A. Gillespie, 2009: Spatial patterns of Holocene glacier advance and retreat in Central Asia. *Quat. Res.*, **72**, 337–346.
- Russell, J., H. Eggermont, R. Taylor, and D. Verschuren, 2009: Paleolimnological records of recent glacier recession in the Rwenzori Mountains, Uganda-D. R. Congo. *J. Paleolimnol.*, **41**, 253–271.
- Ruth, U., et al., 2007: Ice core evidence for a very tight link between North Atlantic and east Asian glacial climate. *Geophys. Res. Lett.*, **34**, L03706.
- Sachs, J. P., D. Sachse, R. H. Smittenberg, Z. H. Zhang, D. S. Battisti, and S. Golubic, 2009: Southward movement of the Pacific intertropical convergence zone AD 1400–1850. *Nature Geosci.*, **2**, 519–525.
- Saenger, C., A. Cohen, D. Oppo, R. Hallé, and J. Carilli, 2009: Surface-temperature trends and variability in the low-latitude North Atlantic since 1552. *Nature Geosci.*, **2**, 492–495.
- Saenko, O. A., A. Schmittner, and A. J. Weaver, 2004: The Atlantic-Pacific Seesaw. *J. Clim.*, **17**, 2033–2038.
- Salisbury, E. J., 1928: On the causes and ecological significance of stomatal frequency, with special reference to the woodland flora. *Philos. Trans. R. Soc. B*, **216**, 1–65.
- Salzer, M., and K. Kipfmüller, 2005: Reconstructed temperature and precipitation on a millennial timescale from tree-rings in the Southern Colorado Plateau, USA. *Clim. Change*, **70**, 465–487.
- Salzmann, U., A. M. Haywood, D. J. Lunt, P. J. Valdes, and D. J. Hill, 2008: A new global biome reconstruction and data-model comparison for the Middle Pliocene. *Global Ecol. Biogeogr.*, **17**, 432–447.
- Sarnthein, M., U. Pflaumann, and M. Weinelt, 2003a: Past extent of sea ice in the northern North Atlantic inferred from foraminiferal paleotemperature estimates. *Paleoceanography*, **18**, 1047.

- Sarnthein, M., S. Van Kreveld, H. Erlenkeuser, P. Grootes, M. Kucera, U. Pflaumann, and M. Schulz, 2003b: Centennial-to-millennial-scale periodicities of Holocene climate and sediment injections off the western Barents shelf, 75°N. *Boreas*, **32**, 447–461.
- Schaefer, J. M., et al., 2009: High-frequency Holocene glacier fluctuations in New Zealand differ from the northern signature. *Science*, **324**, 622–625.
- Scherer, D., M. Gude, M. Gempeler, and E. Parlow, 1998: Atmospheric and hydrological boundary conditions for slushflow initiation due to snowmelt. *Ann. Glaciol.*, **26**, 377–380.
- Schilt, A., M. Baumgartner, T. Blunier, J. Schwander, R. Spahni, H. Fischer, and T. F. Stocker, 2010: Glacial–interglacial and millennial-scale variations in the atmospheric nitrous oxide concentration during the last 800,000 years. *Quat. Sci. Rev.*, **29**, 182–192.
- Schmidt, A., T. Thordarson, L. D. Oman, A. Robock, and S. Sell, 2012a: Climatic impact of the long-lasting 1783 Laki eruption: Inapplicability of mass-independent sulfur isotopic composition measurements. *J. Geophys. Res.*, **117**, D23116.
- Schmidt, G. A., et al., 2011: Climate forcing reconstructions for use in PMIP simulations of the last millennium (v1.0). *Geoscientif. Model Dev.*, **4**, 33–45.
- Schmidt, G. A., et al., 2012b: Climate forcing reconstructions for use in PMIP simulations of the Last Millennium (v1.1). *Geoscientif. Model Dev.*, **5**, 185–191.
- Schmittner, A., E. D. Galbraith, S. W. Hostetler, T. F. Pedersen, and R. Zhang, 2007: Large fluctuations of dissolved oxygen in the Indian and Pacific oceans during Dansgaard-Oeschger oscillations caused by variations of North Atlantic Deep Water subduction. *Paleoceanography*, **22**, PA3207.
- Schmittner, A., et al., 2011: Climate sensitivity estimated from temperature reconstructions of the Last Glacial Maximum. *Science*, **334**, 1385–1388.
- Schneider, B., G. Leduc, and W. Park, 2010: Disentangling seasonal signals in Holocene climate trends by satellite-model-proxy integration. *Paleoceanography*, **25**, PA4217.
- Schneider, D. P., C. M. Ammann, B. L. Otto-Bliesner, and D. S. Kaufman, 2009: Climate response to large, high-latitude and low-latitude volcanic eruptions in the Community Climate System Model. *J. Geophys. Res.*, **114**, D15101.
- Schneider Mor, A., R. Yam, C. Bianchi, M. Kunz-Pirrung, R. Gersonde, and A. Shemesh, 2012: Variable sequence of events during the past seven terminations in two deep-sea cores from the Southern Ocean. *Quat. Res.*, **77**, 317–325.
- Schneider von Deimling, T., H. Held, A. Ganopolski, and S. Rahmstorf, 2006: Climate sensitivity estimated from ensemble simulations of glacial climate. *Clim. Dyn.*, **27**, 149–163.
- Schoof, C., 2012: Marine ice sheet stability. *J. Fluid Mech.*, **698**, 62–72.
- Schrijver, C. J., W. C. Livingston, T. N. Woods, and R. A. Mewaldt, 2011: The minimal solar activity in 2008–2009 and its implications for long-term climate modeling. *Geophys. Res. Lett.*, **38**, L06701.
- Schulz, H., U. von Rad, and H. Erlenkeuser, 1998: Correlation between Arabian Sea and Greenland climate oscillations of the past 110,000 years. *Nature*, **393**, 54–57.
- Schurer, A., G. C. Hegerl, M. E. Mann, S. F. B. Tett, and S. J. Phipps, 2013: Separating forced from chaotic climate variability over the past millennium. *J. Clim.*, **26**, 6954–6973.
- Schurges, G., U. Mikolajewicz, M. Gröger, E. Maier-Reimer, M. Vizcaino, and A. Winguth, 2007: The effect of land surface changes on Eemian climate. *Clim. Dyn.*, **29**, 357–373.
- Screen, J. A., and I. Simmonds, 2010: The central role of diminishing sea ice in recent Arctic temperature amplification. *Nature*, **464**, 1334–1337.
- Scroton, N., S. G. Bonham, R. E. M. Rickaby, S. H. F. Lawrence, M. Hermoso, and A. M. Haywood, 2011: Persistent El Niño-Southern Oscillation variation during the Pliocene Epoch. *Paleoceanography*, **26**, PA2215.
- Seager, R., N. Graham, C. Herweijer, A. Gordon, Y. Kushnir, and E. Cook, 2007: Blueprints for Medieval hydroclimate. *Quat. Sci. Rev.*, **26**, 2322–2336.
- Seki, O., G. L. Foster, D. N. Schmidt, A. Mackensen, K. Kawamura, and R. D. Pancost, 2010: Alkenone and boron-based Pliocene pCO₂ records. *Earth Planet. Sci. Lett.*, **292**, 201–211.
- Semenov, V. A., M. Latif, D. Dommenget, N. S. Keenlyside, A. Strehz, T. Martin, and W. Park, 2010: The Impact of North Atlantic-Arctic multidecadal variability on northern hemisphere surface air temperature. *J. Clim.*, **23**, 5668–5677.
- Seong, Y., L. Owen, C. Yi, and R. Finkel, 2009: Quaternary glaciation of Muztag Ata and Kongur Shan: Evidence for glacier response to rapid climate changes throughout the Late Glacial and Holocene in westernmost Tibet. *Geol. Soc. Am. Bull.*, **129**, 348–365.
- Serreze, M. C., and R. G. Barry, 2011: Processes and impacts of Arctic amplification: A research synthesis. *Global Planet. Change*, **77**, 85–96.
- Serreze, M. C., A. P. Barrett, J. C. Stroeve, D. N. Kindig, and M. M. Holland, 2009: The emergence of surface-based Arctic amplification. *Cryosphere*, **3**, 11–19.
- Servonnat, J., P. Yiou, M. Khodri, D. Swingedouw, and S. Denvil, 2010: Influence of solar variability, CO₂ and orbital forcing between 1000 and 1850 AD in the IPSL-CM4 model. *Clim. Past*, **6**, 445–460.
- Shackleton, N. J., 2000: The 100,000-year ice-age cycle identified and found to lag temperature, carbon dioxide, and orbital eccentricity. *Science*, **289**, 1897–1902.
- Shackleton, N. J., M. F. Sánchez-Góñi, D. Pailler, and Y. Lancelot, 2003: Marine Isotope Substage 5e and the Eemian interglacial. *Global Planet. Change*, **36**, 151–155.
- Shaffer, G., S. M. Olsen, and C. J. Bjerrum, 2004: Ocean subsurface warming as a mechanism for coupling Dansgaard-Oeschger climate cycles and ice-raftering events. *Geophys. Res. Lett.*, **31**, L24202.
- Shakun, J. D., et al., 2012: Global warming preceded by increasing carbon dioxide concentrations during the last deglaciation. *Nature*, **484**, 49–54.
- Shanahan, T. M., et al., 2009: Atlantic forcing of persistent drought in west Africa. *Science*, **324**, 377–380.
- Shapiro, A. I., W. Schmutz, E. Rozanov, M. Schoell, M. Haberreiter, A. V. Shapiro, and S. Nyeki, 2011: A new approach to the long-term reconstruction of the solar irradiance leads to large historical solar forcing. *Astron. Astrophys.*, **529**, 1–8.
- Sheffer, N. A., M. Rico, Y. Enzel, G. Benito, and T. Grodek, 2008: The Palaeoflood record of the Gardon River, France: A comparison with the extreme 2002 flood event. *Geomorphology*, **98**, 71–83.
- Shevenell, A. E., A. E. Ingalls, E. W. Domack, and C. Kelly, 2011: Holocene Southern Ocean surface temperature variability west of the Antarctic Peninsula. *Nature*, **470**, 250–254.
- Shi, F., et al., 2013: Northern hemisphere temperature reconstruction during the last millennium using multiple annual proxies. *Clim. Res.*, **56**, 231–244.
- Shin, S. I., P. D. Sardeshmukh, R. S. Webb, R. J. Oglesby, and J. J. Barsugli, 2006: Understanding the mid-Holocene climate. *J. Clim.*, **19**, 2801–2817.
- Shuman, B., P. Pribyl, T. A. Minckley, and J. J. Shinker, 2010: Rapid hydrologic shifts and prolonged droughts in Rocky Mountain headwaters during the Holocene. *Geophys. Res. Lett.*, **37**, L06701.
- Sicre, M. A., et al., 2008: A 4500-year reconstruction of sea surface temperature variability at decadal time-scales off North Iceland. *Quat. Sci. Rev.*, **27**, 2041–2047.
- Siddall, M., E. J. Rohling, W. G. Thompson, and C. Waelbroeck, 2008: Marine isotope stage 3 sea level fluctuations: Data synthesis and new outlook. *Rev. Geophys.*, **46**, RG4003.
- Siddall, M., E. J. Rohling, T. Blunier, and R. Spahni, 2010: Patterns of millennial variability over the last 500 ka. *Clim. Past*, **6**, 295–303.
- Siddall, M., T. F. Stocker, T. Blunier, R. Spahni, J. F. McManus, and E. Bard, 2006: Using a maximum simplicity paleoclimate model to simulate millennial variability during the last four glacial periods. *Quat. Sci. Rev.*, **25**, 3185–3197.
- Siddall, M., E. J. Rohling, A. Almogi-Labin, C. Hemleben, D. Meischner, I. Schmelzer, and D. A. Smeed, 2003: Sea level fluctuations during the last glacial cycle. *Nature*, **423**, 853–858.
- Siegenthaler, U., et al., 2005: Stable carbon cycle-climate relationship during the late Pleistocene. *Science*, **310**, 1313–1317.
- Sierro, F. J., et al., 2009: Phase relationship between sea level and abrupt climate change. *Quat. Sci. Rev.*, **28**, 2867–2881.
- Sigl, M., et al., 2013: A new bipolar ice core record of volcanism from WAIS Divide and NEEM and implications for climate forcing of the last 2000 years. *J. Geophys. Res.*, **118**, 1151–1169.
- Sime, L. C., E. W. Wolff, K. I. C. Oliver, and J. C. Tindall, 2009: Evidence for warmer interglacials in East Antarctic ice cores. *Nature*, **462**, 342–345.
- Sime, L. C., C. Risbø, J. C. Tindall, J. Sjøltd, E. W. Wolff, V. Masson-Delmotte, and E. Caprona, 2013: Warm climate isotopic simulations: What do we learn about interglacial signals in Greenland ice cores? *Quat. Sci. Rev.*, **67**, 59–80.
- Simms, A. R., K. T. Milliken, J. B. Anderson, and J. S. Wellner, 2011: The marine record of deglaciation of the South Shetland Islands, Antarctica since the Last Glacial Maximum. *Quat. Sci. Rev.*, **30**, 1583–1601.
- Singarayer, J. S., and P. J. Valdes, 2010: High-latitude climate sensitivity to ice-sheet forcing over the last 120 kyr. *Quat. Sci. Rev.*, **29**, 43–55.
- Sinha, A., and L. D. Stott, 1994: New atmospheric pCO₂ estimates from palesols during the late Paleocene/early Eocene global warming interval. *Global Planet. Change*, **9**, 297–307.

- Sinha, A., et al., 2007: A 900-year (600 to 1500 A.D.) record of the Indian summer monsoon precipitation from the core monsoon zone of India. *Geophys. Res. Lett.*, **34**, L16707.
- Sivan, D., K. Lambeck, R. Toueg, A. Raban, Y. Porath, and B. Shirman, 2004: Ancient coastal wells of Caesarea Maritima, Israel, an indicator for relative sea level changes during the last 2000 years. *Earth Planet. Sci. Lett.*, **222**, 315–330.
- Sluijs, A., et al., 2007: Environmental precursors to rapid light carbon injection at the Palaeocene/Eocene boundary. *Nature*, **450**, 1218–1221.
- Smerdon, J. E., 2012: Climate models as a test bed for climate reconstruction methods: pseudoproxy experiments. *Rev. Clim. Change*, **3**, 63–77.
- Smerdon, J. E., A. Kaplan, D. Chang, and M. N. Evans, 2010: A pseudoproxy evaluation of the CCA and RegEM methods for reconstructing climate fields of the last millennium. *J. Clim.*, **23**, 4856–4880.
- Smerdon, J. E., A. Kaplan, E. Zorita, J. F. González-Rouco, and M. N. Evans, 2011: Spatial performance of four climate field reconstruction methods targeting the Common Era. *Geophys. Res. Lett.*, **38**, L11705.
- Smith, J. A., et al., 2011: Deglacial history of the West Antarctic Ice Sheet in the western Amundsen Sea Embayment. *Quat. Sci. Rev.*, **30**, 488–505.
- Smith, R., and J. Gregory, 2012: The last glacial cycle: Transient simulations with an AOGCM. *Clim. Dyn.*, **38**, 1545–1559.
- Smith, R. Y., D. R. Greenwood, and J. F. Basinger, 2010: Estimating paleoatmospheric $p\text{CO}_2$ during the Early Eocene Climatic Optimum from stomatal frequency of Ginkgo, Okanagan Highlands, British Columbia, Canada. *Palaeogeogr. Palaeoclimatol. Palaeoecol.*, **293**, 120–131.
- Smithers, S. G., and C. D. Woodroffe, 2001: Coral microatolls and 20th century sea level in the eastern Indian Ocean. *Earth Planet. Sci. Lett.*, **191**, 173–184.
- Soden, B. J., I. M. Held, R. Colman, K. M. Shell, J. T. Kiehl, and C. A. Shields, 2008: Quantifying climate feedbacks using radiative kernels. *J. Clim.*, **21**, 3504–3520.
- Sokolov, S., and S. R. Rintoul, 2009: Circumpolar structure and distribution of the Antarctic Circumpolar Current fronts: 1. Mean circumpolar paths. *J. Geophys. Res.*, **114**, C11018.
- Solanki, S. K., I. G. Usoskin, B. Kromer, M. Schussler, and J. Beer, 2004: Unusual activity of the Sun during recent decades compared to the previous 11,000 years. *Nature*, **431**, 1084–1087.
- Sosdian, S., and Y. Rosenthal, 2009: Deep-sea temperature and ice volume changes across the Pliocene-Pleistocene climate transitions. *Science*, **325**, 306–310.
- Sowers, T., and M. Bender, 1995: Climate records covering the Last Deglaciation. *Science*, **269**, 210–214.
- Spence, J. P., M. Eby, and A. J. Weaver, 2008: The sensitivity of the Atlantic Meridional Overturning Circulation to freshwater forcing at eddy-permitting resolutions. *J. Clim.*, **21**, 2697–2710.
- Spielhagen, R. F., et al., 2011: Enhanced modern heat transfer to the Arctic by warm Atlantic water. *Science*, **331**, 450–453.
- St. George, S., et al., 2009: The tree-ring record of drought on the Canadian prairies. *J. Clim.*, **22**, 689–710.
- Stager, J. C., D. Ryves, B. F. Cumming, L. D. Meeker, and J. Beer, 2005: Solar variability and the levels of Lake Victoria, East Africa, during the last millennium. *J. Paleolimnol.*, **33**, 243–251.
- Stager, J. C., C. Cocquyt, R. Bonnefille, C. Weyhenmeyer, and N. Bowerman, 2009: A late Holocene paleoclimatic history of Lake Tanganyika, East Africa. *Quat. Res.*, **72**, 47–56.
- Stahle, D. W., et al., 2011: Major Mesoamerican droughts of the past millennium. *Geophys. Res. Lett.*, **38**, L05703.
- Stambaugh, M. C., R. P. Guyette, E. R. McMurry, E. R. Cook, D. M. Meko, and A. R. Lupo, 2011: Drought duration and frequency in the U.S. Corn Belt during the last millennium (AD 992–2004). *Agr. For. Meteorol.*, **151**, 154–162.
- Stanford, J. D., E. J. Rohling, S. Bacon, A. P. Roberts, F. E. Grouset, and M. Bolshaw, 2011: A new concept for the paleoceanographic evolution of Heinrich event 1 in the North Atlantic. *Quat. Sci. Rev.*, **30**, 1047–1066.
- Starkey, L., R. Soja, and D. J. Michczyńska, 2006: Past hydrological events reflected in Holocene history of Polish rivers. *CATENA*, **66**, 24–33.
- Steffensen, J. P., et al., 2008: High-resolution Greenland ice core data show abrupt climate change happens in few years. *Science*, **321**, 680–684.
- Steig, E. J., D. P. Schneider, S. D. Rutherford, M. E. Mann, J. C. Comiso, and D. T. Shindell, 2009: Warming of the Antarctic ice-sheet surface since the 1957 International Geophysical Year. *Nature*, **457**, 459–462.
- Steig, E. J., et al., 2013: Recent climate and ice-sheet changes in West Antarctica compared with the past 2,000 years. *Nature Geosci.*, **6**, 372–375.
- Steinhilber, F., J. Beer, and C. Fröhlich, 2009: Total solar irradiance during the Holocene. *Geophys. Res. Lett.*, **36**, L19704.
- Steinhilber, F., et al., 2012: 9,400 years of cosmic radiation and solar activity from ice cores and tree rings. *Proc. Natl. Acad. Sci. U.S.A.*, **109**, 5967–5971.
- Steinke, S., M. Kienast, J. Groeneveld, L.-C. Lin, M.-T. Chen, and R. Rendle-Bühring, 2008: Proxy dependence of the temporal pattern of deglacial warming in the tropical South China Sea: toward resolving seasonality. *Quat. Sci. Rev.*, **27**, 688–700.
- Steinman, B. A., M. B. Abbott, M. E. Mann, N. D. Stansell, and B. P. Finney, 2013: 1,500 year quantitative reconstruction of winter precipitation in the Pacific Northwest. *Proc. Natl. Acad. Sci. U.S.A.*, **109**, 11619–11623.
- Stendel, M., I. Mogensen, and J. Christensen, 2006: Influence of various forcings on global climate in historical times using a coupled atmosphere–ocean general circulation model. *Clim. Dyn.*, **26**, 1–15.
- Stenni, B., et al., 2010: The deuterium excess records of EPICA Dome C and Dronning Maud Land ice cores (East Antarctica). *Quat. Sci. Rev.*, **29**, 146–159.
- Stenni, B., et al., 2011: Expression of the bipolar see-saw in Antarctic climate records during the last deglaciation. *Nature Geosci.*, **4**, 46–49.
- Steph, S., et al., 2010: Early Pliocene increase in thermohaline overturning: A precondition for the development of the modern equatorial Pacific cold tongue. *Paleoceanography*, **25**, PA2202.
- Stewart, M. M., I. Larocque-Tobler, and M. Grosjean, 2011: Quantitative inter-annual and decadal June–July–August temperature variability ca. 570 BC to AD 120 (Iron Age–Roman Period) reconstructed from the varved sediments of Lake Silvaplana, Switzerland. *J. Quat. Sci.*, **26**, 491–501.
- Stirling, C., T. Esat, K. Lambeck, and M. McCulloch, 1998: Timing and duration of the Last Interglacial: Evidence for a restricted interval of widespread coral reef growth. *Earth Planet. Sci. Lett.*, **160**, 745–762.
- Stocker, T., and S. Johnsen, 2003: A minimum thermodynamic model for the bipolar seesaw. *Paleoceanography*, **18**, 1087.
- Stone, E. J., D. J. Lunt, J. D. Annan, and J. C. Hargreaves, 2013: Quantification of the Greenland ice sheet contribution to Last Interglacial sea level rise. *Clim. Past*, **9**, 621–639.
- Stone, J. O., G. A. Balco, D. E. Sugden, M. W. Caffee, L. C. Sass, S. G. Cowdery, and C. Siddoway, 2003: Holocene Deglaciation of Marie Byrd Land, West Antarctica. *Science*, **299**, 99–102.
- Stott, L., A. Timmermann, and R. Thunell, 2007: Southern hemisphere and deep-sea warming led deglacial atmospheric CO_2 rise and tropical warming. *Science*, **318**, 435–438.
- Stott, L., K. Cannariato, R. Thunell, G. H. Haug, A. Koutavas, and S. Lund, 2004: Decline of surface temperature and salinity in the western tropical Pacific Ocean in the Holocene epoch. *Nature*, **431**, 56–59.
- Stott, L. D., 1992: Higher temperatures and lower oceanic $p\text{CO}_2$: A climate enigma at the end of the Paleocene epoch. *Paleoceanography*, **7**, 395–404.
- Stríkis, N. M., et al., 2011: Abrupt variations in South American monsoon rainfall during the Holocene based on a speleothem record from central-eastern Brazil. *Geology*, **39**, 1075–1078.
- Stuiver, M., and T. F. Braziunas, 1993: Sun, ocean, climate and atmospheric $^{14}\text{CO}_2$: An evaluation of causal and spectral relationships. *Holocene*, **3**, 289–305.
- Sundqvist, H. S., Q. Zhang, A. Moberg, K. Holmgren, H. Körnich, J. Nilsson, and G. Brattström, 2010: Climate change between the mid and late Holocene in northern high latitudes - Part 1: survey of temperature and precipitation proxy data. *Clim. Past*, **6**, 591–608.
- Salgaard, L., and E. W. Cliver, 2010: Heliospheric magnetic field 1835–2009. *J. Geophys. Res.*, **115**, A09111.
- Svensson, A., et al., 2008: A 60 000 year Greenland stratigraphic ice core chronology. *Clim. Past*, **4**, 47–57.
- Swingedouw, D., J. Mignot, P. Braconnot, E. Mosquet, M. Kageyama, and R. Alkama, 2009: Impact of freshwater release in the North Atlantic under different climate conditions in an OAGCM. *J. Clim.*, **22**, 6377–6403.
- Swingedouw, D., L. Terray, C. Cassou, A. Volodire, D. Salas-Mélia, and J. Servonnat, 2011: Natural forcing of climate during the last millennium: Fingerprint of solar variability. *Clim. Dyn.*, **36**, 1349–1364.
- Takemura, T., M. Egashira, K. Matsuzawa, H. Ichijo, R. Oishi, and A. Abe-Ouchi, 2009: A simulation of the global distribution and radiative forcing of soil dust aerosols at the Last Glacial Maximum. *Atmos. Chem. Phys.*, **9**, 3061–3073.

- Tan, L., Y. Cai, R. Edwards, H. Cheng, C. Shen, and H. Zhang, 2011: Centennial- to decadal-scale monsoon precipitation variability in the semi-humid region, northern China during the last 1860 years: Records from stalagmites in Huangye Cave. *Holocene*, **21**, 287–296.
- Tarasov, L., and W. R. Peltier, 2007: Coevolution of continental ice cover and permafrost extent over the last glacial-interglacial cycle in North America. *J. Geophys. Res.*, **112**, F02S08.
- Tarasov, P., W. Granszewski, E. Bezrukova, S. Brewer, M. Nita, A. Abzaeva, and H. Oberhänsli, 2005: Quantitative reconstruction of the last interglacial vegetation and climate based on the pollen record from Lake Baikal, Russia. *Clim. Dyn.*, **25**, 625–637.
- Tarasov, P. E., et al., 2011: Progress in the reconstruction of Quaternary climate dynamics in the Northwest Pacific: A new modern analogue reference dataset and its application to the 430-kyr pollen record from Lake Biwa. *Earth Sci. Rev.*, **108**, 46–79.
- Taylor, K. E., R. J. Stouffer, and G. A. Meehl, 2012: An overview of CMIP5 and the experiment design. *Bull. Am. Meteorol. Soc.*, **93**, 485–498.
- Telford, R. J., C. Li, and M. Kucera, 2013: Mismatch between the depth habitat of planktonic foraminifera and the calibration depth of SST transfer functions may bias reconstructions. *Clim. Past*, **9**, 859–870.
- Tett, S., et al., 2007: The impact of natural and anthropogenic forcings on climate and hydrology since 1550. *Clim. Dyn.*, **28**, 3–34.
- Thomas, E., and J. Briner, 2009: Climate of the past millennium inferred from varved proglacial lake sediments on northeast Baffin Island, Arctic Canada. *J. Paleolimnol.*, **41**, 209–224.
- Thomas, E. R., E. W. Wolff, R. Mulvaney, S. J. Johnsen, J. P. Steffensen, and C. Arrowsmith, 2009: Anatomy of a Dansgaard-Oeschger warming transition: high-resolution analysis of the North Greenland Ice Core Project ice core. *J. Geophys. Res.*, **114**, D08102.
- Thomas, E. R., et al., 2007: The 8.2 ka event from Greenland ice cores. *Quat. Sci. Rev.*, **26**, 70–81.
- Thompson, D. W. J., and S. Solomon, 2002: Interpretation of recent southern hemisphere climate change. *Science*, **296**, 895–899.
- Thompson, D. W. J., and S. Solomon, 2009: Understanding recent stratospheric climate change. *J. Clim.*, **22**, 1934–1943.
- Thompson, W. G., and S. L. Goldstein, 2005: Open-system coral ages reveal persistent suborbital sea level cycles. *Science*, **308**, 401–404.
- Thompson, W. G., H. Allen Curran, M. A. Wilson, and B. White, 2011: Sea level oscillations during the last interglacial highstand recorded by Bahamas corals. *Nature Geosci.*, **4**, 684–687.
- Thordarson, T., and S. Self, 2003: Atmospheric and environmental effects of the 1783–1784 Laki eruption: A review and reassessment. *J. Geophys. Res.*, **108**, D14011.
- Tierney, J., M. Mayes, N. Meyer, C. Johnson, P. Swarzenski, A. Cohen, and J. Russell, 2010: Late-twentieth-century warming in Lake Tanganyika unprecedented since AD 500. *Nature Geosci.*, **3**, 422–425.
- Tierney, J. E., S. C. Lewis, B. I. Cook, A. N. LeGrande, and G. A. Schmidt, 2011: Model, proxy and isotopic perspectives on the east African humid period. *Earth Planet. Sci. Lett.*, **307**, 103–112.
- Tiljander, M. I. A., M. Saarnisto, A. E. K. Ojala, and T. Saarinen, 2003: A 3000-year palaeoenvironmental record from annually laminated sediment of Lake Korttajarvi, central Finland. *Boreas*, **32**, 566–577.
- Timm, O., E. Ruprecht, and S. Kleppek, 2004: Scale-dependent reconstruction of the NAO index. *J. Clim.*, **17**, 2157–2169.
- Timm, O., A. Timmermann, A. Abe-Ouchi, F. Saito, and T. Segawa, 2008: On the definition of seasons in paleoclimate simulations with orbital forcing. *Paleoceanography*, **23**, PA2221.
- Timmermann, A., H. Gildor, M. Schulz, and E. Tziperman, 2003: Coherent resonant millennial-scale climate oscillations triggered by massive meltwater pulses. *J. Clim.*, **16**, 2569–2585.
- Timmermann, A., O. Timm, L. Stott, and L. Menzel, 2009: The roles of CO₂ and orbital forcing in driving southern hemispheric temperature variations during the last 21 000 yr. *J. Clim.*, **22**, 1626–1640.
- Timmermann, A., F. Justino, F. F. Jin, U. Krebs, and H. Goosse, 2004: Surface temperature control in the North and tropical Pacific during the last glacial maximum. *Clim. Dyn.*, **23**, 353–370.
- Timmermann, A., et al., 2010: Towards a quantitative understanding of millennial-scale Antarctic warming events. *Quat. Sci. Rev.*, **29**, 74–85.
- Timmermann, A., et al., 2007: The influence of a weakening of the Atlantic meridional overturning circulation on ENSO. *J. Clim.*, **20**, 4899–4919.
- Timmreck, C., S. J. Lorenz, T. J. Crowley, S. Kinne, T. J. Raddatz, M. A. Thomas, and J. H. Jungclaus, 2009: Limited temperature response to the very large AD 1258 volcanic eruption. *Geophys. Res. Lett.*, **36**, L21708.
- Tingley, M. P., and P. Huybers, 2010: A Bayesian algorithm for reconstructing climate anomalies in space and time. Part I: development and applications to paleoclimate reconstruction problems. *J. Clim.*, **23**, 2759–2781.
- Tingley, M. P., and P. Huybers, 2013: Recent temperature extremes at high northern latitudes unprecedented in the past 600 years. *Nature*, **496**, 201–205.
- Tingley, M. P., P. F. Craigmele, M. Haran, B. Li, E. Mannshardt, and B. Rajaratnam, 2012: Piecing together the past: statistical insights into paleoclimatic reconstructions. *Quat. Sci. Rev.*, **35**, 1–22.
- Tjallingii, R., et al., 2008: Coherent high- and low-latitude control of the northwest African hydrological balance. *Nature Geosci.*, **1**, 670–675.
- Torre, C., and G. P. Compo, 1998: A practical guide to wavelet analysis. *Bull. Am. Meteorol. Soc.*, **79**, 61–78.
- Touchan, R., K. J. Anchukaitis, D. M. Meko, S. Attalah, C. Baisan, and A. Aloui, 2008: Long term context for recent drought in northwestern Africa. *Geophys. Res. Lett.*, **35**, L13705.
- Touchan, R., K. Anchukaitis, D. Meko, M. Sabir, S. Attalah, and A. Aloui, 2011: Spatio-temporal drought variability in northwestern Africa over the last nine centuries. *Clim. Dyn.*, **37**, 237–252.
- Trachsel, M., et al., 2012: Multi-archive summer temperature reconstruction for the European Alps, AD 1053–1996. *Quat. Sci. Rev.*, **46**, 66–79.
- Tripathi, A. K., C. D. Roberts, and R. A. Eagle, 2009: Coupling of CO₂ and ice sheet stability over major climate transitions of the last 20 million years. *Science*, **326**, 1394–1397.
- Trouet, V., J. Esper, N. E. Graham, A. Baker, J. D. Scourse, and D. C. Frank, 2009: Persistent positive north Atlantic oscillation mode dominated the Medieval Climate Anomaly. *Science*, **324**, 78–80.
- Turner, C. S. M., and R. T. Jones, 2010: Does the Agulhas Current amplify global temperatures during super-interglacials? *J. Quat. Sci.*, **25**, 839–843.
- Tzedakis, P. C., H. Hooghiemstra, and H. Pälike, 2006: The last 1.35 million years at Tenaghi Philippon: revised chronostratigraphy and long-term vegetation trends. *Quat. Sci. Rev.*, **25**, 3416–3430.
- Tzedakis, P. C., J. E. T. Channell, D. A. Hodell, H. F. Kleiven, and L. C. Skinner, 2012a: Determining the natural length of the current interglacial. *Nature Geosci.*, **5**, 138–141.
- Tzedakis, P. C., D. Raynaud, J. F. McManus, A. Berger, V. Brovkin, and T. Kiefer, 2009: Interglacial diversity. *Nature Geosci.*, **2**, 751–755.
- Tzedakis, P. C., E. W. Wolff, L. C. Skinner, V. Brovkin, D. A. Hodell, J. F. McManus, and D. Raynaud, 2012b: Can we predict the duration of an interglacial? *Clim. Dyn.*, **8**, 1473–1485.
- Uemura, R., V. Masson-Delmotte, J. Jouzel, A. Landais, H. Motoyama, and B. Stenni, 2012: Ranges of moisture-source temperature estimated from Antarctic ice cores stable isotope records over glacial–interglacial cycles. *Clim. Past*, **8**, 1109–1125.
- Unterman, M. B., T. J. Crowley, K. I. Hodges, S. J. Kim, and D. J. Erickson, 2011: Paleometeorology: High resolution Northern Hemisphere wintertime mid-latitude dynamics during the Last Glacial Maximum. *Geophys. Res. Lett.*, **38**, L23702.
- Urrutia, R., A. Lara, R. Villalba, D. Christie, C. Le Quesne, and A. Cuq, 2011: Multicentury tree ring reconstruction of annual streamflow for the Maule River watershed in south central Chile. *Water Resourc. Res.*, **47**, W06527.
- van de Berg, W. J., M. van den Broeke, J. Ettema, E. van Meijgaard, and F. Kaspar, 2011: Significant contribution of insolation to Eemian melting of the Greenland ice sheet. *Nature Geosci.*, **4**, 679–683.
- van de Plassche, O., K. van der Borg, and A. F. M. de Jong, 1998: Sea level–climate correlation during the past 1400 yr. *Geology*, **26**, 319–322.
- van den Berg, J., R. S. W. van de Wal, G. A. Milne, and J. Oerlemans, 2008: Effect of isostasy on dynamical ice sheet modeling: A case study for Eurasia. *J. Geophys. Res.*, **113**, B05412.
- van der Burgh, J., H. Visscher, D. L. Dilcher, and W. M. Kürschner, 1993: Paleoatmospheric signatures in Neogene fossil leaves. *Science*, **260**, 1788–1790.
- van Leeuwen, R. J., et al., 2000: Stratigraphy and integrated facies analysis of the Saalian and Eemian sediments in the Amsterdam-Terminal borehole, the Netherlands. *Geolog. Mijnbouw / Netherlands J. Geosci.*, **79**, 161–196.
- Varma, V., et al., 2012: Holocene evolution of the Southern Hemisphere westerly winds in transient simulations with global climate models. *Clim. Past*, **8**, 391–402.

- Vasskog, K., Ø. Paasche, A. Nesje, J. F. Boyle, and H. J. B. Birks, 2012: A new approach for reconstructing glacier variability based on lake sediments recording input from more than one glacier. *Quat. Res.*, **77**, 192–204.
- Vaughan, D. G., D. K. A. Barnes, P. T. Fretwell, and R. G. Bingham, 2011: Potential seaways across West Antarctica. *Geochem., Geophys., Geosyst.*, **12**, Q10004.
- Vavrus, S., 2004: The impact of cloud feedbacks on Arctic climate under greenhouse forcing. *J. Clim.*, **17**, 603–615.
- Velichko, A. A., O. K. Borisova, and E. M. Zelikson, 2008: Paradoxes of the Last Interglacial climate: Reconstruction of the northern Eurasia climate based on palaeofloristic data. *Boreas*, **37**, 1–19.
- Verleyen, E., et al., 2011: Post-glacial regional climate variability along the East Antarctic coastal margin—Evidence from shallow marine and coastal terrestrial records. *Earth Sci. Rev.*, **104**, 199–212.
- Verschuren, D., K. Laird, and B. Cumming, 2000: Rainfall and drought in equatorial East Africa during the past 1000 years. *Nature*, **403**, 410–414.
- Verschuren, D., J. S. Sinnninghe Damste, J. Moernaut, I. Kristen, M. Blaauw, M. Fagot, and G. H. Haug, 2009: Half-precessional dynamics of monsoon rainfall near the East African Equator. *Nature*, **462**, 637–641.
- Vettoretti, G., and W. R. Peltier, 2011: The impact of insolation, greenhouse gas forcing and ocean circulation changes on glacial inception. *Holocene*, **21**, 803–817.
- Viau, A. E., M. Ladd, and K. Gajewski, 2012: The climate of North America during the past 2000–years reconstructed from pollen data. *Global Planet. Change*, **84–85**, 75–83.
- Vieira, L. E., S. K. Solanki, A. V. Krivov, and I. G. Usoskin 2011: Evolution of the solar irradiance during the Holocene. *Astron. Astrophys.*, **531**, A6.
- Vieira, L. E. A., and S. K. Solanki, 2010: Evolution of the solar magnetic flux on time scales of years to millennia. *Astron. Astrophys.*, **509**, A100.
- Villalba, R., M. Grosjean, and T. Kiefer, 2009: Long-term multi-proxy climate reconstructions and dynamics in South America (LOTRED-SA): State of the art and perspectives. *Palaeogeogr. Palaeoclimatol. Palaeoecol.*, **281**, 175–179.
- Villalba, R., et al., 2012: Unusual Southern Hemisphere tree growth patterns induced by changes in the Southern Annular Mode. *Nature Geosci.*, **5**, 793–798.
- Vimeux, F., P. Ginot, M. Schwikowski, M. Vuille, G. Hoffmann, L. G. Thompson, and U. Schotterer, 2009: Climate variability during the last 1000 years inferred from Andean ice cores: A review of methodology and recent results. *Palaeogeogr. Palaeoclimatol. Palaeoecol.*, **281**, 229–241.
- Vinther, B., P. Jones, K. Briffa, H. Clausen, K. Andersen, D. Dahl-Jensen, and S. Johnsen, 2010: Climatic signals in multiple highly resolved stable isotope records from Greenland. *Quat. Sci. Rev.*, **29**, 522–538.
- Vinther, B. M., et al., 2009: Holocene thinning of the Greenland ice sheet. *Nature*, **461**, 385–388.
- von Grafenstein, U., E. Erlenkeuser, J. Müller, J. Jouzel, and S. Johnsen, 1998: The cold event 8,200 years ago documented in oxygen isotope records of precipitation in Europe and Greenland. *Clim. Dyn.*, **14**, 73–81.
- von Gunten, L., M. Grosjean, B. Rein, R. Urrutia, and P. Appleby, 2009: A quantitative high-resolution summer temperature reconstruction based on sedimentary pigments from Laguna Aculeo, central Chile, back to AD 850. *Holocene*, **19**, 873–881.
- von Königswald, W., 2007: Mammalian faunas from the interglacial periods in Central Europe and their stratigraphic correlation. In: *Developments in Quaternary Science* [F. Sirocko, M. Claussen, M. F. Sánchez Goñi and T. Litt (eds.)]. Elsevier, Philadelphia, PA, USA, pp. 445–454.
- von Storch, H., E. Zorita, J. Jones, F. González-Rouco, and S. Tett, 2006: Response to comment on "Reconstructing past climate from noisy data". *Science*, **312**, 1872–1873.
- Vuille, M., et al., 2012: A review of the South American Monsoon history as recorded in stable isotopic proxies over the past two millennia. *Clim. Past*, **8**, 1309–1321.
- Waelbroeck, C., et al., 2002: Sea level and deep water temperature changes derived from benthic foraminifera isotopic records. *Quat. Sci. Rev.*, **21**, 295–305.
- Wagner, J. D. M., J. E. Cole, J. W. Beck, P. J. Patchett, G. M. Henderson, and H. R. Barnett, 2010: Moisture variability in the southwestern United States linked to abrupt glacial climate change. *Nature Geosci.*, **3**, 110–113.
- Wagner, S., et al., 2007: Transient simulations, empirical reconstructions and forcing mechanisms for the Mid-holocene hydrological climate in southern Patagonia. *Clim. Dyn.*, **29**, 333–355.
- Wahl, E., et al., 2010: An archive of high-resolution temperature reconstructions over the past 2+ millennia. *Geochem. Geophys. Geosyst.*, **11**, Q01001.
- Wahl, E. R., and J. E. Smerdon, 2012: Comparative performance of paleoclimate field and index reconstructions derived from climate proxies and noise-only predictors. *Geophys. Res. Lett.*, **39**, L06703.
- Wahl, E. R., D. M. Ritson, and C. M. Ammann, 2006: Comment on "Reconstructing past climate from noisy data". *Science*, **312**, 529.
- Walter, K. M., S. A. Zimov, J. P. Chanton, D. Verbyla, and F. S. Chapin, 2006: Methane bubbling from Siberian thaw lakes as a positive feedback to climate warming. *Nature*, **443**, 71–75.
- Wan, S., J. Tian, S. Steinke, A. Li, and T. Li, 2010: Evolution and variability of the East Asian summer monsoon during the Pliocene: Evidence from clay mineral records of the South China Sea. *Palaeogeogr. Palaeoclimatol. Palaeoecol.*, **293**, 237–247.
- Wang, B., and Q. Ding, 2008: Global monsoon: Dominant mode of annual variation in the tropics. *Dyn. Atmos. Oceans*, **44**, 165–183.
- Wang, S., X. Wen, Y. Luo, W. Dong, Z. Zhao, and B. Yang, 2007: Reconstruction of temperature series of China for the last 1000 years. *Chin. Sci. Bull.*, **52**, 3272–3280.
- Wang, Y. J., H. Cheng, R. L. Edwards, Z. S. An, J. Y. Wu, C. C. Shen, and J. A. Dore, 2001: A high-resolution absolute-dated Late Pleistocene monsoon record from Hulu Cave, China. *Science*, **294**, 2345–2348.
- Wang, Y. J., et al., 2008: Millennial- and orbital-scale changes in the East Asian monsoon over the past 224,000 years. *Nature*, **451**, 1090–1093.
- Wang, Y. M., J. Lean, and N. Sheeley, 2005: Modeling the Sun's magnetic field and irradiance since 1713. *Astrophys. J.*, **625**, 522–538.
- Wang, Y. M., S. L. Li, and D. H. Luo, 2009: Seasonal response of Asian monsoonal climate to the Atlantic Multidecadal Oscillation. *J. Geophys. Res.*, **114**, D02112.
- Wanner, H., O. Solomina, M. Grosjean, S. P. Ritz, and M. Jetel, 2011: Structure and origin of Holocene cold events. *Quat. Sci. Rev.*, **30**, 3109–3123.
- Wanner, H., et al., 2008: Mid- to Late Holocene climate change: an overview. *Quat. Sci. Rev.*, **27**, 1791–1828.
- Waple, A. M., M. E. Mann, and R. S. Bradley, 2002: Long-term patterns of solar irradiance forcing in model experiments and proxy based surface temperature reconstructions. *Clim. Dyn.*, **18**, 563–578.
- Wara, M. W., A. C. Ravelo, and M. L. Delaney, 2005: Permanent El Niño-like conditions during the Pliocene Warm Period. *Science*, **309**, 758–761.
- Watanabe, O., J. Jouzel, S. Johnsen, F. Parrenin, H. Shoji, and N. Yoshida, 2003: Homogeneous climate variability across East Antarctica over the past three glacial cycles. *Nature*, **422**, 509–512.
- Watanabe, T., et al., 2011: Permanent El Niño during the Pliocene warm period not supported by coral evidence. *Nature*, **471**, 209–211.
- Weber, S. L., et al., 2007: The modern and glacial overturning circulation in the Atlantic ocean in PMIP coupled model simulations. *Clim. Past*, **3**, 51–64.
- Wegmüller, S., 1992: *Vegetationsgeschichtliche und stratigraphische Untersuchungen an Schieferkohlen des nördlichen Alpenvorlandes*. Denkschriften der Schweizerischen Akademie der Naturwissenschaften, 102, Birkhäuser, Basel, 445–454 pp.
- Wegner, A., et al., 2012: Change in dust variability in the Atlantic sector of Antarctica at the end of the last deglaciation. *Clim. Past*, **8**, 135–147.
- Wei, L. J., E. Mosley-Thompson, P. Gabrielli, L. G. Thompson, and C. Barbante, 2008: Synchronous deposition of volcanic ash and sulfate aerosols over Greenland in 1783 from the Laki eruption (Iceland). *Geophys. Res. Lett.*, **35**, L16501.
- Weldeab, S., 2012: Bipolar modulation of millennial-scale West African monsoon variability during the last glacial (75,000–25,000 years ago). *Quat. Sci. Rev.*, **40**, 21–29.
- Weldeab, S., D. W. Lea, R. R. Schneider, and N. Andersen, 2007a: 155,000 years of West African monsoon and ocean thermal evolution. *Science*, **316**, 1303–1307.
- Weldeab, S., D. W. Lea, R. R. Schneider, and N. Andersen, 2007b: Centennial scale climate instabilities in a wet early Holocene West African monsoon. *Geophys. Res. Lett.*, **34**, L24702.
- Welten, M., 1988: *Neue pollenanalytische Ergebnisse über das jüngere Quartär des nördlichen Alpenvorlandes der Schweiz (Mittel- und Jungpleistozän)*. Beiträge zur Geologischen Karte der Schweiz, 162, Stämpfli, 40 pp.
- Wenzler, T., S. Solanki, and N. Krivova, 2005: Can surface magnetic fields reproduce solar irradiance variations in cycles 22 and 23? *Astron. Astrophys.*, **432**, 1057–1061.
- Wenzler, T., S. K. Solanki, N. A. Krivova, and C. Fröhlich, 2006: Reconstruction of solar irradiance variations in cycles 21–23 based on surface magnetic fields. *Astron. Astrophys.*, **460**, 583–595.
- Werner, J. P., J. Luterbacher, and J. E. Smerdon, 2013: A pseudoproxy evaluation of Bayesian hierarchical modelling and canonical correlation analysis for climate field reconstructions over Europe. *J. Clim.*, **26**, 851–867.

- Westerhold, T., U. Röhl, J. Laskar, I. Raffi, J. Bowles, L. J. Lourens, and J. C. Zachos, 2007: On the duration of magnetochrons C24r and C25n and the timing of early Eocene global warming events: Implications from the Ocean Drilling Program Leg 208 Walvis Ridge depth transect. *Paleoceanography*, **22**, PA2201.
- Whitehouse, P. L., M. J. Bentley, G. A. Milne, M. A. King, and I. D. Thomas, 2012: A new glacial isostatic adjustment model for Antarctica: Calibrated and tested using observations of relative sea level change and present-day uplift rates. *Geophys. J. Int.*, **190**, 1464–1482.
- Widmann, M., H. Goosse, G. van der Schrier, R. Schnur, and J. Barkmeijer, 2010: Using data assimilation to study extratropical Northern Hemisphere climate over the last millennium. *Clim. Past*, **6**, 627–644.
- Wiersma, A., D. Roche, and H. Renssen, 2011: Fingerprinting the 8.2 ka event climate response in a coupled climate model. *J. Quat. Sci.*, **26**, 118–127.
- Wiles, G. C., D. J. Barclay, P. E. Calkin, and T. V. Lowell, 2008: Century to millennial-scale temperature variations for the last two thousand years indicated from glacial geologic records of Southern Alaska. *Global Planet. Change*, **60**, 115–125.
- Wiles, G. C., D. E. Lawson, E. Lyon, N. Wiesenberg, and R. D. D'Arrigo, 2011: Tree-ring dates on two pre-Little Ice Age advances in Glacier Bay National Park and Preserve, Alaska, USA. *Quat. Res.*, **76**, 190–195.
- Wilhelm, B., et al., 2012: 1400 years of extreme precipitation patterns over the Mediterranean French Alps and possible forcing mechanisms. *Quat. Res.*, **78**, 1–12.
- Wilmes, S. B., C. C. Raible, and T. F. Stocker, 2012: Climate variability of the mid- and high-latitudes of the Southern Hemisphere in ensemble simulations from 1500 to 2000 AD. *Clim. Past*, **8**, 373–390.
- Wilson, M. F., and A. Henderson-Sellers, 1985: A global archive of land cover and soils data for use in general circulation climate models. *J. Climatol.*, **5**, 119–143.
- Wilson, R., E. Cook, R. D'Arrigo, N. Riedwyl, M. N. Evans, A. Tudhope, and R. Allan, 2010: Reconstructing ENSO: the influence of method, proxy data, climate forcing and teleconnections. *J. Quat. Sci.*, **25**, 62–78.
- Wilson, R., D. Miles, N. Loader, T. Melvin, L. Cunningham, R. Cooper, and K. Briffa, 2013: A millennial long march–July precipitation reconstruction for southern-central England. *Clim. Dyn.*, **40**, 997–1017.
- Wilson, R., et al., 2007: A matter of divergence: Tracking recent warming at hemispheric scales using tree ring data. *J. Geophys. Res.*, **112**, D17103.
- Winckler, G., R. F. Anderson, M. Q. Fleisher, D. McGee, and N. Mahowald, 2008: Covariant Glacial-Interglacial Dust Fluxes in the Equatorial Pacific and Antarctica. *Science*, **320**, 93–96.
- Winkler, S., and J. Matthews, 2010: Holocene glacier chronologies: Are 'high-resolution' global and inter-hemispheric comparisons possible? *Holocene*, **20**, 1137–1147.
- Winter, A., et al., 2011: Evidence for 800 years of North Atlantic multi-decadal variability from a Puerto Rican speleothem. *Earth Planet. Sci. Lett.*, **308**, 23–28.
- Wolff, C., et al., 2011: Reduced interannual rainfall variability in east Africa during the Last Ice Age. *Science*, **333**, 743–747.
- Wolff, E. W., et al., 2010: Changes in environment over the last 800,000 years from chemical analysis of the EPICA Dome C ice core. *Quat. Sci. Rev.*, **29**, 285–295.
- Woodhouse, C. A., D. M. Meko, G. M. MacDonald, D. W. Stahle, and E. R. Cook, 2010: A 1,200-year perspective of 21st century drought in southwestern North America. *Proc. Natl. Acad. Sci. U.S.A.*, **107**, 21283–21288.
- Woodroffe, C., and R. McLean, 1990: Microatolls and recent sea level change on coral atolls. *Nature*, **344**, 531–534.
- Woodroffe, C. D., H. V. McGregor, K. Lambeck, S. G. Smithers, and D. Fink, 2012: Mid-Pacific microatolls record sea level stability over the past 5000 yr. *Geology*, **40**, 951–954.
- Wunsch, C., 2006: Abrupt climate change: An alternative view. *Quat. Res.*, **65**, 191–203.
- Xie, S. P., Y. Okumura, T. Miyama, and A. Timmermann, 2008: Influences of Atlantic climate change on the tropical Pacific via the Central American Isthmus. *J. Clim.*, **21**, 3914–3928.
- Yadav, R., A. Braeuning, and J. Singh, 2011: Tree ring inferred summer temperature variations over the last millennium in western Himalaya, India. *Clim. Dyn.*, **36**, 1545–1554.
- Yanase, W., and A. Abe-Ouchi, 2010: A numerical study on the atmospheric circulation over the midlatitude North Pacific during the Last Glacial Maximum. *J. Clim.*, **23**, 135–151.
- Yang, B., A. Bräuning, Z. Dong, Z. Zhang, and J. Keping, 2008: Late Holocene monsoonal temperate glacier fluctuations on the Tibetan Plateau. *Global Planet. Change*, **60**, 126–140.
- Yang, B., J. Wang, A. Bräuning, Z. Dong, and J. Esper, 2009: Late Holocene climatic and environmental changes in and central Asia. *Quat. Int.*, **194**, 68–78.
- Yin, Q., and A. Berger, 2012: Individual contribution of insolation and CO₂ to the interglacial climates of the past 800,000 years. *Clim. Dyn.*, **38**, 709–724.
- Yin, Q. Z., and A. Berger, 2010: Insolation and CO₂ contribution to the interglacial climate before and after the Mid-Brunhes Event. *Nature Geosci.*, **3**, 243–246.
- Yin, Q. Z., A. Berger, E. Driesschaert, H. Goosse, M. F. Loutre, and M. Crucifix, 2008: The Eurasian ice sheet reinforces the East Asian summer monsoon during the interglacial 500 000 years ago. *Clim. Past*, **4**, 79–90.
- Yiou, P., J. Servonnat, M. Yoshimori, D. Swingedouw, M. Khodri, and A. Abe-Ouchi, 2012: Stability of weather regimes during the last millennium from climate simulations. *Geophys. Res. Lett.*, **39**, L08703.
- Yokoyama, Y., and T. M. Esat, 2011: Global climate and sea level: Enduring variability and rapid fluctuations over the past 150,000 years. *Oceanography*, **24**, 54–69.
- Yoshimori, M., T. Yokohata, and A. Abe-Ouchi, 2009: A comparison of climate feedback strength between CO₂ doubling and LGM experiments. *J. Clim.*, **22**, 3374–3395.
- Yoshimori, M., J. C. Hargreaves, J. D. Annan, T. Yokohata, and A. Abe-Ouchi, 2011: Dependency of feedbacks on forcing and climate state in physics parameter ensembles. *J. Clim.*, **24**, 6440–6455.
- Young, N. E., J. P. Briner, H. A. M. Stewart, Y. Axford, B. Csatho, D. H. Rood, and R. C. Finkel, 2011: Response of Jakobshavn Isbrae, Greenland, to Holocene climate change. *Geology*, **39**, 131–134.
- Yue, X., H. Wang, H. Liao, and D. Jiang, 2010: Simulation of the direct radiative effect of mineral dust aerosol on the climate at the Last Glacial Maximum. *J. Clim.*, **24**, 843–858.
- Zachos, J. C., G. R. Dickens, and R. E. Zeebe, 2008: An early Cenozoic perspective on greenhouse warming and carbon-cycle dynamics. *Nature*, **451**, 279–283.
- Zachos, J. C., et al., 2005: Rapid acidification of the ocean during the Paleocene-Eocene Thermal Maximum. *Science*, **308**, 1611–1615.
- Zagwijn, W. H., 1996: An analysis of Eemian climate in western and central Europe. *Quat. Sci. Rev.*, **15**, 451–469.
- Zeebe, R. E., J. C. Zachos, and G. R. Dickens, 2009: Carbon dioxide forcing alone insufficient to explain Palaeocene-Eocene Thermal Maximum warming. *Nature Geosci.*, **2**, 576–580.
- Zha, X., C. Huang, and J. Pang, 2009: Palaeofloods recorded by slackwater deposits on the Qishuihe river in the middle Yellow river. *J. Geograph. Sci.*, **19**, 681–690.
- Zhang, P. Z., et al., 2008: A test of climate, sun, and culture relationships from an 1810–year Chinese cave record. *Science*, **322**, 940–942.
- Zhang, Q.-B., and R. J. Hebdon, 2005: Abrupt climate change and variability in the past four millennia of the southern Vancouver Island, Canada. *Geophys. Res. Lett.*, **32**, L16708.
- Zhang, Q., H. S. Sundqvist, A. Moberg, H. Kornich, J. Nilsson, and K. Holmgren, 2010: Climate change between the mid and late Holocene in northern high latitudes—Part 2: Model-data comparisons. *Clim. Past*, **6**, 609–626.
- Zhang, R., and T. L. Delworth, 2005: Simulated tropical response to a substantial weakening of the Atlantic thermohaline circulation. *J. Clim.*, **18**, 1853–1860.
- Zhang, R., and T. L. Delworth, 2006: Impact of Atlantic multidecadal oscillations on India/Sahel rainfall and Atlantic hurricanes. *Geophys. Res. Lett.*, **33**, L17712.
- Zhang, Y., Z. Kong, S. Yan, Z. Yang, and J. Ni, 2009: "Medieval Warm Period" on the northern slope of central Tianshan Mountains, Xinjiang, NW China. *Geophys. Res. Lett.*, **36**, L11702.
- Zheng, W., P. Braconnot, E. Guilyardi, U. Merkel, and Y. Yu, 2008: ENSO at 6ka and 21ka from ocean-atmosphere coupled model simulations. *Clim. Dyn.*, **30**, 745–762.
- Zhou, T., B. Li, W. Man, L. Zhang, and J. Zhang, 2011: A comparison of the Medieval Warm Period, Little Ice Age and 20th century warming simulated by the FGOALS climate system model. *Chin. Sci. Bull.*, **56**, 3028–3041.
- Zhu, H., F. Zheng, X. Shao, X. Liu, X. Yan, and E. Liang, 2008: Millennial temperature reconstruction based on tree-ring widths of Qilian juniper from Wulan, Qinghai province, China. *Chin. Sci. Bull.*, **53**, 3914–3920.
- Zinke, J., M. Pfeiffer, O. Timm, W. C. Dullo, and G. Brummer, 2009: Western Indian Ocean marine and terrestrial records of climate variability: A review and new concepts on land–ocean interactions since AD 1660. *Int. J. Earth Sci.*, **98**, 115–133.

Appendix 5.A: Additional Information on Paleoclimate Archives and Models

Table 5.A.1 | Summary of the Atmosphere-Ocean General Circulation Model (AOGCM) simulations available and assessed for Sections 5.3.5 and 5.5.1. Acronyms describing forcings are: SS (solar forcing, stronger variability), SW (solar forcing, weaker variability), V (volcanic activity), G (greenhouse gases concentration), A (aerosols), L (land use–land cover), and O (orbital). The table is divided into Paleoclimate Modelling Intercomparison Project Phase III (PMIP3) and Coupled Model Intercomparison Project Phase 5 (CMIP5) and non-PMIP3/CMIP5 experiments (Braconnot et al., 2012b; Taylor et al., 2012). Superscript indices in forcing acronyms identify the forcing reconstructions used and are listed in the table footnotes. PMIP3 experiments follow forcing guidelines provided in Schmidt et al. (2011, 2012b). See Fernández-Donado et al. (2013) for more information on pre-PMIP3/CMIP5 forcing configurations. See Chapter 8 and Table 9.1 for the forcing and model specifications of the CMIP5 historical runs. The simulations highlighted in red were excluded from Figures 5.8, 5.9 and 5.12 because they did not include at least solar, volcanic and greenhouse gas forcings, they did not span the whole of the last millennium, or for a reason given in the table notes.

Model	(No. runs) Period	Forcings ^a	Reference
<i>Pre PMIP3/CMIP5 Experiments</i>			
CCSM3	(1x) 1000–2000 (4x) 1500–2000	SS ¹¹ , V ²² , G ^{30,31,35}	Hofer et al. (2011)
CNRM-CM3.3	(1x) 1001–1999	SS ¹¹ , V ²¹ , G ^{30,34,35} , A ⁴⁴ , L ⁵⁴	Swingedouw et al. (2011)
CSM1.4	(1x) 850–1999	SS ¹⁰ , V ²¹ , G ^{30,31,35} , A ⁴¹	Ammann et al. (2007)
CSIRO-MK3L-1-2	(3x) 1–2001 (3x) 1–2001 (3x) 501–2001	SW ¹⁴ SW ¹⁴ , G ³⁴ , O ⁶⁰ SW ¹⁴ , V ²⁴ , G ³⁴ , O ⁶⁰	Phipps et al. (2013)
ECHAM4/OPYC	(1x) 1500–2000	SS ¹¹ , V ^{21,26} , G ³⁸ , A ⁴² , L ⁵⁵	Stendel et al. (2006)
ECHAM5/MPIOM	(5x) 800–2005 (3x) 800–2005	SW ¹³ , V ²⁵ , G ^{34,39} , A ⁴⁰ , L ⁵³ , O ⁶¹ SS ¹⁰ , V ²⁵ , G ^{34,39} , A ⁴⁰ , L ⁵³ , O ⁶¹	Jungclaus et al. (2010)
ECHO-G	(1x) 1000–1990 (1x) 1000–1990 (2x) 7000–1998	SS ¹¹ , V ²⁰ , G ^{31,36,37} SS ¹¹ , V ²⁰ , G ^{31,36,37} SS ¹² , G ³⁰ , O ⁶²	González-Rouco et al. (2003) ^b González-Rouco et al. (2006) Wagner et al. (2007)
HadCM3	(1x) 1492–1999	SS ¹¹ , V ²³ , G ³² , A ⁴³ , L ^{50,54,55} , O ⁶⁰	Tett et al. (2007)
IPSLCM4	(1x) 1001–2000	SS ¹¹ , G ^{30,34,35} , A ⁴⁴ , O ⁶³	Servonnat et al. (2010)
FGOALS-g1	(1x) 1000–1999	SS ¹¹ , V ²⁰ , G ^{30,31,35}	Zhou et al. (2011) ^c
<i>PMIP3/CMIP5 Experiments</i>			
BCC-csm1-1	(1x) 850–2005	SW ¹⁵ , V ²⁴ , G ^{30,33,34} , A ⁴⁵ , O ⁶⁰	
CCSM4	(1x) 850–2004	SW ¹⁵ , V ²⁴ , G ^{30,33,34} , A ⁴⁵ , L ⁵¹ , O ⁶⁰	Landrum et al. (2013)
CSIRO-MK3L-1-2	(1x) 851–2000	SW ¹⁴ , V ²⁵ , G ^{30,33,34} , O ⁶⁰	
GISS-E2-R	(8x) 850–2004	SW ¹⁴ , V ²⁵ , G ^{30,33,34} , A ⁴⁵ , L ⁵¹ , O ⁶⁰ SW ¹⁴ , V ²⁴ , G ^{30,33,34} , A ⁴⁵ , L ⁵¹ , O ⁶⁰ SW ¹⁴ , G ^{30,33,34} , A ⁴⁴ , L ⁵¹ , O ⁶⁰ SW ¹⁵ , V ²⁵ , G ^{30,33,34} , A ⁴⁵ , L ⁵¹ , O ⁶⁰ SW ¹⁵ , V ²⁴ , G ^{30,33,34} , A ⁴⁵ , L ⁵² , O ⁶⁰ SW ¹⁵ , G ^{30,33,34} , A ⁴⁴ , L ⁵¹ , O ⁶⁰ SW ¹⁵ , V ²⁵ , G ^{30,33,34} , A ⁴⁵ , L ⁵² , O ⁶⁰ SW ¹⁵ , V ²⁴ , G ^{30,33,34} , A ⁴⁵ , L ⁵¹ , O ⁶⁰	d
HadCM3	(1x) 800–2000	SW ¹⁴ , V ²⁵ , G ^{30,32,34} , A ⁴³ , L ⁵¹ , O ⁶⁰	Schurer et al. (2013)
IPSL-CM5A-LR	(1x) 850–2005	SW ¹⁵ , V ²⁷ , G ^{30,33,34} , O ⁶⁰	
MIROC-ESM	(1x) 850–2005	SW ¹⁶ , V ²⁵ , G ^{30,34,39} , O ⁶⁰	e
MPI-ESM-P	(1x) 850–2005	SW ¹⁵ , V ²⁵ , G ^{30,33,34} , A ⁴⁵ , L ⁵¹ , O ⁶⁰	

Notes:

^a Key for superscript indices in forcing acronyms:

[1] Solar:

- [10] Bard et al. (2000)
- [11] Bard et al. (2000) spliced to Lean et al. (1995a)
- [12] Solanki et al. (2004)
- [13] Krivova et al. (2007)
- [14] Steinhilber et al. (2009) spliced to Wang et al. (2005)
- [15] Vieira and Solanki (2010) spliced to Wang et al. (2005)
- [16] Delaguerre and Bard (2011) spliced to Wang et al. (2005)

[2] Volcanic:

- [20] Crowley (2000)
- [21] Ammann et al. (2003)
- [22] Total solar irradiances from Crowley (2000) converted to aerosol masses using Ammann et al. (2003) regression coefficients.

[23] Crowley et al. (2003)

[24] Gao et al. (2008). In the GISS-E2-R simulations this forcing was implemented twice as large as in Gao et al. (2008).

[25] Crowley and Unterman (2013)

[26] Robertson et al. (2001)

[27] Ammann et al. (2007)

[3] WMGHGs:

[30] Flückiger et al. (1999; 2002); Machida et al. (1995)

[31] Etheridge et al. (1996)

[32] Johns et al. (2003)

[33] Hansen and Sato (2004)

[34] MacFarling Meure et al. (2006)

[35] Blunier et al. (1995)

[36] Etheridge et al. (1998)

[37] Battle et al. (1996)

[38] Robertson et al. (2001)

[39] CO₂ diagnosed by the model.

[4] Aerosols:

[40] Lefohn et al. (1999)

[41] Joos et al. (2001)

[42] Roeckner et al. (1999)

[43] Johns et al. (2003)

[44] Boucher and Pham (2002)

[45] Lamarque et al. (2010). See Sections 8.2 and 8.3

[5] Land use, land cover:

[50] Wilson and Henderson-Sellers (1985)

[51] Pongratz et al. (2009) spliced to Hurrell et al. (2006)

[52] Kaplan et al. (2011)

[53] Pongratz et al. (2008)

(continued on next page)

Table 5.A.1 Notes (continued)

- [54] Ramankutty and Foley (1999)
 [55] Goldewijk (2001)
[6] Orbital:
 [60] Berger (1978)
 [61] Bretagnon and Francou (1988)
 [62] Berger and Loutre (1991)
 [63] Laskar et al. (2004)
- ^b This simulation was only used in Figure 5.8, using NH temperature adjusted by Osborn et al. (2006).
^c The FGOALS-g1 experiment is available in the PMIP3 repository, but the forcing configuration is different from Schmidt et al (2011; 2012b) recommendations so it is included here within the pre-PMIP3 ensemble.
^d The GISS-E2-R experiments with Gao et al. (2008) volcanic forcing were not used in Figures 5.8, 5.9 or 5.12. See [24].
^e This simulation was only used in Figure 5.8, using drift-corrected NH temperature.

Table 5.A.2 | Summary of atmospheric carbon dioxide (CO_2) proxy methods and confidence assessment of their main assumptions.

Method	Scientific Rationale	Estimated Applicability	Limitations	Main Assumptions (relative confidence)
Alkenone (phytoplankton biomarker) carbon isotopes	Measurements of carbon isotope ratios of marine sedimentary alkenones (or other organic compounds) allows determination of the isotopic fractionation factor during carbon fixation (ϵ_p) from which pCO_2 can be calculated.	100 to ~4000 ppm; 0 to 100 Ma	Alkenones are often rare in oligotrophic areas and sometimes absent. Method relies on empirical calibration and $\delta^{13}\text{C}$ is sensitive to other environmental factors, especially nutrient-related variables. Method has been used successfully to reconstruct glacial-interglacial changes.	Measured alkenone carbon isotope ratio is accurate and precise (high). Ambient aqueous partial pressure of carbon dioxide (pCO_2) has a quantifiable relationship with ϵ_p that can be distinguished from the nutrient-related physiological factors such as algal growth rate, cell size, cell geometry and light-limited growth (medium). Aqueous pCO_2 is in equilibrium with atmospheric pCO_2 (medium). Carbon isotope fractionation in modern alkenone-producing species is the same in ancient species and constant through time (medium). Levels of biological productivity (e.g., dissolved phosphate concentrations) can be calculated (high). Carbon isotope ratio of aqueous CO_2 in the mixed layer can be determined (medium). Sea surface temperature can be determined (high). Atmospheric partial pressure of oxygen (pO_2) is known or assumed (medium). Diagenetic effects are minimal, or can be quantified (medium).
Boron isotopes in foraminifera	Boron isotope ratios ($\delta^{11}\text{B}$) in foraminifera (or other calcifying organisms) give paleo-pH from which pCO_2 can be calculated if a value for a second carbonate system parameter (e.g., alkalinity) is assumed.	100 to ~4000 ppm; 0 to 100 Ma	Calculated pCO_2 is very sensitive to the boron isotope ratio of seawater which is relatively poorly known, especially for the earlier Cenozoic. Effects of foraminiferal preservation are not well understood. Method has been used successfully to reconstruct glacial-interglacial changes.	Measured boron isotope ratio is accurate and precise (high). The equilibrium constant for dissociation of boric acid and boron isotopic fractionation between B(OH)_3 and B(OH)_4^- are well known (high). Boron incorporation into carbonate is predominantly from borate ion (high). Boron isotope ratio of foraminifer calcification reflects ambient surface seawater pH (high). Aqueous pCO_2 is in equilibrium with atmospheric pCO_2 (medium). Habitats of extinct species can be determined (high). There is no vital effect fractionation in extinct species, or it can be determined (medium). The boron isotope ratio of seawater ($\delta^{11}\text{B}_{\text{sw}}$) can be determined (medium). Ocean alkalinity or concentration of Total Dissolved Inorganic Carbon can be determined (high). Sea surface temperature (SST) and salinity (SSS) can be determined (high). Diagenetic effects are minimal or can be quantified (high).
Carbon isotopes in soil carbonate and organic matter	Atmospheric pCO_2 affects the relationship between the $\delta^{13}\text{C}$ of soil CO_2 and the $\delta^{13}\text{C}$ of soil organic matter at depth in certain soil types, hence measurement of these parameters in paleosols can be used to calculate past pCO_2 .	1000 to ~4000 ppm; 0 to 400 Ma	Method works better for some soil types than others. CO_2 loss is difficult to quantify and method and effects of late diagenesis may be difficult to determine.	Isotopic composition of soil CO_2 is reflected in soil carbonates below a depth of 50 cm. (medium). The concentration of respiration CO_2 in the soil is known or assumed (medium). Isotopic composition of atmospheric CO_2 is known or can be inferred (low). Soil carbonates were precipitated in the vadose zone in exchange with atmospheric CO_2 (high). The original depth profile of a paleosol can be determined (low). Burial (late) diagenetic effects are minimal or can be quantified (high).
Stomata in plant leaves	The relative frequency of stomata on fossil leaves (Stomatal Index; (Salisbury, 1928) can be used to calculate past atmospheric CO_2 levels.	100 to ~1000 ppm; 0 to 400 Ma	Closely related species have very different responses to pCO_2 . The assumption that short-term response is the same as the evolutionary response is difficult to test. This and the shape of the calibration curves mean that much greater certainty applies to low pCO_2 and short time scales.	Measured stomatal index is accurate and precise (high). Measured stomatal index is representative of the plant (high). The target plants adjust their stomatal index of leaves to optimize CO_2 uptake (medium). Atmospheric pCO_2 close to the plant is representative of the atmosphere as a whole (medium). The quantitative relationship between stomatal index and CO_2 observed on short time scales (ecophenotypic or 'plastic response') applies over evolutionary time (low). Environmental factors such as irradiance, atmospheric moisture, water availability, temperature, and nutrient availability do not affect the relationship between stomatal index and CO_2 (medium). Stomatal index response to CO_2 of extinct species can be determined or assumed (low). Taphonomic processes do not affect stomatal index counts (high). Diagenetic processes do not affect stomatal index counts (high).

Table 5.A.3 | Summary of sea surface temperature (SST) proxy methods and confidence assessment of their main assumptions.

Method	Scientific Rationale	Estimated Applicability	Limitations	Main Assumptions (relative confidence)
$\delta^{18}\text{O}$ of mixed-layer planktonic foraminifera	Partitioning of $\delta^{18}\text{O}/\delta^{16}\text{O}$ from seawater into calcite shells of all foraminifera is temperature dependent. Verified by theoretical, field and laboratory studies. Utilizes extant and extinct species that resided in the photic zone.	0°C to 50°C; 0 to 150 Ma	The $\delta^{18}\text{O}/\delta^{16}\text{O}$ ratios of recrystallized planktonic foraminifer shells in carbonate-rich sediments are biased toward colder seafloor temperatures, and at most, can only constrain the lower limit of SST. The transition in preservation is progressive with age. Well-preserved forams from clay-rich sequences on continental margins are preferred. Diagenetic calcite is detectable by visual and microscopic techniques.	Analytical errors are negligible (<i>high</i>). Sensitivity to T is high and similar to modern descendants (<i>high</i>). Seawater $\delta^{18}\text{O}$ is known. The uncertainty varies with time depending on presence of continental ice-sheets, though error is negligible in the Pleistocene and during minimal ice periods such as the Eocene ($<\pm 0.25^\circ\text{C}$). Error doubles during periods of Oligocene and early Neogene glaciation because of weak constraints on ice-volume (<i>medium to high</i>). Species lives in the mixed-layer and thus records SST (<i>high</i>). Local salinity/seawater $\delta^{18}\text{O}$ is known (<i>low to medium</i>). Carbonate ion/pH is similar to modern (<i>medium, high</i>). Foraminifera from clay-rich sequences are well preserved and $\delta^{18}\text{O}/\delta^{16}\text{O}$ ratios unaffected by diagenesis (<i>high</i>). Foraminifera from carbonate-rich pelagic sequences are well preserved and ratios unaffected by diagenesis (<i>medium to low</i> ; decreasing confidence with age). Biased towards summer SST in polar oceans (<i>medium</i>).
Mg/Ca in mixed-layer planktonic foraminifera	Partitioning of Mg/Ca from seawater into calcite shells is temperature dependent. Calibration to T is based on empirical field and laboratory culturing studies, as Mg concentrations of inorganically precipitated calcite are an order of magnitude higher than in biogenic calcite. There is no ice-volume influence on seawater Mg/Ca, though sensitivity does change with seawater Mg concentration.	5°C to 35°C; 0 to 65 Ma	Diagenetic recrystallization of foram shells can bias ratios, though the direction of bias is unknown and comparisons with other proxies suggest it is minor. The Mg/Ca is also slightly sensitive to seawater pH. Long-term changes in seawater Mg/Ca, on the order of a 2–5%/10 Myr, must be constrained via models.	Analytical errors are negligible (<i>high</i>). Mg containing oxide and organic contaminants have been removed by oxidative/reductive cleaning (<i>high</i>). Sensitivity to T in extinct species is similar to modern species (<i>medium</i>). Species lives in the mixed-layer and thus records SST (<i>high</i>). Seawater Mg/Ca is known (<i>high to low</i> ; decreasing confidence with time). Surface water carbonate ion/pH is similar to modern (<i>medium</i>). Foraminifera from clay-rich sequences are well preserved and ratios unaffected by diagenesis (<i>high</i>). Foraminifera from carbonate-rich pelagic sequences are well preserved and ratios unaffected by diagenesis (<i>high to low</i> ; decreasing confidence with age). Biased towards summer SST in polar oceans (<i>medium</i>).
TEX_{86} index in Archaea	The ratio of cyclopentane rings in archaeal tetraether lipids (TEX), i.e., isoprenoid glycerol dibiphytanyl glycerol tetraethers (GDGTs), is sensitive to the temperature of growth environment. The relationship and calibration with temperature is empirical (based on core tops), as the underlying mechanism(s) for this relationship has yet to be identified. Verification of field calibrations with laboratory cultures is still in progress. The compounds are extracted from bulk sediments.	1°C to 40°C; 0 to 150 Ma	The depth from which the bulk of sedimentary GDGT's are produced is assumed to be the mixed-layer though this cannot be verified, for the modern or past. At least two species with differing ecologies appear to be producing the tetraethers. The GDGT signal is ultimately an integrated community signal allowing the potential for evolutionary changes to influence regional signals over time. Tetraethers are found in measurable abundances on continental shelves and/or organic rich sediments.	Analytical errors are small (<i>high</i>). Sensitivity to T similar to modern (<i>medium</i>). Species that produced tropical sedimentary GDGT's resided mainly in the mixed-layer and thus records SST (<i>high to medium</i>). Species that produced the sedimentary GDGT's in the sub-polar to polar regions mainly resided in the mixed-layer and thus records SST (<i>low</i>). No alteration of GDGT ratios during degradation of compounds (<i>medium to low</i> ; decreasing confidence with age). No contamination by GDGT's derived from terrestrial sources (<i>high to medium</i> if BIT index <0.3). Biased towards summer SST in polar oceans (<i>medium</i>).
UK_{37} Index in Algae	Based on the relative concentration of C_{37} methyl ketones derived from the cells of haptophyte phytoplankton. Calibrations are empirically derived through field and culture studies.	5°C to 28°C; 0 to 50 Ma	The distribution of haptophyte algae ranges from sub-polar to tropical.	Analytical errors are negligible (<i>high</i>). Sensitivity to SST similar to modern (<i>high to medium</i> ; decreasing confidence with time). Species that produced the sedimentary alkenones lived in the mixed-layer and thus record SST (<i>high</i>). No alteration of alkenone saturation index during degradation of compounds (<i>medium</i> ; decreasing confidence with age). Biased towards summer SST in polar oceans (<i>medium</i>).
Microfossil census modern analogue techniques	Utilises a statistical correlation between extant planktonic microfossil assemblage data (most commonly foraminifera, but also diatoms and radiolarians) and climate parameters. Most commonly used statistical methods are modern analogue technique (MAT) and artificial neural network (ANN).	0°C to 40°C; 0 to 5 Ma	Dependent on quality, coverage, size and representativeness of the core top modern analogue data base. Extant species reduce with increasing age. This and paleogeographic and ocean circulation differences with age-limit applicability to less than 1 Ma.	The composition of modern assemblages can be correlated to SST (<i>high</i>). Sensitivity of paleo-assemblages to SST is similar to modern (<i>high</i> , but decreases with increasing age). Eurythermal assemblages responding to non-temperature (e.g., nutrient availability) influences can be identified (<i>medium</i>). That the extant species used to reconstruct SST mainly reside in the mixed layer (<i>medium to high</i>). Depositional and post-depositional processes have not biased the assemblage (<i>medium to high</i>).

Table 5.A.4 | Assessment of leads and lags between Antarctic, hemispheric temperatures and atmospheric CO₂ concentration during terminations. Chronological synthesis of publications, main findings, incorporation in IPCC assessments and key uncertainties.

Reference	Investigated Period	Source CO ₂ Data	Source Temperature Data	Lag Quantification Method	Lag Between Temperature and CO ₂ (positive, temperature lead)	Key Limitations
<i>TAR: From a detailed study of the last three glacial terminations in the Vostok ice core, Fischer et al., (1999) conclude that CO₂ increases started 600 ± 400 years after the Antarctic warming. However, considering the large uncertainty in the ages of the CO₂ and ice (1000 years or more if we consider the ice accumulation rate uncertainty), Petit et al. (1999) felt it premature to ascertain the sign of the phase relationship between CO₂ and Antarctic temperature at the initiation of the terminations. In any event, CO₂ changes parallel Antarctic temperature changes during deglaciations (Sowers and Bender, 1995; Blunier et al., 1997; Petit et al., 1999).</i>						
Fischer et al. (1999)	Termination I	Taylor Dome, Byrd ^a (CH ₄ synchronized ages scales)	Byrd δ ¹⁸ O, Vostok δD (CH ₄ , synchronized age)	Maximum at onset of interglacial periods	Antarctica: 600 ± 400 years	Ice core synchronization for Termination I (~300 years). Gas age–ice age difference simulated by firn models for interglacial conditions could be overestimated by ~400 years. Signal-to-noise ratio. Resolution of CO ₂ measurements and firnification smoothing (~300 years).
	Terminations I, II, III	Vostok ^a (gas age scales based on firn modelling)	Vostok δD (GT4 ice age scale)	Onset of transitions	Antarctica: in phase within uncertainties Positive	Gas age–ice age difference simulated by firn models for glacial conditions could be overestimated by up to 1500 years. Resolution of CO ₂ measurements and firnification smoothing (~300 years). Signal to noise ratio (1 ice core).
Petit et al. (1999) Pépin et al. (2001)	Terminations I, II, III, IV	Vostok ^a (GT4 gas age scale based on firn modelling)	Vostok δD (GT4 ice age scale)	Lagged generalised least square regression with parametric bootstrap resampling, entire record	Antarctica: 1300 ± 1000 years	
Mudelsee (2001)	0–420 ka	Vostok ^a (GT4 gas age scale)	Vostok δD (GT4 ice age scale)			
<i>AR4: High-resolution ice core records of temperature proxies and CO₂ during deglaciation indicates that Antarctic temperature starts to rise several hundred years before CO₂ (Monnin et al., 2001; Caillon et al., 2003). During the last deglaciation, and possibly also the three previous ones, the onset of warming at both high southern and northern latitudes preceded by several thousand years the first signals of significant sea level increase resulting from the melting of the northern ice sheets. Linked with the rapid warming at high northern latitudes (Petit et al., 1999; Shackleton, 2000; Répin et al., 2001). Current data are not accurate enough to identify whether warming started earlier in the SH or NH, but a major deglacial feature is the difference between North and South in terms of the magnitude and timing of strong reversals in the warming trend, which are not in phase between the hemispheres and are more pronounced in the NH (Blunier and Brook, 2001).</i>						
Monnin et al. (2001)	Termination I	High resolution data from EDC on EDC1 gas age scale (based on firn modelling)	EDC (EPICA (European Project for Ice Coring in Antarctica Dome C) on EDC1 ice age scale)	Crossing points of linear fit	Antarctica: 800 ± 600 years	Gas age–ice age difference (~1000 years). Signal to noise ratio (1 ice core).
Caillon et al. (2003)	Termination III	Vostok on GT4 gas age scale	Vostok δ ⁴⁰ Ar on GT4 gas age scale	Maximum lagged correlation	Antarctica: 800 ± 200 years	Relationship between δ ⁴⁰ Ar and temperature assumed to be instantaneous. The 800 years is a minimum CO ₂ -temperature lag which does not account for a possible delayed response of firn gravitational fractionation to surface temperature change.
Shakun et al. (2012)	Termination I	EDC age scale synchronized to GICC05 ^b (Lemieux-Durand et al., 2010)	NH: stack of 50 records including 2 Greenland ice cores SH: stack of 30 records incl. 4 ice cores (Vostok, EDML, EDC, Dome F) on their original age scale	Lag correlation (20–10 kyr) using Monte-Carlo statistics	SH: 620 ± 660 years NH: -720 ± 660 years Global: -460 ± 340 years	Uncertainties in the original age scales of each record: e.g., reservoir ages of marine sediments, radiocarbon calibration (IntCal04), Antarctic gas/ice chronology. Assumption that time scale errors (e.g., from reservoir ages or ice core chronologies) are independent from each other. This could lead to higher-than-reported lag estimation uncertainties. Similar limitations as in earlier studies for Antarctic temperature lead on CO ₂ . Non stability of the phase lags: global temperature leads CO ₂ at the onset of deglacial warming.

(continued on next page)

Table 5.A.4 (continued)

Reference	Investigated Period	Source CO ₂ Data	Source Temperature Data	Lag Quantification Method	Lag Between Temperature and CO ₂ (positive, temperature lead)	Key Limitations
Pedro et al. (2012)	Siple Dome and Byrd, synchronized to GICC05 ^b age scale	δ ¹⁸ O composite (Law Dome, Siple Dome, Byrd, EDML and TALDICE ^a ice cores) synchronized to GICC05 ^b using firm modeling (Pedro et al., 2011)	Lag correlation (9–21 kyr) and derivative lag correlation	Antarctica: –60 to 380 years	Uncertainty on gas – ice age difference in high accumulation sites (<300 years) and on synchronization methods to GICC05.	
(Parfenin et al., 2013)	EDC, new gas age scale produced from the modified EDC3 ice age scale using lock-in depth derived from δ ¹⁵ N of N ₂ and adjusted to be consistent with GICC05 ^b gas age scale. Processes affecting the gas lock-in depth such as impurities are implicitly taken into account when using δ ¹⁵ N (no use of firm models).	Stack temperature profile derived from water isotopes from EDC ^a , Vostok ^a , Dome Fuji ^a , TALDICE ^a and EDML ^a synchronized to a modified EDC3 ice age scale	Monte-Carlo algorithm at linear break points	Antarctica: Warming onset: –10 ± 160 years Boiling onset: 260 ± 130 years Younger Dryas onset: –60 ± 120 years Holocene onset: 500 ± 90 years	Data resolution (145 year for Byrd CO ₂ , 266 year for Siple CO ₂). The CO ₂ data were resampled at 20 year resolution prior to the lag analysis, which may lead to an underestimation of the statistical error in the lag determination. Temperature versus other (e.g., elevation, moisture origin) signals in coastal ice core δ ¹⁸ O.	

Notes:

^a Names of different Antarctic ice cores (Byrd, Taylor Dome, Vostok, Siple Dome, Law Dome, TALDICE, Dome Fuji, EDML, EDC), with different locations, surface climate and firnification conditions. For the most inland sites (Vostok, EDC, Dome Fuji, Dome Siple Dome), gas ages are lower than ice ages by 1500 to 2000 years (interglacial conditions) and 5000–5500 years (glacial conditions) while this gas age–ice age difference is lower (400 to 800 years) for coastal/higher accumulation sites (Byrd, Law Dome, Siple Dome).

^b GICC05: Greenland Ice Core Chronology 2005, based on annual layer counting in Greenland (NGRIP, GRIP and DYE3 ice cores) (Rasmussen et al., 2006), back to 60 ka (Svensson et al., 2008). The synchronism between rapid shifts in Greenland climate and in atmospheric CH₄ variations allows to transfer GICC05 to Greenland and then to Antarctic CH₄ variations (Blunier et al., 2007).

Additional point: CO₂–Antarctic temperature phase during AIM events.

Studies on CO₂ phasing relative to CH₄ during Dansgaard–Oeschger (DO) event onsets (Ahn and Brook, 2008; Ahn et al., 2012; Bereiter et al., 2012) suggest a lag of maximum CO₂ concentration relative to the Antarctic Isotope Maxima (AIM) 19, 20, 21, 23 and 24 by 260 ± 220 years during MIS5 and 670 to 870 years ± 360 years relative to AIM 12, 14, 17 during MIS3 (Bereiter et al., 2012). Accordingly, the lag is dependent on the climate state. A lag is not discernible for shorter AIM. This study avoids the ice age–gas age difference problem, but relies on the bipolar seesaw concept, i.e., it assumes that maximum Antarctic temperatures are coincident to the onset of DO events and the concurrent CH₄ increase.

Table 5.A.5 | Summary of seasonal estimates of terrestrial surface temperature anomalies ($^{\circ}\text{C}$) for the Last Interglacial (LIG) plotted in Figure 5.6. *pdf*-method stands for probability-density function method. Dating methods: AMS=Accelerator mass spectrometry; IRSL=Infrared stimulated luminescence; OSL=Optically stimulated luminescence; TL=thermoluminescence.

Site	Latitude ($^{\circ}\text{N}$)	Longitude ($^{\circ}\text{E}$)	Elevation (m asl)	Dating	Proxy		Temperature Anomaly ($^{\circ}\text{C}$)	References
					July	January		
Netherlands, Amsterdam Terminal	52.38	4.91	1	Eemian, U/Th	Pollen, diatoms, molluscs, foraminifera, dinoflagellates, ostracods, heavy minerals, paleomagnetism, grain-size, trace elements	2	3	(Zagwijn, 1996; van Leeuwen et al., 2000; Beets et al., 2006)
E Canada, Addington Forks, Nova Scotia	45.65	-62.1	50	Uranium-series	Pollen	4		(Dreimanis, 1992)
NW America, Humptulips	47.28	-123.55	100	Interpolation with ^{14}C dates (peak) of the same core	Pollen	1		(Heusser and Heusser, 1990)
NE Siberia, Lake El'gygytgyn	67.5	172	492	TL	Pollen	6	14	(Lozhkin and Anderson, 2006)
NW Alaska, Squirrel Lake	67.1	-160.38	91	TL	Pollen, plant macrofossils	1.5	-2	(Berger and Anderson, 2000)
SE Baffin Island, Robinson Lake	63.38	-61.25	170	TL, IRSL	Pollen, diatoms, macrofossils	5		(Miller et al., 1999; Fréchette et al., 2006)
Sweden, Leveäniemi	67.63	21.02	380	125 ka	Pollen, <i>pdf</i> method	2.1	6.6	(Kühl, 2003, and ref. therein)
Finland, Eijärvi	63.43	23.33	67	125 ka	Pollen, <i>pdf</i> method	2.3	10.3	(Kühl, 2003, and ref. therein)
Finland, Nöörinkylä	62.58	22.02	110	125 ka	Pollen, <i>pdf</i> method	1.3	7.7	(Kühl, 2003, and ref. therein)
Estland, Prangli	59.65	25.08	5	125 ka	Pollen, <i>pdf</i> method	1.7	3.2	(Kühl, 2003, and ref. therein)
Estland, Weva-Ringen	58.33	26.73	50	125 ka	Pollen, <i>pdf</i> method	1.3	6.8	(Kühl, 2003, and ref. therein)
Norway, Fjøsanger	60.35	5.33	5	125 ka	Pollen, <i>pdf</i> method	2.9	1.6	(Kühl, 2003, and ref. therein)
Denmark, Hollerup	56.7	9.83	40	125 ka	Pollen, <i>pdf</i> method	1.1	3.7	(Kühl, 2003, and ref. therein)
Germany, Husum	54.52	9.17	2	125 ka	Pollen, <i>pdf</i> method	2.3	-0.3	(Kühl, 2003, and ref. therein)
Germany, Rederstall	54.28	9.25	0	125 ka	Pollen, <i>pdf</i> method	0.3	1	(Kühl, 2003, and ref. therein)
Germany, Odderade	54.23	9.28	7	125 ka	Pollen, <i>pdf</i> method	1.8	1.4	(Kühl, 2003, and ref. therein)
Germany, Helgoland	53.95	8.85	-1	125 ka	Pollen & macrofossils, <i>pdf</i> method	2	0.6	(Kühl, 2003, and ref. therein)
Germany, Oerel	53.48	9.07	12.5	125 ka	Pollen, <i>pdf</i> method	1.1	0.6	(Kühl, 2003, and ref. therein)
Germany, Quakenbrück	52.4	7.57	26	125 ka	Pollen, <i>pdf</i> method	1.4	0.3	(Kühl, 2003, and ref. therein)
Netherlands, Amersfoort	52.15	5.38	3	125 ka	Pollen, <i>pdf</i> method	-0.3	0.5	(Kühl, 2003, and ref. therein)
Germany, Wallensen	52	9.4	160	125 ka	Pollen & macrofossils, <i>pdf</i> method	1.9	-0.7	(Kühl, 2003, and ref. therein)
Germany, Neumark-Nord	51.33	11.88	90	125 ka	Pollen & macrofossils, <i>pdf</i> method	1.4	0.5	(Kühl, 2003, and ref. therein)
Germany, Gräbschütz	51.48	12.28	100	125 ka	Pollen & macrofossils, <i>pdf</i> method	1.3	-0.2	(Kühl, 2003, and ref. therein)
Germany, Schönfeld	51.8	13.89	65	125 ka	Pollen, <i>pdf</i> method	-0.5	2.6	(Kühl, 2003, and ref. therein)
Germany, Krittilitz	51.43	14.78	150	125 ka	Pollen, <i>pdf</i> method	2.4	-0.9	(Kühl, 2003, and ref. therein)
Poland, Imbramowice	50.88	16.57	175	125 ka	Pollen & macrofossils, <i>pdf</i> method	2.5	3.4	(Kühl, 2003, and ref. therein)
Poland, Zgierz-Rudniki	51.87	19.42	200	125 ka	Pollen & macrofossils, <i>pdf</i> method	0.2	2.6	(Kühl, 2003, and ref. therein)
Poland, Włodysławow	52.13	18.47	100	125 ka	Pollen & macrofossils, <i>pdf</i> method			(Kühl, 2003, and ref. therein)
Poland, Główczyn	52.48	20.21	124	125 ka	Pollen, <i>pdf</i> method	1.4	3.6	(Kühl, 2003, and ref. therein)
Poland, Gora Kalwaria	51.98	21.18	100	125 ka	Pollen & macrofossils, <i>pdf</i> method	0.3	1.9	(Kühl, 2003, and ref. therein)
Poland, Nakło	53.15	17.6	62	125 ka	Pollen & macrofossils, <i>pdf</i> method	0.6	3	(Kühl, 2003, and ref. therein)
Poland, Grudziądz	53.48	18.75	10	125 ka	Pollen, <i>pdf</i> method	0.5	1.6	(Kühl, 2003, and ref. therein)
England, Wing	52.62	-0.78	119	125 ka	Pollen, <i>pdf</i> method	2.4	-0.5	(Kühl, 2003, and ref. therein)

(continued on next page)

Table 5.A.5 (continued)

Site	Latitude (°N)	Longitude (°E)	Elevation (m asl)	Dating	Proxy		Temperature Anomaly (°C)	References
					July	January		
England, Bobbitshole	52.05	1.15	3	125 ka	Pollen & macrofossils, <i>paf</i> method	2.5	-2.3	(Kühl, 2003, and ref. therein)
England, Selsey	50.42	0.48	0	125 ka	Pollen & macrofossils, <i>paf</i> method	0.7	-2.2	(Kühl, 2003, and ref. therein)
England, Stone	50.42	-1.02	0	125 ka	Pollen & macrofossils, <i>paf</i> method	2.9	-2.3	(Kühl, 2003, and ref. therein)
France, La Grande Pile	47.73	6.5	330	125 ka	Pollen, <i>paf</i> method	0.5	-0.7	(Kühl, 2003, and ref. therein)
Germany, Krumbach	48.04	9.5	606	125 ka	Pollen, <i>paf</i> method	0.5	2.3	(Kühl, 2003, and ref. therein)
Germany, Jammertal	48.1	9.72	578	125 ka	Pollen, <i>paf</i> method	0	0.5	(Kühl, 2003, and ref. therein)
Germany, Sämerberg	47.75	12.2	600	125 ka	Pollen & macrofossils, <i>paf</i> method	2.7	4.1	(Kühl, 2003, and ref. therein)
Germany, Zeifen	47.93	12.83	427	125 ka	Pollen & macrofossils, <i>paf</i> method	3.4	2.5	(Kühl, 2003, and ref. therein)
Austria, Mondsee	47.51	13.21	534	125 ka	Pollen & macrofossils, <i>vmethod</i>	4.3	1.3	(Kühl, 2003, and ref. therein)
Germany, Eurach	47.29	11.13	610	125 ka	Pollen, <i>paf</i> method	6.4	4.7	(Kühl, 2003, and ref. therein)
Germany, Füramoos	47.91	9.95	662	125 ka	Pollen, modern analogue vegetation (MAV) and probability mutual climatic spheres (PCS)	-2.8	-1.2	(Müller, 2001)
Swiss, Gondiswil-Sellern	47.12	7.88	639	125 ka	Pollen, <i>paf</i> method	0.1	0.4	(Kühl, 2003, and ref. therein)
Swiss, Melkirch	47	7.37	620	125 ka	Pollen, <i>paf</i> method	0.3	-0.3	(Kühl, 2003, and ref. therein)
Swiss, Melkirch II	47.01	7.33	620	125 ka	Pollen, modern analogue vegetation (MAV) and probability mutual climatic spheres (PCS)	-1.2	-4.5	(Welti, 1988)
Swiss, Beerenmöli	47.06	7.51	649	125 ka	Pollen, modern analogue vegetation (MAV) and probability mutual climatic spheres (PCS)	-1.1	-5.5	(Wegmüller, 1992)
France, Lac Du Bouchet	44.55	3.47	1200	125 ka	Pollen, <i>paf</i> method	1.7	-0.2	(Kühl, 2003, and ref. therein)
Italia, Valle di Castiglione	41.85	12.73	110	125 ka	Pollen, <i>paf</i> method	-3.4	-5.9	(Kühl, 2003, and ref. therein)
Romania, Turbata	47.25	23.3	275	U/Th, 125 ka	Pollen, <i>paf</i> method	-1.2	2.4	(Kühl, 2003, and ref. therein)
Greece, Tenaghi Phillipon	41.17	24.33	40	125 ka	Pollen, <i>paf</i> method	0.9	2	(Kühl, 2003, and ref. therein)
Greece, Ioannina	39.67	20.85	472	125 ka	Pollen, <i>paf</i> method	-1.9	-1.9	(Kühl, 2003, and ref. therein)
Germany, Bispingen	53.08	9.98	100	TL, 125 ka	Pollen, <i>paf</i> method	1.2	0.9	(Kühl, 2003, and ref. therein)
Germany, Großen	52.02	12.08	95	TL, 125 ka	Pollen & macrofossils, <i>paf</i> method	0.4	1.8	(Kühl, 2003, and ref. therein)
Germany, Klinge	51.75	14.52	10	pollen correlation	Pollen (Grichuk, 1985)	0	2	(Novenko et al., 2008)
Germany, Ober-Rheinebene near Darmstadt	49.82	8.4	90	Eem	Vegetation, mammals			(von Königswald, 2007)
France, La Flachere	45.23	5.58	333	125 ka	Pollen, modern analogue vegetation (MAV) and probability mutual climatic spheres (PCS)	-0.9	-14.4	(Peschke et al., 2000)
France, Lathuile	45.75	6.14	452	125 ka	Pollen, carbon isotopes	-0.5	-2.2	(Klotz et al., 2003)
France, La Grande Pile	47.73	6.5	330	TL, 125 ka	Pollen, modern analogue vegetation (MAV) and probability mutual climatic spheres (PCS)	10	-15	(Rousseau et al., 2007)
Japan, Lake Biwa	35.33	136.17	86	tephrochronological and magnetostratigraphic information	Pollen	-3	-2.5	(Nakagawa et al., 2008)
Siberia, Lake Baikal, Continental Ridge CON01-603-2	53.95	108.9	-386	AMS, 125 ka	Pollen	-5.5	-1.5	(Tarasov et al., 2011)
Bol'shoi Ilyakhovsky Island	73.33	141.5	40	MIS 5, ca. 130–110 ka (IRSL)	Pollen, beetles, Chironomids, rhizopods, palaeomagnetic, BMA	2	-1	(Tarasov et al., 2005)
Wairarapa Valley, New Zealand	-41.37	175.07	10	OSL, MIS 5e	Beetles	4.5	2.8 winter	(Andreev et al., 2004)
						2.1 summer		(Mitra, 2003)

5.A.1 Additional Information to Section 5.3.5

Section 5.3.5 assesses knowledge of changes in hemispheric and global temperature over the last 2 ka from a range of studies, reconstructions and simulations. Tables 5.A.1 and 5.A.6 provide further information about the datasets used in Figures 5.7–5.9 and 5.12, and the construction of Figure 5.8 is described in more detail. All reconstructions assessed in, or published since, AR4 were considered, but those that have been superseded by a related study using an expanded proxy dataset and/or updated statistical methods were excluded.

Figure 5.8 compares simulated and reconstructed NH temperature changes (see caption). Some reconstructions represent a smaller spatial domain than the full NH or a specific season, while annual temperatures for the full NH mean are shown for the simulations. Multi-model means and estimated 90% multi-model ranges are shown by the thick and thin lines, respectively, for two groups of simulations (Table 5.A.1): those forced by stronger (weaker) solar variability in red (blue). Note that the strength of the solar variability is not the only difference between these groups: the GCMs and the other forcings are also different between the groups. In Figure 5.7, the reconstructions are shown as deviations from their 1881–1980 means, which allows them to be compared with the instrumental record. In Figure 5.8a, all timeseries are expressed as anomalies from their 1500–1850 mean (prior to smoothing with a 30-year Gaussian-weighted filter, truncated 7 years from the end of each series to reduce end-effects of the filter) because the comparison of simulations and reconstructions is less sensitive to errors in anthropogenic aerosol forcing applied to the models when a pre-industrial reference period is used, and less sensitive to different realisations of internal variability with a multi-century reference period. The grey shading represents a measure of the overlapping reconstruction confidence intervals, with scores of 1 and 2 assigned to temperatures within ± 1.645 standard deviation (90% confidence range) or ± 1 standard deviation, respectively, then summed over all reconstructions and scaled so that the maximum score is dark grey, and minimum score is pale grey. This allows the multi-model ensembles to be compared with the ensemble of reconstructed NH temperatures, taking into account the published confidence intervals.

The superposed composites (time segments from selected periods positioned so that the years with peak negative forcing are aligned; top panels of Figure 5.8b–d) compare the simulated and reconstructed temperatures (bottom panels) associated with (b) individual volcanic forcing events; (c) multi-decadal changes in volcanic activity; (d) multi-decadal changes in solar irradiance. Only reconstructions capable of resolving (b) interannual or (c, d) interdecadal variations are used. The thick green line in Figure 5.8d shows the composite mean of the volcanic forcing, also band-pass filtered, but constructed using the solar composite periods to demonstrate the changes in volcanic forcing that are coincident with solar variability. The composite of individual volcanic events shown in (b) is formed by aligned time segments centred on the 12 years (1442, 1456, 1600, 1641, 1674, 1696, 1816, 1835, 1884, 1903, 1983 and 1992) during 1400–1999 that the Crowley and Unterman (2013) volcanic forcing history exceeds 1.0 W m^{-2} below the 1500–1899 mean volcanic forcing, excluding events within 7 years (before or after) of a stronger event. The composite of multi-decadal changes in volcanic forcing shown in (c) is formed from 80-year periods

centred on the five years (1259, 1456, 1599, 1695 and 1814) during 850–1999 when the Crowley and Unterman (2013) volcanic forcing, smoothed with a 40-year Gaussian-weighted filter, exceeds 0.2 W m^{-2} below the 1500–1899 mean volcanic forcing, except that a year is not selected if it is within 39 years of another year that has a larger negative 40-year smoothed volcanic forcing. The composite of the strongest multidecadal changes in the solar forcing shown in (d) is formed from 80-year periods centred on the seven years (1044, 1177, 1451, 1539, 1673, 1801 and 1905) during 850–1999 when the Ammann et al. (2007) solar forcing, band-pass filtered to retain variations on time scales between 20 and 160 years, is reduced by at least 0.1 W m^{-2} over a 40-year period. Reconstructed and simulated temperature timeseries were smoothed with a 40-year Gaussian-weighted filter in (c) or 20-to-160-year band-pass filtered in (d), and each composite was shifted to have zero mean during the (b) 5 or (c, d) 40 years preceding the peak negative forcing.

Table 5.A.6 | Hemispheric and global temperature reconstructions assessed in Table 5.4 and used in Figures 5.7 to 5.9.

Reference [Identifier]	Period (CE)	Resolution	Region ^a	Proxy Coverage ^b				Method & Data
				H	M	L	O	
Briffa et al. (2001) [only used in Figure 5.8b-d due to divergence issue]	1402–1960	Annual (summer)	L 20°N to 90°N	*	☒	□	□	Principal component forward regression of regional composite averages. Tree-ring density network, age effect removed via age-band decomposition.
Christiansen and Ljungqvist (2012) [CL12loc]	1–1973	Annual	L+S 30°N to 90°N	*	*	□	□	Composite average of local records calibrated by local inverse regression. Multi-proxy network.
D'Arrigo et al. (2006) [Da06treecps]	713–1995	Annual	L 20°N to 90°N	*	☒	□	□	Forward linear regression of composite average. Network of long tree-ring width chronologies, age effect removed by Regional Curve Standardisation.
Frank et al. (2007) [Fr07treecps]	831–1992	Annual	L 20°N to 90°N	☒	☒	□	□	Variance matching of composite average, adjusted for artificial changes in variance. Network of long tree-ring width chronologies, age effect removed by Regional Curve Standardisation.
Hegerl et al. (2007) [He07tls]	558–1960	Decadal	L 30°N to 90°N	☒	☒	□	□	Total Least Squares regression. Multi-proxy network.
Juckes et al. (2007) [Ju07cvm]	1000–1980	Annual	L+S 0° to 90°N	☒	☒	□	□	Variance matching of composite average. Multi-proxy network.
Leclercq and Oerlemans (2012) [LO12glac]	1600–2000	Multidecadal	L 0° to 90°N L 90S to 0° L 90°S to 90°N	☒	*	☒	□	Inversion of glacier length response model. 308 glacier records.
Ljungqvist (2010) [Lj10cps]	1–1999	Decadal	L+S 30°N to 90°N	*	☒	□	☒	Variance matching of composite average. Multi-proxy network.
Loehle and McCulloch (2008) [LM08ave]	16–1935	Multidecadal	L+S mostly 0° to 90°N	☒	☒	□	☒	Average of calibrated local records. Multi-proxy network (almost no tree-rings).
Mann et al. (2008) [Ma08cpsl] [Ma08eivl] [Ma08eivf] [Ma08min7eivf]	200–1980	Decadal	L [cpsl/eivl] and L+S [eivf] versions, 0° to 90°N, 0° to 90°S, and 90°S to 90°N	*	*	☒	☒	(i) Variance matching of composite average. (ii) Total Least Squares regression. Multi-proxy network. ^c
Mann et al. (2009) [Ma09regm]	500–1849	Decadal	L+S 0 to 90°N	*	*	☒	☒	Regularized Expectation Maximization with Truncated Total Least Squares. Multi-proxy network. ^c
Moberg et al. (2005) [Mo05wave]	1–1979	Annual	L+S 0° to 90°N	☒	*	☒	□	Variance matching of composites of wavelet decomposed records. Tree-ring width network for short time scales; non-tree-ring network for long time scales.
Pollack and Smardon (2004) [PS04bore]	1500–2000	Centennial	L 0° to 90°N L 0° to 90°S L 90°S to 90°N	☒	*	☒	□	Borehole temperature profiles inversion
Shi et al. (2013) [Sh13pcar]	1000–1998	Annual	L 0 to 90°N	*	☒	□	□	Principal component regression with autoregressive timeseries model. Multi-proxy network (tree-ring and non-tree-ring versions).

Notes:

^a Region: L = land only, L+S = land and sea, latitude range indicated.^b Proxy location and coverage: H = high latitude, M = mid latitude, L = low latitude, O = oceans, □ = none or very few, ☒ = limited, * = moderate^c These studies also present versions without tree-rings or without seven inhomogeneous proxies (including the Lake Korttajärvi sediment records; Tiljander et al., 2003). The latter version is used in Figure 5.7a (Ma08min7eivf) in preference to the reconstruction from the full network. The impact of these seven proxies on the other NH reconstructions is negligible (MA08cpsl) or results in a slightly warmer pre-900 reconstruction compared to the version without them (Ma09regm).